The Dissertation Committee for Zhicheng Xiao Certifies that this is the approved version of the following Dissertation:

WAVE TRANSPORT IN PARITY-TIME SYMMETRIC, TIME-VARYING, AND QUASI-PERIODIC SYSTEMS

Committee:

Andrea Alù, Supervisor

Tsampikos Kottos

Ranjit Gharpurey

Daniel Wasserman

Emily Porter

WAVE TRANSPORT IN PARITY-TIME SYMMETRIC, TIME-VARYING, AND QUASI-PERIODIC SYSTEMS

by

Zhicheng Xiao

Dissertation

Presented to the Faculty of the Graduate School of

The University of Texas at Austin

in Partial Fulfillment

of the Requirements

for the Degree of

Doctor of Philosophy

The University of Texas at Austin

MAY 2021

Dedication

To my family

Acknowledgements

The Ph.D. journey is not only an exploration into uncharted scientific territories but also a fruitful odyssey to build vision, cultivate passion, shape personality, fulfill curiosity, and beyond. It's been a great privilege to work with a group of highly intelligent students, postdocs, research scientists and supporting staffs under the support and guidance of Prof. Andrea Alù. Thus, I am forever grateful to Prof. Andrea Alù for his guidance, encouragement, and enduring support.

I would also like to thank Prof. Tsampikos Kottos who spent lots of time discussing with me on our work and checking my calculations step by step. His passion for physics and love for students define a role model of excellent professor. Meanwhile, I am indebted to our collaborators who partially funded and supervised our work: Prof. Dimitrios Sounas at Wayne State University, Prof. Younes Ra'di at City University of New York, Prof. Sergei Tretyakov at Alto University, Prof. Harish Krishnaswamy at Columbia University, Prof. Matteo Rinaldi at Northeastern University. Thanks are due to my committee members Prof. Ranjit Gharpurey, Prof. Emily Porter, and Prof. Daniel Wasserman whose suggestion helped improve this dissertation significantly. I will always cherish the time these group members and friends who accompanied with me over the past several years: Dr. Li Quan, Dr. Hoyeong Kwon, Dr. Mykhailo Tymchenko, Dr. Ahmed Kord, Dr. Guangwei Hu, Dr. Yarden Mazor, Dr. Mohammad-Ali Miri, Dr. Huanan Li, Dr. Xiang Ni, Dr. Sander Mann, Dr. Michele Cotrufo, Dr. Seunghwi Kim, Dr. Jiamin Quan, Diego Farfan, Yoshiaki Kasahara, Curtis Wiederhold, Ahmed Mekkawy, Matthew Byrne, Robert Duggan, Aobo Chen, Hady Moussa, Jiaming Xu, Changyong Hu, Kun Li, Chenchen Liu, Rui Wang, Hui Long, XiangXu Yu, Zuoming Dong, Chenyang Luo, Dr. Junxiao Zhou, Dr. Xinxing Zhou.

Finally, I want to thank my father, mother, sister, for their support and caring in good and bad time.

Abstract

WAVE TRANSPORT IN PARITY-TIME SYMMETRIC, TIME-VARYING, AND QUASI-PERIODIC SYSTEMS

Zhicheng Xiao, Ph. D.

The University of Texas at Austin, 2021

Supervisor: Andrea Alù

The past several decades have witnessed a rapid growth of research interest in the fields of artificial materials and systems, in particular in the areas of parity-time symmetric systems, time-varying systems and quasi-periodic systems. These newly developed material platforms have been enabling many exotic wave-matter interaction phenomena unavailable in nature. In this context, I investigated a series of wave transport and scattering phenomena in parity-time symmetric, time-varying and quasi periodic systems in this dissertation. First, I proposed a sensing circuit based on sixth-order exceptional point (EP), which supports high sensitivity, resolution, and nondegraded thermal noise performance compared with conventional diabolic point (DP) sensing system. I also studied the influence of thermal noise in a general two-level sensing platform based on EP. Second, I demonstrated a robust microwave tunneling device operating in the extreme case in which the transmission channel is shorted through a small reactance. We observed full restoration of information and overall transparency to an external observer through use of a pair of parity-time-symmetric emitter and absorber. Third, I studied the effects of realistic switching parameters and synchronization in a series of nonreciprocal devices based on synchronized loss modulation. The research

showed that the nonreciprocal response of these systems experiences a linear regression of insertion loss and isolation with respect to the timing error among switches. Remarkably, impedance matching, and nonreciprocal phase shifts are immune from synchronization issues, and reasonable levels of synchronization errors still guarantee low insertion loss and good isolation. Fourth, I studied wave scattering phenomena in static and dynamic quasi-periodic LC resonator array, which provides an easily accessible and reconfigurable platform to study fractal energy band and topological edge state. Overall, my explorations have been enabling a new degree of control of waves in circuits and metamaterials, pushing forward the opportunities for extreme wave-matter interactions using gain and time modulations.

Table of Contents

List of Figures

Figure 3.2: One-port scattering setup where a probing channel is side coupled to mode $\omega_1+i\gamma_1$. The decaying matrix is $\Gamma=\begin{bmatrix}\gamma_e & 0\\ 0 & 0\end{bmatrix}$, γ_e is the external loss rate from mode 1 to the waveguide, $\mu=\sqrt{2\gamma_e}$ is the corresponding coupling coefficient. Relation between resonant mode splitting and scattering extremes in EP sensing schemes. (a) Reflectance of the unbalanced loss sensing system. $\gamma_1=-0.01,\gamma_2=-0.05,\gamma_e=0.01$. The exceptional point is $\kappa_{EP}=0.015$ and the resolving threshold point is $\kappa_{TP}=0.034$. (b). Eigenfrequencies and the valleys of the reflectance curve. In the region $\kappa_{EP}<\kappa<\kappa_{TP}$, we can see the bifurcation of eigenfrequency, but we cannot see the valleys the reflectance curve because of the linewidth broadening. In the region $\kappa>\kappa_{TP}$, we can see valleys of the reflectance curve. (c) Reflectance of the PT-symmetric sensing system. $\gamma_1=-0.05,\gamma_2=0.05,\gamma_e=0.01$. The exceptional point is $\kappa_{EP}=0.045$ and the resolving threshold point is $\kappa_{TP}=0.055$. (d). Eigenfrequencies and the peaks of the reflectance curve. In the region $\kappa_{EP}<\kappa<\kappa_{TP}$, we can see the bifurcation of eigenfrequency, but we cannot see the peaks the reflectance curve because of the linewidth broadening. In the region $\kappa>\kappa_{TP}$, we can see peaks of the reflectance curve.....41

Figure 4.1: (a) PT-symmetric wave tunneling and information transfer scheme. A highly reflective obstacle blocks the channel. A gain element $-Z_0$ is placed behind this obstacle and a lossy element R is placed before the obstacle to facilitate full wave transmission. (b) A simplified wired version of PT-symmetric robust information transfer scheme based on transmission line. The obstacle is modeled as a small inductive element L_0. (c) Fundamental odd and even mode profiles of the PT-symmetric absorber-emitter pair. They are significantly different from Hermitian system due to the Neumann boundary condition and PT-symmetry. The point $Z=-\frac{L}{2}$ and $Z=\frac{L}{2}$ marks the location of the loss and gain unit, where L is the electrical length of the transmission connecting these two elements. (d) Tunneling characteristics of the PT-symmetric system. The π phase transmission maxima locates at $\omega=(2k+1)\omega_0,\ k=0,\ 1,\ 2,\ 3\cdots$ and the in-phase transmission peaks are determined by the transcendental equation $\frac{1}{2\alpha}\left(\frac{\omega}{\omega_0}\right)^{-1}=\tan\left(\frac{\pi\ \omega}{2\omega_0}\right)$, where $\alpha=\omega_0 L_0/Z_0$ is the coupling strength between the absorber and emitter, $\omega_0=2\pi/T_0$ is the fundamental resonant frequency.

Figure 4.2: Realistic design and implementation of the PT-symmetric wave tunneling prototype. (a) Circuit schematic. Transmission line is replaced with a π-type transmission line which consists of inductor *L* and capacitor *C*. (b) Photograph of the fabricated PCB prototype. Two big white components are tunable resistors. The black component with six pins is OPA 355-Q1 amplifier. Left and right ports are source port 1 and load port 2 in the schematic. Upper and lower ports are DC bias ports for the amplifier. (c) Dispersion of the impedance of the gain element. Black circle marks the operational point. (d) ADS and Modelithics simulation of the amplitude of scattering parameters. Tunneling point is marked in the figure. (e) Spectral properties of eigenvalues of the scattering matrix. Exact PT-symmetry is achieved at tunneling frequency where eigenvalues obey unitary conditions $\left|\lambda_1\left(\omega_0\right)\lambda_2\left(\omega_0\right)\right|=1$. The coupling coefficient α is 0.13, ensuring robust operation of the whole circuit in presence of obstacle. (f) Numerical transient response at the source port where full absorption is achieved at tunneling frequency. The generator voltage is 1 Volt. (g) Numerical transient response at the obstacle which is short in the steady state. (h) Numerical transient response at the load port where full wave tunneling is observed in the steady state.....61

Chapter 1: Introduction

Electromagnetic wave emission, propagation, scattering and wave-matter interactions represent old yet ever-evolving fields that have been studied for centuries. Natural materials and wave transport channels are generally reciprocal, time-invariant and are bound by constraints dictated by reciprocity, time-bandwidth limits, and degradation from disorder and defects. In the past several decades, a plethora of artificially engineered materials and systems were proposed and demonstrated, such as negative index materials [1]-[2], epsilon-near-zero (ENZ) materials [3]-[5], meta-surfaces [6]-[8], parity-time symmetric systems [9]-[14], spatial-temporally modulated systems [15]-[21], and quasi periodic systems [22]-[23]. These artificially engineered materials and systems open an exciting research avenue for both scientists and engineers. Many exotic wave-matter interaction phenomena, new devices, and applications were developed and demonstrated based on these artificial materials. For example, metamaterials and meta-surface designed based on nonlocal response and Green's function approach can support ultrafast, compact, energy-efficient analogue optical signal processing [24]-[28]. Parity-time (PT)-symmetric systems, combing balanced loss and gain elements, enabled a host of unprecedented wave scattering properties, such as unidirectional invisibility [29], negative refraction [30], perfect imaging [31], robust wireless power transfer [32]-[33], coherent perfect absorber (CPA)-laser[34]-[36], robust wave tunneling [37], and enhanced sensing near exceptional point (EP) [38]-[39]. Spatio-temporally modulated component is another exciting research frontier. Sophisticatedly engineered spatial-temporally modulated materials or discrete electronic components can support wideband and reconfigurable on-chip optical signal isolation and electronic signal routing without the use of bulky magnetic materials. Quasi-periodic systems,

where the resonance of each element is modulated periodically in space, exhibited fractal band structure in the parameter space. The quasi-periodicity in artificially materials allows us to emulate physics of electrons in two-dimensional atomic lattice subjected to a strong vertical magnetic field, opening a new way to study the topological phase transition and edge states.

Considering the above exciting progress, during my PhD I investigated a series of electromagnetic wave scattering phenomena in PT-symmetric, time-varying, and quasiperiodic systems, as described in this dissertation. In the following sections, I will first briefly review some fundamental background knowledge in these research fields and outline the original research I carried out in this framework.

1.1 WAVE SCATTERING IN PT-SYMMETRIC SYSTEMS

A classical interpretation of quantum mechanics dictates that any observable must be represented by self-adjoint operators [40]. In other words, the physical operator is Hermitian, ensuring real eigenvalues, orthogonal eigenstates in Hilbert space, and conservation of probability with time evolution [40]. Interestingly, it was revealed that there is a set of non-Hermitian Hamiltonians whose eigenvalues can be real in the parameter space if they satisfy Parity-Time (PT) symmetry [9]-[11]. PT symmetry means that the Hamiltonian is commutative to the $\hat{P}\hat{T}$ operator, where $\hat{P}$ is the space reversal operator $\left(\mathbf{r} \to -\mathbf{r}\right)$ and $\hat{T}$ is the time reversal operator $\left(t \to -t\right)$. For a time-independent Hamiltonian, PT symmetry indicates that the conjugate of potential under space reversal is equal to the potential itself: $V^*\left(-\mathbf{r}\right) = V\left(\mathbf{r}\right)$, implying balanced gain and loss unit distribution in space.

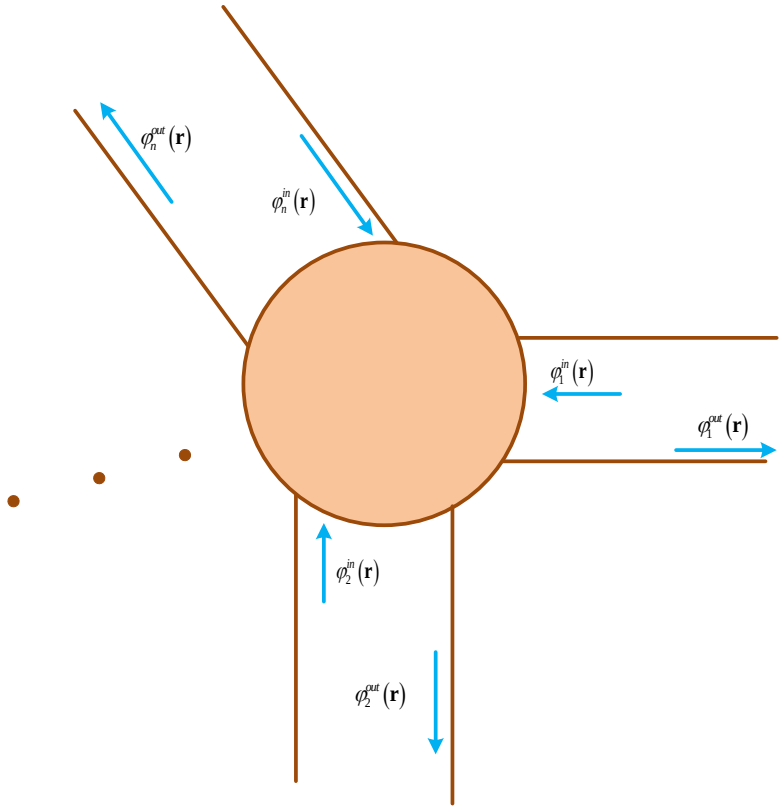

Figure 1.1: A general N-port scattering system.

Following the pioneering work by Bender, theoretical investigations mushroomed in a plethora of physics frontiers, such as quantum field theory [42]-[43], coherent perfect absorber (CPA)[34]-[36], and ideal volumetric imaging for electromagnetic waves [30][31]. Since the paraxial wave equation has a similar form with the 2-D Schrödinger equation of matter wave, the unusual features of PT symmetric systems were also observed experimentally in optics by engineering the refractive index, under the PT-symmetry condition $n(\mathbf{r}) = n^*(-\mathbf{r})$ [44]. As a result, optical waveguiding and scattering systems have become a fertile ground for innovative ideas in this area of research and

facilitated the discovery of a host of new phenomena. Therefore, it's important to review the fundamental scattering properties of electromagnetic waves in PT-symmetric systems.

In general, for an N-port network, the steady state solutions of the scattering fields in channels obey

$$\left[\nabla^2 + \frac{\varepsilon(\mathbf{r})\omega^2}{c^2}\right]\mathbf{E}(\mathbf{r}) = 0, \tag{1.1}$$

where $\mathbf{E}(\mathbf{r},t) = \mathrm{Re}\left[\mathbf{E}(\mathbf{r})e^{-i\omega t}\right]$. Outside the cavity, the electric field has the form

$$\mathbf{E}(\mathbf{r}) = \sum_{i=1}^{i=n} a_i \varphi_i^{in}(\mathbf{r}) + b_i \varphi_i^{out}(\mathbf{r}), \tag{1.2}$$

where a_i, b_i are the amplitudes of the input and output excitations at *i*-th port, respectively, *n* is the total number of ports. They obey the input-output relations

$$b_i = \sum_{m=1}^{m=n} S_{im}(\omega) a_m, \tag{1.3}$$

where $S(\omega)$ is the scattering matrix. In lossless, reciprocal, and time-invariant materials, the scattering matrix is unitary:

$$S^{\dagger}S = \mathbf{I}. \tag{1.4}$$

For a PT-symmetric system, however, the scattering matrix has the following property [34]

$$PTS(\omega^*)PT = S^{-1}, \tag{1.5}$$

where $P=\begin{bmatrix} 0 & 0 & \cdots & 1 \\ 0 & \cdots & 1 & 0 \\ \vdots & 1 & \vdots & 0 \\ 1 & \cdots & 0 & 0 \end{bmatrix}$ is the space reversal operator, T is the time reversal operator. The Hamiltonian matrix obey the following relation: $PHP = H^{\dagger}$, indicating that Hamiltonian and S matrix have different properties.

1.2 WAVE SCATTERING PROPERTIES IN ONE-DIMENSIONAL PT-SYMMETRIC SYSTEM

Consider a PT-symmetric two-port optical network whose scattering matrix reads

$$S=\begin{bmatrix} r_L & t \\ t & r_R \end{bmatrix}. \tag{1.6}$$

where r_L and r_R are the reflection coefficient on the left and right port respectively, t is the transmission coefficient from left port to right port or vice versa. We substitute the properties of scattering matrix [Eq. (1.5)] into the above equation and get

$$\begin{bmatrix} r_R^* & t^* \\ t^* & r_L^* \end{bmatrix}\begin{bmatrix} r_L & t \\ t & r_R \end{bmatrix}=\begin{bmatrix} 1 & 0 \\ 0 & 1 \end{bmatrix}. \tag{1.7}$$

Therefore, we have the following relations for two-port PT-symmetric network [45]

$$\begin{cases} r_L t^* + r_L^* t = 0 \\ r_R t^* + r_R^* t = 0 \\ r_L r_R^* + |t|^2 = 1 \end{cases} \tag{1.8}$$

Assuming that the eigenvectors of the scattering matrix is ψ_n and the corresponding eigenvalues are s_n, we have

$$S\psi_n = s_n \psi_n. \tag{1.9}$$

We substitute Eq. (1.5) into the above equation and get

$$S^*\left(P\psi_n\right) = \frac{1}{s_n}\left(P\psi_n\right). \tag{1.10}$$

We apply a complex conjugate operation over the above equation and get

$$S\left(P\psi_n^*\right) = \frac{1}{s_n^*}\left(P\psi_n^*\right). \tag{1.11}$$

Now, we figure out the relation between $P\psi_n^*$ and ψ_n. From the characteristic equation (1.9), we have two eigenvalues and two eigenstates

$$\begin{cases} s_+ = \dfrac{r_L + r_R + \sqrt{\left(r_L - r_R\right)^2 + 4t^2}}{2}, s_- = \dfrac{r_L + r_R - \sqrt{\left(r_L - r_R\right)^2 + 4t^2}}{2}, . \\ \psi_+ = \begin{bmatrix} \dfrac{r_L - r_R + \sqrt{\left(r_L - r_R\right)^2 + 4t^2}}{2t} \\ 1 \end{bmatrix}, \psi_- = \begin{bmatrix} \dfrac{r_L - r_R - \sqrt{\left(r_L - r_R\right)^2 + 4t^2}}{2t} \\ 1 \end{bmatrix}. \end{cases} \tag{1.12}$$

When $\left(r_R - r_L\right)^2 + 4t^2 < 0$, the scattering system is in the exact phase regime, the eigenstate can be expressed as

$$\psi_+ = \frac{1}{\sqrt{2\cos\alpha}} \begin{bmatrix} e^{i\frac{\alpha}{2}} \\ e^{-i\frac{\alpha}{2}} \end{bmatrix}, \psi_- = \frac{i}{\sqrt{2\cos\alpha}} \begin{bmatrix} e^{-i\frac{\alpha}{2}} \\ -e^{i\frac{\alpha}{2}} \end{bmatrix}, \tag{1.13}$$

where $\cos\alpha = \frac{\sqrt{\left|\left(r_L - r_R\right)^2 + 4t^2\right|}}{\left|2t\right|}, \sin\alpha = \frac{r_L - r_R}{\left|2t\right|}$. Therefore, we have $P\psi_{\pm}^{*} = PT\psi_{\pm} = \psi_{\pm}$

, which indicates that PT and S share the same eigenstates in the exact phase regime. Then, Eq. (1.11) will simplify to

$$S\psi_{\pm} = \frac{1}{s_{\pm}^{*}}\psi_{\pm}. \tag{1.14}$$

We have

$$\left|s_{+}\right| = \left|s_{-}\right| = 1. \tag{1.15}$$

According to Eq. (1.12), we have $s_{+}^{*} = s_{-}$.

Above the exceptional point, the eigenstate can be expressed as

$$\psi_{+} = \begin{bmatrix} \alpha + \beta \\ 1 \end{bmatrix}, \psi_{-} = \begin{bmatrix} \alpha - \beta \\ 1 \end{bmatrix}, \tag{1.16}$$

$\alpha = \frac{r_L - r_R}{2t}$, $\beta = \frac{\sqrt{\left(r_L - r_R\right)^2 + 4t^2}}{2t}$, $\left|\alpha\right|^2 - \left|\beta\right|^2 = 1$. Therefore, we have

$$P\psi_{\pm}^{*} = PT\psi_{\pm} = \psi_{\mp}, \tag{1.17}$$

Then, the $S\psi_{\pm} = \frac{1}{s_{\mp}^{*}}\psi_{\pm}.$, we have

$$\left|s_{+}\right| = \frac{1}{\left|s_{-}\right|}. \tag{1.18}$$

In summary, for one-dimensional PT-symmetric scattering system, there are unitary scattering region where both eigenvalues satisfy $\left|s_{+}\right| = \left|s_{-}\right| = 1$ and nonunitary scattering

region where eigenvalues satisfy $|s_+| = \frac{1}{|s_-|}$. These two regions are separated by the exceptional point of the system.

1.3 WAVE SCATTERING IN TIME-VARYING SYSTEMS

Another important topic in this dissertation is wave scattering in time-varying system. In this section, we provide a very basic tutorial about time-modulated resonator where the main results are from refs [46]-[47]. As shown Fig.1.2, a resonator with time varying resonant frequency is side coupled to two waveguides. Assuming that port 1 is excited with wave $s_1^+ = S_1^+ e^{-i\omega t}$, the CMT equation is

$$\begin{cases} \dfrac{da}{dt} = \left(-i\omega(t) - \gamma_e\right)a + \sqrt{\gamma_e}s_1^+, \\ \begin{bmatrix} s_1^- \\ s_2^- \end{bmatrix} = -\begin{bmatrix} s_1^+ \\ 0 \end{bmatrix} + \begin{bmatrix} \sqrt{\gamma_e} \\ \sqrt{\gamma_e} \end{bmatrix} a, \end{cases} \tag{1.19}$$

where γ_e is the decaying rate between the resonator and the waveguide, s_1^+ is the excitation at the left port, s_2^- is the transmitted wave, and s_1^- is the reflected wave, $a(t)$ is the field amplitude in the cavity. The solution of the field amplitude is:

$$a(t) = e^{-\int i\omega(t)+\gamma_e \mathrm{dt}} \int \sqrt{\gamma_e} S_1^+ e^{-i\omega t} e^{\int i\omega(t)+\gamma_e \mathrm{dt}} \mathrm{dt}. \tag{1.20}$$

We substitute the expression $\omega(t) = \omega_0 + \Delta\omega\cos(\omega_m t)$ into the above equation and get the field amplitude

$$a(t) = e^{-(i\omega_0+\gamma_e)t - i\frac{\Delta\omega}{\omega_m}\sin\omega_m t} \int \sqrt{\gamma_e} S_1^+ e^{-i\omega t} e^{(i\omega_0+\gamma_e)t + i\frac{\Delta\omega}{\omega_m}\sin\omega_m t} \mathrm{dt}. \tag{1.21}$$

We employ the following identity:

$$e^{i\frac{\Delta\omega}{\omega_m}\sin\omega_m t} = \sum_{n=-\infty}^{n=+\infty} J_n\left(\frac{\Delta\omega}{\omega_m}\right) e^{in\omega_m t}, \tag{1.22}$$

and simplify Eq. (1.21):

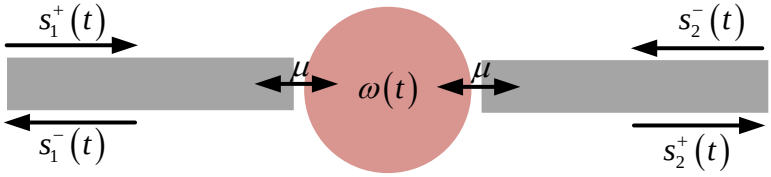

Figure 1.2: Schematic of periodically modulated resonator. The resonant frequency is $\omega(t)=\omega_0+\Delta\omega\cos(\omega_m t)$, where ω_0 is the static resonant frequency, $\Delta\omega$ is the modulation depth, ω_m is the modulation frequency.

$$a(t)=\sum_{k=-\infty}^{k=+\infty}\sum_{n=-\infty}^{n=+\infty}J_k\left(\frac{\Delta\omega}{\omega_m}\right)J_n\left(\frac{\Delta\omega}{\omega_m}\right)\frac{\sqrt{\gamma_e}S_1^+}{i(\omega_0-\omega+n\omega_m)+\gamma_e}e^{-i[\omega+(k-n)\omega_m]t} \tag{1.23}$$

where J_n is the *Bessel function of the first kind* [48]. The above equation looks very complicated. However, it represents a rigorous solution of the field amplitude inside the cavity. When the modulation depth $\Delta\omega=0$, only the terms $n=k=0$ are nonzero. The above equation can be then simplified to

$$a(t)\big|_{\Delta\omega=0}=\frac{\sqrt{\gamma_e}}{i(\omega_0-\omega)+\gamma_e}S_1^+e^{-i\omega t}, \tag{1.24}$$

which corresponds to the static case.

As a result, the reflection and transmission coefficient in time domain is

$$\begin{cases} S_{11}(t)=-1+\sum_{k=-\infty}^{k=+\infty}\sum_{n=-\infty}^{n=+\infty}J_k\left(\frac{\Delta\omega}{\omega_m}\right)J_n\left(\frac{\Delta\omega}{\omega_m}\right)\frac{\gamma_e}{i(\omega_0-\omega+n\omega_m)+\gamma_e}e^{-i(k-n)\omega_m t}, \\ S_{21}(t)=\sum_{k=-\infty}^{k=+\infty}\sum_{n=-\infty}^{n=+\infty}J_k\left(\frac{\Delta\omega}{\omega_m}\right)J_n\left(\frac{\Delta\omega}{\omega_m}\right)\frac{\gamma_e}{i(\omega_0-\omega+n\omega_m)+\gamma_e}e^{-i(k-n)\omega_m t}. \end{cases} \tag{1.25}$$

It is easy to convert the above time domain scattering parameters to frequency domain since they are expressed in Fourier series:

$$\begin{cases} S_{11}^{(n)}(\omega) = \begin{cases} -1 + \sum_{p=-\infty}^{p=+\infty} J_p^2\left(\frac{\Delta\omega}{\omega_m}\right) \frac{\gamma_e}{i(\omega_0 - \omega) + \gamma_e}, n = 0 \\ \sum_{p=-\infty}^{p=+\infty} J_{n+p}\left(\frac{\Delta\omega}{\omega_m}\right) J_p\left(\frac{\Delta\omega}{\omega_m}\right) \frac{\gamma_e}{i(\omega_0 - \omega + p\omega_m) + \gamma_e}, n \neq 0 \end{cases} \\ S_{21}^{(n)}(\omega) = \sum_{p=-\infty}^{p=+\infty} J_{n+p}\left(\frac{\Delta\omega}{\omega_m}\right) J_p\left(\frac{\Delta\omega}{\omega_m}\right) \frac{\gamma_e}{i(\omega_0 - \omega + p\omega_m) + \gamma_e} \end{cases} \tag{1.26}$$

Since the resonator is time-varying, the scattered fields have infinite number of harmonics, which can be expressed as

$$\begin{cases} s_1^- = \sum_{n=-\infty}^{n=+\infty} S_{11}^{(n)}(\omega) S_1^+ e^{-i(\omega + n\omega_m)t} \\ s_2^- = \sum_{n=-\infty}^{n=+\infty} S_{21}^{(n)}(\omega) S_1^+ e^{-i(\omega + n\omega_m)t} \end{cases} \tag{1.27}$$

1.3.1 Adiabatic limit

When the modulation frequency ω_m is sufficiently low, the mode amplitude evolves in time in a quasi-static frequency $\omega(t)$. Assume that the solution of the field amplitude can be expressed as $a(t) = A(t)e^{-i\omega t}$. Then $\frac{\mathrm{d}a(t)}{\mathrm{d}t} = \frac{\mathrm{d}A(t)}{\mathrm{d}t} e^{-i\omega t} - i\omega A(t) e^{-i\omega t}$. For adiabatic limit, $\left|\frac{\mathrm{d}A(t)}{\mathrm{d}t}\right| << \left|-i\omega A(t)\right|$ and we have $\frac{\mathrm{d}a(t)}{\mathrm{d}t} \approx -i\omega A(t) e^{-i\omega t}$. This assumption is very much like the slowly varying envelope approximation of optical beams. Then the field amplitude is

$$a(t) = A(t)e^{-i\omega t} = \frac{\sqrt{\gamma_e} S_1^+}{i(\omega(t) - \omega) + \gamma_e} e^{-i\omega t}. \tag{1.28}$$

and the time-domain transmission coefficient is

$$S_{21}(t) = \frac{\gamma_e}{i(\omega(t) - \omega) + \gamma_e} \tag{1.29}$$

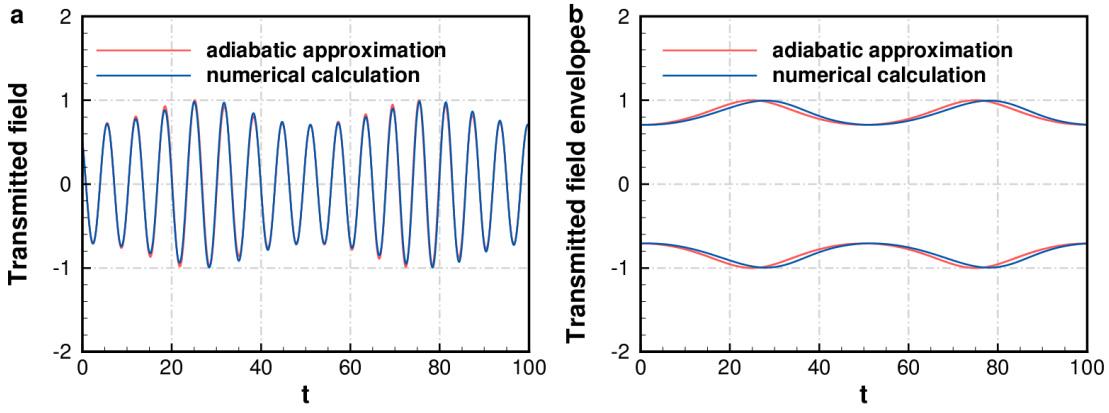

Figure 1.3: The transmitted field amplitude and envelope in adiabatic limit.

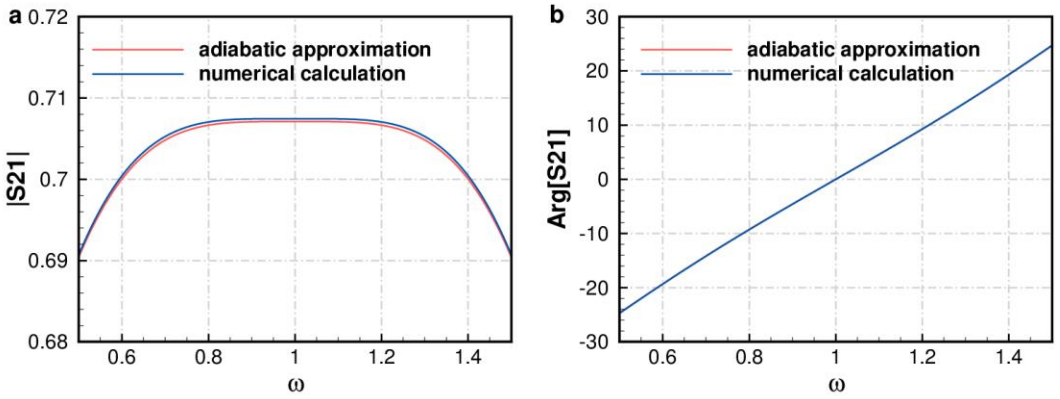

Figure 1.4: Amplitude and phase of the scattering parameter of the fundamental tone in adiabatic limit.

The adiabatic limit $\left|\frac{\mathrm{d}A(t)}{\mathrm{d}t}\right| << \left|-i\omega A(t)\right|$ can be simplified to

$$\frac{\Delta\omega}{\omega_m} << \frac{\omega_0\gamma_e}{\omega_m^2} \tag{1.30}$$

Now, we provide an example to compare the approximate solution with the full-wave numerical simulation. Assume that $\omega_0 = 1, \omega_m = \frac{\pi}{50}, \gamma_e = \frac{\pi}{5}, \Delta\omega = \frac{\pi}{5}, \omega = 1$. The input port is excited with wave $s_1^+(t) = e^{-i\omega_0 t}$. In this case, the system complies with the adiabatic approximation. The output signal in time domain are plotted in the following

figure where the adiabatic approximation results agree well with our numerical simulations.

It is also interesting to study the scattering parameter of the fundamental tone. In the adiabatic limit, the transmission coefficient of the fundamental tone is the time-average value of the time-domain transmission coefficient:

$$S_{21}^{(0)}(\omega)=\frac{1}{\mathrm{T}_m}\int_0^{\mathrm{T}_m} S_{21}(t)\,\mathrm{dt}=\frac{1}{\mathrm{T}_m}\int_0^{\mathrm{T}_m}\frac{\gamma_e}{i(\omega(t)-\omega)+\gamma_e}\,\mathrm{dt}=\frac{\gamma_e}{\sqrt{\left[i(\omega-\omega_0)-\gamma_e\right]^2+\Delta\omega^2}}. \quad (1.31)$$

We compare our adiabatic approximation results with the numerical results in Eq. (1.26), which demonstrate excellent agreement with each other.

1.4.1 High frequency limit

In the high modulation frequency limit, we have $\omega_m >> \gamma_e$. If the excitation is $s_1^- = e^{-i\omega_0 t}$, then the transmitted field can be expressed as

$$s_2^- = \sum_{n=-\infty}^{n=+\infty} S_{21}^{(n)}(\omega_0)\,e^{-i(\omega_0+n\omega_m)t} \quad (1.32)$$

where the scattering parameter of the *n*-th order harmonics is $S_{21}^{(n)}(\omega_0)=\sum_{p=-\infty}^{p=+\infty} J_{n+p}\left(\frac{\Delta\omega}{\omega_m}\right)J_p\left(\frac{\Delta\omega}{\omega_m}\right)\frac{\gamma_e}{ip\omega_m+\gamma_e}$. Since $\omega_m >> \gamma_e$ the term p=0 is much larger than other terms. Therefore, we have

$$S_{21}^{(n)}(\omega_0)=J_n\left(\frac{\Delta\omega}{\omega_m}\right)J_0\left(\frac{\Delta\omega}{\omega_m}\right), \quad (1.33)$$

The transmitted field is simplified to

$$s_2^- = \sum_{n=-\infty}^{n=+\infty} J_n\left(\frac{\Delta\omega}{\omega_m}\right)J_0\left(\frac{\Delta\omega}{\omega_m}\right)e^{-i(\omega_0+n\omega_m)t} \quad (1.34)$$

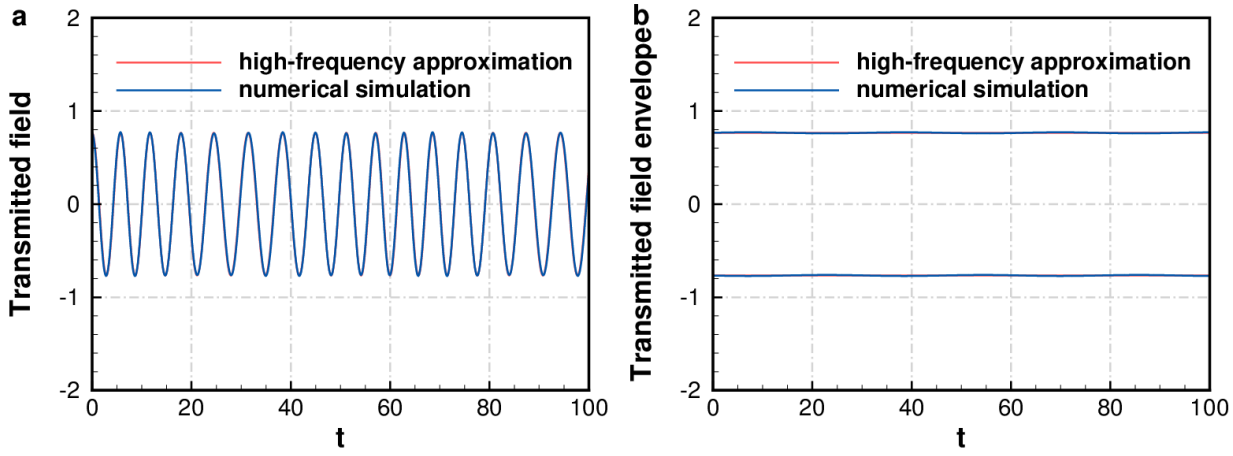

Figure 1.5: The transmitted field amplitude and envelope in high frequency limit.

We provide an example to compare the approximate solution with the numerical simulation. Assume that $\omega_0 = 1, \omega_m = 0.1, \gamma_e = 0.005, \Delta\omega = 0.1, \omega = 1$. The output signal in time domain is plotted in the Fig. 1.5 where the high-frequency approximation results agree quite well with our numerical simulations.

Now, we study the scattering parameter of the fundamental tone. From Eq. (1.26) , we can infer that the scattering parameter of the fundamental tone is

$$S_{21}^{(0)}(\omega) = \sum_{p=-\infty}^{p=+\infty} J_p^2\left(\frac{\Delta\omega}{\omega_m}\right) \frac{\gamma_e}{i(\omega_0 - \omega + p\omega_m) + \gamma_e}, \tag{1.35}$$

The above equation indicates that transmission coefficient is maximal when $\omega = \omega_0 + p\omega_m$. When the frequency $\omega \neq \omega_0 + p\omega_m$, the transmission coefficient is almost zero. Therefore, the transmission spectrum is essentially a series of Lorentzian curve with amplitude $J_p^2\left(\frac{\Delta\omega}{\omega_m}\right)$. The study of scattering properties of single time-varying resonator can be easily extrapolated to a one-dimensional resonator array or even higher-dimensional scenarios.

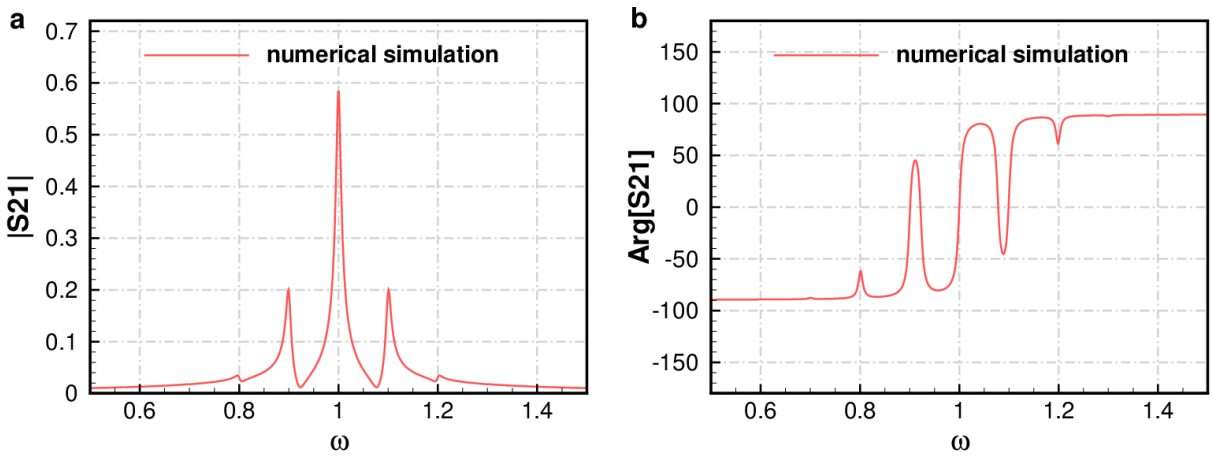

Figure 1.6: Amplitude and phase of the scattering parameter of the fundamental tone in high frequency limit.

1.4 ORGANIZATION OF THIS DISSERTATION

In the following, I discuss intriguing electromagnetic wave scattering and transport phenomena in PT-symmetric, time-varying and quasi-periodic structures. In the second chapter, I discuss a sensing circuit based on a sixth-order exceptional point. The sensitivity of the system is shown to be significantly higher than the one of a conventional Hermitian sensing system due to the exotic topological feature around exceptional point. In Chapter 3, I put forward a theoretical model to analyze the Green's function, scattering signal, and integrated thermal noise in a general two-level sensing system. A circuit model is proposed to confirm our theoretical analysis. In Chapter 4, I proposed and demonstrated wave tunneling in a PT-symmetric microwave circuit. The system is based on a synchronized wave absorber and emitter. The whole circuit is also proven to be stable despite the presence of gain element. In chapter 5, I investigated the synchronization issue in nonreciprocal devices based on commutated transmission lines.

My study shows that insertion loss of the nonreciprocal device experience linear degradation while the impedance matching remains unaffected. I also proposed mitigation methods for the isolator design. In chapter 6, I studied the eigenfrequency distribution of spatially modulated coupled resonator arrays. The system shows a fractal band structure and looks like a butterfly. Meanwhile, I also studied the scattering properties of associated systems in which the resonant frequency is modulated periodically in time.

Chapter 2: Enhanced Sensing in an Electronic Circuit with a Sixth-Order Exceptional Point[1]

In this chapter, I present an enhanced sensing design in an electronic circuit with a sixth-order exceptional point. The influence of thermal noise on the measurements and the signal to noise ratio (SNR) are systemically analyzed and compared with sensing protocol in Hermitian counterpart. The main results of this chapter are from ref [49].

2.1 INTRODUCTION

Sensing is of fundamental importance in modern society, ranging from industrial process monitoring [50], biomedical sample ingredient analysis [51], to massive deployment of wireless sensor network for the internet of things [53]-[54]. Most sensors rely on resonant structures, analyzing spectrum shifts of a single resonance or spectrum splitting of two degenerate modes when a perturbation to be sensed occurs. Typical examples include nanoparticle detection with ultrahigh-Q photonic microresonators [56] and wireless sensors based on LC microwave resonators [57]. In general, the magnitude of frequency splitting is linearly proportional to the perturbation strength due to the Hermitian nature of these sensing systems [58]-[59]. The degenerate sensing point in these Hermitian systems is thus known as diabolic point (DP).

Recent advances in the fields of non-Hermitian physics and PT symmetry [60]-[71] have revealed that enhanced sensitivity can be achieved based on a new type of degenerate point, known as exceptional point (EP). At EPs, two or more eigenvalues and their corresponding eigenvectors coalesce, leading to a nondiagonalizable Hamiltonian that demonstrates an Nth-order root law of eigenfrequency splitting when N degenerate

[1] This chapter is published in ref [49]. Zhicheng Xiao, Huanan Li, Tsampikos Kottos, and Andrea Alu are coauthors. Zhicheng Xiao proposed the idea, run simulation, wrote the manuscript, Hunan Li and Tsampikos Kottos helped write and revise the manuscript, Andrea Alu wrote the manuscript and supervised the project.

eigenmodes are lifted by the perturbation [72]: $\Delta\omega \propto \varepsilon^{1/N}$, where ε is the perturbation strength. The sensitivity is thus proportional to $\varepsilon^{1/N-1}$, which, for small perturbation, is much higher than the linear sensitivity $\Delta\omega \propto \varepsilon$ of DPs, as evidenced by some experimental demonstrations [68]-[71].

Nonetheless, the possibility to implement EP sensing in various setups has triggered an ongoing debate over the past several years [73]-[78]. On the one hand, there is a fundamental resolution limit for EP sensing schemes based on purely lossy systems due to the presence of imaginary part of the eigenfrequencies [73]. This imaginary component leads to a broadening of the reflection or transmission spectrum and further sets a fundamental resolution limit on the sensitivity of the device. This bound is analogous, in another context, to conventional optical diffraction limit, where the angular resolution is limited by resolvable distance between two overlapping Airy disk diffraction patterns from two adjacent point sources [79]-[80]. On the other hand, PT-symmetric sensing systems with balanced loss and gain units can potentially improve the resolution limit, given that proper readout design and perturbation strategy are deployed. However, these gain and loss elements unavoidably add noise into the system, imposing another fundamental bound on the sensitivity.

In this chapter, we endeavor to address these issues by proposing an enhanced sensing scheme based on a sixth-order EP supported by a PT -symmetric electronic circuit [see Fig. 1.1 (a)]. Instead of detecting the resonant frequency splitting, we detect the eigenfrequency shift by measuring the reflected signals at the lossy side of our circuit. First, we set our system to a static EP with zero eigenfrequency. When the system is perturbed from the ideal EP condition, a reflection dip emerges, and shifts away from the static point. The reflection dip exactly matches the purely real eigenfrequency of the system under perturbation and shows a resonant shift following a fourth-order root law

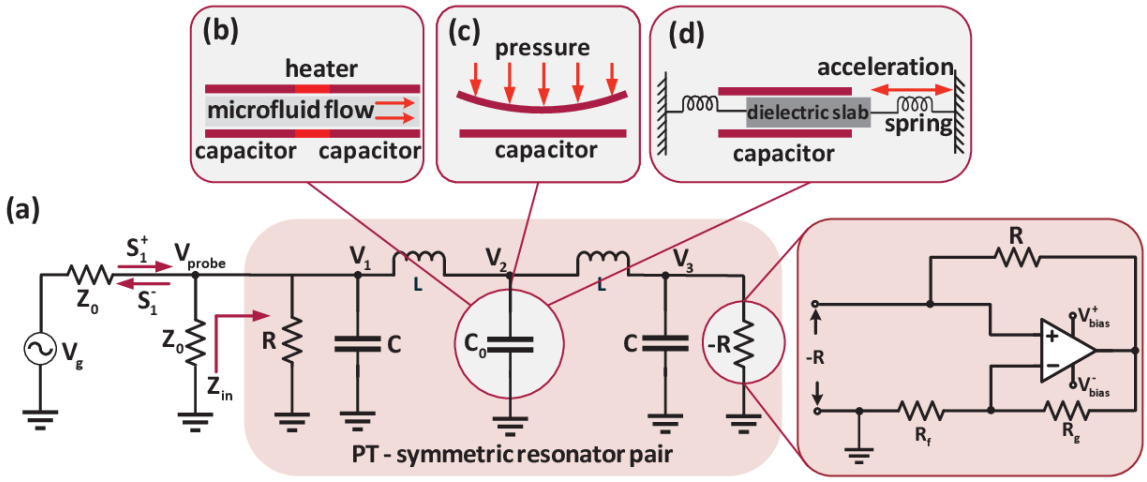

Figure 2.1: Hypersensitive PT-symmetric sensing circuit design and its possible application scenarios. (a) PT-symmetric sensing circuit. The pink region consists of a pair of PT-symmetric resonators. The negative impedance -R is realized by an amplifier feedback circuit with noninverting configuration, where the gain coefficient is $1+R_g/R_f$. The PT-symmetric resonator pair is connected in shunt to are resistance $1+R_g/R_f$ and then in series to a microwave generator with internal impedance Z_0 and voltage V_g. (b) Supersensitive microfluid flow sensor based on capacitive perturbation. The microfluid speed is sensed by measuring the temperature gradient created by the heater. (c) Supersensitive pressure sensor based on capacitive perturbation. A pressure sensitive membrane responds to external pressure and changes the effective capacitance of C_0. (d) Supersensitive accelerometer based on capacitive perturbation. Acceleration is sensed by attaching a dielectric slab sandwiched within the capacitor plates and connected to two springs.

with respect to the perturbation strength. These resonant shifts can be measured with high resolution, even for very weak perturbations. We further verify this claim through a comparative study of our EP sensing scheme with a DP sensing protocol supported by a similar circuit layout. As we show in the following, due to the low-pass feature of our sensing circuit, thermal noises are alleviated to an identical level as the corresponding DP sensing scheme.

2.2 SIXTH-ORDER EXCEPTIONAL POINT SENSING SYSTEM

Our sensing scheme is based on a PT -symmetric circuit supporting a sixth-order EP. The circuit design is shown in Fig. 2.1 (a). In the pink-highlighted region, two resonators formed by a grounded capacitor C and a floating inductor L, are coupled with a grounded capacitor C_0 . A positive resistor R and a negative resistor -R are connected in parallel with the left and right resonator, respectively. To reveal the sensing mechanism in our scheme, we formulate the corresponding non-Hermitian Hamiltonian and study its eigenfrequency. Using Kirchhoff's laws, the dynamics of the voltages at various nodes of the isolated system follow these equations:

$$\begin{cases} \ddot{V}_1 + \gamma \dot{V}_1 + V_1 - V_2 = 0, \\ \ddot{V}_2 + 2\mu \dot{V}_2 - \mu V_1 - V_3 = 0, \\ \ddot{V}_3 - \gamma \dot{V}_3 - V_2 + V_3 = 0, \end{cases} \tag{2.1}$$

where $\dot{V}_n = \frac{dV_n}{d\tau}$, $\ddot{V}_n = \frac{d\dot{V}_n}{d\tau}$, $n = 1,2,3$, $\tau = \omega_0 t$ is the normalized time, $\gamma = \frac{1}{R}\sqrt{\frac{L}{C}}$ is the intrinsic gain or loss rate of the LC resonator, $\mu = C/C_0$ is the coupling coefficient between the two resonators. It is easy to show that Eq. (2.1) is invariant under a joint time-reversal and parity operation, and therefore the system is PT symmetric [62]. Constructing a state vector for this six-variable linear system $\Psi = \begin{bmatrix} V_1 & V_2 & V_3 & \dot{V}_1 & \dot{V}_2 & \dot{V}_3 \end{bmatrix}^T$, we can recast Eq. (2.1) into the Schrodinger-type equation:

$$i\frac{d\Psi}{d\tau} = \begin{bmatrix} 0 & 0 & 0 & i & 0 & 0 \\ 0 & 0 & 0 & 0 & i & 0 \\ 0 & 0 & 0 & 0 & 0 & i \\ -i & i & 0 & -i\gamma & 0 & 0 \\ i\mu & -2i\mu & i\mu & 0 & 0 & 0 \\ 0 & i & -i & 0 & 0 & i\gamma \end{bmatrix} \Psi = H_{eff}\Psi, \tag{2.2}$$

where H_{eff} is the effective Hamiltonian describing the dynamics of our circuit. The eigenfrequencies are found through the associated characteristic equation $\mathrm{Det}\left|H_{eff}-\mathbf{I}\,\omega\right|=0$:

$$\omega^2\left[\omega^4+\left(\gamma^2-2-2\mu\right)\omega^2+1+2\mu-2\mu\ \gamma^2\right]=0, \tag{2.3}$$

where $\mathbf{I}$ is the six-dimensional unity matrix. Solving Eq. (2.3), we find six eigenfrequencies:

$$\begin{cases}\omega_{1,2}=\pm\dfrac{1}{\sqrt{2}}\sqrt{2+2\mu-\gamma^2+\sqrt{4\mu^2-4\gamma^2+4\mu\ \gamma^2+\gamma^4}}, \\ \omega_{1,2}=\pm\dfrac{1}{\sqrt{2}}\sqrt{2+2\mu-\gamma^2+\sqrt{4\mu^2-4\gamma^2+4\mu\ \gamma^2+\gamma^4}}, \\ \omega_{3,4}=0.\end{cases} \tag{2.4}$$

There is always a pair of eigenfrequencies corresponding to the dc solution of the system, with the eigenstate $\Psi=\left[1\quad 1\quad 1\quad 0\quad 0\quad 0\right]^T$. This sixth-order EP occurs for the following:

$$\gamma_{EP}=\frac{\sqrt{5}+1}{2};\ \mu_{EP}=\frac{\sqrt{5}-1}{4}, \tag{2.5}$$

which are inherent properties of the circuit topology. It's possible to show that the exceptional point is sixth order by transforming the effective Hamiltonian into a Jordan

normal form: $H_{eff} = SJS^{-1}$, where the Jordan matrix J and transformation matrix S are:

$$J = \begin{bmatrix} 0 & 1 & 0 & 0 & 0 & 0 \\ 0 & 0 & 1 & 0 & 0 & 0 \\ 0 & 0 & 0 & 1 & 0 & 0 \\ 0 & 0 & 0 & 0 & 1 & 0 \\ 0 & 0 & 0 & 0 & 0 & 1 \\ 0 & 0 & 0 & 0 & 0 & 0 \end{bmatrix},$$

$$S = \begin{bmatrix} 1 & j\left(-1-\sqrt{5}\right) & -3-\sqrt{5} & j\left(3+\sqrt{5}\right) & 1+\sqrt{5} & 0 \\ 1 & \dfrac{j\left(-1-\sqrt{5}\right)}{2} & -1 & 0 & 0 & 0 \\ 1 & 0 & 0 & 0 & 0 & 0 \\ 0 & j & 1+\sqrt{5} & j\left(-3-\sqrt{5}\right) & -3-\sqrt{5} & j\left(1+\sqrt{5}\right) \\ 0 & j & \dfrac{1+\sqrt{5}}{2} & -j & 0 & 0 \\ 0 & j & 0 & 0 & 0 & 0 \end{bmatrix}. \quad (2.6)$$

The number of off-diagonal "1" in the Jordan matrix clearly shows that the exceptional point is sixth order. The sixth-order EP can also be verified in the parameter space of coupling and gain/loss rate [see Fig. 2.2].

This sixth-order EP is ideally suited for sensing applications if we consider a perturbation to the system. Here, we assume that the perturbation is applied to the coupling capacitor with $\mu = \mu_{EP}\left(1+\varepsilon\right)$, modeling the realistic scenario where the capacitor serves as a small sensing platform [see Figs. 2.1 (b)–1(d)]. In the following subsections, we will study the relation between the sensed quantity and the perturbation strength.

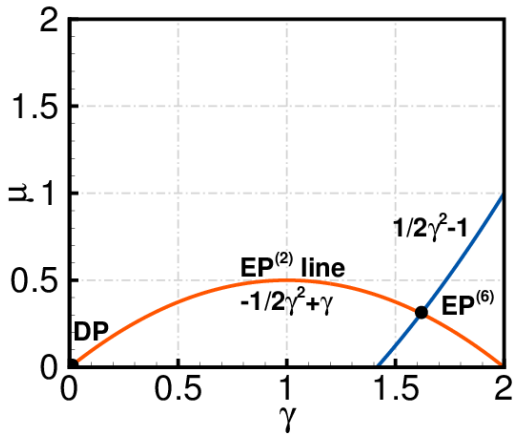

Figure 2.2: Second order exceptional line, diabolic point, and sixth-order EP in the parameter space.

2.2.1 Hypersensitive microfluid speed sensor (or temperature sensor)

The microfluid speed sensor design in this work essentially consists of two temperature sensors and a heater which creates a flow direction dependent asymmetric temperature profile. The fluid speed is determined by measuring the temperature difference using the two temperature sensors. To simplify the study, we assume that the fluid is water, which has an empirical temperature-dependent relative dielectric constant:

$$\varepsilon_r = c_1 - c_2 T, \tag{2.7}$$

where $c_1 = 197$, $c_2 = 0.4\text{K}^{-1}$, K is Kelvin, T is the temperature of water. The above equation is applicable for temperatures ranging from 273 K to 373 K. Assume that the system is set at the sixth-order EP with a reference temperature $T^{EP} = 300K$, which means the capacitance value of the coupling capacitor is

$$C_0^{EP} = \varepsilon_0 \left(c_1 - T^{EP} c_2 \right) \frac{A}{d}, \tag{2.8}$$

where A is the effective area of the capacitor plates and d is the distance of between the two plates. When the temperature of the liquid increases, the system drifts away from the sixth-order EP with a temperature-dependent coupling capacitance

$$C_0(T) = \varepsilon_0 (c_1 - Tc_2) \frac{A}{d}, \tag{2.9}$$

where T is the temperature to be sensed. According to the relation between the coupling coefficient and the perturbation strength in previous section, we find the relation between the temperature drift and the perturbation strength:

$$\varepsilon = \frac{\alpha\ \delta T}{1 - \alpha\ \delta T} \approx \alpha\ \delta T, \tag{2.10}$$

where $\alpha = \frac{c_2}{c_1 - 300c_2} = 5.2 \times 10^{-3} K^{-1}$, $\delta T = T - T^{EP}$. The above equation indicates that when the temperature drift under perturbation is small enough, the perturbation strength is linearly proportional to the temperature drift.

2.2.2 Hypersensitive pressure sensor

Assume that the capacitor consists of two circular metallic plates with radius r and thickness t. The top plate is pressure sensitive and stretchable while the bottom plate is fixed. Without any pressure on the upper plate, the system should operate in the sixth-order EP. The coupling capacitance is

$$C_0^{EP} = \varepsilon_0 \varepsilon_r \frac{\pi r^2}{d}, \tag{2.11}$$

ε_r is the relative permittivity of the slab, ε_0 is the vacuum permittivity, d is the distance between the plates. When a small pressure P is applied on the upper plate, the displacement on the centroid of the upper plate is

$$\Delta d = \frac{3r^4 (1 - \upsilon^2)}{16Et^2} P, \tag{2.12}$$

where υ is the Poison ratio, E is the Young's modulus. Then the capacitance of the coupling capacitor under pressure is

$$C_0\left(P\right)=\varepsilon_0\varepsilon_r\frac{\pi r^2}{d}\frac{\tanh^{-1}\sqrt{\frac{\Delta d}{d}}}{\sqrt{\frac{\Delta d}{d}}}. \tag{2.13}$$

Therefore, the relation between the perturbation strength and the pressure is

$$\left|\varepsilon\right|\approx\frac{1}{3}\frac{3r^4\left(1-\upsilon^2\right)}{16Et^2}P. \tag{2.14}$$

Note that in this design, the perturbation strength ε is negative since the coupling coefficient μ decreases after perturbation. Nevertheless, our protocol still holds. The only difference is that now one needs to substitute in the expression for the resonant shift the absolute value of ε.

2.2.3 Hypersensitive accelerometer

When the acceleration is zero, the system should operate in the sixth-order EP, which means the dielectric slab is fully matched with the plates of the capacitor. The coupling capacitance can be expressed as

$$C_0^{EP}=\varepsilon_0\varepsilon_r\frac{A}{d}, \tag{2.15}$$

where ε_r is the relative permittivity of the slab, ε_0 is the vacuum permittivity, *A* is the area of the plates of the capacitor, *d* is the distance between the plates. When we apply the acceleration, the slab will move out of the plates, changing the effective capacitance value of the capacitor:

$$C_0\left(a\right)=\varepsilon_0\varepsilon_r\frac{A}{d}\left[1+\left(\frac{1}{\varepsilon_r}-1\right)\frac{2ma}{kL}\right], \tag{2.16}$$

where *m* is the mass of the dielectric slab, *k* is the stiffness coefficient of the spring, *L* is the length of the capacitor plate, *a* is the absolute value of the acceleration. The edge effect is ignored here, and a rigorous simulation on the electromagnetic field should be engaged for practical implementations. According to the definition of the coupling

coefficient and the perturbation strength in previous section, the relation between the perturbation strength and the acceleration is easily obtained:

$$\varepsilon \approx \left(1-\frac{1}{\varepsilon_r}\right)\frac{2ma}{kL}, \tag{2.17}$$

which clearly shows that the perturbation strength is linearly proportional to the acceleration.

2.3 ONE-PORT SCATTERING AND READOUT SETUP

We connect the PT -symmetric resonator pair in shunt to a resistor Z_0 and in series with a microwave generator having same internal impedance Z_0. This readout design ensures that the whole sensing network remains matched around the EP to the internal impedance of the generator, avoiding backward propagating waves reflected into the generator [81]. According to the readout circuit design in Fig. 2.1 (a), the reflection coefficient can be expressed as

$$S_{11} = -\frac{Z_0}{2Z_{in}+Z_0}, \tag{2.18}$$

where Z_{in} is the input impedance of the PT-symmetric resonator pair,

$$Z_{in} = \frac{i\gamma R\left[\omega^4 - i\gamma\ \omega^3 - \left(1+2\mu\right)\omega^2 + 2i\gamma\ \mu\ \omega + \mu\right]}{\omega\left[\omega^4 + \left(\gamma^2 - 2 - 2\mu\right)\omega^2 + 1 + 2\mu - 2\mu\ \gamma^2\right]}. \tag{2.19}$$

As expected, the denominator of Z_{in} corresponds to the characteristic equation of the PT -symmetric system, which implies that the resonant dips of S_{11} directly correspond to the system eigenfrequency. The dependence of the resonant shift on a small perturbation ε can be found by solving the eigenvalue problem:

$$H_{eff}\left(\gamma=\gamma_{EP}, \mu=\mu_{EP}, \varepsilon\right)\Psi\left(\varepsilon\right) = \omega\left(\varepsilon\right)\Psi\left(\varepsilon\right), \tag{2.20}$$

where the eigenvalues are:

$$\begin{cases} \omega_{1,2} = \pm\dfrac{1}{2}\sqrt{\left(\sqrt{5}-1\right)\varepsilon - \sqrt{16\varepsilon + \left(\sqrt{5}-1\right)^2\varepsilon^2}}, \\ \omega_{3,4} = \pm\dfrac{1}{2}\sqrt{\left(\sqrt{5}-1\right)\varepsilon + \sqrt{16\varepsilon + \left(\sqrt{5}-1\right)^2\varepsilon^2}}, \\ \omega_{5,6} = 0 \end{cases} \tag{2.21}$$

If perturbation strength is relatively small, we can expand the above equation in Newton-Puiseux series [72]:

$$\begin{cases} \omega_{1,2} = \pm i\left[\varepsilon^{\frac{1}{4}} + \dfrac{1-\sqrt{5}}{8}\varepsilon^{\frac{3}{4}} + o\left(\varepsilon^{\frac{5}{4}}\right) + \cdots\right], \\ \omega_{3,4} = \pm\left[\varepsilon^{\frac{1}{4}} + \dfrac{-1+\sqrt{5}}{8}\varepsilon^{\frac{3}{4}} + o\left(\varepsilon^{\frac{5}{4}}\right) + \cdots\right], \\ \omega_{5,6} = 0, \end{cases} \tag{2.22}$$

The corresponding eigenvectors are:

$$\begin{cases} \left|\Psi_1\right\rangle\left(\omega = i\varepsilon^{\frac{1}{4}}\right) = \left[1 \quad 1 - \dfrac{1+\sqrt{5}}{2}\varepsilon^{\frac{1}{4}} + \varepsilon^{\frac{1}{2}} \quad 1 - \left(1+\sqrt{5}\right)\varepsilon^{\frac{1}{4}} + \left(3+\sqrt{5}\right)\varepsilon^{\frac{1}{2}} \quad -\varepsilon^{\frac{1}{4}} \quad -\varepsilon^{\frac{1}{4}} \quad -\varepsilon^{\frac{1}{4}}\right]^T, \\ \left|\Psi_2\right\rangle\left(\omega = -i\varepsilon^{\frac{1}{4}}\right) = \left[1 \quad 1 + \dfrac{1+\sqrt{5}}{2}\varepsilon^{\frac{1}{4}} + \varepsilon^{\frac{1}{2}} \quad 1 + \left(1+\sqrt{5}\right)\varepsilon^{\frac{1}{4}} + \left(3+\sqrt{5}\right)\varepsilon^{\frac{1}{2}} \quad \varepsilon^{\frac{1}{4}} \quad \varepsilon^{\frac{1}{4}} \quad \varepsilon^{\frac{1}{4}}\right]^T, \\ \left|\Psi_3\right\rangle\left(\omega = \varepsilon^{\frac{1}{4}}\right) = \left[1 \quad 1 + i\dfrac{1+\sqrt{5}}{2}\varepsilon^{\frac{1}{4}} - \varepsilon^{\frac{1}{2}} \quad 1 + i\left(1+\sqrt{5}\right)\varepsilon^{\frac{1}{4}} - \left(3+\sqrt{5}\right)\varepsilon^{\frac{1}{2}} \quad j\varepsilon^{\frac{1}{4}} \quad j\varepsilon^{\frac{1}{4}} \quad j\varepsilon^{\frac{1}{4}}\right]^T, \\ \left|\Psi_4\right\rangle\left(\omega = -\varepsilon^{\frac{1}{4}}\right) = \left[1 \quad 1 - i\dfrac{1+\sqrt{5}}{2}\varepsilon^{\frac{1}{4}} - \varepsilon^{\frac{1}{2}} \quad 1 - i\left(1+\sqrt{5}\right)\varepsilon^{\frac{1}{4}} - i\left(3+\sqrt{5}\right)\varepsilon^{\frac{1}{2}} \quad -j\varepsilon^{\frac{1}{4}} \quad -j\varepsilon^{\frac{1}{4}} \quad -j\varepsilon^{\frac{1}{4}}\right]^T, \\ \left|\Psi_5\right\rangle\left(\omega_5 = 0\right) = \left[1 \quad 1 \quad 1 \quad 0 \quad 0 \quad 0\right]^T, \\ \left|\Psi_6\right\rangle\left(\omega_6 = 0\right) = \left[1 \quad 1 \quad 1 \quad 0 \quad 0 \quad 0\right]^T, \end{cases}$$

(2.23)

The above analysis indicates that if the resonant frequency shift is:

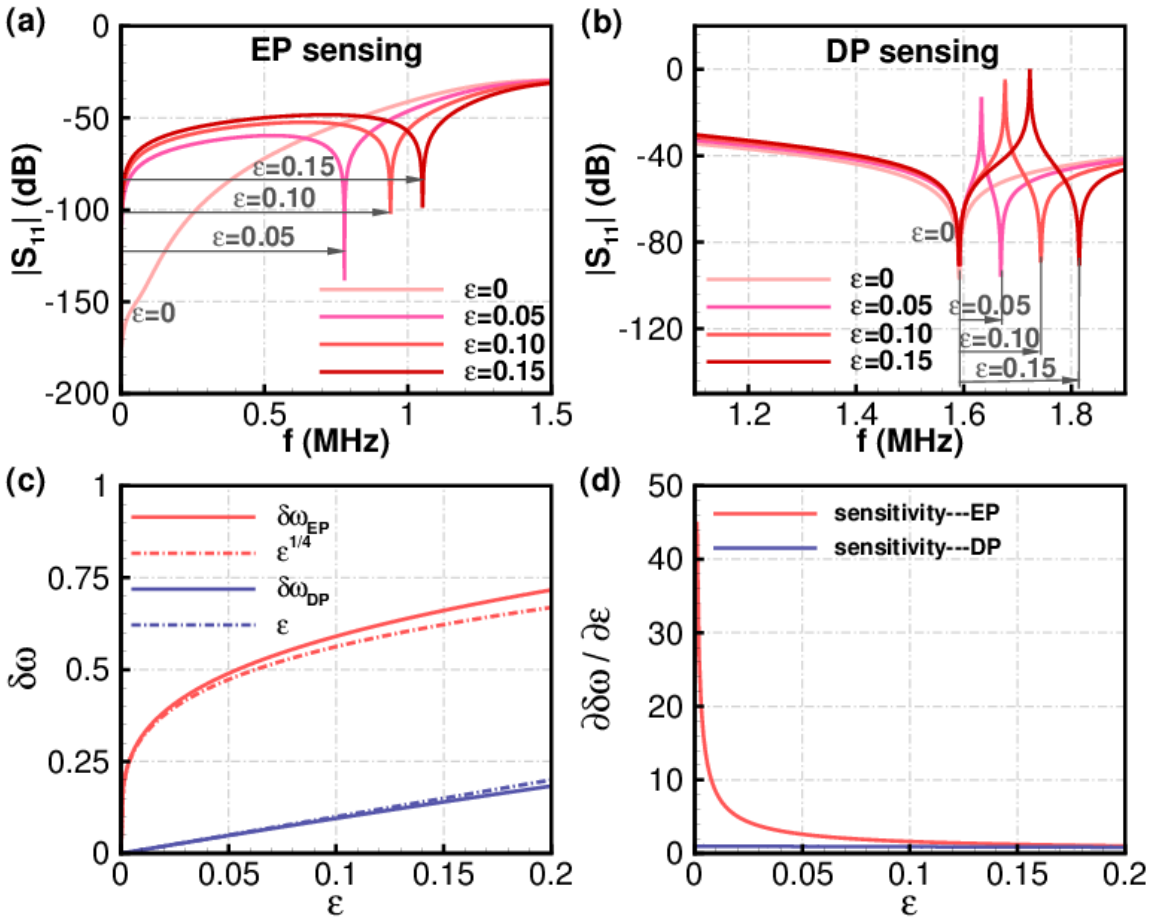

Figure 2.3: Amplitude of reflection coefficient, eigenfrequency shift, and sensitivity at EP and DP. (a) Amplitude of reflection coefficient with different perturbation strength for EP sensing system. (b) Amplitude of reflection coefficient for DP sensing system. (c) Eigenfrequency shift at EP and DP, dashed lines represent the corresponding series expansion truncated to the first order. (d) Sensitivity at EP and DP versus the perturbation. The components are chosen as follows: $L = 100\ \mu\text{H}$, $C = 100\ \text{pF}$, $R = 618.03\ \Omega$, Z_0=50 Ω. For EP sensing system $C_0 = 323.6\ \text{pF}$; for DP system $C_0 = 0.1\ \mu\text{F}$. The above ADS simulation results confirmed our theory (see the Appendix A for circuit schematic).

$$\delta\ \omega_{EP} = \varepsilon^{\frac{1}{4}} + \frac{-1+\sqrt{5}}{8}\varepsilon^{\frac{3}{4}} + o\left(\varepsilon^{\frac{5}{4}}\right) + \cdots \tag{2.24}$$

We confirm our theoretical analysis by simulating the reflection amplitude for different perturbation strengths in Fig. 2.3 (a). When the perturbation ϵ is 0, the system exactly operates at a sixth-order EP with eigenfrequency $\omega_{EP} = 0$ leading to a resonant dip on the reflection spectrum. When the coupling coefficient μ increases, the whole sensing system deviates from the sixth-order EP. Consequently, another resonant dip arises and shifts to the right, clearly seen in Fig. 2.3 (a). We extract these resonant dips $\delta\omega_{EP}$ and show them in Fig. 2.3 (c). Our data indicate that the resonant frequency shift is proportional to the fourth-order root of the perturbation strength, as expected.

To prove that the higher-order EP in our electronic circuit offers enhanced sensitivity compared to conventional sensors, we study an analogous Hermitian sensing circuit supporting a DP. Referring to Fig. 2.1 (a), the Hermitian counterpart of our circuit layout can be realized by removing both the loss element R and the gain element -R. The Hermitian system operates at a second order DP as the coupling coefficient μ goes to 0. In Fig. 2.3 (b), we report the reflection amplitude associated with this circuit for various perturbation strengths. The corresponding eigenfrequency shift $\delta\omega_{DP}$ is also shown in Fig. 2.3 (c). Both curves confirm that the resonant frequency shift is linearly proportional to the perturbation strength for DP sensing. We compare the sensitivity of our EP and DP sensing schemes in Fig. 2.3 (d), showing that the higher-order EP sensing scheme indeed provides enhanced sensitivity.

A perturbation on the resistor, inductor, or capacitor in the resonator, in principle, can result in frequency shift or splitting. However, these perturbation schemes inevitably bring in complex eigenfrequencies, which broaden the line shape and create a wide unresolvable region, as shown in previous EP sensor demonstrations [68][69]. Our design is devoid of these complex eigenfrequencies and therefore

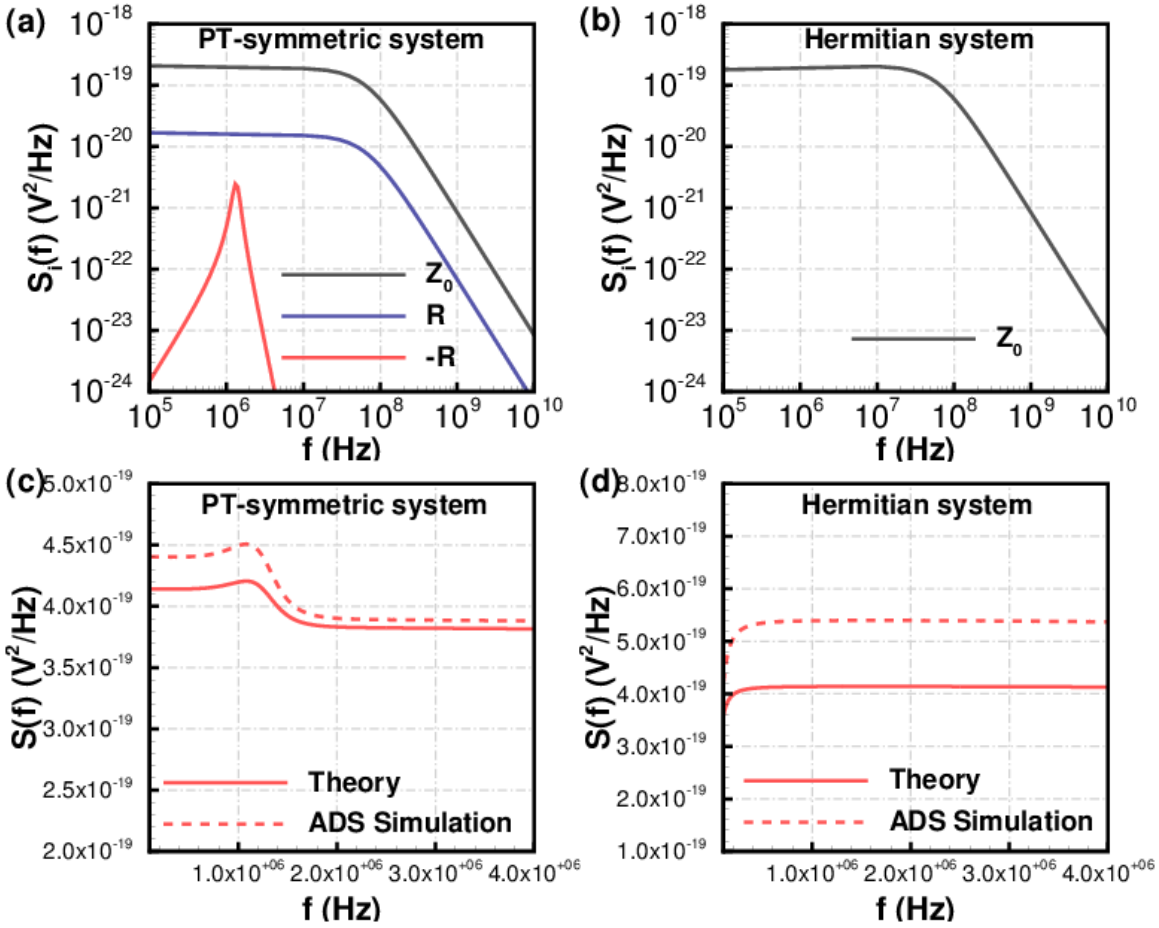

Figure 2.4: Thermal noise power spectral density. The circuit parameters are identical to Fig. 2. (a) Thermal noise power spectral density from the impedance Z0, from the resistor R, and from the gain element -R, respectively, in the PT -symmetric system. (b) Thermal noise power spectral density from the impedance Z_0 in the corresponding Hermitian system. (c) Total thermal noise power spectral density in the PT symmetric system, dashed line indicates the ADS simulation results. (d) Total thermal noise power spectral density in the corresponding Hermitian system, the dashed line indicates ADS simulation results (see the Appendix A for circuit schematic).

dramatically improves the sensing resolution, especially for small perturbations. Our assessments are further confirmed in the Appendix A. In practice, sophisticated

techniques should be involved to maintain a good match between the gain and loss parameter [77].

2.4 MITIGATING THERMAL NOISE

PT -symmetric circuitry relies on additional gain and loss elements, prone to add noise to the system. This issue has raised a degree of skepticism from the community concerning the effectiveness of EP sensing protocols. There are shot noise, flicker noise, and thermal noise in an electronic circuit. Since the shot noise mainly exists in circuits with tunneling diode or vacuum tube, and flicker noise can be significantly reduced below the level of thermal noise by choosing wirewound resistors [82]-[85], we aim for analyzing thermal noise in this work. In the following, we will show how thermal noise is alleviated in our sensing scheme.

Thermal noise in an electronic circuit is characterized by the power spectral density (PSD) which reads: $S_i(f) = 4k_B T \left| H_i(f) \right|^2 R_i$ [84][85], where k_B is the Boltzmann constant, T is the temperature, R_i is the resistance of the noise source, and $H_i(f)$ is the transfer function. The latter defines the voltage ratio between the probing point [see Fig. 2.1 (a)] and the noise source. We first investigate the PSD associated with the internal impedance of the generator. Assuming that there is an equivalent voltage noise source in series with the internal impedance Z_0, we find that the transfer function takes the form $H_1 = Z_{in} / (2Z_{in} + Z_0)$. Since the resistor Z_0 is in shunt with the internal impedance Z_0, the transfer function is $H_2 = H_1$, leading to an identical PSD to the internal impedance Z_0 . For the loss element R, the transfer function is $H_3 = Z_0 Z_{in} / (Z_{in} Z_0 + R Z_0 + 2R Z_{in})$. The noise from the negative impedance -R is more complicated to assess because it depends on the specific circuit design implementing the negative impedance. Here, we assume to use an amplifier circuit with noninverting

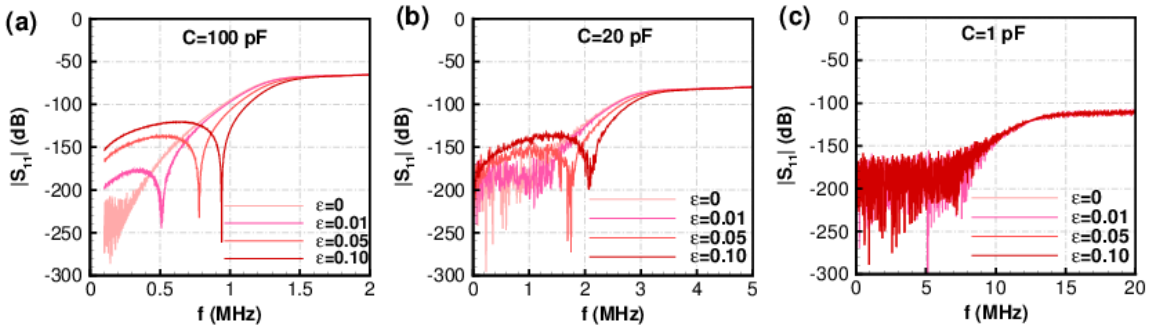

Figure 2.5: Simulation of measurement results under the influence of thermal noise. The circuit parameters are identical to Fig. 2.3, except for the capacitor C in the resonator. The temperature T is 300 K and the voltage of the generator V_g is 1 Volt. (a) Amplitude of reflection coefficient, with $C = 100$ pF. (b) Amplitude of reflection coefficient, with $C = 20$ pF. (c) Amplitude of reflection coefficient, with $C = 1$ pF.

feedback configuration. The feedback impedance is thus set to R, which indicates that the noise PSD is proportional to R. The thermal noise PSD from each noise source is shown in Fig. 2.4 (a), which indicates that the noise PSD from the gain and loss elements are negligible compared to those stemming from the two Z_0 elements. We conclude therefore that the total thermal noise PSD in the PT -symmetric sensing system and its corresponding Hermitian system are almost identical. Figures 2.4 (c) and 2.4 (d) show the theoretical and numerical thermal noise PSD provided by ADS software, which are in excellent agreement with each other.

Integrated noise power and signal to noise ratio (SNR) are important metrics of thermal noise as well. In a circuit with N independent noise sources, the total noise power can be expressed as

$$P_{noise} = \overline{v_{noise}^2} = \sum_{i=1}^{N} \int_0^{\infty} S_i(f)\mathrm{d}f, \tag{2.25}$$

where V_{noise} is the noise voltage, N is the total number of noise sources. Since the noise power from the resistor R and -R are negligible compared with the impedance Z_0, we

only consider the noise power from the internal impedance Z_0 and shunt resistor Z_0. Substituting the transfer function into Eq. (2.25), the approximate thermal noise power from each Z_0 takes the form: $k_B T/2C$, indicating that the noise power is independent of the impedance value Z_0, the inductance L, and the coupling capacitance C_0. Therefore, the noise power in our PT -symmetric sensing network and the Hermitian counterpart are:

$$P_{noise}^{PT} \approx P_{noise}^{Hermitian} \approx \frac{k_B T}{C}. \tag{2.26}$$

an expression identical to the integrated noise of a low pass RC filter [85]. This result indicates that the integrated thermal noise of the PT -symmetric and Hermitian sensing systems are identical due to the low pass feature of our design. When the system is perturbed, the total noise power slightly changes, but this variation is negligible. At EP or DP, the resonator pair is essentially open, which results in $V_g/2$ signal voltage at the probing point, where V_g is the voltage of the generator. Therefore, the SNR at EP or DP is

$$SNR^{EP} \approx SNR^{DP} = \frac{CV_g^2}{4k_B T}. \tag{2.27}$$

Finally, we study the influence of thermal noise on measurement results. The probing voltage V_{probe} and the reflection coefficient S_{11} in our sensing network has an intuitive relation:

$$S_{11} = 2\left(V_{probe} + V_{noise}\right)/V_g - 1. \tag{2.28}$$

Therefore, the deviation of the reflection coefficient is

$$D\left[S_{11}\right]^{PT} \approx D\left[S_{11}\right]^{Hermitian} = \frac{4k_B T}{CV_g^2}, \tag{2.29}$$

where “D” indicates the deviation. Equations (2.27)-(2.29) prove that our EP sensing system shares the same thermal noise performance compared with the corresponding DP sensing scheme. Figure 2.5 shows the simulation of measurements under the influence of

thermal noise. Figure 2.5 (a) corresponds to the sensing circuit we designed in this work, where thermal noise has little influence on the measurement results, confirming that thermal noise in our EP sensing system is fully manageable by choosing a proper working capacitance value in the resonator. Figure 2.5 (b) shows a marginal design, for which the measurement results can still be recorded. Figure 2.5 (c) demonstrates a failed design, where the signal is fully buried by thermal noise and no sensing can be performed.

2.5 CONCLUSIONS

In this chapter, we have put forward a sensing circuit based on a sixth-order EP, showing an enhanced resonant shift proportional to the fourth-order root of the perturbation strength. Due to the balanced loss and gain configuration and our perturbation scheme, the resolution is also improved. Our PT -symmetric system not only serves as a sensing platform, but also filters out high-frequency thermal noise, leading to a nearly identical thermal noise level compared to the corresponding Hermitian DP sensing scheme. Considering the combined high-sensitivity, improved resolution, and nondegraded thermal noise performance, we envision that accelerometers, pressure sensors, or microfluid flow speed sensors may be implemented following this scheme with unprecedented sensitivity, resolution, and excellent thermal noise performance, as sketched in Fig. 2.1.

Chapter 3: Noise Performance of Enhanced Sensing based on Second-Order Exceptional Points[2]

In this chapter, continuing on the previous analysis, I present a general study of the Green's function, scattering poles, and thermal noise performance of enhanced sensing around exceptional points. A circuit example is proposed based on a second-order exceptional point to confirm the theoretical analysis. The main results are from the ref. [86] , which is under review.

3.1 INTRODUCTION

Bifurcation occurs when a physical system's topological features experience sharp transitions in response to a smooth change of a certain parameter within the system [87]-[88]. It can be ubiquitous in nature and of fundamental importance in characterizing a plethora of intriguing dynamic processes, such as the onset of lasing behavior in a pumped cavity [89]-[90], outbreak of insects in a forest [91], and self-oscillating chemical reactions [92]. In recent years, a new category of bifurcation, known as exceptional points (EP), has attracted widespread attention and excited intense interest in the fields of photonics [14],[66], acoustics [94]-[95] and electronics [62]-[63],[96]. Exceptional points are degeneracies in the spectrum of non-Hermitian operators where two (or in general N) eigenvalues and their corresponding eigenvectors coalesce resulting in a collapse of the eigenbasis [72]. Due to the exotic topological feature at these branch points, many fascinating applications were developed, such as mode switching [98] , topological energy transfer [99], and polarization state conversion [100]. More recently, enhanced sensing utilizing the sharp eigenvalue bifurcation around EP has facilitated a

[2] This chapter is in preparation and going to be submitted to a journal.

series of experimental demonstrations [68]-[71], [101]-[104]. By lifting the N-fold non-Hermitian degeneracy at EP, the eigenfrequencies of an open system undergo a splitting with N-th order root law [97], which is highly sensitive to parametric perturbation compared with the linear response of diabolic point (DP) sensing in Hermitian systems.

However, these enhanced sensing demonstrations based on EP in various non-Hermitian platforms have led to a series of arguments concerning their sensitivity, resolution, and signal to noise ratio performance [73]-[77], [105]-[106]. Langbein studied the mode amplitude of unbalanced-loss sensing system and argued that these perturbed mode amplitudes scale linearly with the perturbation strength [73]. Lau *et al.* investigated the quantum EP sensing and claimed that nonreciprocal EP sensing setup shows the prospect of enhanced sensitivity and favorable noise performance [74]. On the other hand, Wang *et al.* have experimentally demonstrated that enhanced sensing near EP is masked by simultaneously enhanced Petermann factor due to the nonorthogonality of modes at EP [78]. Despite the fundamental importance of understanding the effects of quantum noise in the EP-sensing, in many sensing schemes the dominant issue is classical noise and its mitigation. In this work, we attempt to provide a unified theoretical framework to analyze the sensitivity, resolution, and classical thermal noise performance of two-level EP and DP sensing systems. We pay close attention to the self-orthogonality of degenerate eigenmodes at EP and decompose the Green's function of the effective Hamiltonian by reconstructing the collapsed eigenspace using Jordan vectors [107]-[109]. Our study shows that, it's possible to have enhanced sensitivity, resolution, and nondegraded thermal noise performance in a one-port reflective EP sensing setup. Our

theoretical results are further confirmed with concrete simulations of EP sensing in an electronic circuit and show an exciting prospect for EP sensing in optomechanical, electromechanical, acoustic, and open quantum systems [110].

3.2 SENSITIVITY AND SCATTERING ANALYSIS OF NON-HERMITIAN SENSING SYSTEMS

3.2.1 Eigenfrequency and mode bifurcation of non-Hermitian sensing systems

In this work, we aim to analyze EP and DP sensing in two-level systems, which are described by Hamiltonian $H=\begin{bmatrix} \omega_1+i\gamma_1 & \kappa \\ \kappa & \omega_2+i\gamma_2 \end{bmatrix}$, where ω_i is the resonant frequency of the mode *i*, γ_i is the associated gain or loss rate, positive γ_i represents gain and negative γ_i represents loss, $i=1,2$. κ is the coupling rate between these two resonant modes or cavities. Various combination of resonances, loss (gain) rate or coupling rate can lead to different non-Hermitian and Hermitian systems. To simplify our study, we employ a simple one-port sensing network to probe the eigenfrequency of the system [see Fig. 3.1]. The eigenfrequencies are obtained by solving the eigenvalue problems $H_{eff}\mathbf{u}=\omega\mathbf{u}$ and $\mathbf{v}^T H_{eff}=\omega\mathbf{v}^T$:

$$\omega_{\pm}=\frac{1}{2}\left(\omega_1+\omega_2\right)+\frac{i}{2}\left(\gamma_1^{'}+\gamma_2\right)\pm\frac{1}{2}\sqrt{\left(\omega_1+i\gamma_1^{'}+\omega_2+i\gamma_2\right)^2+4\left(\kappa^2+\gamma_1^{'}\gamma_2-\omega_1\omega_2-i\gamma_1^{'}\omega_2-i\gamma_2\omega_1\right)} \tag{3.1}$$

where $H_{eff}=H-i\Gamma$, $\Gamma=\begin{bmatrix} \gamma_e & 0 \\ 0 & 0 \end{bmatrix}$ is the external decaying matrix, $\gamma_1^{'}=\gamma_1-\gamma_e$, $\mathbf{u}$ and $\mathbf{v}^T$ are right and left eigenvectors, respectively.

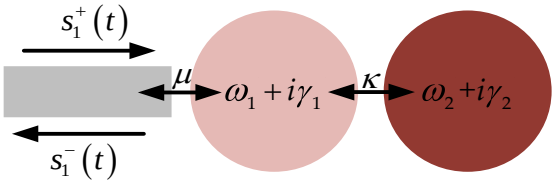

Figure 3.1: One-port scattering setup where a probing channel is side coupled to mode $\omega_1+i\gamma_1$. The decaying matrix is $\Gamma=\begin{bmatrix}\gamma_e & 0\\ 0 & 0\end{bmatrix}$, γ_e is the external loss rate from mode 1 to the waveguide, $\mu=\sqrt{2\gamma_e}$ is the corresponding coupling coefficient.

EP or DP sensing requires the system to be initialized to an EP or DP where the eigenvalues are degenerate. For unbalanced loss system, unbalanced loss/gain system, and parity-time (PT)-symmetric system, the condition for EP is $\omega_1=\omega_2=\omega_0, \kappa_{EP}=\frac{\left|\gamma_1^{'}-\gamma_2\right|}{2}$, where the system has a degenerate eigenfrequency $\omega_{EP}=\omega_0+\frac{i}{2}\left(\gamma_1^{'}+\gamma_2\right)$. For Hermitian system, DP condition is: $\omega_1=\omega_2=\omega_0$, κ_{DP}=0, $\gamma_1=\gamma_2=0$, where the degenerate eigenfrequency is $\omega_{DP}=\omega_0$. After setting these non-Hermitian and Hermitian systems to the degenerate point, we apply a perturbation on the system where the perturbed Hamiltonian can be expressed as $H_{eff}\left(\varepsilon\right)=H_0+H_1\varepsilon+\mathrm{O}\left(\varepsilon^2\right)$, H_0 is the Hamiltonian at EP or DP, ε is the relative perturbation strength, H_1 is the first-order perturbation matrix, O is an asymptotic notation. When the sensing system is perturbed around the EP, we have eigenvalue problems $H_{eff}\left(\varepsilon\right)\mathbf{u}=\omega\mathbf{u}$ and $\mathbf{v}^T H_{eff}=\omega\mathbf{v}^T$, which leads to the following eigenfrequencies

$$\omega_{\pm}(\varepsilon) \approx \omega_{EP} \pm \sqrt{\mathbf{v}_0^T H_1 \mathbf{u}_0}\,\varepsilon^{\frac{1}{2}}, \tag{3.2}$$

where ω_{EP} is the degenerate eigenfrequency at EP, $\mathbf{u}_0$ and $\mathbf{v}_0^T$ are right and left eigenstates at EP, which are defined by $H_0\mathbf{u}_0 = \omega_{EP}\mathbf{u}_0$ and $\mathbf{v}_0^T H_0 = \omega_{EP}\mathbf{v}_0^T$, $\mathbf{u}_1$ and $\mathbf{v}_1^T$ are right and left Jordan chain vectors defined by $H_0\mathbf{u}_1 = \omega_{EP}\mathbf{u}_1 + \mathbf{u}_0$ and $\mathbf{v}_1^T H_0 = \omega_{EP}\mathbf{v}_1^T + \mathbf{v}_0^T$. The following normalization conditions are adopted in our derivation: $\mathbf{v}_0^T\mathbf{u}_0 = 0, \mathbf{v}_1^T\mathbf{u}_0 = \mathbf{v}_0^T\mathbf{u}_1 = 1, \mathbf{v}_1^T\mathbf{u}_1 = 0$. Perturbation at EP results in a mode splitting $\Delta\omega_{EP} \approx 2\sqrt{\mathbf{v}_0^T H_1 \mathbf{u}_0}\,\varepsilon^{\frac{1}{2}}$, which demonstrates an enhanced sensitivity compared with linear mode splitting. Note that $\sqrt{\mathbf{v}_0^T H_1 \mathbf{u}_0}$ is not necessarily a purely real parameter, indicating that unproper perturbation scheme may bring in unwanted imaginary part, leading to broadened spectrum and reduced resolution.

For DP sensing, the effective Hamiltonian at DP is $H_0 = \begin{bmatrix} \omega_0 & 0 \\ 0 & \omega_0 \end{bmatrix}$. Since perturbation on the resonance will only shift one of the resonances, we assume a perturbation on the coupling coefficient with perturbation matrix $H_1 = \begin{bmatrix} 0 & \omega_0 \\ \omega_0 & 0 \end{bmatrix}$. Therefore, the eigenfrequencies are

$$\omega_{\pm}(\varepsilon) = \omega_0 \pm \omega_0\varepsilon, \tag{3.3}$$

with $\Delta\omega_{DP} = 2\omega_0\varepsilon$ scaling linearly versus the perturbation strength. Equations (3.2) and (3.3) are the main evidence supporting the claim that EP sensing offers enhanced sensitivity compared with DP sensing. However, as argued in many papers, these eigenfrequencies are not direct observables. Therefore, it is important to unveil the relation between these eigenfrequencies and scattering peaks and valleys in a realistic sensing setup.

3.2.2 Green's function and scattering extremes

We have studied the mode bifurcation and sensitivity of EP and DP sensing systems in previous subsection. Now, we reveal the relation between the eigenfrequency and the resonant dips or peaks of scattering spectrum, which is largely unexploited in current literature. This line of study helps define the fundamental resolution limit of our EP and DP sensing schemes. Coupled mode theory (CMT) is a powerful tool to characterize the dynamic evolution of the mode amplitude and the scattered fields [111][112]:

$$\begin{cases} \dfrac{\mathrm{d}\mathbf{a}(t)}{\mathrm{dt}} = (-iH - \Gamma)\mathbf{a}(t) + K^T \mathbf{s}^+(t), \\ \mathbf{s}^-(t) = C\mathbf{s}^+(t) + K\mathbf{a}(t), \end{cases} \tag{3.4}$$

where $\mathbf{a}(t) = \begin{bmatrix} a_1(t) & a_2(t) \end{bmatrix}^T$ is the field amplitude of the cavity or mode. T is a transpose operator, K is the coupling matrix which defines the coupling between the cavity and the probing waveguide, $\Gamma = K^\dagger K/2$ is the decaying loss matrix, $\dagger$ is a conjugate transpose operator, $C = \begin{bmatrix} r & t \\ t & r \end{bmatrix}$ is the scattering matrix when the non-Hermitian sensing system is totally disconnected from the probing waveguide. r is the reflection coefficient and t is the transmission coefficient, and the whole matrix satisfies passivity condition $C^\dagger C = \mathbf{I}$, where $\mathbf{I}$ is a two by two identity matrix. $\mathbf{s}^\pm(t) = \begin{bmatrix} s_1^\pm(t) & s_2^\pm(t) \end{bmatrix}^T$ are the input and output state vectors, respectively.

By performing a Fourier transform over Eq. (3.4) and using the relation $CK^* = -K$ dictated by time-reversal symmetry, we obtain the scattering matrix:

$$S = C + iKGK^T, \tag{3.5}$$

where S is defined by the relation $\mathbf{s}^-(\omega) = S\mathbf{s}^+(\omega)$, $\mathbf{I}$ is a two by two identity matrix, $G = \left(\omega\mathbf{I} - H_{eff}\right)^{-1}$ is the Green's function. It determines the joint spectral response of the

isolated system and its associated probing waveguide. The Green's function is singular if $Det\left|\omega\mathbf{I}-H_{eff}\right|=0$, corresponding to the case where the excitation signal frequency is equal to one of the eigenfrequencies of the effective Hamiltonian. Therefore, we employ modal expansion approach to clearly show the relation between Green's function, scattering poles and eigenvectors of effective Hamiltonian:

$$G\left(\omega,\varepsilon\right)=\frac{1}{\omega-\omega_{+}}\frac{\mathbf{u}_{+}\mathbf{v}_{+}^{T}}{\mathbf{v}_{+}^{T}\mathbf{u}_{+}}+\frac{1}{\omega-\omega_{-}}\frac{\mathbf{u}_{-}\mathbf{v}_{-}^{T}}{\mathbf{v}_{-}^{T}\mathbf{u}_{-}}\left(\omega\neq\omega_{\pm},\varepsilon\neq0\right), \tag{3.6}$$

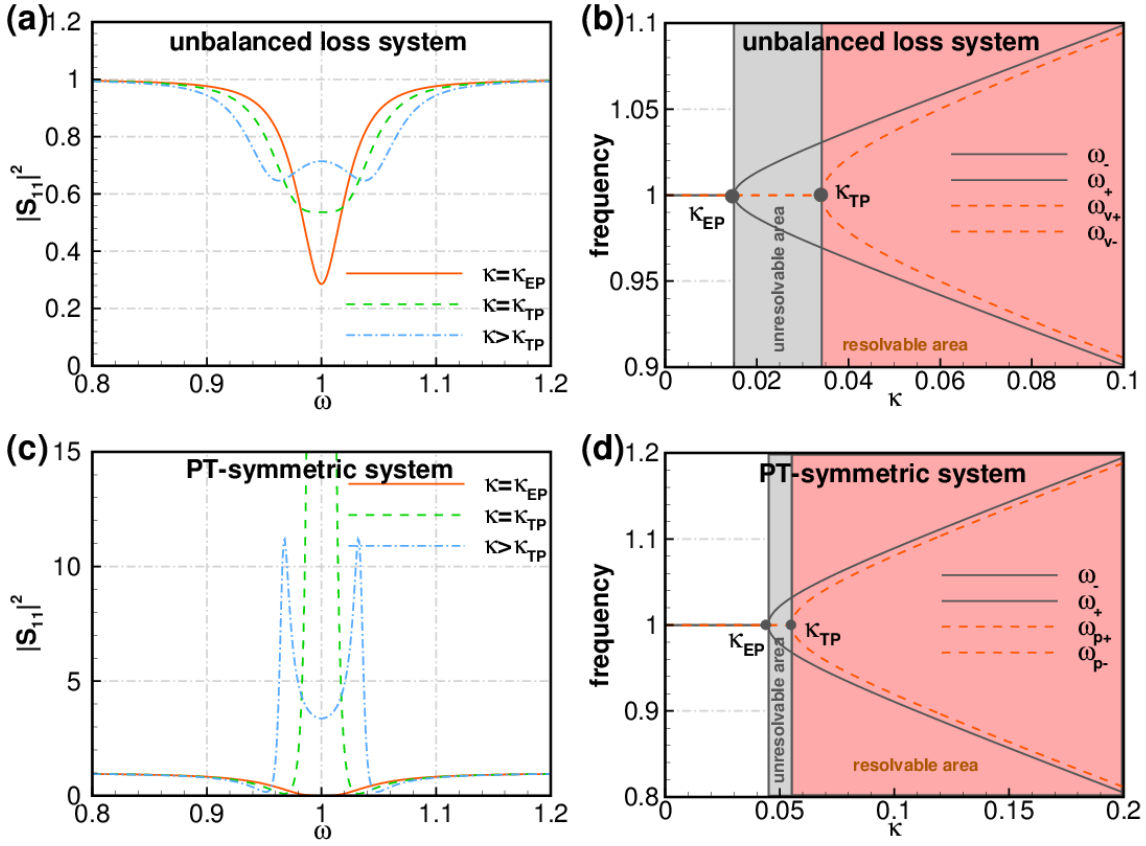

Figure 3.2: One-port scattering setup where a probing channel is side coupled to mode $\omega_1+i\gamma_1$. The decaying matrix is $\Gamma=\begin{bmatrix}\gamma_e & 0\\ 0 & 0\end{bmatrix}$, γ_e is the external loss rate from mode 1 to the waveguide, $\mu=\sqrt{2\gamma_e}$ is the corresponding coupling coefficient. Relation between resonant mode splitting and scattering extremes in EP sensing schemes. (a) Reflectance of the unbalanced loss sensing system. $\gamma_1=-0.01, \gamma_2=-0.05, \gamma_e=0.01$. The exceptional point is $\kappa_{EP}=0.015$ and the resolving threshold point is $\kappa_{TP}=0.034$. (b). Eigenfrequencies and the valleys of the reflectance curve. In the region $\kappa_{EP}<\kappa<\kappa_{TP}$, we can see the bifurcation of eigenfrequency, but we cannot see the valleys the reflectance curve because of the linewidth broadening. In the region $\kappa>\kappa_{TP}$, we can see valleys of the reflectance curve. (c) Reflectance of the PT-symmetric sensing system. $\gamma_1=-0.05, \gamma_2=0.05, \gamma_e=0.01$. The exceptional point is $\kappa_{EP}=0.045$ and the resolving threshold point is $\kappa_{TP}=0.055$. (d). Eigenfrequencies and the peaks of the reflectance curve. In the region $\kappa_{EP}<\kappa<\kappa_{TP}$, we can see the bifurcation of eigenfrequency, but we cannot see the peaks the reflectance curve because of the linewidth broadening. In the region $\kappa>\kappa_{TP}$, we can see peaks of the reflectance curve.

where ε is the relative strength of perturbation on the effective Hamiltonian, $\omega_\pm$ are the eigenvalues of $H_{eff}(\varepsilon)$, $\mathbf{u}_\pm$ and $\mathbf{v}_\pm^T$ are the right and left eigenstates of the effective Hamiltonian $H_{eff}(\varepsilon)$, which are defined by eigenvalue problems $H_{eff}(\varepsilon)\mathbf{u}_\pm=\omega_\pm\mathbf{u}_\pm$ and $\mathbf{v}_\pm^T H_{eff}(\varepsilon)=\omega_\pm\mathbf{v}_\pm^T$.

The above equation is valid for both EP and DP sensing systems, but its behavior is significantly different at EPs and DPs. In the limit of $\varepsilon\to 0$, the system locates exactly at the exceptional point. Both left and right eigenstates become self-orthogonal ($\lim_{\varepsilon\to\infty}\mathbf{v}_+^T\mathbf{u}_+=\mathbf{v}_-^T\mathbf{u}_-=0$), which results in ill-defined Green's function. It's necessary to employ Jordan decomposition of the effective Hamiltonian $H_{eff}(\varepsilon)$ to deal with the dot product and cross product of these eigenvectors, which leads to the following Green's function at EP:

$$G(\omega,\varepsilon=0)\approx\frac{\mathbf{u}_0\mathbf{v}_0^T}{(\omega-\omega_{EP})^2}+\frac{\mathbf{u}_0\mathbf{v}_1^T+\mathbf{u}_1\mathbf{v}_0^T}{\omega-\omega_{EP}}(\omega\neq\omega_{EP}) \tag{3.7}$$

where ω_{EP} is the degenerate eigenfrequency at EP, $\mathbf{u}_0$ and $\mathbf{v}_0^T$ are right and left eigenstates at EP, which are defined by $H_0\mathbf{u}_0=\omega_{EP}\mathbf{u}_0$ and $\mathbf{v}_0^TH_0=\omega_{EP}\mathbf{v}_0^T$, $\mathbf{u}_1$ and $\mathbf{v}_1^T$ are right and left Jordan chain vectors defined by $H_0\mathbf{u}_1=\omega_{EP}\mathbf{u}_1+\mathbf{u}_0$ and $\mathbf{v}_1^TH_0=\omega_{EP}\mathbf{v}_1^T+\mathbf{v}_0^T$. For DP sensing system, the eigenspace remains untouched by Hermitian degeneracy, resulting in the following Green's function at DP:

$$G(\omega,\varepsilon=0)=\frac{1}{\omega-\omega_{DP}}\left(\frac{\mathbf{u}_0\mathbf{v}_0^T}{\mathbf{v}_0^T\mathbf{u}_0}+\frac{\mathbf{u}_0\mathbf{v}_0^T}{\mathbf{v}_0^T\mathbf{u}_0}\right), \tag{3.8}$$

where $\omega_{DP}=\omega_0$ is the degenerate eigenfrequency at DP, $\mathbf{u}_0$ and $\mathbf{v}_0^T$ are right and left eigenstates at DP, which are defined by $H_0\mathbf{u}_0=\omega_{DP}\mathbf{u}_0$ and $\mathbf{v}_0^TH_0=\omega_{DP}\mathbf{v}_0^T$. Armed with Eqs. (3.6)-(3.8), we are now ready to analyze the effects of noise to the sensitivity of EP and DP sensing.

Substituting Eq. (3.6) into Eq. (3.5), we obtain the reflectance of our one-port sensing network:

$$|S_{11}|^2=\frac{(\omega-\omega_0)^4+\left[(\gamma_1+\gamma_e)^2+\gamma_2^2-2\kappa^2\right](\omega-\omega_0)^2+\left[(\gamma_1+\gamma_e)\gamma_2+\kappa^2\right]^2}{(\omega-\omega_0)^4+\left[(\gamma_1-\gamma_e)^2+\gamma_2^2-2\kappa^2\right](\omega-\omega_0)^2+\left[(\gamma_1-\gamma_e)\gamma_2+\kappa^2\right]^2}. \tag{3.9}$$

The reflectance peaks or valleys, which are employed to characterize the mode splitting of the non-Hermitian sensing system, also demonstrate square root splitting with respect to the perturbation strength. However, these peaks or valleys are always smaller than the eigenfrequencies of the non-Hermitian system. In Fig. 3.2, we show the reflectance, scattering extremes, and eigenfrequency of unbalanced loss sensing system and PT-symmetric system. It indicates that there is always an unresolvable region for EP sensing and PT-symmetric sensing system can help improve resolution limit compared with unbalanced loss system.

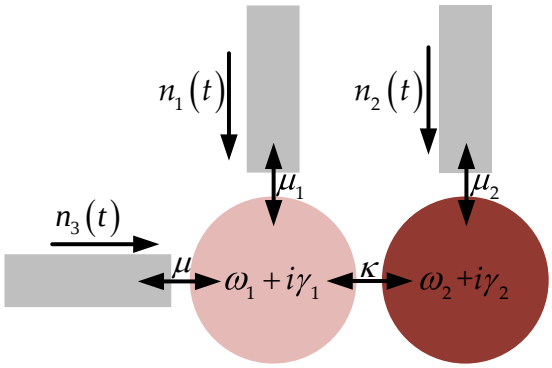

Figure 3.3: Thermal noise model. Two thermal baths $n_1(t)$, $n_2(t)$ are connected with mode 1 and 2, respectively. Another thermal bath $n_3(t)$ represents the external thermal fluctuation pumped into the resonant mode 1. The coupling rate for internal thermal bath is $\mu_i = \sqrt{2|\gamma_i|}$; the coupling rate for external thermal bath is $\mu = \sqrt{2\gamma_e}$; the temperature of all the thermal baths is T.

3.3 THERMAL NOISE PERFORMANCE

The past several years has witnessed a series of arguments against EP sensing. One of the major concerns is about the thermal noise which can potentially mask the supersensitive mode splitting. In this section, we will show the influence of thermal noise on the measurement results and demonstrate that proper design of EP sensing protocols can help mitigate the unwanted thermal noise effects. Thermal noise model is shown in Fig. 3, where three thermal baths of temperature T are coupled to the modes with coupling coefficient $\mu_1 = \sqrt{2|\gamma_1|}$, $\mu_2 = \sqrt{2|\gamma_2|}$, and $\mu = \sqrt{2\gamma_e}$, respectively. The Langevin equation governing the time evolution of the mode amplitudes reads:

$$\frac{\mathrm{d}\mathbf{a}(t)}{\mathrm{dt}} = -iH_{eff}\mathbf{a}(t) + \mathrm{K}^{\mathrm{T}}\mathbf{n}(t), \tag{3.10}$$

where $\mathbf{a}(t)=\begin{bmatrix} a_1(t) & a_2(t) \end{bmatrix}^T$ is the amplitude of modes due to the excitation of random thermal noise, $\mathrm{K}^{\mathrm{T}}=\begin{bmatrix} \sqrt{2|\gamma_1|} & 0 & \sqrt{2\gamma_e} \\ 0 & \sqrt{2|\gamma_2|} & 0 \end{bmatrix}$ is the coupling matrix between the thermal baths and the modes, $\mathbf{n}(t)=\begin{bmatrix} n_1(t) & n_2(t) & n_3(t) \end{bmatrix}^T$ is the random thermal fluctuation associated with the gain/loss elements, which satisfy $\langle n_i(t)\rangle=0$, $\langle n_i^*(t)n_i(t')\rangle=\Theta(\omega)\delta(t-t')$, $\langle n_i^*(t)n_j(t')\rangle=0$. "$\delta$" is the Dirac-Delta function, "$\langle\ \rangle$" means the expectation value of a stochastic process, $\Theta(\omega)=\dfrac{\hbar\omega}{\exp(\hbar\omega/k_BT)-1}$ is the Bose Einstein distribution, $\hbar$ is the Planck's constant, k_B is the Boltzmann constant.

Since the coupled modes are connected with three thermal baths, random thermal noise will emit to the probing waveguide. Power spectral density (PSD) is an important parameter to characterize the thermal noise. To this end, we perform a Fourier transform over Eq. (3.10) and figure out the amplitudes of modes excited by random noise: $\tilde{\mathbf{a}}(\omega)=iG\mathrm{K}^{\mathrm{T}}\tilde{\mathbf{n}}(\omega)$. As a result, the emitted noise amplitude in frequency domain is:

$$\tilde{n}_{noise}(\omega)=i\sqrt{2\gamma_e}\left[\sqrt{2|\gamma_1|}G_{11}\tilde{n}_1(\omega)+\sqrt{2|\gamma_2|}G_{12}\tilde{n}_2(\omega)+\sqrt{2\gamma_e}G_{11}\tilde{n}_3(\omega)\right], \quad (3.11)$$

where G_{11} and G_{12} are matrix elements of the Green's function. According to the Wiener-Khinchin theorem, the PSD of emitted thermal noise is:

$$S(\omega)=4\gamma_e\left[\left(|\gamma_1|+\gamma_e\right)|G_{11}|^2+|\gamma_2||G_{12}|^2\right]\Theta(\omega), \quad (3.12)$$

where relations $\langle n_i^*(\omega)n_i(\omega')\rangle=\delta(\omega-\omega')\Theta(\omega)$ and $\langle n_1^*(\omega)n_2(\omega')\rangle=\langle n_2^*(\omega)n_1(\omega')\rangle=0$ are used. We substitute the expression of Green's function from Eq. (3.6) into the above equation and get the PSD of emitted thermal noise:

$$S(\omega)=\frac{4\gamma_e\left\{\left(|\gamma_1|+\gamma_e\right)\left[(\omega-\omega_0)^2+\gamma_2^2\right]+|\gamma_2|\kappa^2\right\}\Theta(\omega)}{(\omega-\omega_0)^4+\left[(\gamma_1-\gamma_e)^2+\gamma_2^2-2\kappa^2\right](\omega-\omega_0)^2+\left[(\gamma_1-\gamma_e)\gamma_2+\kappa^2\right]^2}, \quad (3.13)$$

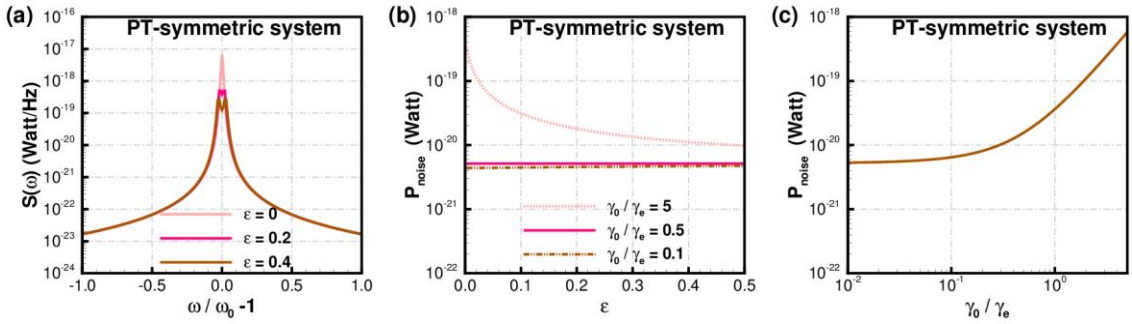

Figure 3.4: Power spectral density of thermal noise and integrated thermal noise. (a) Thermal noise power spectral density in PT-symmetric sensing system. γ_0=0.05, $\gamma_e = 0.02, T = 300K\ \hbar\omega_0 / k_B T << 1$. (b) Integrated thermal noise versus perturbation strength. (c) Integrated thermal noise versus γ_0/γ_e. γ_0=0.05, ε=0, $T = 300K$.

where we assume $\kappa = \kappa_{EP}(1+\varepsilon), \kappa_{EP} = \dfrac{|\gamma_1 - \gamma_e - \gamma_2|}{2}$. At EP, the PSD of the emitted thermal noise reduces to:

$$S(\omega, \varepsilon = 0) \approx \frac{4\gamma_e \left\{ \left(|\gamma_1| + \gamma_e \right) \left[(\omega - \omega_0)^2 + \gamma_2^2 \right] + |\gamma_2| \kappa_{EP}^2 \right\} \Theta(\omega)}{|\omega - \omega_{EP}|^4}. \tag{3.14}$$

Since measurements are influenced by the emitted noise in the whole spectrum, it's equally important to analyze the total noise power, which is defined as: $\mathrm{P}_{noise} = \int_{-\infty}^{+\infty} S(\omega) d\omega$. It's possible to show that to have small noise power for weak perturbation, we must have $\gamma_1 > 0, \gamma_2 < 0$. To simplify our study, we assume the system is PT-symmetric, which means $\gamma_1 = \gamma_0, \gamma_2 = -\gamma_0, \gamma_0 > 0$. Fig. 3.4 (b) shows that when $\gamma_0/\gamma_e \le 0.5$, total noise power decreases as the system approaches to EP, which is very favorable for EP sensing. At EP, the integrated noise power is:

$$\mathrm{P}_{\mathrm{noise}}^{EP} = 8\pi\ \gamma_0 \left[4(\gamma_e/\gamma_0)^2 - 2\gamma_e/\gamma_0 + 1 \right] \Theta(\omega_0). \tag{3.15}$$

Figure 3.4 (c) shows the noise power versus γ_e/γ_0, indicating that for $\gamma_0/\gamma_e \le 0.5$, the noise power almost keeps constant. Minimal noise power at EP becomes

$\mathrm{P}_{\mathrm{noise}}^{EP}\big|_{\min} = 6\pi\ \gamma_0\Theta(\omega_0)$ as $\gamma_0/\gamma_e = \frac{1}{4}$. Figure 3.4 (b) shows the emitted thermal noise PSD with different perturbation strength.

3.4 REALISTIC EP SENSING DESIGN

To further confirm our theoretical analysis, we present a realistic EP sensing design exhibiting enhanced sensitivity, resolution, and favorable thermal noise level. As shown in Fig. 3.5, we put forward a realistic electronic circuit supporting a 2nd order EP, which can be used for enhanced sensing. A lossy resonator with loss element R and a gain resonator with gain element -R are coupled with inductor L_0, obeying PT-symmetry. According to Kirchhoff's current and voltage laws, voltages V_1 and V_2 follow the relations:

$$\begin{cases} \frac{\mathrm{d}^2 V_1}{\mathrm{d}\ \tau^2} + \gamma \frac{\mathrm{d}V_1}{\mathrm{d}\ \tau} + (1+\mu)V_1 - \mu V_2 = 0, \\ \frac{\mathrm{d}^2 V_2}{\mathrm{d}\ \tau^2} - \gamma \frac{\mathrm{d}V_2}{\mathrm{d}\ \tau} + (1+\mu)V_2 - \mu V_1 = 0, \end{cases} \tag{3.16}$$

where $\omega_0 = \frac{1}{\sqrt{LC}}$, $\mu = \frac{L}{L_0}$, $\gamma = \frac{1}{R}\sqrt{\frac{L}{C}}$, $\tau = \omega_0 t$. We construct a state vector $|\Psi\rangle = \begin{bmatrix} V_1 & V_2 & \dot{V}_1 & \dot{V}_2 \end{bmatrix}^T$, with $\dot{V}_1 = \frac{dV_1}{d\tau}, \dot{V}_2 = \frac{dV_2}{d\tau}$. We substitute the state vector into Eq. (3.16) and get effective Hamiltonian matrix of our system

$$H_{eff} = \begin{bmatrix} 0 & 0 & i & 0 \\ 0 & 0 & 0 & i \\ -i(\mu+1) & i\mu & -i\gamma & 0 \\ i\mu & -i(\mu+1) & 0 & i\gamma \end{bmatrix}, \tag{3.17}$$

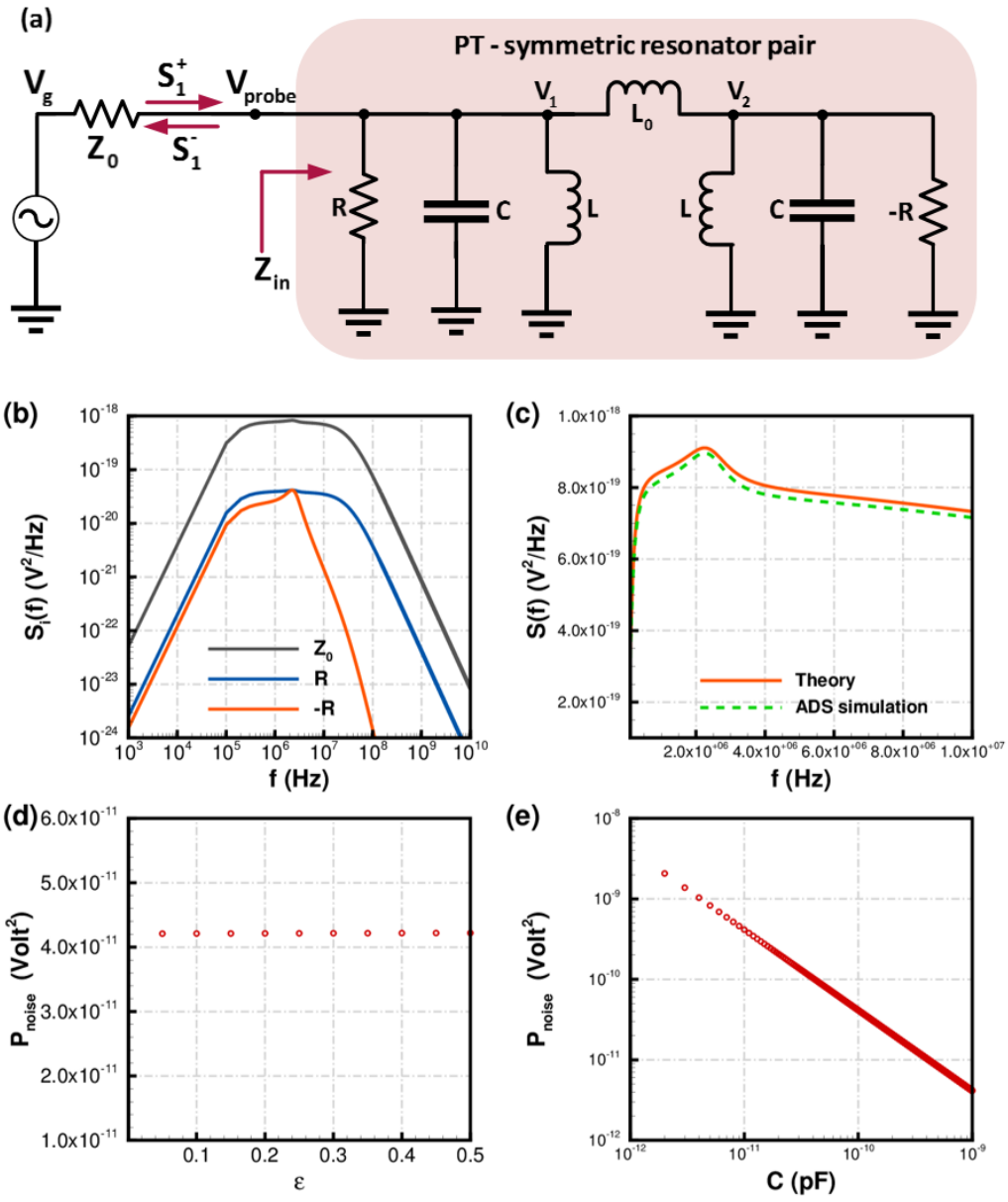
(a)
PT - symmetric resonator pair
V_g
Z_0
S_1^+
S_1^-
V_probe
Z_in
R
C
L
V_1
L_0
V_2
L
C
-R
(b)
S_i(f) (V^2/Hz)
f (Hz)
Z_0
R
-R
(c)
S(f) (V^2/Hz)
f (Hz)
Theory
ADS simulation
(d)
P_noise (Volt^2)
ε
(e)
P_noise (Volt^2)
C (pF)

Figure 3.5: PT-Symmetric enhanced sensing circuit and its nondegraded thermal noise performance. (a) Circuit schematic. The PT-symmetric pair is connected in series to a microwave generator with internal impedance Z_0 and voltage V_g. (b) Power spectral density of thermal noise at the probing point from the noise source $Z_0, R, -R$, respectively. The components are chosen as follows: $L = 100\ \mu\text{H}$, $C = 100\ \text{pF}$, $Z_0 = 50\Omega$, $R = 1000\ \Omega$, $L_0 = \frac{2}{3}L$ (c) Theory and simulation of total thermal noise power spectral density. (d) Total noise power versus the relative perturbation strength. (e) Total noise power versus the capacitance in the resonator.

where the system obeys the dynamic evolution equation $i\frac{d}{d\tau}\left|\Psi\right\rangle = H_{eff}\left|\Psi\right\rangle$. By solving the characteristic equation of the system $\text{Det}\left[H_{eff} - \mathbf{I}\,\omega\right] = 0$, we have the eigenfrequencies of the PT-symmetric system:

$$\begin{cases} \omega_{1,2} = \pm\dfrac{\sqrt{2+2\mu-\gamma^2+\sqrt{4\mu^2-4\gamma^2-4\mu\ \gamma^2+\gamma^4}}}{\sqrt{2}}, \\ \omega_{3,4} = \pm\dfrac{\sqrt{2+2\mu-\gamma^2-\sqrt{4\mu^2-4\gamma^2-4\mu\ \gamma^2+\gamma^4}}}{\sqrt{2}}, \end{cases} \tag{3.18}$$

The above equation indicates that the system operates at a second order EP if the coupling and gain/loss rate satisfies $\mu = \frac{1}{2}\gamma^2 \pm \gamma$. When a perturbation is applied upon the coupling element $\mu = \left(\frac{1}{2}\gamma^2 + \gamma\right)(1+\varepsilon)$, resonant mode splitting can be expressed as:

$$\Delta\omega = \gamma\sqrt{\frac{2+\gamma}{1+\gamma}}\varepsilon^{\frac{1}{2}} + o\left(\varepsilon^{\frac{3}{2}}\right) + \cdots \tag{3.19}$$

The above mode splitting can be detected by measuring the reflection coefficient of our sensing system.

We proceed to evaluate thermal noise performance of our design. For electronic circuit, the thermal noise power spectral density (PSD) reads: $S_i(f) = 4k_B T\left|H_i(f)\right|^2 R_i$, where k_B is the Boltzmann constant, T is the temperature, R_i is the resistance of noise

source, $H_i(f)$ is the transfer function defining the ratio of voltages between the probing point and noise source. In our EP sensing design, there are one external noise source from the impedance Z_0, and another two internal noise sources from the lossy and gain resonators. Rigorous theoretical analysis shows that

$$\begin{cases} S_{Z_0}(f) = 4k_B T Z_0 \left| \dfrac{Z_{in}}{Z_{in}+Z_0} \right|^2, \\ S_R(f) = 4k_B T \dfrac{Z_0^2}{R} \left| \dfrac{Z_{in}}{Z_{in}+Z_0} \right|^2, \\ S_{-R}(f) = 4k_B T \dfrac{Z_0^2}{R} \left| \dfrac{Z_{in}}{Z_{in}+Z_0} \right|^2 \left| \dfrac{i\mu}{i\omega^2 - \omega\ \gamma - i(1+\mu)} \right|^2, \end{cases} \tag{3.20}$$

where $Z_{in} = \dfrac{R\gamma\ \omega\left[-i\omega^2 + \gamma\ \omega + i(1+\mu)\right]}{\omega^4 + \left[\gamma^2 - 2(1+\mu)\right]\omega^2 + 1 + 2\mu}$ is the input impedance of the PT-symmetric circuit. Equation (3.20) indicates that if $Z_0/R << 1$, the thermal noise power spectral density at probing point almost depends on the external noise source, leading to a smooth response of noise fluctuation when the system is perturbed at EP. This is the scenario we discussed in section 3.2, where we showed that if $\gamma_0/\gamma_e \le 0.5$, the thermal noise is almost a constant for various perturbation strengths. Figure 5(b) demonstrates the PSD from each noise source, indicating that external noise from Z_0 is dominant; fig. 3.5 (c) shows the total noise PSD both from theoretical analysis and ADS simulation, which agrees well with each other; fig. 3.5(d) shows the integrated thermal noise power versus perturbation strengths, which is robust for sensing; fig. 5(e) shows the integrated thermal noise versus the capacitance in the resonator.

3.5 CONCLUSIONS

In this Section, we have provided a unified theoretical framework to analyze the sensitivity, resolution, and thermal noise performance of two-level EP and DP sensing protocols. Our study indicates that, although the Green's function of EP sensing systems shows a combination of square Lorentzian and Lorentzian noise spectra at the EP compared with conventional DP sensing system, the integrated thermal noise is still manageable if proper ratios of internal and external decaying rates are chosen. These arguments are confirmed with a judiciously designed 2^{nd} order EP sensing circuit and unveil a bright future for EP sensing applications in many other fields, including optomechanical, acoustic and open quantum systems.

Chapter 4: Robust Wave Tunneling and Information Transfer based on Parity-Time-Symmetric Emitter-Absorber Pairs[3]

Robust signal transfer in the form of electromagnetic waves is of fundamental importance in modern technology, yet its operation is often challenged by unwanted modifications of the channel connecting transmitter and receiver. Parity-time (PT) symmetric systems, combining active and passive elements in a balanced form, provide an interesting route in this context. In this chapter, we demonstrate a PT-symmetric microwave system operating in the extreme case in which the channel is shorted through a small reactance, which acts as a nearly impenetrable obstacle and it is therefore expected to induce large reflections and poor transmission. After placing a gain element behind the obstacle, and a balanced lossy element in front of it, we observe full restoration of information and overall transparency to an external observer, despite the presence of the obstacle. Our theory, simulations and experiments unambiguously demonstrate stable and robust wave tunneling and information transfer supported by PT-symmetry, opening opportunities for efficient communication through channels with dynamic changes, active filtering and active metamaterial technology. The main results of this chapter are from ref [37].

4.1 INTRODUCTION

Information transfer in the form of electromagnetic waves is ubiquitous in today's world, from free space (wireless) to transmission-line (guided) channels [113]-[116]. The channels connecting transmitter and receiver are typically time-varying and are affected by the presence of various obstacles. Therefore, the wave must tunnel through non-ideal

[3] This chapter is published in ref [37]. Y. R., S. T., and A. A. conceived the idea, Z. X. and Y. R. performed the simulation, Z. X. and Y. R. did the measurements, Z. X. contributed to the first draft of the paper, all the authors worked on the paper, and A. A. supervised and funded the research.

channels, with strong insertion loss. Resonant transmission, such as electron tunneling through quantum wells, resonant photon tunneling through optical barriers, and microwave tunneling through extremely squeezed or bent channels can address this issue to some extent, but typically with severe trade-offs in terms of bandwidth, sensitivity and complexity, among others [117]-[120]. In most practical scenarios, dynamic and complex electromagnetic environments pose challenges to the system operation and make these solutions even more challenging. For instance, in applications where dynamic obstacles are inevitable, like communicating with biomedical implants such as artificial cardiac pacemakers [121] or interrogating embedded health sensors in civil infrastructures [122], engineers need to adaptively tune complex matching networks or the operational frequency to maximize the transmission efficiency. In extreme scenarios, the channel between transmitter and receiver may be completely blocked, which cannot be addressed by dynamically tuning the matching network. In such practical scenarios, transferring the signal over the channel may be impossible.

In a recent theoretical work [123], we showed that in such systems instead of transferring the input signal to the receiving port through a channel with dynamic changes, one can just transfer a little information about the input signal during the transient, and replicate the entire signal at the output port using this information based on a different form of signal tunneling driven by parity-time (PT) symmetry. Quite interestingly, in contrast to conventional solutions, in such a system, the input and output ports do not have to stay connected throughout the whole information transfer process.

Here, we experimentally prove that, by placing a shunt lossy element in the transmitting node before the obstacle and a judiciously designed gain element in the receiving node, forming a PT-symmetric conjugate pair [124]-[133], we can restore full transmission at the operational frequency, despite the presence of a nearly unitary

reflective obstacle blocking the transmission channel. The obstacle in our experiment is modelled as a shorting element along a transmission line. The lossy element paired with the obstacle is designed to behave as a Salisbury screen absorber [134], while the gain element acts as a synchronized emitter operating as the time-reversed version of a Salisbury absorber. This PT-symmetric wave tunneling, and information transfer system enables robust full-wave transmission through an otherwise impenetrable barrier.

4.2 PT-SYMMETRIC WAVE TUNNELING AND INFORMATION TRANSFER SYSTEM

PT-symmetric tunneling and robust information transfer is schematically sketched in Fig. 4.1 (a), where the signal is transported wirelessly via an air channel from a transmitting to a receiving antenna. When a reflective obstacle is inserted within the transmission channel, information transfer efficiency is expected to drop dramatically. To

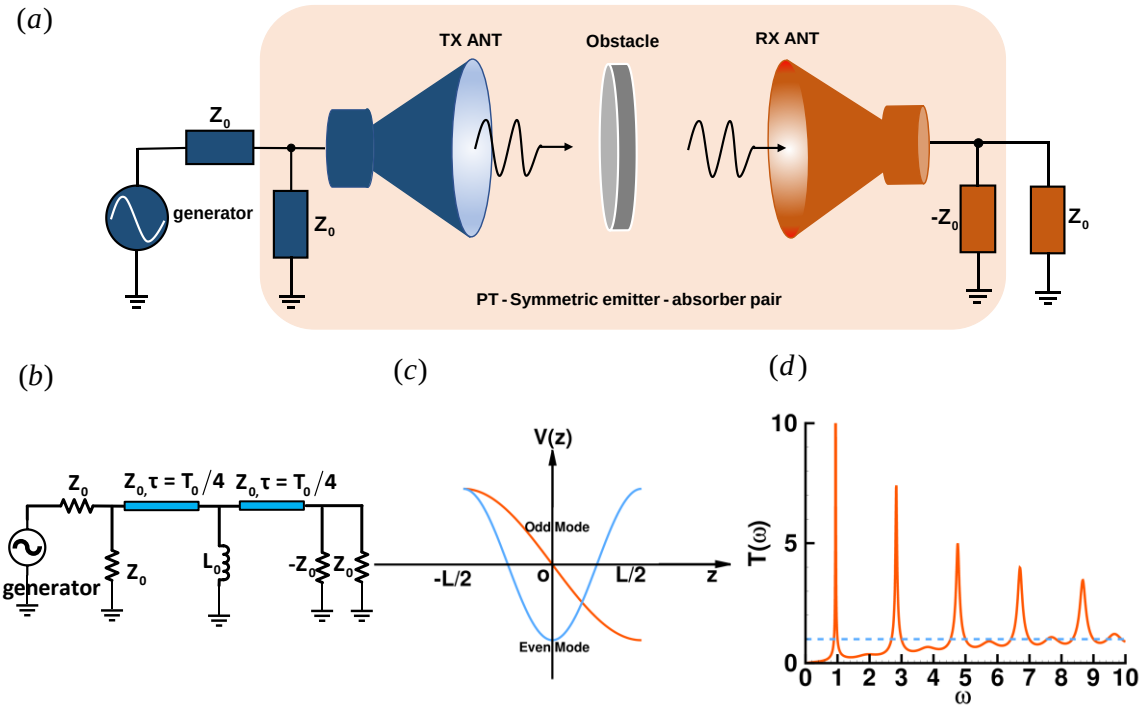

Figure 4.1: (a) PT-symmetric wave tunneling and information transfer scheme. A highly reflective obstacle blocks the channel. A gain element $-Z_0$ is placed behind this obstacle and a lossy element R is placed before the obstacle to facilitate full wave transmission. (b) A simplified wired version of PT-symmetric robust information transfer scheme based on transmission line. The obstacle is modeled as a small inductive element L_0. (c) Fundamental odd and even mode profiles of the PT-symmetric absorber-emitter pair. They are significantly different from Hermitian system due to the Neumann boundary condition and PT-symmetry. The point $Z=-\frac{L}{2}$ and $Z=\frac{L}{2}$ marks the location of the loss and gain unit, where L is the electrical length of the transmission connecting these two elements. (d) Tunneling characteristics of the PT-symmetric system. The π phase transmission maxima locates at $\omega=(2k+1)\omega_0$, $k=0,\ 1,\ 2,\ 3\cdots$ and the in-phase transmission peaks are determined by the transcendental equation $\frac{1}{2\alpha}\left(\frac{\omega}{\omega_0}\right)^{-1}=\tan\left(\frac{\pi}{2}\frac{\omega}{\omega_0}\right)$, where $\alpha=\omega_0 L_0/Z_0$ is the coupling strength between the absorber and emitter, $\omega_0=2\pi/T_0$ is the fundamental resonant frequency.

restore full wave transmission, in this work we add a gain element $-Z_0$ behind the reflecting obstacle and a conjugate lossy element Z_0 in front of it to form a PT-symmetric conjugate pair, where Z_0 is the characteristic impedance of the transmission channel [see Fig. 4.1(a)]. As we show in the following, this combination can largely restore transmission through the channel, despite the presence of the largely reflective obstacle. In order to prove this principle, we model the wireless information transmission channel with a basic transmission line, as shown in Fig. 4.1(b), and the highly reflective obstacle with a small inductor L_0, close to a short and therefore highly reflective. Since we utilize the resonant tunneling feature of the PT-symmetric system, the transmission line is set at half-wavelength of the impinging wave. As a result, the loss element Z_0, the first quarter-wavelength transmission channel, and the highly reflective obstacle behave

like a Salisbury screen absorber. The obstacle, the second quarter-wavelength transmission channel, together with the gain element $-Z_0$ work as a synchronized information transmitter, a time-reversed replica of a Salisbury absorber, which emits in sync with the absorbing portion. We show that in steady state the whole PT-symmetric system works as a tunneling channel for impinging waves, mimicking a lossless, ideally transmitting channel.

To begin with, we analyze the resonant transmission mode and frequency of the PT-symmetric wave tunneling and information transfer system. We define the steady state voltage on the transmitting node, obstacle and receiving node as V_{source}, $V_{obstacle}$, and V_{load}, which form the state vector $|\psi\rangle = \begin{bmatrix} V_{source} & V_{obstacle} & V_{load} \end{bmatrix}^{\mathrm{T}}$. The characteristic equation reads $PT|\psi\rangle = \lambda|\psi\rangle$, which supports even and odd eigenstates $|\psi_+\rangle = \begin{bmatrix} 1 & -1 & 1 \end{bmatrix}^{\mathrm{T}}$, $|\psi_-\rangle = \begin{bmatrix} 1 & 0 & -1 \end{bmatrix}^{T}$, and eigenvalues $\lambda_\pm = \pm 1$, where $P = \begin{bmatrix} 0 & 0 & 1 \\ 0 & 1 & 0 \\ 1 & 0 & 0 \end{bmatrix}$ is the parity operator, T is the time reversal operator (equivalent to complex conjugation for steady state), and T is the transpose operator. As we can infer from the above analysis, the obstacle is a short and contributes no phase delay at odd resonant tunneling states. Therefore, the total phase delay of the transmitted wave is $\omega \frac{T_0}{2} = (2k+1)\pi$ with $\omega = (2k+1)\omega_0$, $k = 0,\ 1,\ 2,\ 3\cdots$, $\omega_0 = 2\pi/T_0$ being the resonant frequency of the fundamental standing mode. For the even scattering state, we sum up the phase delay on the transmission line and the inductor:

$$-\omega \frac{T_0}{4} + 2\arctan\frac{Z_0}{2\omega L_0} - \omega \frac{T_0}{4} = 2k\pi, \tag{4.1}$$

which can be simplified to the characteristic equation

$$\frac{1}{2\alpha}\left(\frac{\omega}{\omega_0}\right)^{-1} = \tan\left(\frac{\pi}{2}\frac{\omega}{\omega_0}\right), \tag{4.2}$$

where $\alpha = \omega_0 L_0 / Z_0$ is the coupling strength between the Salisbury screen absorber and its conjugate emitter, and Z_0 is the characteristic impedance of the transmission line. The eigen-equation of even standing modes is a transcendental equation, which requires a numerical evaluation. As α approaches zero, the circuit is shorted by the obstacle and the wave cannot tunnel through the system; as α approaches infinity, the load can be neglected and the even mode has the close-form solution $\omega = 2k\omega_0$, $k = 0,1,2,3\cdots$. An alternative approach to find the resonant frequencies of the system is to employ the transfer matrix method and the generalized conservation law, with detailed calculations presented in the Appendix B. The standing even/odd mode solutions $|\psi_{\pm}\rangle$ explicitly show that the absorber and emitter exhibit identical amplitudes and 0/π phase difference, which is direct evidence of synchronized wave absorption at the input port and emission at the output port. We demonstrate the standing wave profile of this PT-symmetric absorber-emitter pair in Fig. 4.1 (c). The unusual standing mode profile, considering the presence of the reflective obstacle, is a direct manifestation of PT-symmetry and Neumann boundary conditions at the ports. We also show the power transmission spectrum in Fig. 4.1 (d), which demonstrates full wave tunneling at the resonant frequencies. The tunneling mechanism satisfies the generalized flux conservation law applicable to any two-port PT symmetric network, which reads $T - 1 = |r_L r_R| e^{i(\phi_L - \phi_R + \pi)}$, where T is the power transmission coefficient, r_L and r_R are the amplitude reflection coefficients on the left and right ports of the system, ϕ_L and ϕ_R are the corresponding phase of the amplitude reflection coefficients. As a result, the system demonstrates super-unitary power transmission inside the region bounded by any pair of even and odd tunneling eigenfrequencies. Note that, due to the presence of gain in the system, the

transmission may go over unity at frequencies close to the tunneling frequency, however the system remains stable.

To better understand the PT-symmetric wave tunneling, it is of interest to investigate the scattering properties at resonance and analyze the PT phase transition of the scattering state. Rigorous transfer matrix analysis enables us to express the scattering properties of even and odd resonant states of this two-port information transfer network as

$$S_{\pm} = \begin{bmatrix} 0 & \pm 1 \\ \pm 1 & \pm \dfrac{2j}{\alpha}\left(\dfrac{\omega}{\omega_0}\right)^{-1} \end{bmatrix}, \tag{4.3}$$

where S_+ and S_- are scattering matrices of even and odd resonant modes, respectively, obeying the symmetry relation $PS_{\pm}^{*}(\omega)PS_{\pm}(\omega) = \mathbf{I}$. Wave tunneling happens at the resonant frequencies and it is totally independent of the obstacle strength α or its type (inductive, capacitive, resistive or any combination of these) between the Salisbury absorber and the synchronized emitter, since the obstacle is effectively shorted in steady state. This offers unique flexibility to maintain the transmissivity of the proposed system for arbitrary variations of the obstacle, ensuring stable operation. Even for dynamically varying obstacles, the system is capable of self-tuning to a stable full transmission region. However, if the obstacle has scattering loss the system will fail to recover the signal.

The scattering matrix in Eq. (4.3) has two eigenvalues $\lambda_{1,2} = \dfrac{-j \pm \sqrt{\left(\alpha\omega/\omega_0\right)^2 - 1}}{\alpha\omega/\omega_0}$. At $\alpha = \left(\omega/\omega_0\right)^{-1}$ these two eigenvalues coalesce, supporting a non-Hermitian degeneracy. This exceptional point (EP) separates the scattering system from its PT-symmetric phase when $\alpha > \left(\omega/\omega_0\right)^{-1}$ and its broken-PT-

symmetric phase when $\alpha > \left(\omega/\omega_0\right)^{-1}$. We substitute the eigenfrequencies of even and odd scattering states $\alpha < \left(\omega/\omega_0\right)^{-1}$ into the expression $\alpha = \left(\omega/\omega_0\right)^{-1}$ to find the EPs

$$\begin{cases} \alpha_{EP}^{Even} = \dfrac{\pi}{2\arctan\dfrac{1}{2} + 2k\pi}, k = 0,1,2\cdots \\ \alpha_{EP}^{Odd} = \dfrac{1}{2k+1}, k = 0,1,2\cdots \end{cases} \tag{4.4}$$

Depending on the reflectivity of the obstacle, i.e., how close to zero is its reactance, the resonant tunneling state can be in the exact PT-symmetry phase with unitary eigenvalues $\left|\lambda_1\right| = \left|\lambda_2\right| = 1$, or in the broken PT-symmetry phase with $\left|\lambda_1\right| = 1/\left|\lambda_2\right| > 1$. The PT tunneling functionality is independent of the PT-symmetry phase transition point. The stability analysis is presented in the Appendix B, which shows inherent stability for any finite value of the obstacle reflectivity [$0 < \alpha < \infty$].

4.3 EXPERIMENTAL REALIZATION AND ROBUSTNESS ANALYSIS

We experimentally demonstrate a robust proof-of-concept PT-symmetric microwave tunneling prototype [see Figs. 4.2(a) and 4.2(b)]. The gain unit is realized through a dispersive negative impedance converter (NIC) based on a non-inverting feedback amplifier configuration [see Fig. 4.2(a)]. A compensating inductor L_c in series with the non-inverting port realizes a purely negative impedance $-Z_0$ at the operational frequency. The dispersion relation of the NIC follows

$$Z_{NIC}\left(s\right) = \frac{s + A_0\beta\,\omega_p}{s + A_0\left(\beta - 1\right)\omega_p} Z_F + sL_c, \tag{4.5}$$

where A_0 is the open-loop gain of the amplifier, ω_p is the pole frequency of the amplifier, $\beta = R_f \big/ \left(R_f + R_g\right)$ is the feedback factor, $Z_F = 2Z_0$ is the feedback resistor, and s is the complex frequency. We choose a compensating inductor $L_c = 3Z_0/\omega_{3dB}$ and the operational frequency $\omega_0 = \omega_{3dB}/\sqrt{3}$, where $\omega_{3dB} = A_0\omega_p/2$ is the 3-dB

frequency of the closed-loop gain coefficient. The NIC dispersion is shown in Fig. 4.2(c), showing a negative impedance $-Z_0$ at the operational frequency ω_0.

Our prototype is designed to work at the fundamental odd scattering state. We realize the transmission line through a π-type LC resonator to reduce the form factor [see Fig. 4.2(a)], which offers unitary transmission as well as π/2 phase delay at resonant frequency to mimic a quarter-wavelength transmission line segment. The impedance is automatically matched at both transmitting and receiving nodes, as we choose $L = Z_0/\omega_0$ and $C = 1/Z_0/\omega_0$. This compact design significantly reduces the form factor of our device from $\lambda/2$ to a deeply subwavelength scale $\lambda/50$. The fabricated device is shown in Fig. 4.2(b), with a size of approximately 2 cm by 2 cm. We confirm our theoretical analysis with a co-simulation between ADS and the Modelithics package, which shows excellent PT-symmetric tunneling at 48.7 MHz. The scattering properties are demonstrated in Fig. 4.2(d) with a tunneling point of -0.01 dB transmission and -28.8 dB reflection. Finally, we confirm the PT-symmetry of our designed circuit by graphing the spectral properties of the eigenvalues of the scattering

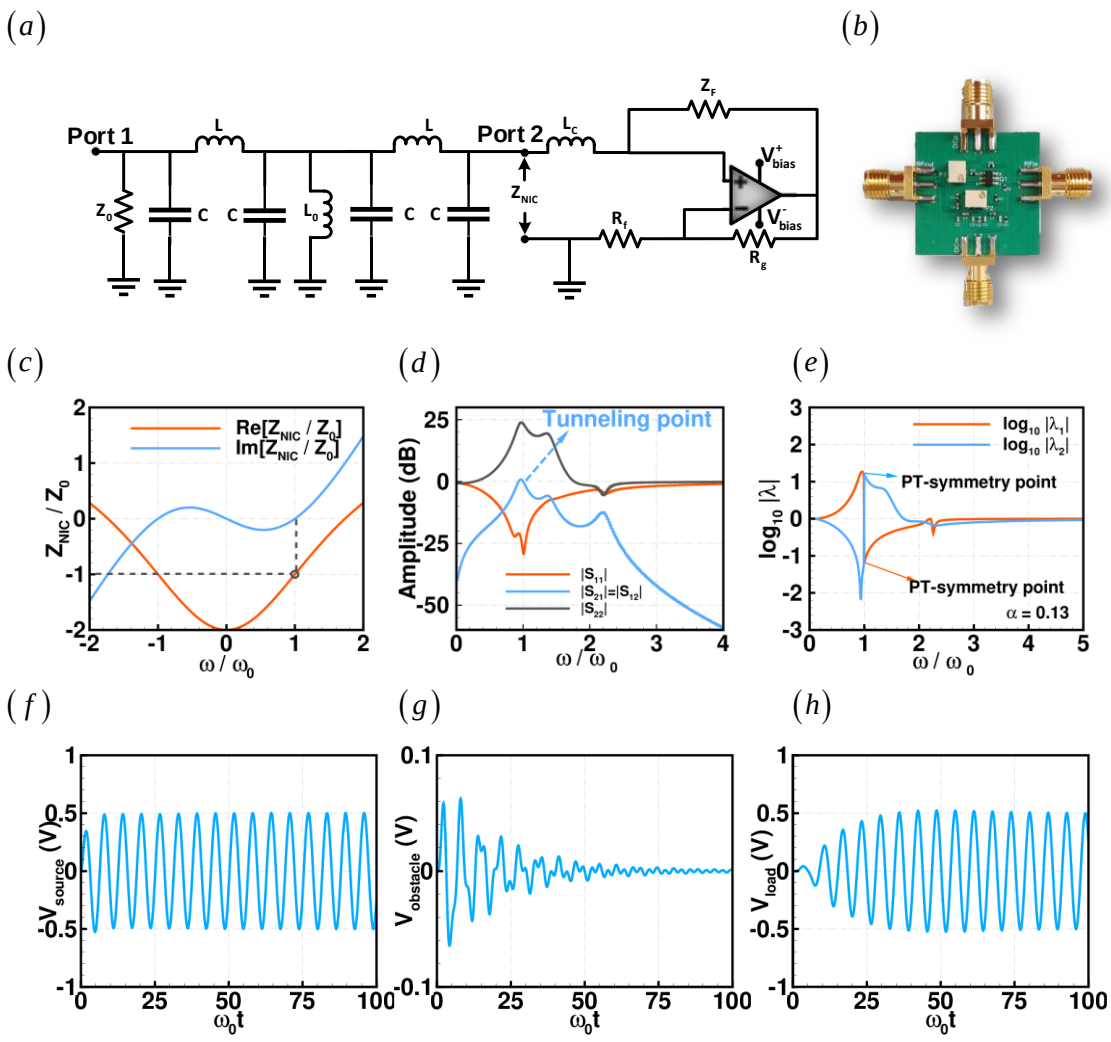
(a)
(b)
Port 1
Port 2
L
L
C
C
C
C
L_0
L_c
Z_0
Z_{NIC}
Z_F
R_f
R_g
V^+_{bias}
V^-_{bias}
(c)
(d)
(e)
$Re[Z_{NIC}/Z_0]$
$Im[Z_{NIC}/Z_0]$
Z_{NIC}/Z_0
ω/ω_0
Tunneling point
Amplitude (dB)
$|S_{11}|$
$|S_{21}|=|S_{12}|$
$|S_{22}|$
$\log_{10}|\lambda_1|$
$\log_{10}|\lambda_2|$
$\log_{10}|\lambda_i|$
PT-symmetry point
PT-symmetry point
$\alpha = 0.13$
(f)
(g)
(h)
V_{source} (V)
$V_{obstacle}$ (V)
V_{load} (V)
$\omega_0 t$

Figure 4.2: Realistic design and implementation of the PT-symmetric wave tunneling prototype. (a) Circuit schematic. Transmission line is replaced with a π-type transmission line which consists of inductor *L* and capacitor *C*. (b) Photograph of the fabricated PCB prototype. Two big white components are tunable resistors. The black component with six pins is OPA 355-Q1 amplifier. Left and right ports are source port 1 and load port 2 in the schematic. Upper and lower ports are DC bias ports for the amplifier. (c) Dispersion of the impedance of the gain element. Black circle marks the operational point. (d) ADS and Modelithics simulation of the amplitude of scattering parameters. Tunneling point is marked in the figure. (e) Spectral properties of eigenvalues of the scattering matrix. Exact PT-symmetry is achieved at tunneling frequency where eigenvalues obey unitary conditions $\left|\lambda_1(\omega_0)\lambda_2(\omega_0)\right|=1$. The coupling coefficient α is 0.13, ensuring robust operation of the whole circuit in presence of obstacle. (f) Numerical transient response at the source port where full absorption is achieved at tunneling frequency. The generator voltage is 1 Volt. (g) Numerical transient response at the obstacle which is short in the steady state. (h) Numerical transient response at the load port where full wave tunneling is observed in the steady state.

matrix in Fig. 2(e). With coupling coefficient $\alpha=0.13$, the eigenvalues demonstrate unitary property $\left|\lambda_1\right|=1/\left|\lambda_2\right|$ at ω_0, which is a typical hallmark of PT-symmetry in the broken symmetry phase. No other PT-symmetry point is found in the full spectra.

To better understand how this PT-symmetric wave tunneling circuit works, we plot the temporal response at source, obstacle and load nodes in Figs. 2(f)-(h). We place a microwave generator $V_g=\sin\omega_0 t$ with internal impedance Z_0 in the source node. The voltage at this port initially experiences a small reflection and then rapidly reaches steady state $V_{source}=\frac{1}{2}\sin\omega_0 t$, indicating that the impinging wave is fully absorbed by the shunt resistor Z_0. The obstacle node demonstrates a purely decaying response, confirming our previous steady state analysis in the ideal PT-symmetric configuration $V_{obstacle}=0$. The load port is essentially an emitter, and it demonstrates an exponentially growing trend towards steady state $V_{load}=-\frac{1}{2}\sin\omega_0 t$. Since it operates at the fundamental odd

resonant tunneling state, the emitted wave has a π phase shift with respect to the impinging wave.

Apart from the PT-symmetric full wave tunneling functionality, our design is stable and robust to parameter detuning and reasonable fabrication errors. To study the stability issue, it is important to investigate the voltages at source, obstacle, and load in the complex frequency domain. Application of the Kirchhoff's current and voltage laws leads to a set of linear equations

$$\begin{bmatrix} 2+\frac{s}{\omega_0}+\left(\frac{s}{\omega_0}\right)^{-1} & -\left(\frac{s}{\omega_0}\right)^{-1} & 0 \\ \left(\frac{s}{\omega_0}\right)^{-1} & -2\frac{s}{\omega_0}-\left(1+\frac{1}{\alpha}\right)\left(\frac{s}{\omega_0}\right)^{-1} & \left(\frac{s}{\omega_0}\right)^{-1} \\ 0 & \left(\frac{s}{\omega_0}\right)^{-1} & -\frac{s}{\omega_0}-\left(\frac{s}{\omega_0}\right)^{-1}-\frac{Z_0}{Z_{NIC}} \end{bmatrix} \begin{bmatrix} \tilde{V}_{source}(s) \\ \tilde{V}_{obstacle}(s) \\ \tilde{V}_{load}(s) \end{bmatrix} = \begin{bmatrix} \tilde{V}_g(s) \\ 0 \\ 0 \end{bmatrix}, \tag{4.6}$$

where $\tilde{V}_g(s)$ is the voltage of the microwave generator, $\tilde{V}_{source}(s), \tilde{V}_{obstacle}(s), \tilde{V}_{load}(s)$ are the complex voltages on source, obstacle, and load nodes, respectively. Here we define the transfer function as the voltage ratio between load versus generator: $\tilde{H}(s)=\tilde{V}_{load}(s)/\tilde{V}_g(s)$. To maintain a stable operation, the impulse response should have a finite energy, which is equivalent to requiring that all the poles of the transfer function lie on the left hemi-Riemann sphere Equation (4.6) indicates that the relative pole locations only depend on the strength of the obstacle. As α approaches to zero, the transfer function turns to zero and it is meaningless to study the stability issue. As α

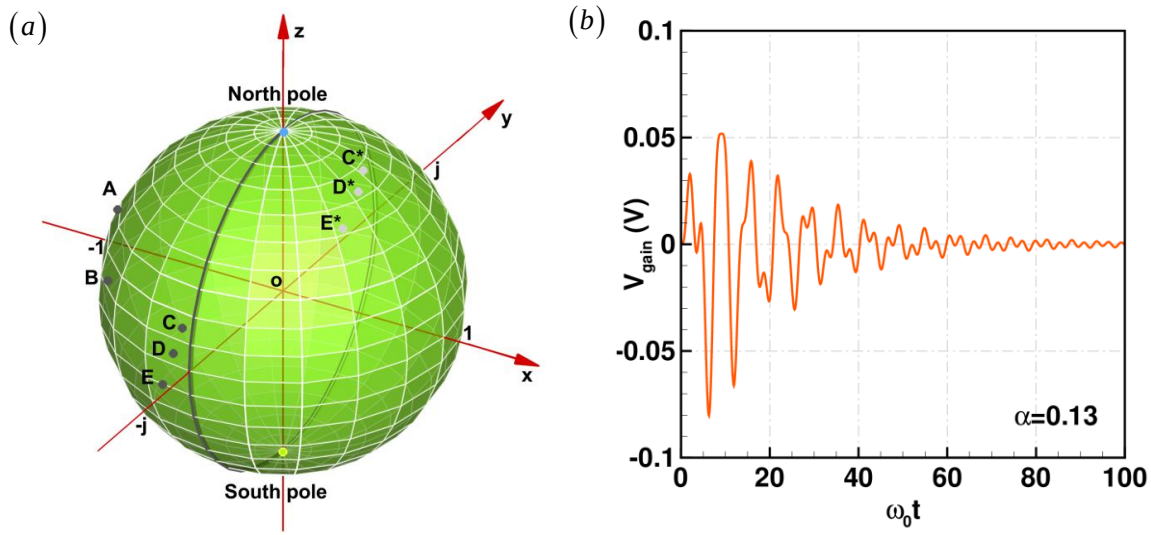

Figure 4.3: Realistic design and implementation of the PT-symmetric wave tunneling prototype. Pole diagram and impulse response. (a) Pole distribution of the transfer function on a Riemann surface. Grey solid line (Prime meridian) marks the watershed between stable and unstable regions. North pole is the pole in the case $\alpha = \infty$, corresponding to an open obstacle and leading to marginally stable operation. For the prototype we fabricated $\alpha = 0.13$, there are eight poles in the transfer function, A, B, C, D, E, C^*, D^*, E^*, where C^*, D^*, E^* are the conjugates of C, D, E, respectively. A and B are located on the 90-degree west longitude; C, D, E are located close to the prime meridian but to the left; C^*, D^*, E^* are located in the back surface. All these eight poles are in the stable region. (b) Numerical impulse response at the gain unit. The input port is excited with a pulse $V_{generator} = \delta(t)$.

goes to infinity, the emitter is directly connected with the absorber, creating a marginally stable point on the north pole [see Fig. 3(a)]. In this scenario, any small perturbation on the system will move the marginally stable point and transform it into eight poles on the right hemi-Riemann sphere. Numerical computation indicates that our circuit operates robustly as the coupling strength varies between 0.1 and 0.3. As our realistic design involves both dispersive negative feedback and a π-type transmission line, they place a more stringent condition on stability compared with the ideal model where the stable

condition is $0 < \alpha < \infty$. In our fabricated prototype, we carefully choose α = 0.13 to ensure a stable operation within expected fabrication imperfections. Figure 4.3 demonstrates the pole distributions as well as the impulse response of our design. There are eight poles on the left hemi-Riemann sphere when $\alpha = 0.13$, indicating that our fabricated prototype is stable.

4.4 OBSERVATION OF PT TUNNELING AND INFORMATION TRANSFER

Figures 4.4(a) and 4.4(b) show the experimentally measured and theoretically calculated forward transmission spectrum and phase. A PT-symmetric unitary transmission was observed at 44.8 MHz with 180-degree phase, which agrees with our simulation. Meanwhile, the reflection is fully suppressed at this point, as shown in Figs. 4.4(c) and 4.4(d). The experimental reflection phase at resonance is essentially undefined due to the zero amplitude, causing fast oscillations around the resonance, as shown in Fig. 4.4(d). It is worth mentioning that at resonance, the experimental backward reflection amplitude $|S_{22}|$ is 15 dB and the phase $\mathrm{Arg}[S_{22}]$ is -90 degree, confirming that our PT-symmetric system has asymmetric reflections and satisfies the generalized conservation law. Since the system is linear and time-invariant, reciprocity is satisfied and the transmission coefficients in forward and backward directions are identical. The observed tunneling frequency is smaller than the simulation results, which may stem from the fabrication error where the inductance or capacitance values in the transmission line is smaller than designed ones. The scattering parameters in a narrower or wider spectrum are demonstrated in Figures 4. 5 and 4.6. In the Fig. 4.7, we show the

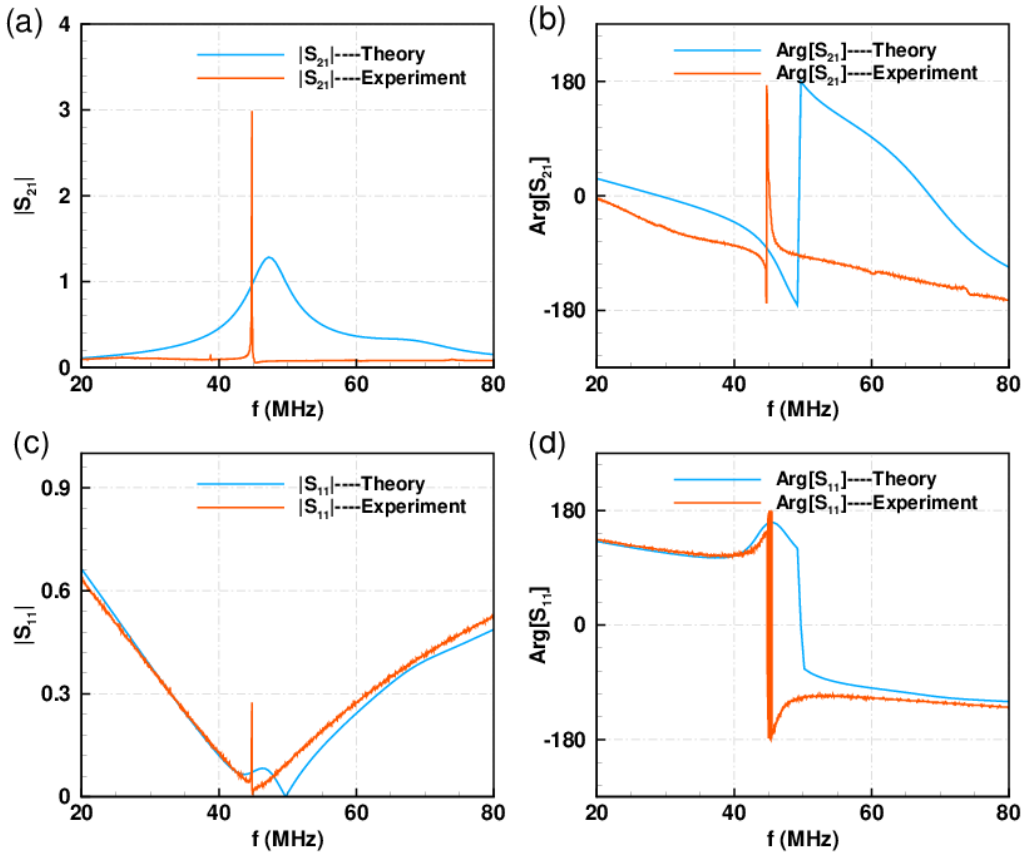

Figure 4.4: Measurements of the amplitude transfer characteristics and reflection coefficient. (a) Forward transmission spectrum. Resonant tunneling occurs at 44. 8 MHz. (b) Phase diagram of the transmission coefficient. Tunneling field experiences π phase shift at resonant frequency. (c) Reflection at input port. -50 dB reflection is observed at 44.8 MHz, indicating that matching network works quite well. (d) Phase diagram of reflection coefficient at input port. Measured data in a wider (20-200 MHz) and narrower (40-50 MHz) spectrum are presented in the extended data Figs 3 and 4 in the supplementary document.

linearity of our tunneling circuit, which demonstrates an excellent linear relation between input and output power at tunneling frequency. This graph clearly shows that although at the steady state the output is completely disconnected from the input (since the inductive load is fully shorted), the output can still linearly follow the input. In other words, if after reaching the steady state, any change happens to the input signal, the system goes into the

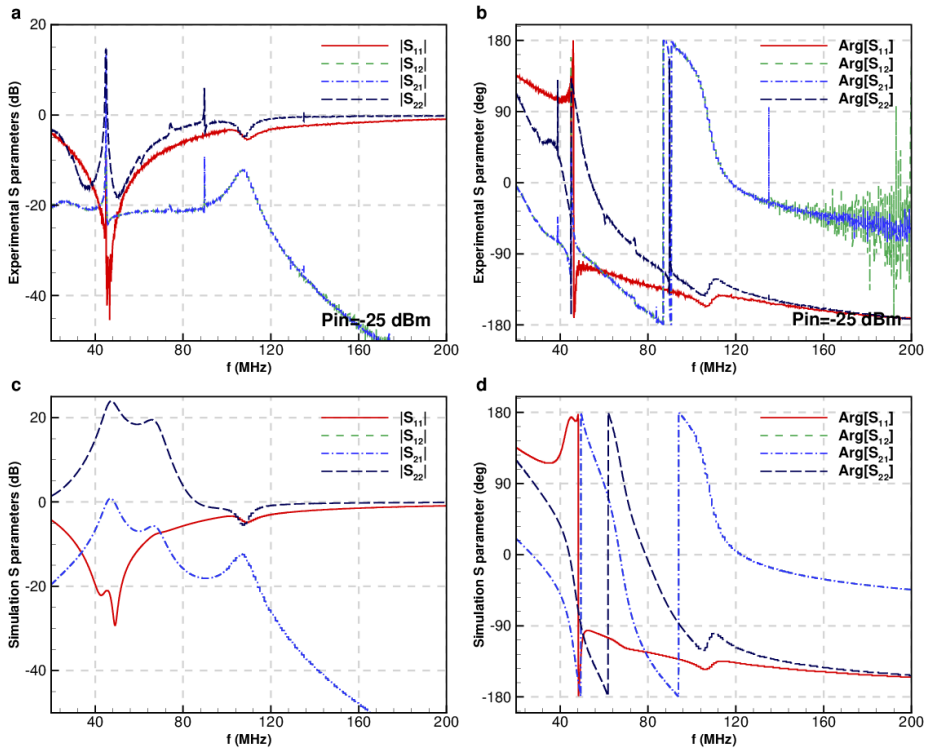

Figure 4.5: Comparison between experimental S parameters and simulation S parameters. The input signal power is -25 dBm. **a**. Amplitude of experimental scattering parameters ranging from 20MHz to 200MHz. **b**. Phase of experimental scattering parameters ranging from 20MHz to 200MHz. **c**. Amplitude of simulation scattering parameters ranging from 20MHz to 200MHz. **d.** Phase of simulation scattering parameters ranging from 20MHz to 200MHz.

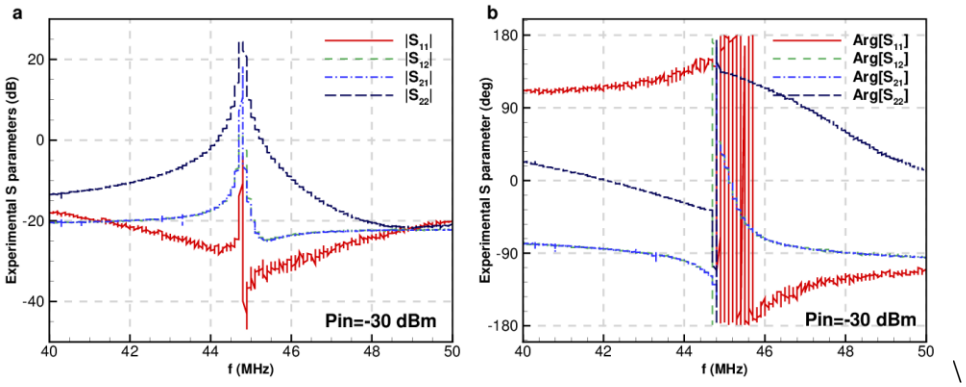

Figure 4.6: A closer look into the S parameter, ranging from 40MHz to 50MHz. **a**. Amplitude of experimental scattering parameters. **b**. Phase of experimental scattering parameters. Reflection coefficient experiences large oscillation from 44 to 46 MHz. This is due to the undefined phase at singular point.

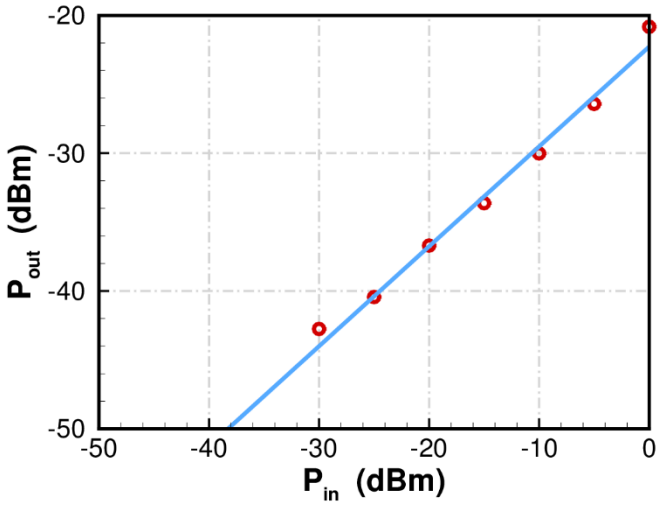

Figure 4.7: Linearity of the tunneling device. Straight line represents the fitting curve of the input-output power relation. Dots are measured experimental data. The system shows an excellent linear power response from -25 dBm to -5 dBm.

transient regime for a very short period of time, during which the information of the input signal is communicated towards the output port and then output reaches the steady state again and fully replicates the input signal.

4.5 MATERIALS AND METHODS

4.5.1 Circuit design and fabrication

The design of the circuit and fabricated prototype are shown in Fig. 4.2(a) and 4.2(b). In the NIC part, we use amplifier OPA 355-Q1 from Texas Instrument. This amplifier has a 200 MHz gain bandwidth product, with open loop gain $A_0 = 10^5$ and pole frequency $\omega_p = 2\pi \times 2000$ Hz. The effective impedance of the NIC in Fourier

domain can be easily inferred from equation. by replacing complex frequency s with physical frequency $j\omega$:

$$Z_{NIC} = Z_F \frac{\omega^2 + \left(A_0\omega_p\right)^2 \beta\left(\beta-1\right)}{\omega^2 + \left[A_0\left(\beta-1\right)\omega_p\right]^2} + j\left\{\frac{-\omega A_0\omega_p Z_F}{\omega^2 + \left[A_0\left(\beta-1\right)\omega_p\right]^2} + \omega L_c\right\}. \tag{4.7}$$

To have purely negative impedance $-Z_0$, the real part of the above equation should be $-Z_0$ and the imaginary part of the effective impedance should be 0. Then, we have the following operational conditions

$$\begin{cases} \omega = A_0\omega_p\sqrt{\dfrac{\left(1-\beta\right)\left[Z_F\beta - Z_0\left(1-\beta\right)\right]}{Z_F + Z_0}}, \\ L_c = \dfrac{Z_F + Z_0}{\left(1-\beta\right)A_0\omega_p}, \end{cases} \tag{4.8}$$

where $Z_0 = 50\ \Omega$, $Z_F = 100\ \Omega$, $\beta = R_f \big/ \left(R_f + R_g\right) = 0.5$, $R_f = R_g = 560\ \Omega$. Here, the feedback resistor Z_F is chosen as $2Z_0$ due to the dispersion of the one-pole model amplifier. We substitute these values into the above equation and get the operational frequency $f = \omega/2\pi = 57.74$ MHz of the negative impedance converter and the compensating inductor $L_c = 238.7$ nH. In circuit simulation, we use two inductors with inductance value 120 nH. Then, we co-simulate our circuit with ADS and Modelithics to check the effective negative impedance. Our simulations demonstrate a $-50.9\ \Omega$ negative impedance at 50.2 MHz. The shift of the design frequency can be contributed to the parasitic effect and possible high-order poles in the amplifier. The inductor $L = 150$ nH and capacitor $C = 68$ pF in the transmission line are chosen to match both the operational frequency of NIC and the characteristic impedance of the port. The reflective obstacle is modeled as an inductor $L_0 = 20$ nH, leading to a coupling factor $\alpha = 0.13$ and ensuring robust operation of the system.

The circuit is fabricated on a 0.062-inch-thick FR-4 substrate with relative permittivity 4.4 and dissipation factor 0.017. The following components are surface mounted on the PCB board: (1) characteristic impedance Z_0 from KOA Speer with part number RK73B1ETTP510J; (2) feedback resistor Z_F from KOA Speer with part number RK73B1ETTP910J; (3) feedback resistor .. R_f .. from KOS Speer with part number RK73B1ETTP561J; (4) two variable resistors from Bourns Inc. with part number 3223W-1-101ETR-ND and 3223W-1-200ETR-ND; (5) capacitor in the resonator from Murata Inc. with part number GRM1552C2A680GA01#; (6) inductors from Coilcraft with part numbers 0402HPHR15X, 0402CS20N, and 0402CS12X; (7) amplifier from Texas Instrument with part number OPA355QDBVRQ1; (8) port connectors from Amphenol with part number 132322.

4.5.2 Stability analysis

A linear, time-invariant, causal circuit is stable if and only if the impulse response is absolutely integrable, which means

$$\int_0^\infty \left| H(t) \right| dt = \text{finite}, \tag{4.9}$$

where $H(t) = \sum_{n=0}^{\infty} c_n e^{p_n t}$ is the impulse response, p_n is the *n*-th pole of the transfer function $H(s) = \sum_{n=0}^{\infty} \frac{c_n}{s - p_n}$, c_n is the amplitude coefficient of each Laplace component

Therefore, to operate in the stable region, all the real parts of the poles must be negative:

$$\forall n, \text{Re}\left[p_n \right] < 0, \tag{4.10}$$

which is the stability condition of a linear, causal and time invariant circuit.

In our circuit, we assume the system is excited with a power source V_g which has an internal impedance Z_0. The transfer function $\tilde{H}(s)$ can be defined as ratio between $\tilde{V}_{load}(s)$ and $\tilde{V}_g(s)$. According to Kirchhoff's current and voltage laws, we express currents and voltages in Laplace domain

$$\begin{cases} I_1 = \tilde{V}_{source}\left(\frac{1}{Z_0} + sC\right) + I_2; \\ I_2 = \tilde{V}_{obstacle}\left(2sC + \frac{1}{sL_0}\right) + I_3; \\ I_3 = \tilde{V}_{load}\left(sC + \frac{1}{Z_0} + \frac{1}{Z_{NIC}}\right); \end{cases} \begin{cases} \tilde{V}_g - \tilde{V}_{source} = I_1 Z_0; \\ \tilde{V}_{source} - \tilde{V}_{obstacle} = I_2 sL; \\ \tilde{V}_{obstacle} - \tilde{V}_{load} = I_3 sL; \end{cases} \tag{4.11}$$

where $Z_{NIC} = 2Z_0\left[\frac{s+\sqrt{3}\omega_0}{s-\sqrt{3}\omega_0} + \frac{\sqrt{3}s}{2\omega_0}\right]$. We solve the above linear equation set and get the transfer function

$$\tilde{H}(s) = \frac{s}{\omega_0}\alpha\left(2\sqrt{3} - \frac{s}{\omega_0} + \sqrt{3}\left(\frac{s}{\omega_0}\right)^2\right) \times \begin{Bmatrix} 2\sqrt{3} + \left[5\sqrt{3}(\alpha+1) - 1\right]\frac{s}{\omega_0} + \left(7\sqrt{3} - 2 - 2\alpha\right)\left(\frac{s}{\omega_0}\right)^2 \\ + \left(8\sqrt{3} - 2 - 4\alpha + 23\sqrt{3}\alpha\right)\left(\frac{s}{\omega_0}\right)^3 + \left(6\sqrt{3} - 2 - 8\alpha + 24\sqrt{3}\alpha\right)\left(\frac{s}{\omega_0}\right)^4 \\ + \left(3\sqrt{3} - 1 - 6\alpha + 22\sqrt{3}\alpha\right)\left(\frac{s}{\omega_0}\right)^5 + \left(\sqrt{3} - 4\alpha + 14\sqrt{3}\alpha\right)\left(\frac{s}{\omega_0}\right)^6 \\ + \left(6\sqrt{3}\alpha - 2\alpha\right)\left(\frac{s}{\omega_0}\right)^7 + 2\sqrt{3}\alpha\left(\frac{s}{\omega_0}\right)^8 \end{Bmatrix}^{-1}. \tag{4.12}$$

Simple numerical calculation is employed to solve the pole locations of the above transfer function. Our calculation indicates that for stable operation of the PT-symmetric circuit, the coupling coefficient must meet the following condition

$$0.1 < \alpha < 0.3. \tag{4.13}$$

It is also equally important to investigate the impulse response and confirm the stability of our PT-symmetric system in time domain. We substitute the solutions of the poles into the following equation of impulse response

$$H(t)=\sum_{n=1}^{\infty}\mathrm{Res}\left[e^{st}H(s)\right]_n, \tag{4.14}$$

where "Res" means the residue of a complex function. Appendix B demonstrates the impulse responses with parameter detuning, which shows that the impulse response has a finite energy and evolves in a stable fashion in time domain. Both frequency and time domain analyses prove that our system is immune from reasonable unwanted perturbation and fabrication error and maintains stable operation. It's important to note that the stability issue inherently relies on the measurement circuit (where the generator, source and load impedance are included), rather than the isolated PT-symmetric tunneling system.

5. CONCLUSIONS

In this Chapter, we have demonstrated microwave tunneling and information transfer through a PT-symmetric absorber-emitter pair. Our study represents a landmark towards realistic implementation of information transfer systems with extreme robustness, able to tunnel the input signal through otherwise impenetrable obstacles with large robustness, and it shows promises to spawn a series of applications. For instance, our loss-neutral-gain arrangement exhibits a third-order exceptional point in the bound state. By properly designing the system at this higher order exceptional point, the eigenfrequency splitting of the corresponding Hamiltonian matrix shows an enhanced high sensitivity proportional to the cubic root of the perturbation strength on the system, which is very favorable to design ultrasensitive microsensors. Meanwhile, this prototype can be used as a bandpass active filter which allows for simultaneous narrow-band signal

filtering and amplification. Furthermore, our design provides relevant insights into realization of active cloaking devices and active metasurfaces which exhibit unique properties not available in passive counterparts. In summary, the design strategies and stability analysis in this work pave the way towards future realizations of PT-symmetric functionalities in optics and microwave regimes. Considering the extensive connections between electromagnetic, mechanic, and matter waves, our study can also spur practical applications of PT-symmetry in these other fields of research.

Chapter 5: Role of Synchronization in Nonreciprocal Devices with Commutated Transmission Lines[4]

Commutated transmission lines have been recently explored as an interesting way to break Lorentz reciprocity, avoiding any resonant structure, and enabling broad bandwidths with giant isolation combined with lenient requirements on the modulation frequency. The scheme relies on precise synchronization among different switches connected through transmission lines, offering in principle infinite bandwidth. In this chapter, we investigated the effects of realistic switching parameters and synchronization on the device performance, providing interesting physical insights on the operation of these devices. Our results shows that the nonreciprocal response of these systems experiences a linear regression of insertion loss and isolation with respect to the timing error among switches. Remarkably, impedance matching, and nonreciprocal phase shifts are immune from synchronization issues, and reasonable levels of synchronization errors still guarantee low insertion loss and good isolation. Our study also provides practical guidelines to envision nonreciprocal devices based on commutated modulation of conductivity, opening interesting opportunities for several fields of technology, including wireless communications, quantum technologies and photonic circuits. The main results of this chapter are from ref [138].

5.1 Introduction

Time reversal symmetry (TRS) is a fundamental property of many classical physical systems, which dictates that a system remains symmetric under the time reversal operation [139]-[142]. In linear time-invariant (LTI) and non-gyrotropic electromagnetic

[4] This chapter is previously published in ref [138], Zhicheng Xiao did theoretical analysis and run circuit simulation, Dimitrios Sounas did theoretical analysis, Aravind Nagulu run circuit simulation, all the coauthors contribute to write the manuscript, H. Krishnaswamy and A. Alu supervised and funded the work.

systems, TRS leads to the well-known Lorentz reciprocity theorem. Breaking Lorentz reciprocity allows creating asymmetric transmission when exciting from different directions, and it has been an exciting research topic over the past decade [143]-[158], since it shows great promise for novel devices and applications, such as on-chip optical diodes, superconducting quantum circuits, and circulators for full-duplex communication systems [156]-[163].

The conventional approach to break Lorentz reciprocity is to bias a system with a quantity that is odd-symmetric under time reversal operation, such as linear velocity, conduction current, or magnetic field. Among all these approaches, magnetic bias is by far the most common for microwave and optical nonreciprocal devices. However, devices based on this approach tend to be bulky, expensive, and incompatible with chip-scale fabrication processes, due to lattice mismatch between magnetic nonreciprocal media and semiconductors. Nonlinear Kerr effects in asymmetric resonant structures provides solutions to several of these problems, including bias-free non-reciprocity, small form factor, and compatibility with integrated systems technology. Unfortunately, however, nonlinear nonreciprocity is characterized by fundamental limitations, such as narrow dynamic range, intensity-dependent operation, sensitivity to noise, a trade-off between insertion loss and transmission, and operation for non-simultaneous excitation from different ports [164]-[166]. Another approach that has proven very attractive for the design of magnetless nonreciprocal devices without the problems of nonlinear systems is based on time modulation of permittivity. Different types of such linear time-variant (LTV) systems have been proposed so far, including systems with travelling wave modulation, effective gauge fields and angular momentum biasing, which have proven to be dynamic and versatile platforms for many nonreciprocal devices.

A related approach to realize nonreciprocal devices is based on transmission-line commutation. Such LTV devices leverage the fact that conductivity can be modulated with a large contrast, exceeding 10^5 between ON and OFF states at frequencies up to tens of GHz. Such modulation can be typically achieved using transistors as switches, making it particularly attractive to realize miniaturized and fully integrable non-reciprocal devices. Synchronized conductivity modulation has been employed to realize isolators and gyrators with theoretically infinite bandwidth, as well as the first circulator fully integrated in a 65nm CMOS chip [158]. Synchronized conductivity modulation across transmission lines has enabled high-performance circulators, making these approaches viable to commercial applications. Specifically, transmission line commutation has enabled CMOS integrated circulators in the millimeter-wave frequency range (25GHz operation in and 60GHz operation in) as well as circulators with insertion losses of around 2dB, isolation greater than 40dB and watt-level power handling at radio frequencies. Conductivity modulation is preferable over temporal modulation of the real part of permittivity, since the latter is a weak effect, as well as over capacitance modulation in varactors, whose nonlinearity makes them not ideal for high-power applications. Nevertheless, the performance of these devices relies heavily on synchronization of the clocking signals.

In this chapter, we explore the effects of realistic switch de-synchronization on the performance of this class of nonreciprocal devices, analyzing to what degree this effect may degrade the device performance. We quantitatively evaluate the impact of timing errors on various key metrics, focusing on three types of nonreciprocal devices originally introduced in: a gyrator, an isolator, and a circulator, which respectively exhibit nonreciprocal phase response, nonreciprocal amplitude response, and unidirectional flow of signals. In Sections 2, 3, 4, we present ideal singly-balanced

nonreciprocal designs and explain how commutated switches can be employed to create nonreciprocal phase or amplitude responses. Then, we study realistic scenarios in which synchronization issues arise. Our study indicates that the network is still perfectly matched in the presence of a switch timing error. However, the transmission and insertion loss experience a linear recession versus. A differential configuration is then analyzed, with ideally infinite bandwidth. Compared with singly-balanced configurations, differential geometries offer the additional advantage that the insertion loss is independent of the input signal frequency in the presence of timing errors. Finally, we discuss practical implementation guidelines for the considered devices and provide an outlook on these results and their implications on technology.

5.2 GYRATORS

A gyrator is a nonreciprocal phase shifter offering 180 degrees phase shift difference when excited from opposite directions [167][168]. Tellegen was the first to show that a combination of gyrators and other reciprocal lumped elements can implement any linear operation of interest [167]. In this section, we review how commutated transmission -lines can be employed to create a nonreciprocal phase response, and introduce singly-balanced and differential gyrator designs, studying the effect of synchronization issues. Our calculations and modeling are based on time and frequency domain analyses, further validated numerically using the homemade Floquet Scattering Matrix (FSM) approach [169] and commercial Advanced Design System (ADS) software.

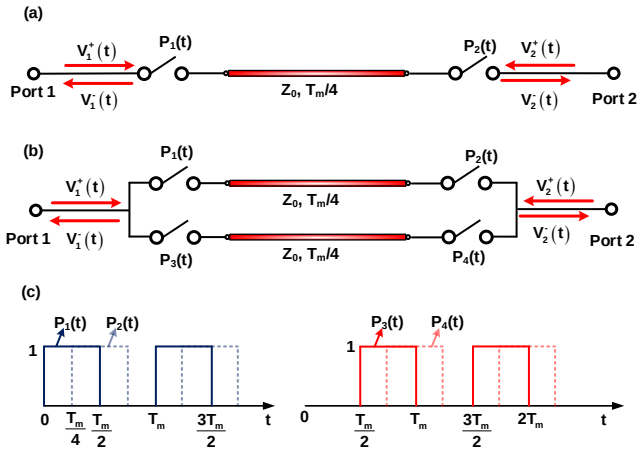

Figure 5.1: Circuit schematic and modulation signals of the gyrator. (a) Circuit schematic of a single branch gyrator. (b) Circuit schematic of a singly-balanced gyrator. (c) Modulation signals. "1" stands for "on", and "0" stands for "off".

5.2.1 Singly-balanced gyrator

A schematic of a singly balanced nonreciprocal phase shifter is shown in Fig. 5.1(a). A lossless transmission line segment is sandwiched between two switches, with switching signals $P_1(t)$ and $P_2(t)$ shown in Fig 5.1(c), where "1" and "0" represent "infinite" and "zero" conductivity (full and zero transmission), respectively. The second switch P_2 is delayed by a quarter period of the modulation signal compared to the first switch P_1. The transmission line delay is chosen to be also equal to a quarter period of the modulation signal, and assuming non-dispersive propagation. When we apply an excitation at port 1 and switch 1 is on, the signal passes through the transmission line and switch 2, traveling to port 2. If the switch 1 is off, the input signal is totally reflected at port 1. On the other hand, a signal incident at port 2 when switch 2 is closed, after propagation through the delay line, finds switch 1 in its open state and is reflected towards port 2. Upon reaching this port, switch 2 is also open and the signal experiences another reflection towards port 1, where it eventually is transmitted after traveling along

the transmission line three times. If switch 2 is open, the incident signal at port 2 is totally reflected. The temporal responses of the output signals at the two ports are hence described by:

$$V_2^-(t) = V_1^+\left(t - \frac{T_m}{4}\right) P_1\left(t - \frac{T_m}{4}\right), \tag{5.1}$$

$$V_1^-(t) = V_1^+(t)\left[1 - P_1(t)\right], \tag{5.2}$$

$$V_1^-(t) = V_2^+\left(t - \frac{3T_m}{4}\right) P_2\left(t - \frac{3T_m}{4}\right), \tag{5.3}$$

$$V_2^-(t) = V_2^+(t)\left[1 - P_2(t)\right], \tag{5.4}$$

where T_m is the modulation period, $V_i^+(t)$ is the input signal at *i*-th port, and $V_i^-(t)$ is the output signal at *i*-th port. Eqs. (5.1)-(5.2) and (5.3)-(5.4) apply for excitation from ports 1 and 2, respectively.

As we see from Eqs. (5.1)-(5.2) and (5.3)-(5.4), the time delay of forward and backward transmitted signals is nonreciprocal, and equal to $T_m/4$ and $3T_m/4$, respectively, which results in direction dependent phase. This is reflected in the frequency response of the system, which is rigorously derived in Appendix C. By looking at the zero-th Fourier harmonic, we readily obtain the non-reciprocal scattering matrix of the fundamental tone:

$$S(\omega) = \frac{1}{2}\begin{bmatrix} 1 & e^{-j\omega\frac{3T_m}{4}} \\ e^{-j\omega\frac{T_m}{4}} & 1 \end{bmatrix}, \tag{5.5}$$

which is consistent with the time-domain description above. Equation (5.5) clearly shows a nonreciprocal phase response for forward and backward transmitted signals. When the input frequency satisfies the condition $\omega = (2k+1)\omega_m$, where $k = 0,\ 1,\ 2\ldots$, the phase difference between forward and backward transmitted signals becomes π and the device operates as a lossy gyrator.

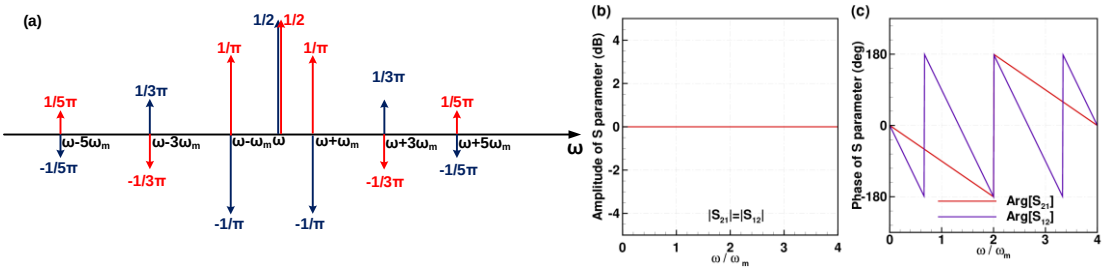

Figure 5.2: Harmonics of forward transmitted signal and S parameters of the singly-balanced gyrator. (a) Harmonics of forward transmitted signal. Blue line marks the harmonics of the first branch with switches P1 and P2. Red line stands for the harmonics of the complementary branch with switches P3 and P4. (b) Magnitude of S parameters of a singly balanced gyrator. (c) Phase of S parameters of a singly balanced gyrator.

From the frequency-domain standpoint, each switch acts as a frequency mixer, which converts the incoming signal from either of the two ports into an infinite discrete series of harmonics with certain phases. Each of these harmonics propagate along the transmission line and, upon reaching the second switch, the signal experiences another mixing event, which partially converts these harmonics to the fundamental tone, leading to an overall 6 dB insertion loss [factor $1/2$ in Eq. (5.5)]. During the mixing events, the signals pick up modulation phases with positive/negative sign at the first/second switch, respectively. As a result, the output signal acquires an additional phase equal to the phase difference between switches. Since the two switches are closed with a delay $T_m/4$ and $3T_m/4$ with respect to each other in the forward and backward directions respectively, the phase of the output signal is different in opposite directions, as observed in Eq. (5.5).

The 6 dB insertion loss of the single-branch gyrator described in Eq. (5.5) can be compensated by adding a second branch with complementary clocks, as shown in Fig. 5.1(b). In this case, the output signal is the superposition of the transmitted signal through the top branch, given by Eqs. (5.1)-(5.4), and the one through the bottom branch, which

can be derived by applying a $T_m/2$ delay to all switches. Then, it is easy to find that the total output signals at the ports are given by

$$\begin{cases} V_2^-(t) = V_1^+\left(t - T_m/4\right), \\ V_1^-(t) = 0, \end{cases} \tag{5.6}$$

for excitation from port 1 and

$$\begin{cases} V_1^-(t) = V_2^+\left(t - \dfrac{3T_m}{4}\right), \\ V_2^-(t) = 0, \end{cases} \tag{5.7}$$

for excitation from port 2. By converting Eqs. (5.6) and (5.7) to frequency domain, we find that the scattering matrix for the fundamental tone is

$$S(\omega) = \begin{bmatrix} 0 & e^{-j\omega\frac{3T_m}{4}} \\ e^{-j\omega\frac{T_m}{4}} & 0 \end{bmatrix}. \tag{5.8}$$

A π nonreciprocal phase shift occurs at $\omega = (2k+1)\omega_m$, where $k = 0, 1, 2, 3, \ldots$, at which the device operates as an ideal, infinite bandwidth, lossless gyrator. Figures 5.2(b) and (c) show the amplitude and phase characteristics of the forward and backward transmission coefficients S_{21} and S_{12}, respectively. Indeed, the amplitude of transmission coefficient is unitary and frequency-independent, while the π nonreciprocal phase shift occurs at discrete frequency points. The suppression of insertion loss in this system can also be understood by looking at the spectrum of the output signal from the two branches, presented in Fig. 5.2(a) (blue and red for the top and bottom branches, respectively). We can see that higher-order harmonics experience opposite phase shift in the two branches, leading to destructive interference at the output ports. On the other hand, the fundamental tone maintains the same phase shift in both branches, leading to constructive superposition at the output port. In other words, while each transmission-line arm sustains propagation of many harmonics, essentially the

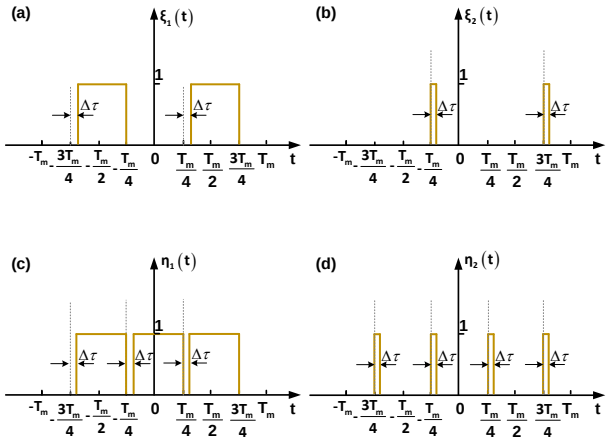

Figure 5.3: Envelope of modulated signals of the gyrator with timing error. (a) Forward transmitted signal envelope from excitation at port 1 of a single branch gyrator with time delay $T_m/4$; (b) forward transmitted signal envelope from excitation at port 1 of a single branch gyrator with time delay $3T_m/4$; (c) forward transmitted signal envelope from excitation at port 1 of a singly balanced gyrator with time delay $3T_m/4$; (d) forward transmitted signal envelope from excitation at port 1 of a singly balanced gyrator with time delay $T_m/4$.

sampling of the input signal split into the two parallel lines, at the two ports the synchronization of the switches allows to recombine ideally the signal, without any distortion. The overall transfer function operates as a pseudo-linear-time-invariant system, in which no frequency conversion occurs. It is obvious that this ideal response is not possible in absence of ideal synchronization, hence it is important to consider the effect of imperfections in the switching network on the overall Floquet transfer matrix of the system.

In this context, consider the single branch gyrator design in Fig. 1(a) and assume now that the second switch has a small timing error $\Delta\tau$ with respect to the first one, $P_2(t) = P_1(t - T_m/4 - \Delta\tau)$. For a monochromatic excitation $e^{j\omega t}$ at port 1, most part of the signal, overlapping with the waveform in Fig. 3(a), passes through the second switch

with a time delay $T_m/4$, while a small tail, overlapping with the waveform in Fig. 3(b), bounces twice inside the transmission line and transmits through the second switch with time delay $3T_m/4$. The reflected signal $V_1^-(t)$ is not affected by the timing error. For monochromatic excitation $e^{j\omega t}$ at port 2, most of the signal, overlapping with the waveform in Fig. 3(a), passes through the first switch with delay $3T_m/4$, while a small tail overlapping with the waveform in Fig. 5.3(b), is transmitted through the transmission line with delay $T_m/4$. The time domain response of this slightly desynchronized gyrator is described by:

$$V_2^-(t) = V_1^+\left(t-\frac{T_m}{4}\right)\xi_1(t) + V_1^+\left(t-\frac{3T_m}{4}\right)\xi_2(t), \tag{5.9}$$

$$V_1^-(t) = V_1^+(t)\left[1-P_1(t)\right], \tag{5.10}$$

$$V_1^-(t) = V_2^+\left(t-\frac{3T_m}{4}\right)\xi_1\left(t-\frac{3T_m}{4}\right) + V_2^+\left(t-\frac{T_m}{4}\right)\xi_2\left(t-\frac{T_m}{4}\right), \tag{5.11}$$

$$V_2^-(t) = V_2^+(t)\left[1-P_2(t)\right], \tag{5.12}$$

where Eqs. (5.9)-(5.10) and (5.11)-(5.12) correspond to excitation from port 1 and port 2, respectively. The functions $\xi_1(t)$, $\xi_2(t)$ are envelopes of modulated signals and have a period T_m [see Figs. 5.3(a) and (b)]. The scattering matrix for the fundamental frequency component is readily obtained (see Appendix A):

$$S = \begin{bmatrix} \frac{1}{2} & \frac{|\Delta\tau|}{T_m}e^{-j\omega\frac{T_m}{4}} + \left(\frac{1}{2}-\frac{|\Delta\tau|}{T_m}\right)e^{-j\omega\frac{3T_m}{4}} \\ \left(\frac{1}{2}-\frac{|\Delta\tau|}{T_m}\right)e^{-j\omega\frac{T_m}{4}} + \frac{|\Delta\tau|}{T_m}e^{-j\omega\frac{3T_m}{4}} & \frac{1}{2} \end{bmatrix}, \tag{5.13}$$

which indicates that, at the operational frequency $\omega = (2k+1)\omega_m$, $k = 0,\ 1,\ 2,\ 3\ldots$, the single branch gyrator exhibits additional insertion loss of $2|\Delta\tau|/T_m$, proportional to the timing error.

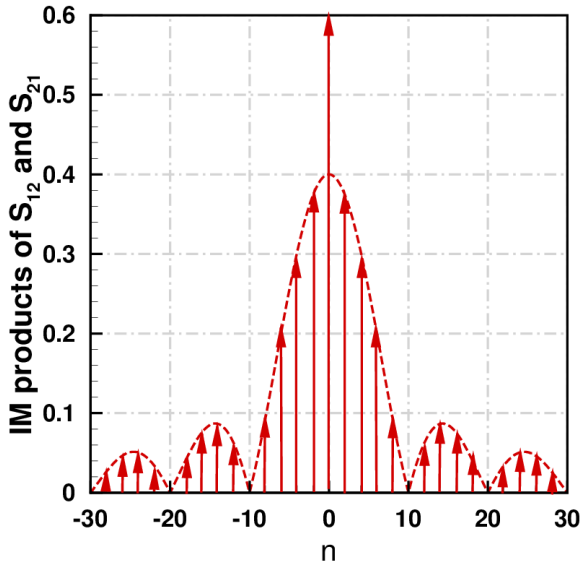

Figure 5.4: Inter-modulation (IM) products a singly balanced gyrator with relative timing error $|\Delta\ \tau|/T_m = 0.1$. *n* stands for the order of harmonics and *y* axis is the amplitude of each harmonics.

Next, we study the balanced gyrator with timing error, and assume that the same timing error as between switches P_1 and P_2 is also applied to switches P_3 and P_4, i.e. $P_4(t) = P_3(t - T_m/4 - \Delta\ \tau)$. This assumption is practically reasonable because we can use single-pole-double-throw switches to replace P_1 and P_3, and P_2 and P_4. The temporal responses are then given by

$$V_2^-(t) = V_1^+\left(t - \frac{T_m}{4}\right)\eta_1(t) + V_1^+\left(t - \frac{3T_m}{4}\right)\eta_2(t), \tag{5.14}$$

$$V_1^-(t) = 0, \tag{5.15}$$

$$V_1^-(t) = V_2^+\left(t - \frac{3T_m}{4}\right)\eta_1\left(t - \frac{3T_m}{4}\right) + V_2^+\left(t - \frac{T_m}{4}\right)\eta_2\left(t - \frac{T_m}{4}\right), \tag{5.16}$$

$$V_2^-(t) = 0. \tag{5.17}$$

Again, here Eqs. (5.14)-(5.15) and (5.16)-(5.17) correspond to excitation from port 1 and 2, respectively. $\eta_1(t)$, $\eta_2(t)$ are envelopes of modulated signals [see Figs. 5.3(c)

and (d)]. Remarkably, despite the synchronization error, the network remains ideally matched at both ports. This result stems from the fact that the desynchronized tail transmits through the two-port network rather than bouncing back to the source.

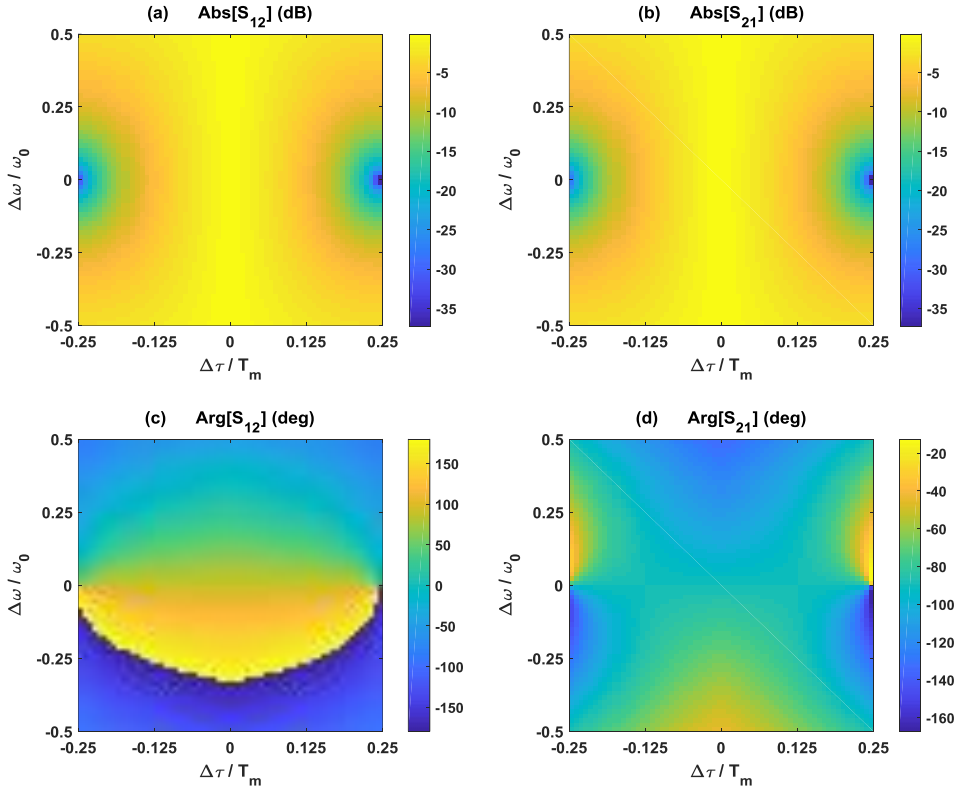

Figure 5.5: Inter-modulation (IM) products a singly balanced gyrator with relative timing error $\left|\Delta\ \tau\right|/T_m = 0.1$. *n* stands for the order of harmonics and *y* axis is the amplitude of each harmonics. Scattering properties of a singly balanced gyrator with timing error. (a) Magnitude of the backward transmission S_{12}; (b) Magnitude of the forward transmission S_{21}; (c) Phase of the backward transmission S_{12}; (d) Phase of the forward transmission S_{21}. ω_0 is the operational frequency and $\Delta\omega$ is the input frequency shift.

Harmonic analysis of this singly balanced gyrator with timing error is given in Appendix C.

Figure 4 shows the amplitude of harmonics of a singly-balanced gyrator with a relative timing error $\left|\Delta\ \tau\right|/T_m = 10\%$ and operational frequency $\omega = \omega_m$. The fundamental tone amplitude is $1-4\left|\Delta\ \tau\right|/T_m = 0.6$ and higher-order harmonics are enveloped by $4\left|\Delta\ \tau\right|/T_m \operatorname{sinc}\left(n\pi\left|\Delta\ \tau\right|/T_m\right)$. Expectedly, as the timing error $\Delta\ \tau$ approaches zero, residual even-order harmonics disappear, and the fundamental tone approaches full transmission. The fundamental-tone scattering parameters of the singly-balanced gyrator can be found from the results in Appendix C as

$$S = \begin{bmatrix} 0 & \dfrac{2\left|\Delta\ \tau\right|}{T_m} e^{-j\omega\frac{T_m}{4}} + \left(1-\dfrac{2\left|\Delta\ \tau\right|}{T_m}\right) e^{-j\omega\frac{3T_m}{4}} \\ \left(1-\dfrac{2\left|\Delta\ \tau\right|}{T_m}\right) e^{-j\omega\frac{T_m}{4}} + \dfrac{2\left|\Delta\ \tau\right|}{T_m} e^{-j\omega\frac{3T_m}{4}} & 0 \end{bmatrix}. \tag{5.18}$$

From Eq. (5.18), we gather an important conclusion: impedance matching and nonreciprocal phase shift of a singly-balanced gyrator at the fundamental frequency are immune to switch timing errors. On the other hand, the insertion loss, $1-4\left|\Delta\ \tau\right|/T_m$, increases linearly with the timing error. Fig. 5.5 shows the scattering matrix as a function of input signal frequency and switch timing error. Furthermore, insertion loss increases as we depart from the frequency of optimal operation $\left(2k+1\right)\omega_m, k = 0,\ 1,\ 2,\ 3,\ldots$. In order to have an insertion loss of less than 3dB, the resulting maximum timing error is 7.3%. In IC implementations, it is feasible to keep the timing errors well below these levels, as well as to include calibration circuitry that corrects such timing errors.

5.2.1 Differential gyrator

As shown in the previous subsection, a singly-balanced gyrator exhibits full transmission over a bandwidth limited only by the dispersion of transmission lines in

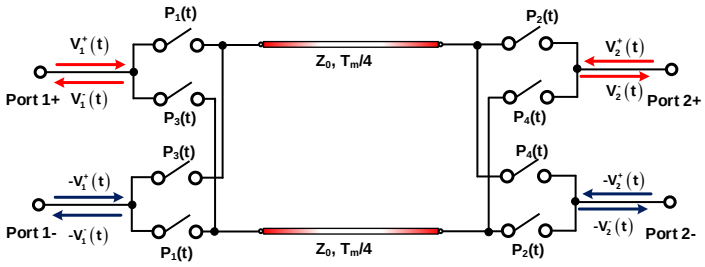

Figure 5.6: Circuit schematic of the differential gyrator. Switching signals are the same as Fig. 5.1.

absence of synchronization errors. However, the gyrator functionality, i.e., a nonreciprocal phase difference of π, is available only at discrete frequencies $\omega=(2k+1)\omega_m, k=0,1,2,3,\ldots$. This problem can be overcome using a differential configuration, which exhibits a nonreciprocal π phase shift over an infinite bandwidth under ideal conditions (ideal switches, dispersion-free transmission lines, no timing errors). The circuit schematic is shown in Fig. 5.6. For excitation from port 1, the signal is fully transmitted through the network with a time delay $V_2^-(t)=V_1^+(t-T_m/4)$. For excitation from differential port 2, the signal is flipped due to the differential arrangement of the switches. Therefore, the transmitted signal is $V_1^-(t)=-V_2^+(t-T_m/4)$. The scattering parameters can be expressed as

$$S(\omega)=\begin{bmatrix} 0 & e^{-j\omega\frac{T_m}{4}+j\pi} \\ e^{-j\omega\frac{T_m}{4}} & 0 \end{bmatrix}. \tag{5.19}$$

The transmission is unitary, and the nonreciprocal phase difference is π at all frequencies, making it an ideal gyrator.

In presence of switch desynchronization, the performance is deteriorated: for excitation from port 1, a major part of the signal overlapping with $\eta_1(t)$ in Fig. 5.3(c) passes through the network with time delay $T_m/4$, while a small desynchronized tail overlapping with $\eta_2(t)$ in Fig. 5.3(d) is transmitted through the gyrator with flipped

polarity. For backward excitation from differential port 2, the large part of the signal overlapping with $\eta_1(t)$ in Fig. 5.3(c) is flipped, and a small tail overlapping with $\eta_2(t)$ in Fig. 5.3(d) propagates without flipping of the polarity. The above time-domain operation is described by the equations

$$V_2^-(t) = V_1^+\left(t - \frac{T_m}{4}\right)\eta_1(t) - V_1^+\left(t - \frac{T_m}{4}\right)\eta_2(t), \tag{5.20}$$

$$V_1^-(t) = 0, \tag{5.21}$$

$$V_1^-(t) = -V_2^+\left(t - \frac{T_m}{4}\right)\eta_1\left(t - \frac{T_m}{4}\right) + V_2^+\left(t - \frac{T_m}{4}\right)\eta_2\left(t - \frac{T_m}{4}\right), \tag{5.22}$$

$$V_2^-(t) = 0. \tag{5.23}$$

Again, here Eqs. (5.20)-(5.21) and (5.22)-(5.23) correspond to excitation from port 1 and 2, respectively.

The corresponding scattering matrix for the fundamental tone, derived rigorously in Appendix C, reads

$$S = \begin{bmatrix} 0 & -\left(1 - \dfrac{4|\Delta\ \tau|}{T_m}\right)e^{-j\omega\frac{T_m}{4}} \\ \left(1 - \dfrac{4|\Delta\ \tau|}{T_m}\right)e^{-j\omega\frac{T_m}{4}} & 0 \end{bmatrix}. \tag{5.24}$$

Eq. (5.24) indicates that the differential gyrator also maintains a zero return loss even in the presence of timing errors. In addition, the differential gyrator has the advantage of having a non-reciprocal phase response that is not affected by desynchronization, owing to the differentially arranged switches. Although the insertion loss is affected by the timing error, the impact is nondispersive, indicating that the bandwidth is not affected either.

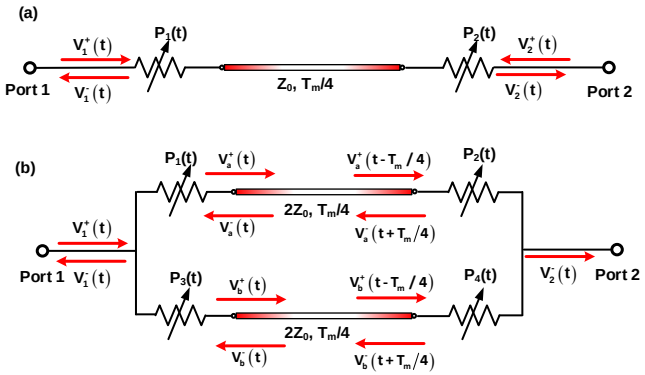

Figure 5.7: Circuit schematic of the isolator. (a) Single branch isolator, modulation signals P1 and P2 are the same as Figure 1. (b) Singly balanced isolator, modulation signals P1, P2, P3, and P4 are the same as Figure 1. The characteristic impedance of the transmission line is $2Z_0$.

5.3 ISOLATORS

In the previous section, we have characterized singly-balanced and differential gyrator designs by modulating the switch conductivity between zero and infinity. While this configuration can realize gyration and nonreciprocal phase shifts, nonreciprocal transmission magnitude cannot be realized with this strategy, because the circuit, in the the absence of frequency conversion, is lossless, and it is impossible to realize isolation in lossless, linear devices. A two-port isolator design necessarily involves finite loss to absorb the energy in the direction of isolation. In this section, we relax this assumption and discuss the design of singly-balanced and ultra-broadband doubly-balanced isolators based on modulating the conductivity over a finite range, which allows the presence of absorption. We then investigate synchronization issues and remedy strategies are proposed to counterbalance these imperfections.

5.3.1 Singly-balanced isolator

Figure 5.7(a) shows an isolator design, based on a transmission line sandwiched between two modulated resistances, where the conductivity is modulated between infinity, i.e., perfect transmission, and a finite value R_m. In time domain, the modulation follows the same pattern as in the case of the gyrator. By tracking the propagation of input signals through the system as in the gyrator case, the output signals can be expressed as

$$V_2^-(t) = V_1^+\left(t-\frac{T_m}{4}\right)P_1\left(t-\frac{T_m}{4}\right) + \mathrm{T}^2 V_1^+\left(t-\frac{T_m}{4}\right)\left[1-P_1\left(t-\frac{T_m}{4}\right)\right], \tag{5.25}$$

$$V_1^-(t) = \Gamma V_1^+(t)\left[1-P_1(t)\right] + \Gamma\mathrm{T}V_1^+\left(t-\frac{T_m}{2}\right)\left[1-P_1\left(t-\frac{T_m}{2}\right)\right], \tag{5.26}$$

$$V_1^-(t) = \mathrm{T}V_2^+\left(t-\frac{T_m}{4}\right) + \Gamma^2 V_2^+\left(t-\frac{3T_m}{4}\right)P_2\left(t-\frac{3T_m}{4}\right), \tag{5.27}$$

$$V_2^-(t) = \Gamma V_2^+(t)\left[1-P_2(t)\right] + \Gamma\mathrm{T}V_2^+\left(t-\frac{T_m}{2}\right)P_2\left(t-\frac{T_m}{2}\right), \tag{5.28}$$

where Eqs. (5.25)-(5.26) are the temporal responses for excitation at port 1, Eqs. (5.27)-(5.28) are the temporal responses for excitation at port 2, and $P_1(t)$ and $P_2(t)$ are the switching signals, provided in Fig. 1(c) (here, "0" stands for finite conductivity, namely resistance R_m, while "1" stands for infinite conductivity, i.e., perfect transmission). $\Gamma = R_m\left(R_m+2Z_0\right)^{-1}$ is the reflection coefficient when the resistance is R_m, and $\mathrm{T}=1-\Gamma$ is the corresponding transmission coefficient. Equations (5.25)-(5.28) simplify into Eqs. if the resistance R_m approaches infinity ($\Gamma=1$, $\mathrm{T}=0$), as expected. The scattering matrix for the fundamental tone is given by

$$S = \begin{bmatrix} \frac{\Gamma}{2}\left(1+\mathrm{T}e^{-j\omega\frac{T_m}{2}}\right) & \mathrm{T}e^{-j\omega\frac{T_m}{4}} + \frac{1}{2}\Gamma^2 e^{-j\omega\frac{3T_m}{4}} \\ \frac{1}{2}\left(1+\mathrm{T}^2\right)e^{-j\omega\frac{T_m}{4}} & \frac{\Gamma}{2}\left(1+\mathrm{T}e^{-j\omega\frac{T_m}{2}}\right) \end{bmatrix}. \tag{5.29}$$

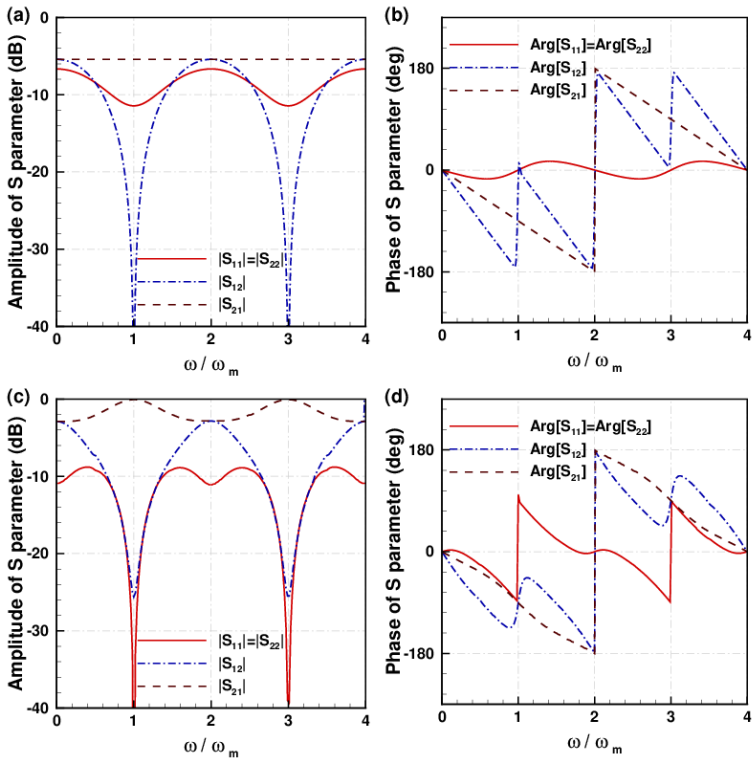

Figure 5.8: S parameter of the isolator. (a) Magnitude of the S parameter of a single branch isolator. (b) Phase of the S parameter of a single branch isolator. (c) Magnitude of the S parameter of a singly balanced branch isolator. (d) Phase of the S parameter of a singly balanced isolator.

The above result encompasses many interesting scenarios. When $\Gamma = 0$, it corresponds to the case in which the switch is always on, and hence we achieve a reciprocal response, $S_{12} = S_{21} = \exp\left(-j\omega T_m/4\right)$, and zero return loss, $S_{11} = S_{22} = 0$. When $\Gamma = 1$, the circuit is a single-branch gyrator, consistent with the previous section, with a return loss of $6\,dB$, $S_{11} = S_{22} = \frac{1}{2}$, and nonreciprocal phase transmission [see Eq. (5.5)]. Interestingly, the same model can provide full isolation for appropriately selected values of Γ and T. In particular, if we require full isolation ($S_{12} = 0$), we find that it is obtained for $\omega = \left(2k+1\right)\omega_m$, $k = 0,\ 1,\ 2,\ 3,\ldots$, and $R_m = R_{iso} = 2\left(1+\sqrt{3}\right)Z_0$. Isolation in this case is the result of destructive interference at port 1 of the signals that

reach this port after 1 and 3 paths through the transmission line, as evidenced by the phase of the two terms in the expression of S_{12}. Under these circumstances, we find that return and insertion loss are given by $|S_{11}| = |S_{22}| = 2-\sqrt{3}$ and $|S_{21}| = 2\left(2-\sqrt{3}\right)$, respectively.

It is interesting to note that these quantities do not depend on the parameters of the system (T_m and Z_0), but instead are inherent properties of the considered circuit topology. Figs. 8(a) and 8(b) plot amplitude and phase of the scattering parameters for this isolator design. At $\omega = \omega_m$ and $\omega = 3\omega_m$, full isolation is achieved, whereas at $\omega = 2\omega_m$ we find reciprocal transmission $S_{21} = S_{12} = -2\left(2-\sqrt{3}\right)$. It is interesting that the transmission amplitude in the forward direction is the same for all frequencies, which can also be seen from Eq. (5.29). The forward-propagating signal always experiences a finite reflection Γ, due to the finite resistance value R_m. In order to eliminate this return loss, we consider a differential topology [Fig. 7(b)], in which the characteristic impedance of the two parallel transmission lines is tuned to $2Z_0$ to match the port impedance. The reflection coefficient for each individual signal pass in this case is frequency-dependent, and a rigorous temporal analysis is presented in Appendix C. The S parameters at $\omega = (2k+1)\omega_m$ become

$$S\big|_{\omega=(2k+1)\omega_m} = \begin{bmatrix} 0 & j(-1)^{k+1}\left(\mathscr{T}^2 - \mathscr{R}^2\right) \\ j(-1)^{k+1} & 0 \end{bmatrix}, \tag{5.30}$$

where $\mathscr{T} = 8Z_0\left(R_m + 8Z_0\right)^{-1}$ and $\mathscr{R} = R_m\left(R_m + 8Z_0\right)^{-1}$ are the transmission and reflection coefficients experienced by the signal during each pass. Interestingly, the above equation indicates that impedance is automatically matched at operation frequencies. The condition for complete backward isolation is $\mathscr{R} = \mathscr{T}$, thereby leading to an isolation resistance $R_m = R_{iso} = 8Z_0$ for full isolation. R_{iso} marks the boundary

of the nonreciprocal phase difference for transmission, where $R_m < R_{iso}$ indicates zero phase difference between S_{21} and S_{12}, and $R_m > R_{iso}$ provides to π phase difference. In the extreme case $R_m \to 0$, the design recedes to a transmission line with characteristic impedance Z_0. In the extreme scenario $R_m \to \infty$, the circuit becomes the differential gyrator we discussed in previous section.

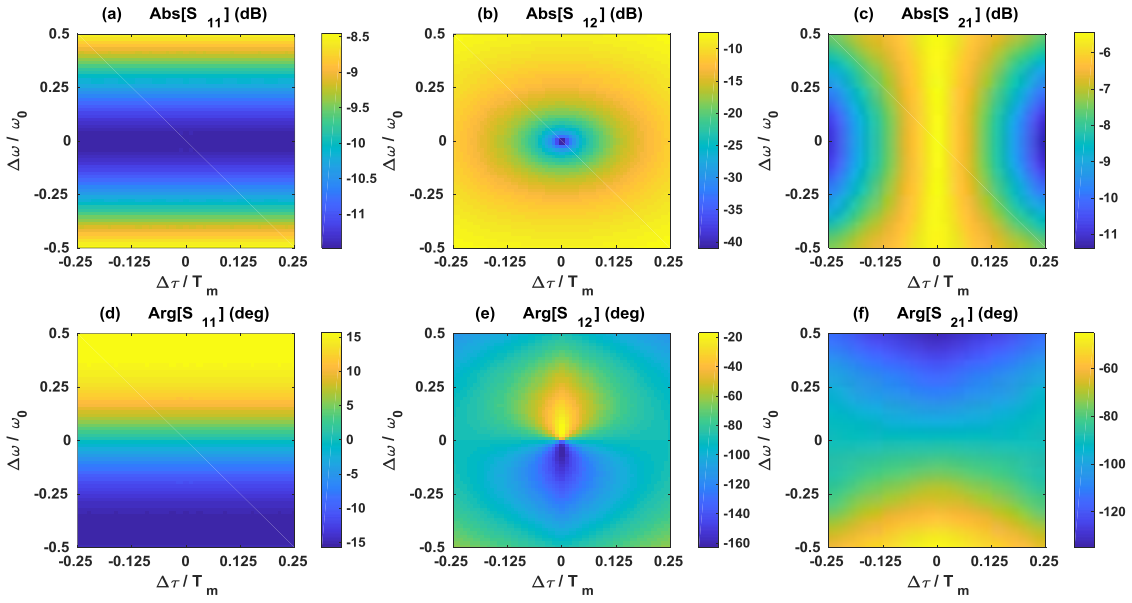

Figure 5.9: S parameter of a single branch isolator with timing error. (a) Magnitude of the return loss S_{11} of a single branch isolator. (a) Magnitude of the isolation S_{12} of a single branch isolator. (c) Magnitude of the transmission S_{21} of a single branch isolator. (d) Phase of the isolation S_{11} of a single branch isolator. (e) Phase of the isolation S_{12} of a single branch isolator. (f) Phase of the transmission S_{21} of a single branch isolator.

To further validate our temporal analysis across the full spectrum band, we use the composite Floquet Scattering Matrix (FSM) method, as described in to compute the scattering parameters [Figs. 5.8(c) and (d)] for isolation resistance $R_{iso} = 8Z_0$. Our

numerical results from composite FSM method are in excellent agreement with the analytical results and also with numerical simulations using Keysight ADS, which are not shown here for space limitations.

Now, we consider a single-branch isolator with a small timing error, where $P_2(t) = P_1(t - T_m/4 - \Delta\ \tau)$ and $|\Delta\ \tau| < T_m/4$. A rigorous temporal and frequency analysis, similar to the one presented for the gyrators in the previous section, is performed in Appendix B. We obtain the S parameters

$$S = \begin{bmatrix} \frac{\Gamma}{2}\left(1 + \mathrm{T}e^{-j\omega\frac{T_m}{2}}\right) & \left(\mathrm{T} + \frac{\Gamma^2|\Delta\ \tau|}{T_m}\right)e^{-j\omega\frac{T_m}{4}} + \left(\frac{1}{2}\Gamma^2 - \frac{\Gamma^2|\Delta\ \tau|}{T_m}\right)e^{-j\omega\frac{3T_m}{4}} \\ \left(\frac{1+\mathrm{T}^2}{2} - \frac{\Gamma^2|\Delta\ \tau|}{T_m}\right)e^{-j\omega\frac{T_m}{4}} + \frac{\Gamma^2|\Delta\ \tau|}{T_m}e^{-j\omega\frac{3T_m}{4}} & \frac{\Gamma}{2}\left(1 + \mathrm{T}e^{-j\omega\frac{T_m}{2}}\right) \end{bmatrix}. \quad (5.31)$$

Interestingly, the timing error of the second switch has no influence on the return loss at either port. This is a major advantage of the synchronized loss modulation design. Assuming no timing error, when port 1 is excited by an input signal $\exp(j\omega t)$, it passes through the transmission line and the second switch consecutively during the first half of the modulation period. The signal in the second half of the modulation period is partially reflected at port 1, transported through the delay line, reflected at port 2, and, finally, partially transmits through the first switch. The return signal is essentially a superposition of the first-time reflection and another second-time reflection with a delay $T_m/4$, leading to a phase delay $\exp(-j\omega T_m/2)$ in the second term of S_{11} and S_{22}. In the presence of a timing error, the second reflection (the one happening when switch 1 is open) occurs over the time $T_m/2 - \Delta\ \tau$, instead of $T_m/2$. However, there is an extra reflection with the same scaling factor ΓT and time delay $T_m/2$, occurring over an

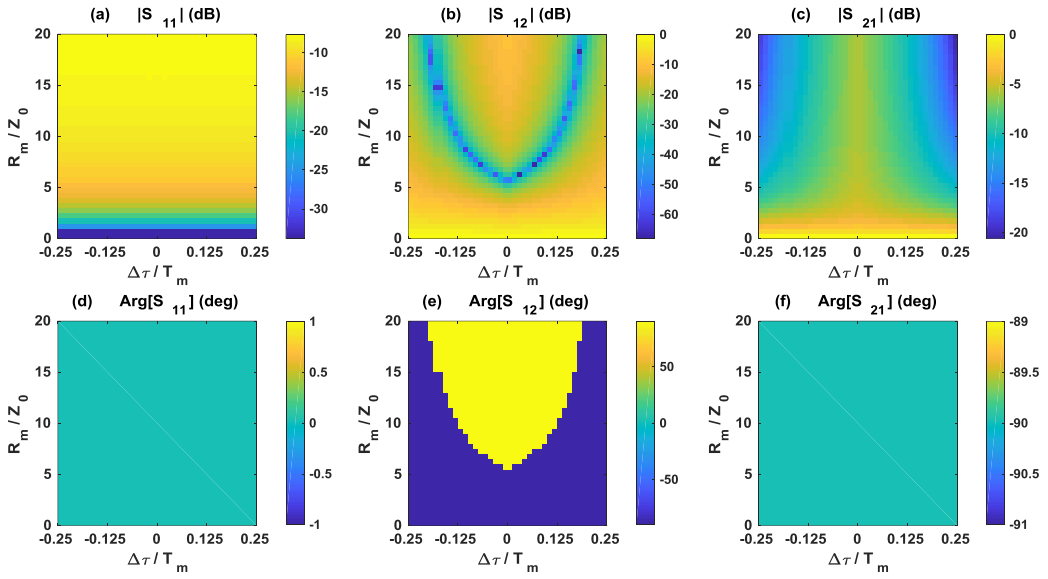

Figure 5.10: S parameter of a single branch isolator with timing error Variation of S parameters of the single branch isolator in presence of timing error, as a function of the switch resistance. (a) Magnitude of the return loss $S_{11} = S_{22}$ of a single branch isolator. (a) Magnitude of the isolation S_{12} of a single branch isolator. (c) Magnitude of the transmission S_{21} of a single branch isolator. (d) Phase of the return loss $S_{11} = S_{22}$ of a single branch isolator. (e) Phase of the isolation S_{12} of a single branch isolator. (f) Phase of the transmission S_{21} of a single branch isolator.

additional time $\Delta\ \tau$ right after switch 1 is closed, during which the signal finds switch 2 in the open state. This additional reflection compensates for the reduced duration of the main reflection at the fundamental tone, leading to the same reflection coefficient as when there is no timing error, although it affects the intermodulation products. In other words, the sole effect of the timing error is redistribution of power among the intermodulation harmonics. For the transmitted signals, the timing error results in a signal tail bouncing back and forth inside the delay line before finding its way out, leading to an extra average insertion loss $\Gamma^2 \left|\Delta\ \tau\right| / T_m$ over the modulation period, as shown in S_{12}

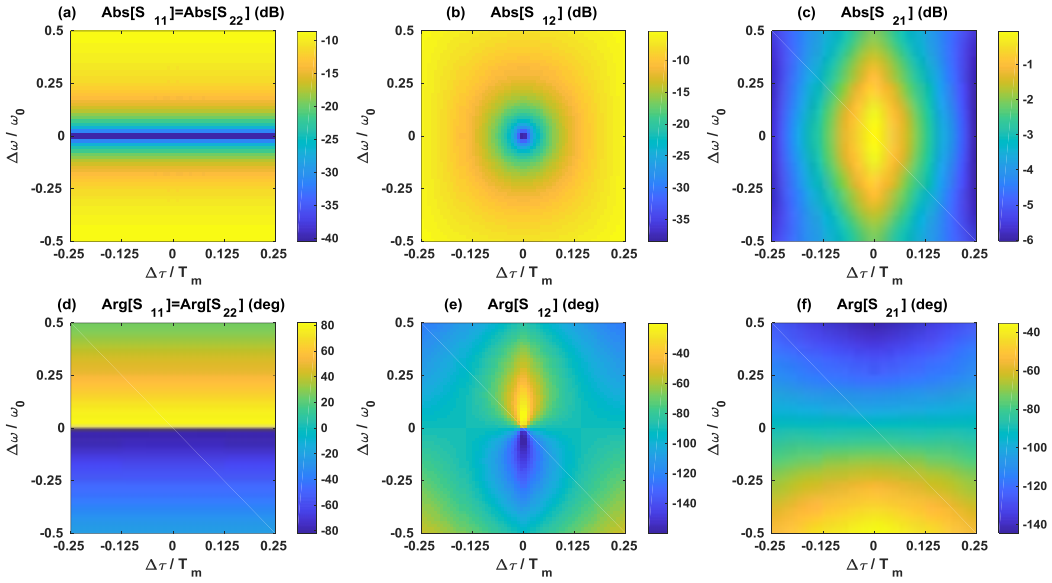

Figure 5.11: S parameter of the singly-balanced isolator with timing error. (a) Magnitude of the return loss S_{11} of a singly-balanced branch isolator. (b) Magnitude of the isolation S_{12} of a singly -balanced branch isolator. (c) Magnitude of the transmission S_{21} of a singly-balanced branch isolator. (d) Phase of the return loss S_{11} of a singly-balanced branch isolator. (d) Phase of the isolation S_{12} of a balanced singly-branch isolator. (c) Phase of the transmission S_{21} of a singly-balanced branch isolator.

and S_{21} in Eq. (5.31). In Figure 5.9, we plot scattering parameters computed using the composite FSM method, which show good agreement with analytical results from Eq. (5.31) and our theoretical analysis in the previous paragraph. To maintain -20 dB isolation, the relative timing error should be less than 10.9%. The corresponding fractional bandwidth is 12.5%.

Another degree of freedom in the isolator design is the resistor value, which we can tune to optimize the isolation in presence of timing error. Figure 5.10 shows the modification of the scattering parameters as we vary $\Delta\tau$ and R_m, as from Eq. (5.31). As seen in Fig. 5.10(b), the isolation map shows a dip for certain combinations of $\Delta\tau$

and R_m. An abrupt phase jump in S_{12} shown in Fig. 5.10(e) indicates that ideal isolation is indeed possible. We closely studied the backward propagation coefficient in Eq. (5.31), and derived an analytical expression for optimal resistance as a function of $\Delta\tau$ and R_m:

$$R_{optimal} = 2Z_0\left[1+\sqrt{3-\frac{8|\Delta\tau|}{T_m}}\right]\left(1-\frac{4|\Delta\tau|}{T_m}\right)^{-1}, \tag{5.32}$$

which perfectly matches our numerical simulation and ensures ideal isolation. The insertion loss grows as we tune the resistor to improve isolation upon a given timing error, as shown in Fig. 5.10(c), implying a trade-off between isolation and insertion loss as the timing error grows.

The singly-balanced isolator simultaneously enables perfect impedance matching, full transmission, and full isolation at its operation frequencies. Figure 5.11 shows the scattering parameters plotted versus timing error in the proximity of the operation frequency. As we see in Fig. 5.11(a), the return loss is immune to synchronization issues and it remains as low as 40 dB when relative timing error varies from -0.25 to 0.25. The sharp phase transition from -90 deg to 90 deg along $\Delta\omega = 0$ in Fig. 5.11(d) is consistent with the region with zero return loss. At the operational frequency, the scattering matrix can be written as

$$S\big|_{\omega=(2k+1)\omega_m} = \begin{bmatrix} 0 & j(-1)^{k+1}\left[-\mathscr{R}^2+\mathscr{T}^2+\frac{2|\Delta\tau|\left(1+\mathscr{R}^2-\mathscr{T}^2\right)}{T_m}\right] \\ j(-1)^{k+1}\left[1-\frac{2|\Delta\tau|\left(1+\mathscr{R}^2-\mathscr{T}^2\right)}{T_m}\right] & 0 \end{bmatrix}. \tag{5.33}$$

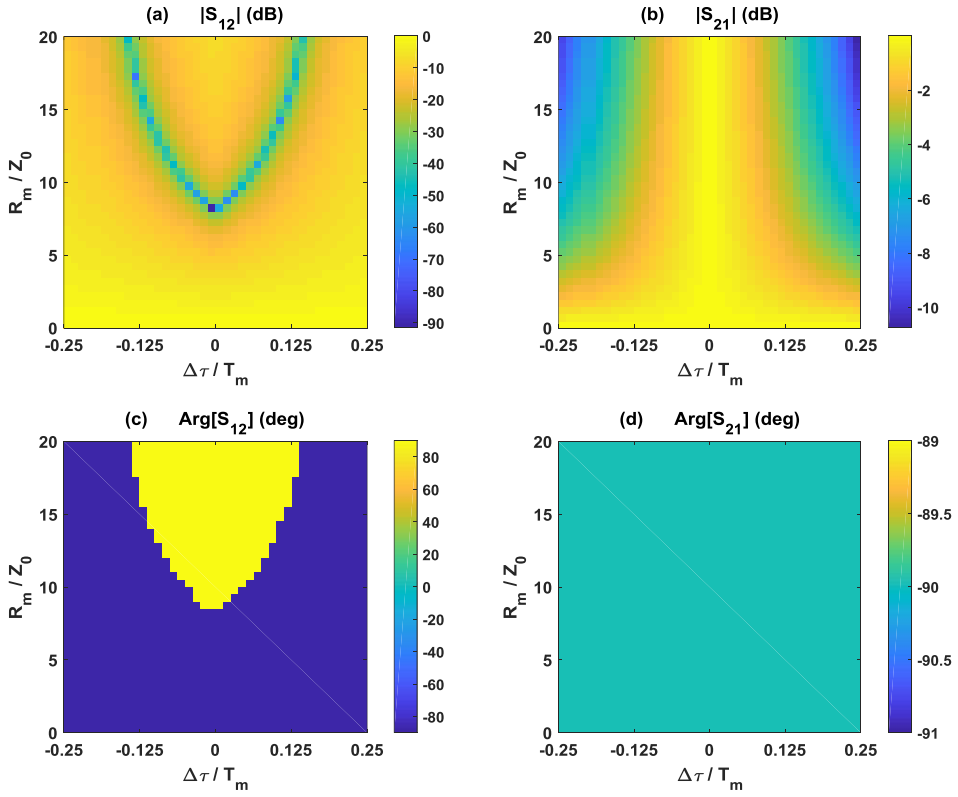

Figure 5.12: Variation of the singly-balanced isolator in presence of timing error, as a function of the switch resistance. (a) Magnitude of the isolation S_{12} of a singly-balanced branch isolator. (c) Magnitude of the transmission S_{21} of a singly-balanced branch isolator. (d) Phase of the isolation S_{12} of a singly-balanced branch isolator. (c) Phase of the transmission S_{21} of a singly-balanced branch isolator.

This equation describes many interesting scenarios. For instance, $\mathscr{R}$=1 corresponds to a desynchronized gyrator [Eq. (5.18)], $|\Delta\tau|=0$ represents an ideally synchronized isolator [Eq. (5.30)], $|\Delta\tau|=0\,\&\,\mathscr{R}$=1 denotes a perfect gyrator [Eq. (5.8)] and $\mathscr{R}$=0 implies a reciprocal transmission line. The insertion loss exhibits a linear decay $1-2|\Delta\tau|/T_m$ with synchronization issues, and the isolation increases linearly with the relative delay $2|\Delta\tau|/T_m$ when $\mathscr{R}=\mathscr{T}$. To maintain a 3 dB insertion loss and 20 dB isolation, the relative timing error should stay within 5%. Backward

transmission can be made identically zero (i.e., infinite isolation), when the open switch resistance is tuned to the optimal value

$$R_{optimal} = 8Z_0\left(1-4\left|\frac{\Delta\ \tau}{T_m}\right|\right)^{-1}. \tag{5.34}$$

By tuning the resistor to this value, the system ensures ideally infinitely isolation and transmission loss below 3 dB, even with 11% relative timing error, readily achievable in IC implementations. Figure 5.12 shows this trade-off in the case of the double branch isolator in presence of timing errors.

5.3.2 Ultra-broadband isolator

Another way to obtain an isolator is to add a differential dissipative port in parallel to port 1 in a singly-balanced gyrator, which can absorb the energy for backward excitation from port 2 [see Fig. 5.13]. For excitation from port 1, the circuit behaves like a quarter-wavelength transmission line: $V_2^-(t) = V_1^+(t - T_m/4)$. For excitation from port 2, during the first half of the modulation period, the signal passes through switch P_2 and meets an open circuit at port 1. However, switch P_3 is on and port 3 is loaded with a characteristic impedance Z_0. Therefore, the signal is fully absorbed at port 3. For the second half of the modulation period, the signal is transmitted through switches P_4 and P_1, when excited from port 1, and is again fully dissipated at port 3, when excited from port 2. The scattering parameters of this isolator are

$$S(\omega) = \begin{bmatrix} 0 & 0 \\ e^{-j\omega\frac{T_m}{4}} & 0 \end{bmatrix}. \tag{5.35}$$

The operational bandwidth of this isolator is ideally infinite compared with the singly-balanced isolator which operates at a discrete set of frequencies.

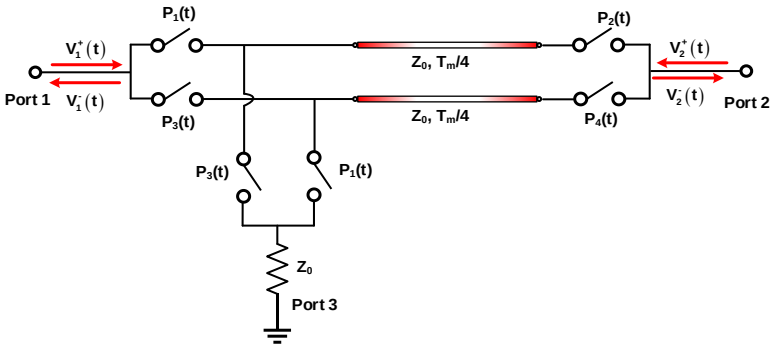

Figure 5.13: Circuit schematic of the ultra-broadband isolator. Modulation signals P1, P2, P3, and P4 are the same as Fig. 1.

Consider now synchronization issues in this isolator. When port 1 is excited by a monochromatic signal $e^{j\omega t}$, most of the signal overlapping with $\eta_1(t)$ in Fig. 5.3(c) passes through the transmission line and reaches port 2. A small tail of the signal, with duration $\Delta\tau$, overlaps with $\eta_2(t)$ in Fig. 3(d) and is reflected to port 3, where it is absorbed. Hence, the transmitted signal is $V_2^-(t) = V_1^+(t - T_m/4)\eta_1(t)$. Since no signal is reflected to the input port, return loss is zero. For excitation from port 2, most of the signal overlaps with $\eta_1(t)$ in Fig. 5.3(c) and is absorbed at port 3, apart from a small tail overlapping with $\eta_2(t)$ in Fig. 5.3(d), which passes through port 1, leading to a transmitted signal $V_1^-(t) = V_2^+(t - T_m/4)\eta_2(t - T_m/4)$. The scattering matrix of the fundamental tone is extracted from Eq. in Appendix B:

$$S(\omega) = \begin{bmatrix} 0 & \dfrac{2|\Delta\tau|}{T_m} e^{-j\omega\frac{T_m}{4}} \\ \left(1 - \dfrac{2|\Delta\tau|}{T_m}\right) e^{-j\omega\frac{T_m}{4}} & 0 \end{bmatrix}. \tag{5.36}$$

The timing error affects only isolation and insertion loss through the term $2|\Delta\tau|/T_m$. Intermodulation products of this isolator with timing error are plot in Fig. 14, showing little influence on the overall spectrum of the transmitted signal for moderate delays.

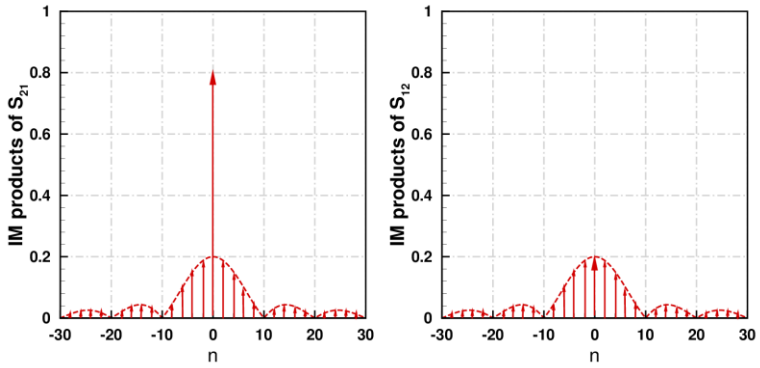

Figure 5.14: IM products of an ultra-broadband isolator with relative timing error $|\Delta\ \tau|/T_m = 0.1$. n stands for the order of harmonics and y axis is the amplitude of each harmonics.

5.4 CIRCULATORS

In this section, we present three circulator designs and investigate their performance in presence of synchronization issues. The first design is a singly-balanced circulator, which is based on an extension of the singly-balanced gyrator described in Section II. The second circulator is a doubly balanced circulator based on differential gyrator. The third circulator is based on the ultra-broadband isolator design discussed in the previous section, where we remove the load Z_0 and add port 3 in its replacement.

5.4.1 Singly-balanced circulator

A circulator is a multiport device that routes the signal with a given handedness from port to port. One approach to obtain a circulator is to embed a gyrator in a transmission-line ring, as in Fig. 5.15, where we have used the balanced gyrator from Sec. II as the basic element to yield nonreciprocity. Isolation at the various ports arises due to destructive interference from the reciprocal and nonreciprocal paths in the loop. At frequency $\omega = (2k+1)\omega_m$, $k = 0, 1, 2, 3\ldots$, the gyrator provides $(2k+1)3\pi/2$ and $(2k+1)\pi/2$ phases in the two opposite directions. If a monochromatic signal $e^{j\omega t}$

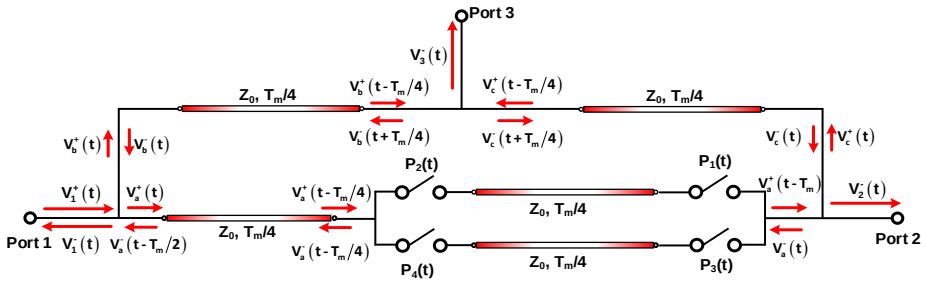

Figure 5.15: Singly-balanced circulator. Modulation signals P1, P2, P3, and P4 are the same as Fig. 1.

enters from port 1, it is split into two signals with identical amplitudes. One takes the path via port 3, and the other goes directly from port 1 to port 2. These signals experience a relative π phase shift and interfere destructively at port 2, leading to full isolation, $S_{21}=0$. On the other hand, at port 3 these signals interfere constructively, leading to a unitary transmission, $S_{31}=-j$. We can analyze the responses of excitation at port 2 and port 3 in a similar way and obtain

$$S\big|_{\omega=(2k+1)\omega_m}=\begin{bmatrix} 0 & -1 & 0 \\ 0 & 0 & j(-1)^{k+1} \\ j(-1)^{k+1} & 0 & 0 \end{bmatrix}. \tag{5.37}$$

A more thorough theoretical analysis is presented in Appendix C, where the responses at all frequencies are derived. This circulator is essentially asymmetric, since the transmission coefficients are not identical: $S_{31}=S_{23}\neq S_{12}$. The directionality of the circulator can be reversed by reversing the nonreciprocal phase response of the gyrator.

In order to validate our analysis, we numerically evaluate the scattering parameters using the composite FSM method. Figures 5.16(a) and 5.16(b) demonstrate amplitudes and phases of scattering parameters at port 1. As we see, the circulator exhibits isolation in S_{21} larger than 40 dB and full transmission at frequency $\omega=\omega_m$ and $\omega=3\omega_m$. The phase discontinuity of S_{21} and the $-\pi/2$ phase shift of S_{31} at

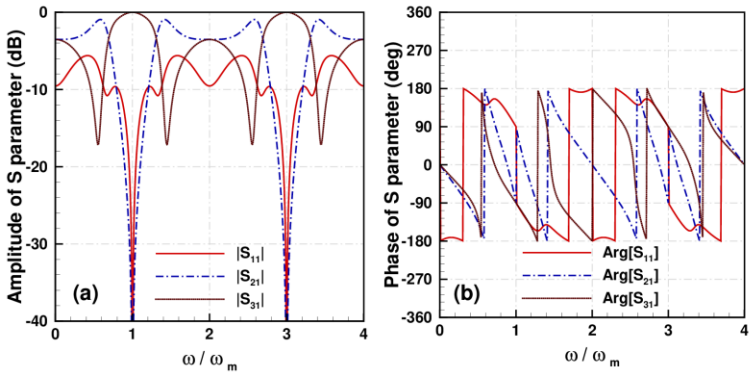

Figure 5.16: S parameter of the singly-balanced circulator. (a) Magnitude of the S parameter at Port 1 of a singly-balanced circulator. (b) Phase of the S parameter at Port 1 of a singly-balanced circulator.

$\omega = \omega_m$ and $\omega = 3\omega_m$ are consistent with theoretical predictions in Eq. (5.37). The scattering matrix accounting for timing errors is

$$S\big|_{\omega=(2k+1)\omega_m} = \begin{bmatrix} 0 & -\left(1-2\dfrac{|\Delta\ \tau|}{T_m}\right) & j(-1)^{k+1}\dfrac{2|\Delta\ \tau|}{T_m} \\ -\dfrac{2|\Delta\ \tau|}{T_m} & 0 & j(-1)^{k+1}\left(1-\dfrac{2|\Delta\ \tau|}{T_m}\right) \\ j(-1)^{k+1}\left(1-\dfrac{2|\Delta\ \tau|}{T_m}\right) & j(-1)^{k+1}\dfrac{2|\Delta\ \tau|}{T_m} & 0 \end{bmatrix}. \quad (5.38)$$

From Eq. (5.38), we see that the insertion loss and isolation deteriorate as the timing error increases. The return loss remains identically zero, unaffected by the presence of synchronization issues. For the insertion loss to be smaller than 3 dB and the isolation larger than 20 dB, the timing error needs to be smaller than 5%. A full picture of the *S*-parameters for excitation from port 1 versus the timing error and input frequency is provided in Fig. 5.17 by using FSM numerical simulations.

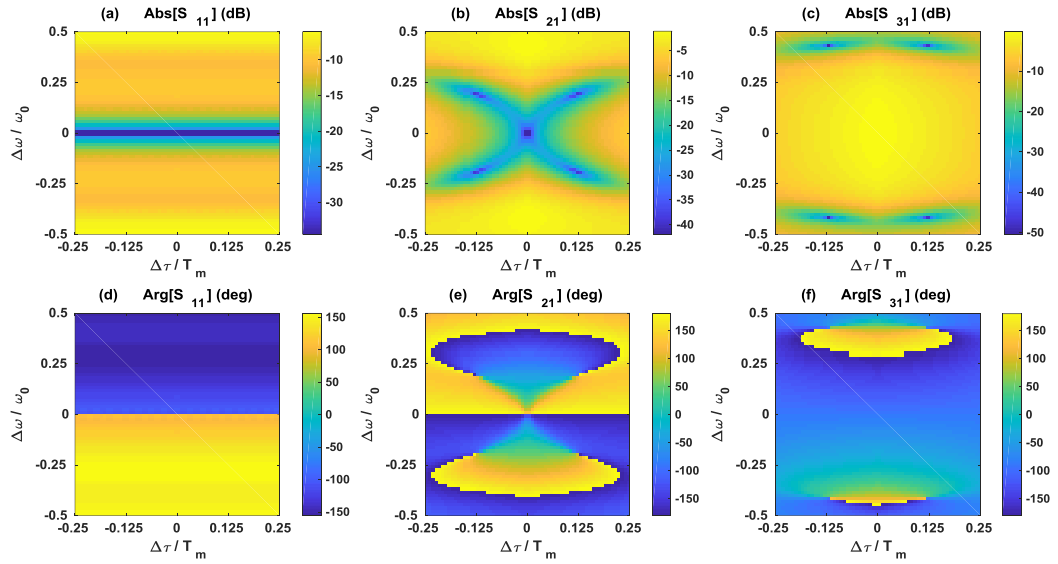

Figure 5.17: S parameter of a singly-balanced circulator with timing error. (a) Magnitude of the return loss S_{11} of a singly-balanced circulator. (b) Magnitude of the isolation S_{21} of a singly-balanced circulator. (c) Magnitude of the transmission S_{31} of a singly-balanced circulator. (d) Phase of the return loss S_{11} of a singly-balanced circulator. (e) Phase of the isolation S_{21} of a singly-balanced circulator. (f) Phase of the transmission S_{31} of a singly-balanced circulator.

5.4.2 Doubly-balanced circulator

The circulator can also be designed leveraging the differential gyrator where the nonreciprocal phase response has an ideally infinite bandwidth. Figure 5.18 demonstrates the design of our doubly-balanced circulator. Due to the similarity between doubly and singly balanced circulator design, the scattering parameters at frequencies $\omega=\left(2k+1\right)\omega_m,\ \ k=0,\ 1,\ 2,\ 3\ldots$ are identical to Eq. (5.37). However, the responses at other frequencies are slightly different from the singly balanced circulator due to different phase response in the gyrator. A detailed and rigorous theoretical analysis is presented in Appendix C. Our results indicate that doubly-balanced circulator offers a

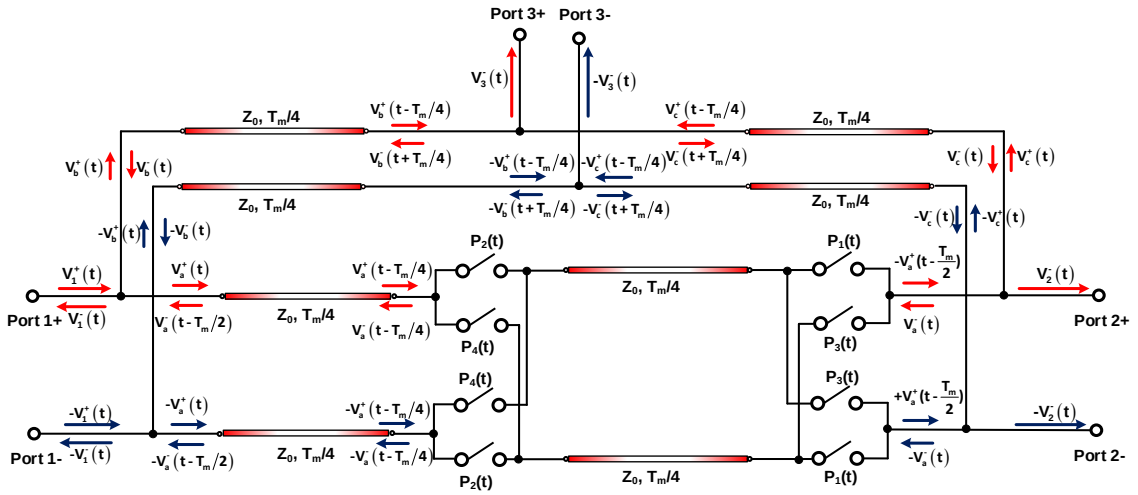

Figure 5.18: Doubly-balanced circulator. Modulation signals P1, P2, P3, and P4 are the same as Fig. 5. 1.

larger bandwidth compared with the singly-balanced circulator. We also confirm our theoretical results using FSM numerical methods and plot the amplitude and phase of scattering parameters in Fig. 5.19 for the case when the port 1 is excited.

As timing error exists in the device, the scattering parameters at the operational frequencies are

$$S\big|_{\omega=(2k+1)\omega_m} = \begin{bmatrix} 0 & -\left(1-2\dfrac{|\Delta\ \tau|}{T_m}\right) & j(-1)^{k+1}\dfrac{2|\Delta\ \tau|}{T_m} \\ -\dfrac{2|\Delta\ \tau|}{T_m} & 0 & j(-1)^{k+1}\left(1-\dfrac{2|\Delta\ \tau|}{T_m}\right) \\ j(-1)^{k+1}\left(1-\dfrac{2|\Delta\ \tau|}{T_m}\right) & j(-1)^{k+1}\dfrac{2|\Delta\ \tau|}{T_m} & 0 \end{bmatrix}, \qquad (5.39)$$

which are identical to the circulator based on singly-balanced gyrator in Eq. (5.38).

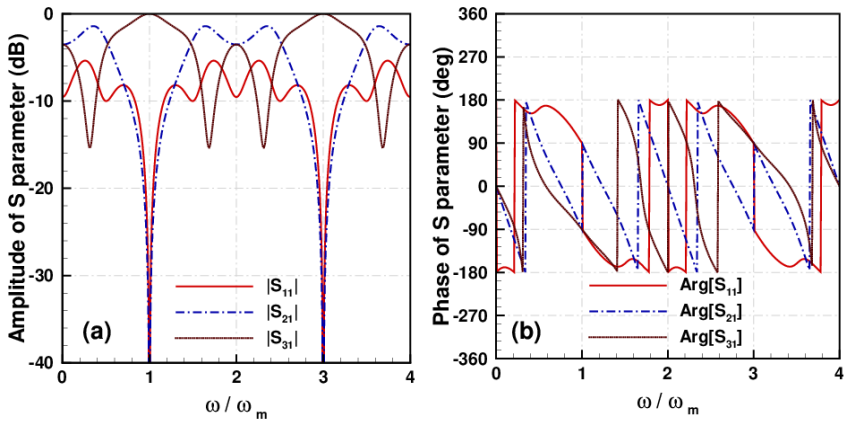

Figure 5.19: S parameter of the doubly-balanced circulator. (a) Magnitude of the S parameter at Port 1 of a singly-balanced circulator. (b) Phase of the S parameter at Port 1 of a singly-balanced circulator.

5.4.2 Ultra-broadband circulator

A circulator can also be obtained by adding a differential port 3 in parallel with port 1 in the ultra-broadband isolator design, as sketched in Fig. 5.20. The time-domain analysis here is quite straightforward. For excitation from port 1, the signal passes through the transmission line with time delay $T_m/4$ and arrives at port 2: $V_2^-(t)=V_1^+(t-T_m/4)$. For excitation from port 2, the signal reaches port 3 with a quarter-period delay: $V_3^-(t)=V_2^+(t-T_m/4)$. For excitation from port 3, the signal passes through the transmission line, reflects at port 2 and arrives at port 1 with a delay $T_m/2$: $V_1^-(t)=V_3^+(t-T_m/2)$. The scattering parameters of this ultra-broadband circulator are

$$S(\omega)=\begin{bmatrix} 0 & 0 & e^{-j\omega\frac{T_m}{2}} \\ e^{-j\omega\frac{T_m}{4}} & 0 & 0 \\ 0 & e^{-j\omega\frac{T_m}{4}} & 0 \end{bmatrix}. \tag{5.40}$$

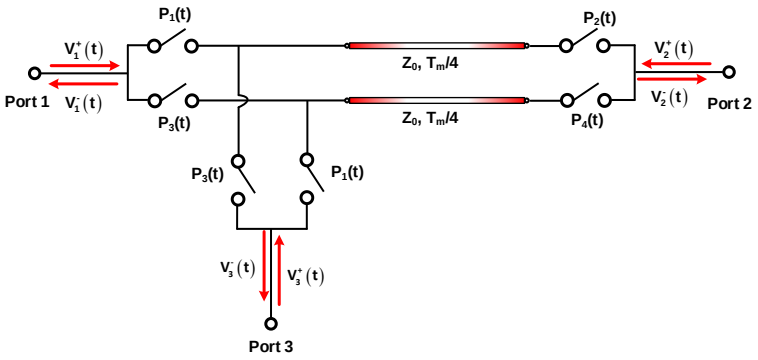

Figure 5.20: Circuit schematic of the ultra-broadband circulator. Modulation signals P1, P2, P3, and P4 are the same as Fig. 5. 1.

Consider now the case of synchronization delays: when excitation is applied to port 1, most of the signal passes through the transmission line and reaches port 2, apart from a small tail that is reflected to port 3 with a delay $T_m/2$. The output signals at ports 2 and 3 are $V_2^-(t)=V_1^+(t-T_m/4)\eta_1(t)$ and $V_3^-(t)=V_1^+(t-T_m/2)\eta_2(t-T_m/4)$, respectively, where $\eta_1(t)$ and $\eta_2(t)$ are the pulse sequences in Figs. 3(c), (d). We performed similar analyses on port 2 and 3 and obtained the following scattering matrix in presence of a timing error:

$$S(\omega)=\begin{bmatrix} 0 & \frac{2|\Delta\ \tau|}{T_m}e^{-j\omega\frac{T_m}{4}} & \left(1-\frac{2|\Delta\ \tau|}{T_m}\right)e^{-j\omega\frac{T_m}{2}} \\ \left(1-\frac{2|\Delta\ \tau|}{T_m}\right)e^{-j\omega\frac{T_m}{4}} & 0 & \frac{2|\Delta\ \tau|}{T_m}e^{-j\omega\frac{T_m}{4}} \\ \frac{2|\Delta\ \tau|}{T_m}e^{-j\omega\frac{T_m}{2}} & \left(1-\frac{2|\Delta\ \tau|}{T_m}\right)e^{-j\omega\frac{T_m}{4}} & 0 \end{bmatrix}. \quad (5.41)$$

It is seen that the timing error has no effect on the return loss also in this case, while it increases the insertion loss and reduces isolation by a factor of $2|\Delta\ \tau|/T_m$. Eq. (5.41) holds for any frequency, in contrast to Eq. (5.38), which holds only at frequencies $\omega=(2k+1)\omega_m$, consistent with the fact that the singly-balanced circulator has a limited

bandwidth, whereas this design offers, in principle infinite bandwidth, only limited by the dispersion of the transmission-lines and finite fall and rise times of the switches.

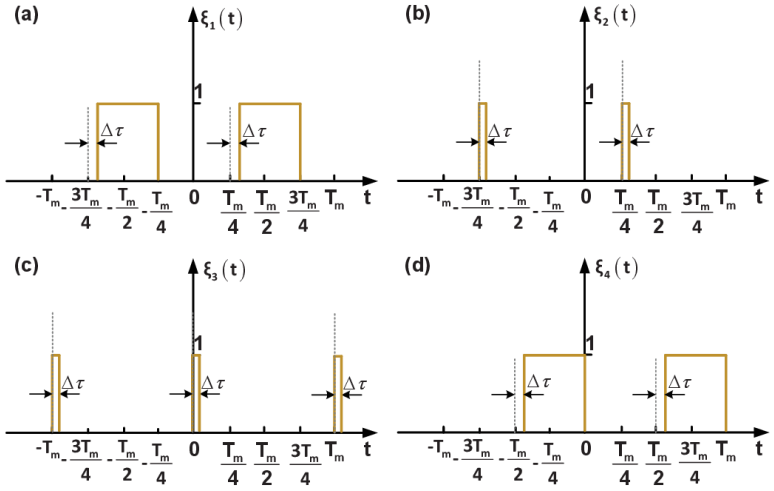

Figure 5.21: Envelope of modulated signals of a single branch isolator with timing error. (a) Forward transmitted signal envelope from excitation at port 1; (b) forward transmitted signal envelope tail from excitation at port 1; (c) backward transmitted signal envelope tail from excitation at port 2; (d) backward transmitted signal envelope from excitation at port 2.

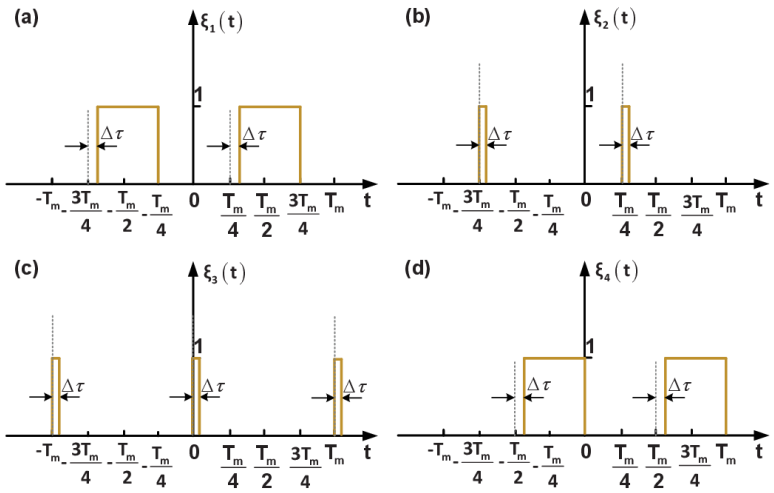

Figure 5.22: Envelope of modulated signals of a single branch isolator with timing error. (a) Forward transmitted signal envelope from excitation at port 1; (b) forward transmitted signal envelope tail from excitation at port 1; (c) backward transmitted signal envelope tail from excitation at port 2; (d) backward transmitted signal envelope from excitation at port 2.

5.5 CONCLUSIONS

In this chapter, we have presented several nonreciprocal devices based on commutated switch networks and analyzed the effects of switch desynchronization on their performance. Our main conclusion is that commutated switch networks provide an excellent platform to realize nonreciprocal devices, such as gyrators, isolators and circulators, with excellent performance metrics. Timing errors in the switching schemes do not affect return loss in all these devices. In turn, insertion loss and isolation degrade linearly with an increase in timing error. In general, there is an upper bound for the timing error for the insertion loss and isolation to remain below certain thresholds, but these limits are readily achievable in conventional integrated circuit layouts. Furthermore, integrated-circuit implementations enable the design of calibration circuitry that corrects for timing errors, and our results provide guidelines for the nature and extent of the errors that should be calibrated. We found that for isolation larger than 20 dB and insertion loss smaller than 3 dB, the timing error should be smaller than 7.3%, 5%, 5% for the gyrator, isolator and circulator, respectively. We have presented opportunities to realize very large (in principle infinite) isolation, circulation and nonreciprocal phase shifts, and in some instances these bandwidths can be preserved even in the presence of timing errors by suitably controlling the switch resistance. In practice, there are more non-idealities that can be investigated in these systems, including dispersion in the delay line sections, finite rise and fall times of the switches, and other desynchronization scenarios. These

phenomena go beyond the scope of this work. Overall, our results show a positive outlook for commutated switching networks for nonreciprocal functionalities, given their direct integrability in a vast family of circuit technologies, and their very small footprint. We envision that similar concepts may be extended also to acoustics and photonics, opening exciting opportunities to broaden the family of efficient magnet-free nonreciprocal devices based on spatial-temporal modulation.

Chapter 6: Wave Scattering in Time-Varying and Quasi-Periodic Coupled Resonator Chain

Recent progress in topological materials and systems has garnered tremendous attention from scientists [173]-[175]. Fractal band structures, like Hofstadter butterfly [176], are of great importance and interest considering its capability of supporting topological edge states [177] and relation with quantized Hall conductance [173]. This intriguing band pattern is conventionally realized by biasing Bloch electrons in a strong magnetic field. As the ratio between the number of states per Landu level eB/h and the number of states per Bloch band $1/a^2$ becomes irrational, self-similar recursive energy spectrum appears [B is the magnetic field, h is the Planck constant, a is the lattice constant]. Experimental realization of the Hofstadter butterfly band pattern generally requires good matching between the magnetic length and the Bloch wavelength, which is unfeasible due to the need of extremely strong magnetic fields [178]-[179]. Therefore, scientists have started to realize it in semiconductor heterostructures and 2D materials without using magnetic fields. Here, we propose an alternative path to realize the Hofstadter butterfly pattern by using a chain of quasi-periodic LC resonators. This approach provides an easily accessible and reconfigurable platform to fractal energy band. We also propose a one-port scattering network to probe the eigenfrequency in a single measurement, which is devoid of tedious onsite measurement on each resonator. At the same time, time modulation provides a very exciting route to realize exotic scattering properties. Finally, we investigated the influence of time modulation on the band structure and scattering properties.

6.1 STATIC QUASI-PERIODIC RESONATOR ARRAY

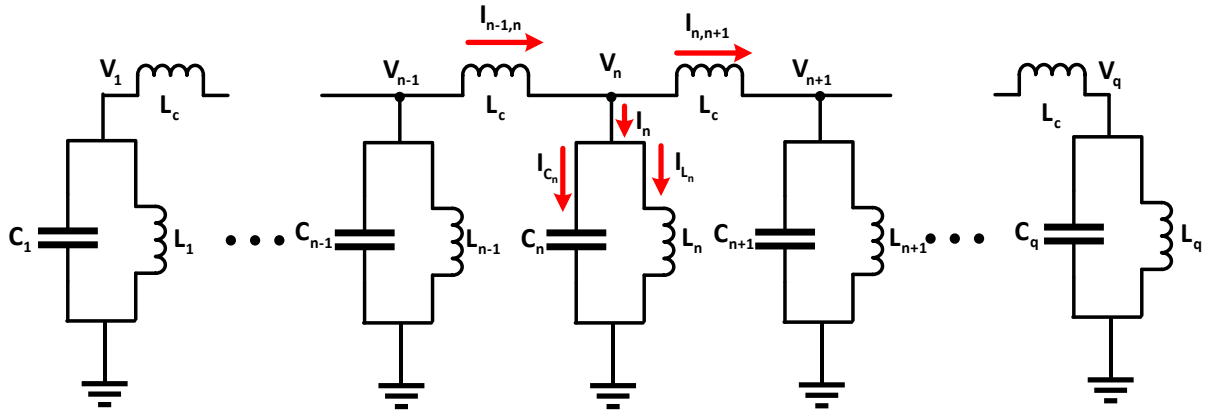

Figure 6.1: The circuit scheme to realize Hofstadter butterfly band diagram. The *n*-th resonator consists of shunt inductor L_n and capacitor C_n. The resonators are mutually coupled through an inductor L_c. The total number of resonators is *q*.

Figure 6.1 demonstrates the circuit model that can show a Hofstadter butterfly band diagram. We write the Kirchhoff's current and voltage law as

$$\begin{cases} I_n = C_n \dfrac{dV_n}{dt} + I_{L_n}, \\ I_{n-1,n} = I_n + I_{n,n+1}, \end{cases}$$
$$\begin{cases} V_n = L_n \dfrac{dI_{L_n}}{dt}, \\ V_{n-1} - V_n = L_c \dfrac{dI_{n-1,n}}{dt}, \\ V_n - V_{n+1} = L_c \dfrac{dI_{n,n+1}}{dt}, \end{cases} \tag{6.1}$$

which can be recast into the following second order differential equation set:

$$\frac{d^2 V_n}{dt^2} = -\left(1 + 2\frac{L_n}{L_c}\right)\frac{1}{L_n C_n} V_n + \frac{L_n}{L_c}\frac{1}{L_n C_n} V_{n-1} + \frac{L_n}{L_c}\frac{1}{L_n C_n} V_{n+1}. \tag{6.2}$$

Since the voltage on the resonator node is not directly related to the total energy stored in the LC resonator, we define two complex variables

$$a_n^{\pm}(t) = \sqrt{\frac{C_n}{2}}\left(V_n \pm i\sqrt{\frac{L_n}{C_n}} I_{L_n} \right), \tag{6.3}$$

where $\left|a_n^{\pm}(t)\right|^2$ stands for the electric and magnetic energy at the *n*-th resonator. We perform a time derivate over the above equation, employ the relation $V_n = L_n \frac{dI_{L_n}}{dt}$ and get the following relation

$$\frac{da_n^{\pm}(t)}{dt} = \sqrt{\frac{C_n}{2}}\left(\frac{dV_n}{dt} \pm i\frac{1}{\sqrt{L_n C_n}} V_n \right). \tag{6.4}$$

Therefore, the voltage on *n*-th resonator can be expressed with the mode amplitude of the resonator:

$$\begin{cases} V_n = -i\sqrt{\frac{L_n}{2}}\left(\frac{da_n^{+}}{dt} - \frac{da_n^{-}}{dt} \right) \\ \frac{dV_n}{dt} = \frac{1}{\sqrt{2C_n}}\left(\frac{da_n^{+}}{dt} + \frac{da_n^{-}}{dt} \right) \end{cases}. \tag{6.5}$$

We substitute the above equation into Eq. (6.2) and have

$$\frac{da_n^{\pm}}{dt} = \pm i\left(1 + 2\frac{L_n}{L_c}\right)\frac{1}{\sqrt{L_n C_n}} a_n^{\pm} \mp i\frac{L_n}{L_c}\frac{1}{\sqrt{L_n C_n}} a_{n-1}^{\pm} \mp i\frac{L_n}{L_c}\frac{1}{\sqrt{L_n C_n}} a_{n+1}^{\pm}. \tag{6.6}$$

Since $a_n^{\pm}$ is a conjugate pair, we only need to solve one of the differential equations:

$$\frac{da_n}{dt} = i\left(1 + 2\frac{L_n}{L_c}\right)\frac{1}{\sqrt{L_n C_n}} a_n - i\frac{L_n}{L_c}\frac{1}{\sqrt{L_n C_n}} a_{n-1} - i\frac{L_n}{L_c}\frac{1}{\sqrt{L_n C_n}} a_{n+1}. \tag{6.7}$$

If we assume that the inductor in each unit is identical $L_1 = L_2 = \cdots L_n = L_0$ and the capacitor is distributed as $C_n = C_0 + \Delta C \sin\left(\frac{2n\pi p}{q}\right)$, we can define the resonant frequency of *n*-th resonator as $\omega_n = \frac{1}{\sqrt{L_n C_n}} \approx \omega_0\left[1 - \frac{\Delta C}{2C_0}\sin\left(\frac{2n\pi p}{q}\right)\right]$ $\left(\text{assuming } \left|\frac{\Delta C}{C_0}\right| << 1\right)$. We also define the mutual coupling coefficient as $\kappa = \frac{L_n}{L_c}$. Then, Eq. (6.7) can be simplified to

$$\frac{da_n}{dt} = i\left(1+2\kappa\right)\omega_n a_n - i\kappa\ \omega_n a_{n-1} - i\kappa\ \omega_n a_{n+1}, \tag{6.8}$$

In the weak coupling regime $\kappa << 1$, $\kappa\ \omega_n = \omega_0\left[\kappa - \kappa \times \frac{\Delta C}{2C_0}\sin\left(\frac{2n\pi p}{q}\right)\right] \approx \omega_0\kappa$, the above equation is approximately

$$\frac{da_n}{dt} \approx i\omega_0\left(1+2\kappa\right)\left[1-\frac{\Delta C}{2C_0}\sin\left(\frac{2n\pi p}{q}\right)\right]a_n - i\kappa\ \omega_0 a_{n-1} - i\kappa\ \omega_0 a_{n+1}, \tag{6.9}$$

which is the Harper equation. We define a variable $\tau = \omega_0 t$ and simplify the above equation to

$$-i\frac{da_n}{d\tau} = \left(1+2\kappa\right)\left[1-\frac{\Delta C}{2C_0}\sin\left(\frac{2n\pi p}{q}\right)\right]a_n - \kappa a_{n-1} - \kappa a_{n+1} \tag{6.10}$$

As a result, we can write the Hamiltonian matrix of this coupled resonator system a

$$H = \begin{bmatrix} \left(1+\kappa\right)\left[1-\frac{\Delta C}{2C_0}\sin\left(\frac{2\pi p}{q}\right)\right] & -\kappa & 0 & \cdots & 0 \\ -\kappa & \left(1+2\kappa\right)\left[1-\frac{\Delta C}{2C_0}\sin\left(\frac{4\pi p}{q}\right)\right] & -\kappa & \cdots & 0 \\ \cdots & \cdots & \cdots & \cdots & 0 \\ \cdots & \cdots & \cdots & \cdots & -\kappa \\ 0 & 0 & 0 & -\kappa & \left(1+\kappa\right)\left[1-\frac{\Delta C}{2C_0}\sin\left(2\pi p\right)\right] \end{bmatrix}$$

(6.11)

The eigenfrequency of this Hamiltonian is shown in Fig. 6.2 for a simple case where the number of resonators is 100.

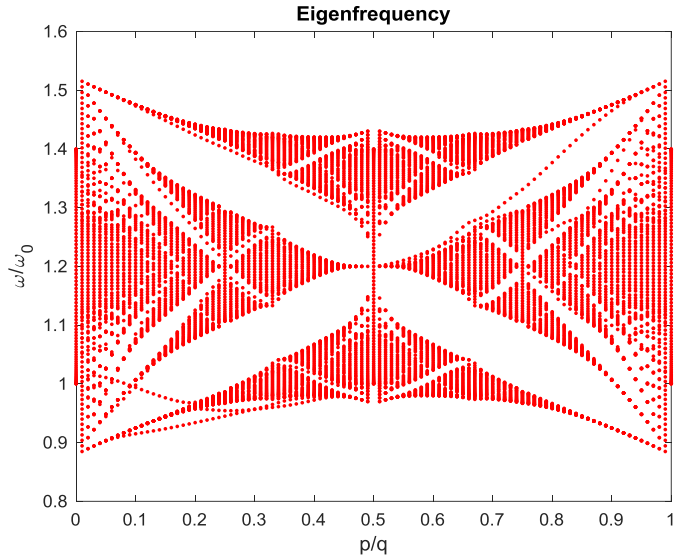

Figure 6.2: Eigenfrequency distribution of the coupled LC resonator system. The number of resonators is 100. The coupling coefficient between the resonator is $\kappa = 0.1$. The variation amplitude of the capacitor is $\frac{\Delta C}{2C_0} = 0.1$.

6.2 ONE-PORT EIGENFREQUENCY MEASUREMENT SETUP

The conventional way to measure the eigenfrequency of this coupled resonator system is to excite the resonators with voltage waves and measure the responses at each resonator. This approach is tedious and time consuming when the number of resonators is large. In this work, we use a one-port scattering network to probe the eigenfrequency of the system, which is shown in Fig. 6.3. We add a probing waveguide or transmission line to the resonator on the end of the resonator chain. The coupled mode equation of this system reads:

$$\begin{cases} \dfrac{\mathrm{d}\mathbf{a}(t)}{\mathrm{dt}} = (-iH - \Gamma)\mathbf{a}(t) + \mathrm{K}^{\mathrm{T}}\mathbf{s}^{+}(t) \\ \mathbf{s}^{-}(t) = C\mathbf{s}^{+}(t) + \mathrm{K}\mathbf{a}(t) \end{cases} \tag{6.12}$$

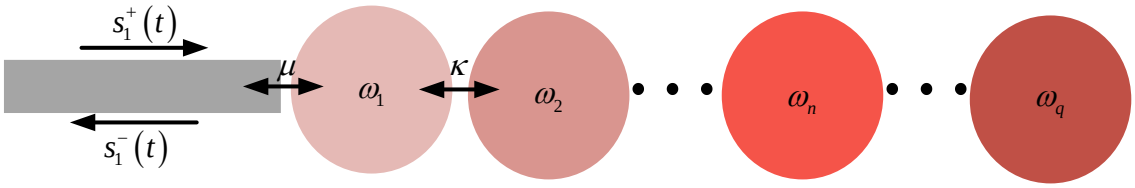

Figure 6.3: One-port network structure to probe the eigenfrequencies of the coupled resonator system where $\omega_n = \omega_0 + \Delta\omega\cos\left(\frac{2n\pi p}{q}\right)$.

where $\mathbf{a}(t) = \left[a_1(t) \quad a_2(t) \quad \cdots \quad a_q(t)\right]^{\mathrm{T}}$ is the field amplitude vector, $H = \begin{bmatrix} \omega_1 & \kappa & 0 & 0 & 0 \\ \kappa & \omega_2 & \kappa & 0 & 0 \\ 0 & \kappa & \omega_3 & \kappa & 0 \\ 0 & 0 & 0 & \ddots & \kappa \\ 0 & 0 & 0 & \kappa & \omega_q \end{bmatrix}$ is the Hamiltonian, $\Gamma = \begin{bmatrix} \gamma & 0 & 0 & 0 & 0 \\ 0 & \ddots & 0 & 0 & 0 \\ 0 & 0 & \ddots & 0 & 0 \\ 0 & 0 & 0 & \ddots & 0 \\ 0 & 0 & 0 & 0 & 0 \end{bmatrix}$ is the decaying matrix, $\mathrm{K} = \begin{bmatrix} \sqrt{2\gamma} & 0 & 0 & 0 & 0 \\ 0 & \ddots & 0 & 0 & 0 \\ 0 & 0 & \ddots & 0 & 0 \\ 0 & 0 & 0 & \ddots & 0 \\ 0 & 0 & 0 & 0 & 0 \end{bmatrix}$ is the coupling matrix, $C = -\mathbf{I}$, $\mathbf{s}^-(t) = \left[s_1^-(t) \quad 0 \quad \cdots \quad 0\right]^{\mathrm{T}}$ is the reflected wave, $\mathbf{s}^+(t) = \left[s_1^+(t) \quad 0 \quad \cdots \quad 0\right]^{\mathrm{T}}$ is the excitation. The coupled mode equation can be simplified a step further:

$$\begin{cases} \dfrac{\mathrm{d}\mathbf{a}(t)}{\mathrm{dt}} = (-iH - \Gamma)\mathbf{a}(t) + \mathrm{K}^{\mathrm{T}}\mathbf{s}^+(t) \\ s_1^-(t) = -s_1^+(t) + \sqrt{2\gamma}a_1(t) \end{cases} \tag{6.13}$$

which indicates that the reflected field only depends on the field in the first cavity.

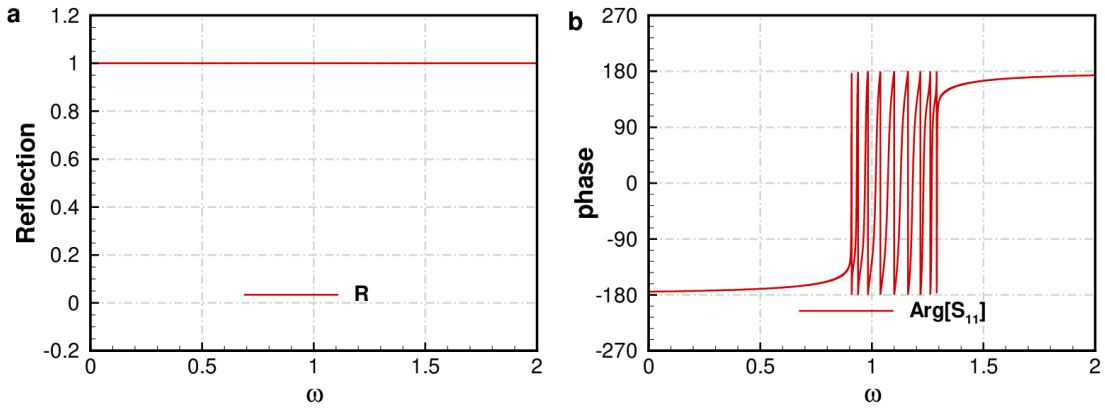

Figure 6.4: The reflection coefficient of 10 resonator array based on coupled mode theory. $\omega_n = \omega_0 + \Delta\omega\cos\left(\frac{2n\pi p}{q}\right)$, $\omega_0 = 1$, $\Delta\omega = 0.1$, $\kappa = 0.1$, $\gamma = 0.05$, $p = 0$, $q = 10$.

We performed a Fourier transform over the above equation and get the field amplitude:

$$\tilde{a}(\omega) = \frac{i\sqrt{2\gamma}\,\mathrm{Det}[M]\,s_1^+(\omega)}{\mathrm{Det}[\omega\mathbf{I} - H(t) + i\Gamma]}, \tag{6.14}$$

where $M = \begin{bmatrix} \omega-\omega_2 & \kappa & 0 & 0 \\ \kappa & \omega-\omega_3 & \kappa & 0 \\ 0 & 0 & \ddots & \kappa \\ 0 & 0 & \kappa & \omega-\omega_q \end{bmatrix}$, which is a $(q-1)\times(q-1)$ matrix.

Therefore, the reflection coefficient is

$$S_{11}(\omega) = \frac{s_1^-(\omega)}{s_1^+(\omega)} = \frac{-\mathrm{Det}[\omega\mathbf{I} - H] + i\gamma\,\mathrm{Det}[M]}{\mathrm{Det}[\omega\mathbf{I} - H] + i\gamma\,\mathrm{Det}[M]}. \tag{6.15}$$

Since $\mathrm{Det}[\omega\mathbf{I} - H]$ and $\mathrm{Det}[M]$ are real, we have $|S_{11}(\omega)| = 1$. If the frequency of the excitation wave is the eigenfrequency, we have $\mathrm{Det}[\omega\mathbf{I} - H] = 0$. This assumption leads to $S_{11}(\omega) = 1$, meaning that the zero-phase point of $S_{11}(\omega)$ corresponds to the eigenfrequency of the system. The simulation results are shown in Fig.

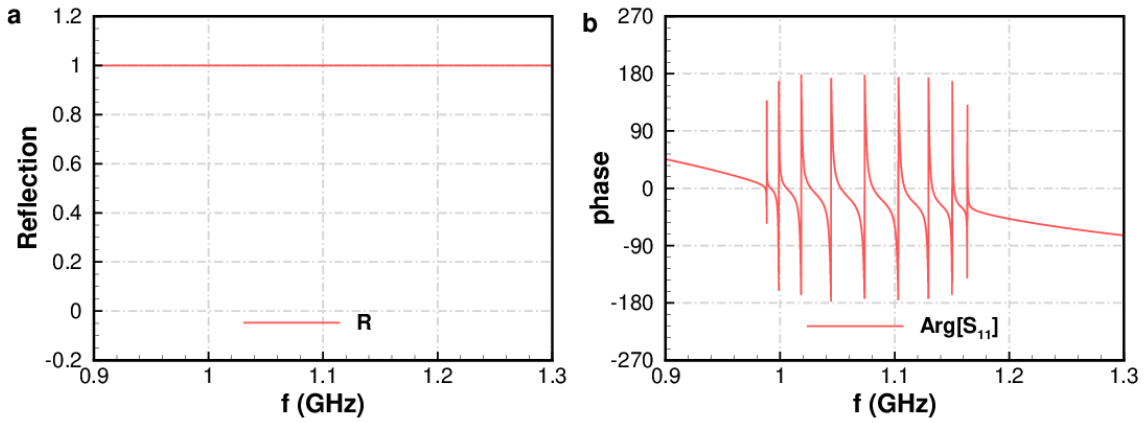

Figure 6.5: The reflection coefficient of 10 coupled LC resonator array in ADS software. $C_n = C_0 + \Delta C \cos\left(\frac{2n\pi p}{q}\right)$ $C_0 = 5pF$, $\Delta C = 0.2pF$ $L_0 = 5nH$ $L_p = 50nH$ $p = 0$ $q = 10$ where L_p is the coupling inductance and L_0 is the inductance in the resonator.

6.5. To further verify our approach, we run circuit simulation with ADS software, which is shown in Fig. 6.5. The phase in Fig. 6.5 is flipped compared with Fig. 6.4 because "*j*" is defined as the imaginary unit in ADS software.

6.3 TIME-MODULATED QUASIPERIODIC RESONATOR ARRAY

Time modulation is a very interesting route to realize novel scattering parameters. The coupled mode equation of the above system reads

$$\begin{cases} \dfrac{\mathrm{d}\mathbf{a}(t)}{\mathrm{d}t} = \left(-iH(t) - \Gamma\right)\mathbf{a}(t) + \mathrm{K}^{\mathrm{T}}\mathbf{s}^{+}(t), \\ \mathbf{s}^{-}(t) = C\mathbf{s}^{+}(t) + \mathrm{K}\mathbf{a}(t), \end{cases} \tag{6.16}$$

where $\mathbf{a}(t)=\left[a_1(t)\ \ a_2(t)\ \ \cdots\ \ a_q(t)\right]^{\mathrm{T}}$ is the field amplitude vector, $H=\begin{bmatrix}\omega_1(t) & \kappa & 0 & 0 & 0\\ \kappa & \omega_2(t) & \kappa & 0 & 0\\ 0 & \kappa & \omega_3(t) & \kappa & 0\\ 0 & 0 & 0 & \ddots & \kappa\\ 0 & 0 & 0 & \kappa & \omega_q(t)\end{bmatrix}$ is the time-varying Hamiltonian, $\Gamma=\begin{bmatrix}\gamma & 0 & 0 & 0 & 0\\ 0 & \ddots & 0 & 0 & 0\\ 0 & 0 & \ddots & 0 & 0\\ 0 & 0 & 0 & \ddots & 0\\ 0 & 0 & 0 & 0 & 0\end{bmatrix}$ is the decaying matrix, $\mathrm{K}=\begin{bmatrix}\sqrt{2\gamma} & 0 & 0 & 0 & 0\\ 0 & \ddots & 0 & 0 & 0\\ 0 & 0 & \ddots & 0 & 0\\ 0 & 0 & 0 & \ddots & 0\\ 0 & 0 & 0 & 0 & 0\end{bmatrix}$ is the coupling matrix, $C=-\mathbf{I}$, $\mathbf{s}^{-}(t)=\left[s_1^{-}(t)\ \ 0\ \ \cdots\ \ 0\right]^{\mathrm{T}}$ is the reflected wave, $\mathbf{s}^{+}(t)=\left[s_1^{+}(t)\ \ 0\ \ \cdots\ \ 0\right]^{\mathrm{T}}$ is the excitation. The coupled mode equation can be simplified a step further:

$$\begin{cases}\dfrac{\mathrm{d}\mathbf{a}(t)}{\mathrm{dt}}=\left(-iH(t)-\Gamma\right)\mathbf{a}(t)+\mathrm{K}^{\mathrm{T}}\mathbf{s}^{+}(t),\\ s_1^{-}(t)=-s_1^{+}(t)+\sqrt{2\gamma}a_1(t),\end{cases}\tag{6.17}$$

which indicates that the reflected field only depends on the field in the first cavity. The solution of the field amplitude is easily obtained by employing the theory of differential equation:

$$\mathbf{a}(t)=e^{-\int iH(t)+\Gamma\mathrm{dt}}\int\mathrm{K}^{\mathrm{T}}\mathbf{s}^{+}(t)e^{\int iH(t)+\Gamma\mathrm{dt}}\mathrm{dt}.\tag{6.18}$$

The solution is extremely complicated and only numerical solution is possible. However, in the low-frequency limit, we can solve Eq. (6.18) analytically.

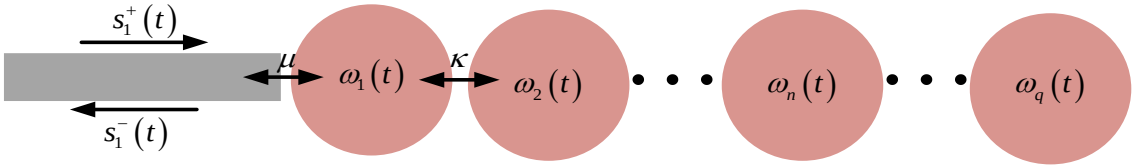

Figure 6.6: Schematic of periodically modulated resonator array. The resonant frequency is $\omega_n(t)=\omega_0+\Delta\omega\cos\left(\frac{2n\pi p}{q}+\omega_m t\right)$, where ω_0 is the static resonant frequency, $\Delta\omega$ is the modulation depth, ω_m is the modulation frequency, q is the total number of resonator, the coupling coefficient between resonator is κ, the coupling coefficient between the first resonator and the waveguide is μ.

Assume that the field amplitude can be expressed as $\mathbf{a}(t)=\mathbf{A}(t)e^{-i\omega t}$, the first order derivative can be expressed as $\frac{\mathrm{d}\mathbf{a}(t)}{\mathrm{dt}}=\frac{\mathrm{d}\mathbf{A}(t)}{\mathrm{dt}}e^{-i\omega t}-i\omega\mathbf{A}(t)e^{-i\omega t}\approx-i\omega\mathbf{A}(t)e^{-i\omega t}$ when the modulation frequency is very small. Meanwhile, assume that the excitation is $\mathbf{s}^+(t)=\mathbf{S}^+e^{-i\omega t}$. Eq. (6.18) can be simplified to

$$\mathbf{A}(t)=\left[iH(t)-i\omega+\Gamma\right]^{-1}\mathrm{K}^{\mathrm{T}}\mathbf{S}^+ \tag{6.19}$$

We substitute the excitation vector $\mathbf{S}^+$ and the coupling matrix K into the above equation

$$\mathbf{A}(t)=i\left[\omega\mathbf{I}-H(t)+i\Gamma\right]^{-1}\begin{bmatrix}\sqrt{2\gamma}S_1^+\\0\\0\\\vdots\\0\end{bmatrix}, \tag{6.20}$$

where $\mathbf{I}$ is a unitary matrix having the same dimension with the Hamiltonian matrix $H(t)$. According to Cramer's rule, the solution of the field envelope in the first resonator is

$$A_1(t)=\frac{\mathrm{Det}\left[M\right]i\sqrt{2\gamma}S_1^+}{\mathrm{Det}\left[\omega\mathbf{I}-H(t)+i\Gamma\right]}, \tag{6.21}$$

where $M=\begin{bmatrix} \omega-\omega_2(t) & \kappa & 0 & 0 \\ \kappa & \omega-\omega_3(t) & \kappa & 0 \\ 0 & 0 & \ddots & \kappa \\ 0 & 0 & \kappa & \omega-\omega_q(t) \end{bmatrix}$, which is a $(q-1)\times(q-1)$ matrix. Therefore, the time-domain reflection coefficient is

$$S_{11}(t)=\frac{-\mathrm{Det}\left[\omega\mathbf{I}-H(t)\right]+i\gamma\mathrm{Det}\left[M\right]}{\mathrm{Det}\left[\omega\mathbf{I}-H(t)\right]+i\gamma\mathrm{Det}\left[M\right]} \tag{6.22}$$

There are a few important results stemming from the above equation:

1. The excitation is fully reflected, because $\mathrm{Det}\left[\omega\mathbf{I}-H(t)\right]$ and $\mathrm{Det}\left[M\right]$ are real, leading to unitary reflection $\left|S_{11}(t)\right|=1$. This is reasonable, considering there is no loss in the resonator array.
2. For static resonator array, there is no frequency mixing. The frequency domain reflection coefficient is $S_{11}(\omega)=\frac{-\mathrm{Det}\left[\omega\mathbf{I}-H\right]+i\gamma\mathrm{Det}\left[M\right]}{\mathrm{Det}\left[\omega\mathbf{I}-H\right]+i\gamma\mathrm{Det}\left[M\right]}$. We have $\left|S_{11}(\omega)\right|=1$. If the frequency of the excitation wave is the eigenfrequency, we have $\mathrm{Det}\left[\omega\mathbf{I}-H\right]=0$. This assumption leads to $S_{11}(\omega)=1$, meaning that the zero-phase point of $S_{11}(\omega)$ corresponds to the eigenfrequency of the system.
3. For a dynamic resonator array, it's possible to find the reflection coefficient of the fundamental tone

$$S_{11}^{(0)}(\omega)=\frac{1}{T_m}\int_0^{T_m}\frac{-\mathrm{Det}\left[\omega\mathbf{I}-H(t)\right]+i\gamma\mathrm{Det}\left[M\right]}{\mathrm{Det}\left[\omega\mathbf{I}-H(t)\right]+i\gamma\mathrm{Det}\left[M\right]}\mathrm{d}t, \tag{6.23}$$

where $T_m=\frac{2\pi}{\omega_m}$ is the modulation period. Figure 6.7 demonstrates the scattering properties of this one-port time-varying network.

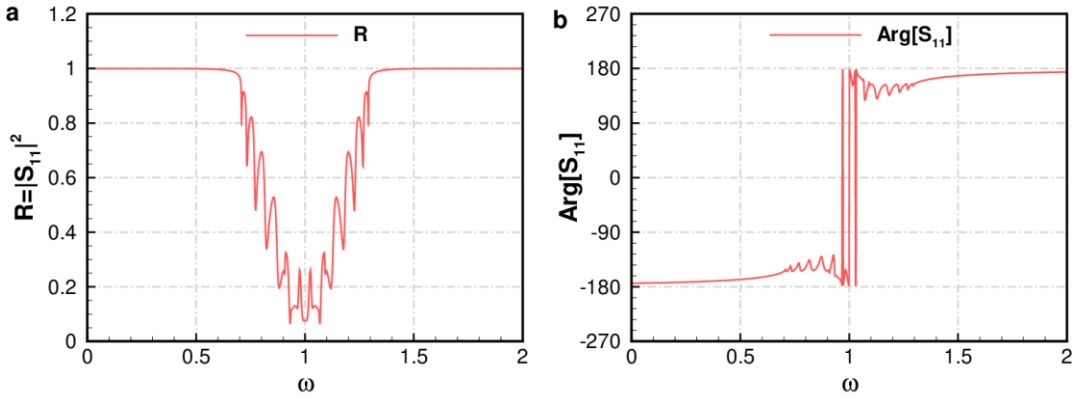

Figure 6.7: Scattering parameter of the fundamental tone in a time-varying coupled resonator chain. There are 10 coupled dynamic resonators with resonant frequency $\omega_n = \omega_0 + \Delta\omega\cos\left(\frac{2n\pi p}{q} + \omega_m t\right)$, $\omega_0 = 1$, $\Delta\omega = 0.1$, $\omega_m = \pi/50$, $\kappa = 0.1$, $\gamma = 0.05$, $p = 0$, $q = 10$.

Chapter 7: Summary

In conclusion, during my PhD I have investigated a series of wave transport phenomena in parity-time-symmetric, time-varying, and quasi-periodic systems. In the second chapter, I have put forward a sensing circuit based on a sixth-order EP, showing an enhanced resonant shift proportional to the fourth-order root of the perturbation strength. Due to the balanced loss and gain configuration and our perturbation scheme, the resolution is also improved. Our PT -symmetric system not only serves as a sensing platform, but also filters out high-frequency thermal noise, leading to a nearly identical thermal noise level compared to the corresponding Hermitian DP sensing scheme. Considering the combined high-sensitivity, improved resolution, and nondegraded thermal noise performance, we envision that accelerometers, pressure sensors, or microfluid flow speed sensors may be implemented following this scheme with unprecedented sensitivity, resolution, and excellent thermal noise performance.

In chapter 3, I have developed a unified theoretical framework to help analyze the sensitivity, resolution, and thermal noise performance of two-level EP and DP sensing protocols. Our study indicates that although Green's function of EP sensing system shows a combination of square Lorentzian and Lorentzian noise spectra at EP compared with conventional DP sensing system, the integrated thermal noise is still manageable if proper ratio of internal and external decaying rate is chosen. These arguments are confirmed with a judiciously designed 2^{nd} order EP sensing circuit and unveil a bright future for EP sensing applications in many other fields, including optomechanical, acoustic, and open quantum systems.

In Chapter 4, I have demonstrated microwave tunneling and information transfer through a PT-symmetric absorber-emitter pair. Our study represents a landmark towards realistic implementation of information transfer systems with extreme robustness, able to

tunnel the input signal through otherwise impenetrable obstacles with large robustness, and it shows promises to spawn a series of applications. For instance, our loss-neutral-gain arrangement exhibits a third-order exceptional point in the bound state. By properly designing the system at this higher order exceptional point, the eigenfrequency splitting of the corresponding Hamiltonian matrix shows an enhanced high sensitivity proportional to the cubic root of the perturbation strength on the system, which is very favorable to design ultrasensitive microsensors. Meanwhile, this prototype can be used as a bandpass active filter which allows for simultaneous narrow-band signal filtering and amplification. Furthermore, our design provides relevant insights into realization of active cloaking devices and active metasurfaces which exhibit unique properties not available in passive counterparts. In summary, the design strategies and stability analysis in this work pave the way towards future realizations of PT-symmetric functionalities in optics and microwave regimes. Considering the extensive connections between electromagnetic, mechanic, and matter waves, our study can also spur practical applications of PT-symmetry in these other fields of research.

In Chapter 5, I have presented several nonreciprocal devices based on commutated switch networks and analyzed the effects of switch desynchronization on their performance. Our main conclusion is that commutated switch networks provide an excellent platform to realize nonreciprocal devices, such as gyrators, isolators and circulators, with excellent performance metrics. Timing errors in the switching schemes do not affect return loss in all these devices. In turn, insertion loss and isolation degrade linearly with an increase in timing error. In general, there is an upper bound for the timing error for the insertion loss and isolation to remain below certain thresholds, but these limits are readily achievable in conventional integrated circuit layouts. Furthermore, integrated-circuit implementations enable the design of calibration circuitry that corrects

for timing errors, and our results provide guidelines for the nature and extent of the errors that should be calibrated. We found that for isolation larger than 20 dB and insertion loss smaller than 3 dB, the timing error should be smaller than 7.3%, 5%, 5% for the gyrator, isolator and circulator, respectively. We have presented opportunities to realize very large (in principle infinite) isolation, circulation and nonreciprocal phase shifts, and in some instances these bandwidths can be preserved even in the presence of timing errors by suitably controlling the switch resistance. In practice, there are more non-idealities that can be investigated in these systems, including dispersion in the delay line sections, finite rise and fall times of the switches, and other desynchronization scenarios. These phenomena go beyond the scope of this work. Overall, our results show a positive outlook for commutated switching networks for nonreciprocal functionalities, given their direct integrability in a vast family of circuit technologies, and their very small footprint. We envision that similar concepts may be extended also to acoustics and photonics, opening exciting opportunities to broaden the family of efficient magnet-free nonreciprocal devices based on spatial-temporal modulation.

In chapter 6, I have studied the band structure of a quasi-periodic LC resonator array. A one-port reflective sensing network is proposed to measure the eigenfrequency of the system without the need of tedious measurement on each resonator.

Appendix A

In this appendix, EP sensing circuit schematic with ADS is presented. We also present other sensing protocols based on perturbation over the capacitor and inductor in the lossy resonator, which are different from the one we adopted in Chapter 2. Our theoretical derivations and ADS simulations indicate that the resolution of the first scheme is $\varepsilon \approx 0.8$, where ε is the perturbation strength; while the second scheme is completely useless due to the large linewidth broadening.

1. EP SENSING CIRCUIT SCHEMATIC

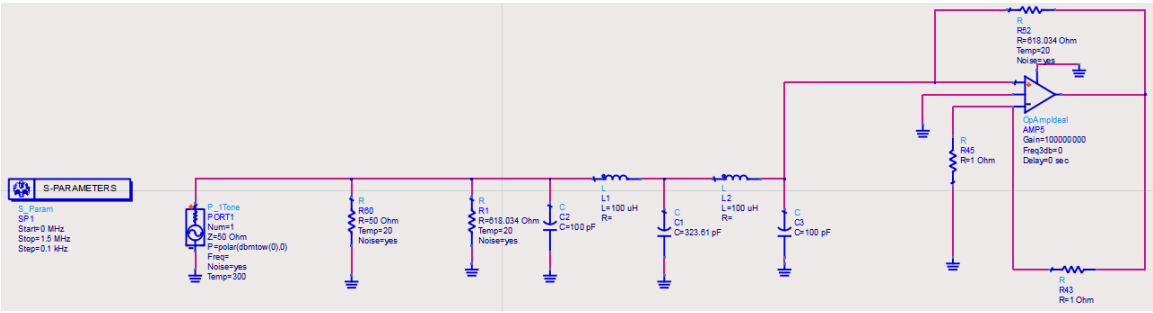

Figure A.1: EP sensing circuit schematic. A port with 50Ω characteristic impedance is connected to the lossy side of the PT-symmetric circuit. S-PARAMETERS simulator is used to simulate the scattering parameters. The port is excited with a monochromatic wave sweeping from 0 MHz to 1.5 MHz with step size 0.1 kHz.

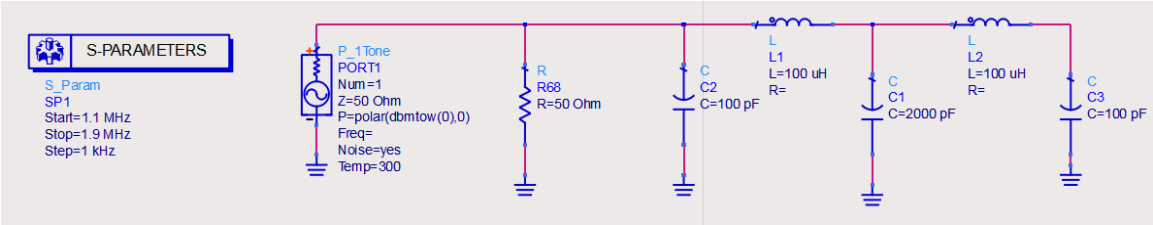

Figure A.2: DP sensing circuit schematic. A port with 50Ω characteristic impedance is connected to the left side of the coupled resonator. S-PARAMETERS simulator is used to simulate the scattering parameters. The port is excited with a monochromatic wave sweeping from 1.1 MHz to 1.9 MHz with step size 1 kHz.

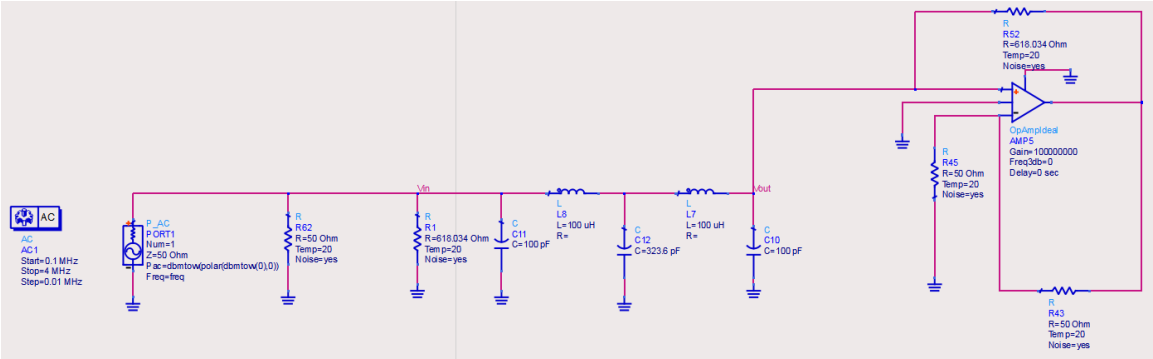

Figure A.3: Noise simulation of EP sensing circuit. A port with 50Ω characteristic impedance is connected to the lossy side of the PT-symmetric circuit. AC simulator is used to simulate the noise voltages at various nodes of the circuit. The port is excited with a monochromatic wave sweeping from 0.1 MHz to 4 MHz with step size 0.01 MHz.

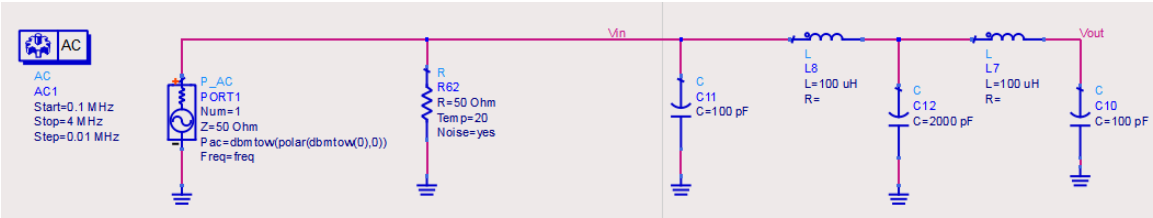

Figure A.4: Noise simulation of DP sensing circuit. A port with 50Ω characteristic impedance is connected to the left side of the coupled resonator. AC simulator is used to simulate the noise voltages at various nodes of the circuit. The port is excited with a monochromatic wave sweeping from 0.1 MHz to 4 MHz with step size 0.01 MHz.

2. SENSING PROTOCOL BASED ON PERTURBATION OVER THE CAPACITOR IN THE LOSSY RESONATOR

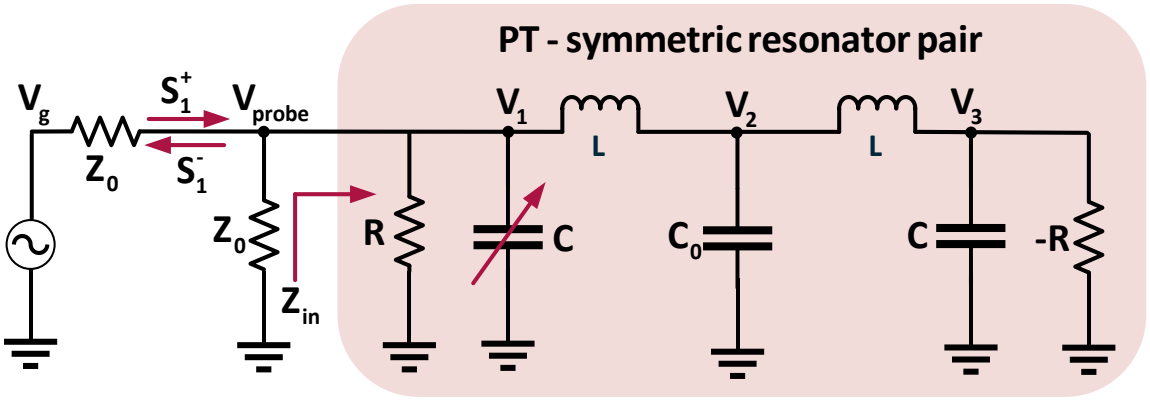

Figure A.5: Sensing circuit design based on perturbation over the capacitor in the lossy resonator.

Figure A.5 demonstrates an interesting sensing protocol where the capacitor in the lossy resonator is perturbed around the sixth-order exceptional point. Therefore, the capacitance value in the lossy resonator can be expressed as: $C(\varepsilon)=C(1+\varepsilon)$, where ε is the perturbation strength. According to Kirchhoff's current and voltage laws, we express the voltages at various nodes in the isolated PT-symmetric system as follows:

$$\begin{cases} (1+\varepsilon)\dfrac{\mathrm{d}^2V_1}{\mathrm{d}\,\tau^2}+\gamma\dfrac{\mathrm{d}V_1}{\mathrm{d}\,\tau}+V_1-V_2=0, \\ \dfrac{\mathrm{d}^2V_2}{\mathrm{d}\,\tau^2}+2\mu V_2-\mu V_1-\mu V_3=0, \\ \dfrac{\mathrm{d}^2V_3}{\mathrm{d}\,\tau^2}-\gamma\dfrac{\mathrm{d}V_3}{\mathrm{d}\,\tau}-V_2+V_3=0, \end{cases} \tag{7.1}$$

where $\tau=\omega_0 t$ is the normalized time, $\omega_0=\dfrac{1}{\sqrt{LC}}$ is the resonant frequency of the resonator, $\gamma=\dfrac{1}{R}\sqrt{\dfrac{L}{C}}$ is the gain/loss parameter, $\mu=\dfrac{C}{C_0}$ is the coupling coefficient

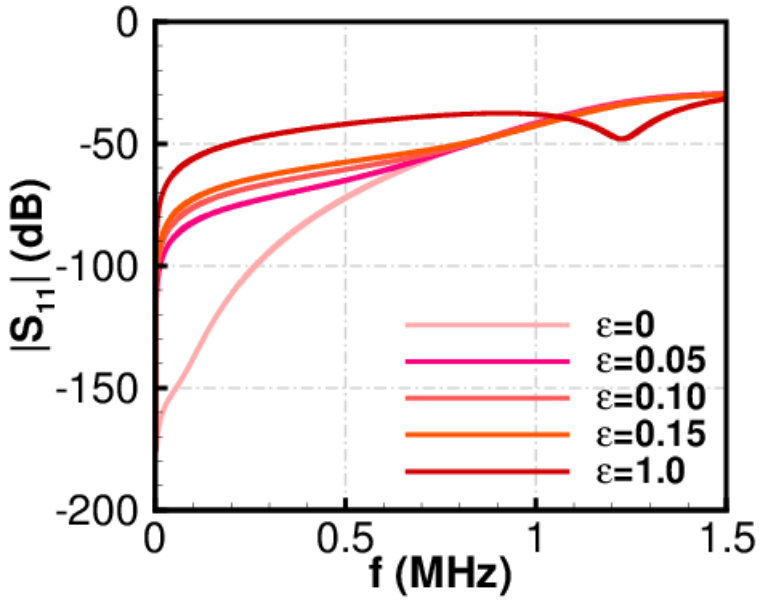

Figure A.6: Amplitude of the reflection coefficient with different perturbation strengths. When the perturbation is weak, the resonant dip is invisible. When the perturbation ε is 1, we can see a resonant dip. The circuit components are identical to the Fig.2 in the associated paper.

between the two resonators. The effective Hamiltonian of the PT-symmetric system can be expressed as:

$$H_{eff} = \begin{bmatrix} 0 & 0 & 0 & i & 0 & 0 \\ 0 & 0 & 0 & 0 & i & 0 \\ 0 & 0 & 0 & 0 & 0 & i \\ \dfrac{-i}{1+\varepsilon} & \dfrac{i}{1+\varepsilon} & 0 & \dfrac{-i\gamma}{1+\varepsilon} & 0 & 0 \\ i\mu & -2i\mu & i\mu & 0 & 0 & 0 \\ 0 & i & -i & 0 & 0 & i\gamma \end{bmatrix}. \quad (7.2)$$

We substitute the conditions （$\mu = \dfrac{\sqrt{5}-1}{4}, \gamma = \dfrac{\sqrt{5}+1}{2}$）for sixth-order EP into the above equation and find the associated characteristic equation of the Hamiltonian:

$$\omega^2\left[4(1+\varepsilon)\omega^4 - 2i\left(1+\sqrt{5}\right)\varepsilon\ \omega^3 - 2\left(1+\sqrt{5}\right)\varepsilon\ \omega^2 + 4i\varepsilon\ \omega + \left(\sqrt{5}-1\right)\varepsilon\right] = 0. \quad (7.3)$$

The full expressions of the eigenfrequencies are extremely lengthy. Here, we just list a series expansion of the solutions:

$$\begin{cases} \omega_{1,2}(\varepsilon) = 0.5272(1 \pm i)\varepsilon^{\frac{1}{4}} + \mathrm{O}\left(\varepsilon^{\frac{1}{2}}\right) + \cdots, \\ \omega_{3,4}(\varepsilon) = 0.5272(-1 \pm i)\varepsilon^{\frac{1}{4}} + \mathrm{O}\left(\varepsilon^{\frac{1}{2}}\right) + \cdots, \\ \omega_{5,6}(\varepsilon) = 0, \end{cases} \tag{7.4}$$

where "O" stands for higher-order term. The above eigenfrequencies are complex and therefore can potentially mask the hypersensitive resonant shift in our sensing circuit. We confirm our claim by running ADS simulations. Figure A.6 clearly shows that the sensing system cannot resolve small perturbation. Our numerical study proves that the resolution limit is $\varepsilon \approx 0.8$.

3. SENSING PROTOCOL BASED ON PERTURBATION OVER THE INDUCTOR IN THE LOSSY RESONATOR

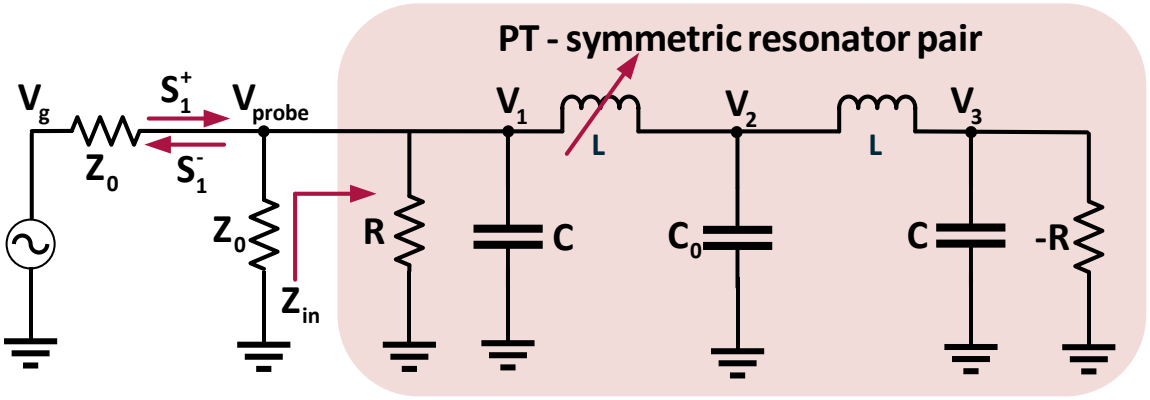

Figure A.7: Sensing circuit design based on perturbation over the inductor in the lossy resonator.

The above circuit demonstrates another sensing protocol where the inductor in the lossy resonator is perturbed around the sixth-order exceptional point. Therefore, the inductance value in the lossy resonator can be expressed as: $L(\varepsilon)=L(1+\varepsilon)$, where ε is the perturbation strength. According to Kirchhoff's current and voltage laws, we express the voltages at various nodes in the isolated PT-symmetric system as follows:

$$\begin{cases} (1+\varepsilon)\dfrac{\mathrm{d}^2V_1}{\mathrm{d}\,\tau^2}+\gamma(1+\varepsilon)\dfrac{\mathrm{d}V_1}{\mathrm{d}\,\tau}+V_1-V_2=0, \\ \dfrac{\mathrm{d}^2V_2}{\mathrm{d}\,\tau^2}+2\mu V_2-\mu V_1-\mu V_3=0, \\ \dfrac{\mathrm{d}^2V_3}{\mathrm{d}\,\tau^2}-\gamma\dfrac{\mathrm{d}V_3}{\mathrm{d}\,\tau}-V_2+V_3=0, \end{cases} \tag{7.5}$$

where $\tau=\omega_0 t$ is the normalized time, $\omega_0=\dfrac{1}{\sqrt{LC}}$ is the resonant frequency of the resonator, $\gamma=\dfrac{1}{R}\sqrt{\dfrac{L}{C}}$ is the gain/loss parameter, $\mu=\dfrac{C}{C_0}$ is the coupling coefficient between the two resonators. The effective Hamiltonian of the sensing system can be expressed as:

$$H_{eff}=\begin{bmatrix} 0 & 0 & 0 & i & 0 & 0 \\ 0 & 0 & 0 & 0 & i & 0 \\ 0 & 0 & 0 & 0 & 0 & i \\ \dfrac{-i}{1+\varepsilon} & \dfrac{i}{1+\varepsilon} & 0 & -i\gamma & 0 & 0 \\ i\mu & -2i\mu & i\mu & 0 & 0 & 0 \\ 0 & i & -i & 0 & 0 & i\gamma \end{bmatrix}. \tag{7.6}$$

We substitute the conditions ($\mu=\dfrac{\sqrt{5}-1}{4}, \gamma=\dfrac{\sqrt{5}+1}{2}$) for sixth-order EP into the above equation and find the associated characteristic equation of the Hamiltonian:

$$\omega\left[4(1+\varepsilon)\omega^5+4\varepsilon\,\omega^3-2i\left(1+\sqrt{5}\right)\varepsilon\,\omega^2-\left(3+\sqrt{5}\right)\varepsilon\,\omega+2i\varepsilon\right]=0, \tag{7.7}$$

which has no analytical solutions. Numerical calculations indicate that the eigenfrequencies take the following form:

$$\begin{cases} \omega_{1,2}(\varepsilon) = \pm a + ib, \\ \omega_{3,4}(\varepsilon) = \pm c + id, \\ \omega_{5}(\varepsilon) = if, \\ \omega_{6}(\varepsilon) = 0, \end{cases} \tag{7.8}$$

where *a*, *b*, *c*, *d*, *f* are real parameters determined by the perturbation strength ε. The above eigenfrequencies ($\omega_{1,2}$ and $\omega_{3,4}$) are complex and therefore can potentially mask the hypersensitive resonant shift in our sensing circuit. We confirm our claim by running ADS simulations. Figure A.8 clearly shows that the sensing based on this protocol is completely useless.

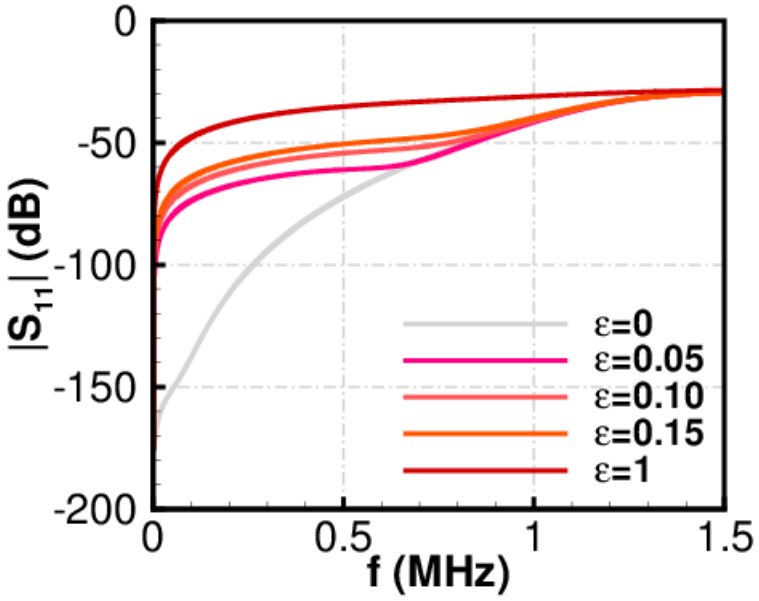

Figure A.8: Amplitude of the reflection coefficient with different perturbation strengths. The resonant dips are invisible for any perturbation strengths. The circuit components are identical to the Fig. 2.2.

Appendix B

1. SCATTERING PROPERTIES OF IDEAL PT-SYMMETRIC WAVE TUNNELING CIRCUIT

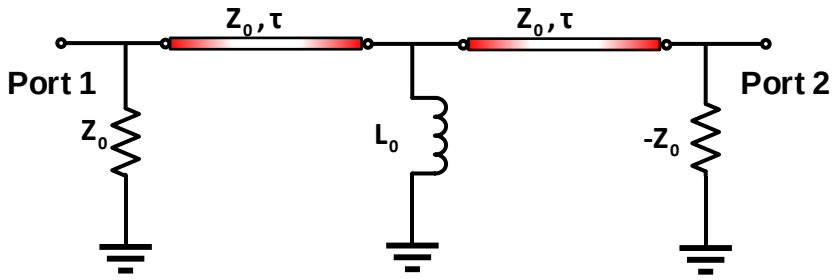

Figure B.1: PT-symmetric resonant transmission circuit model.

Figure. B.1 demonstrates the circuit model of the PT-symmetric resonant transmission device. The transfer matrix of the two-port network can be expressed as:

$$T=\begin{bmatrix}1 & 0\\ \frac{1}{Z_0} & 1\end{bmatrix}\begin{bmatrix}\cos\omega\ \tau & jZ_0\sin\omega\ \tau\\ \frac{j}{Z_0}\sin\omega\ \tau & \cos\omega\ \tau\end{bmatrix}\begin{bmatrix}1 & 0\\ \frac{1}{j\omega L_0} & 1\end{bmatrix}\begin{bmatrix}\cos\omega\ \tau & jZ_0\sin\omega\ \tau\\ \frac{j}{Z_0}\sin\omega\ \tau & \cos\omega\ \tau\end{bmatrix}\begin{bmatrix}1 & 0\\ -\frac{1}{Z_0} & 1\end{bmatrix}, \quad (8.1)$$

where Z_0 is the characteristic impedance of the transmission line, τ is the time delay in the transmission line, ω is the signal frequency, L_0 is the inductance of the shunt inductor. By simplifying Eq. (8.1), the following four matrix elements are obtained:

$$\begin{cases} T_{11}=\cos 2\omega\ \tau+\dfrac{Z_0}{2L_0\omega}\sin 2\omega\ \tau+j\left[-\dfrac{Z_0}{2L_0\omega}+\dfrac{Z_0}{2L_0\omega}\cos 2\omega\ \tau-\sin 2\omega\ \tau\right],\\ T_{12}=jZ_0\left[\dfrac{Z_0}{2L_0\omega}+\sin 2\omega\ \tau-\dfrac{Z_0}{2L_0\omega}\cos 2\omega\ \tau\right],\\ T_{21}=\dfrac{-j}{L_0\omega},\\ T_{22}=\cos 2\omega\ \tau+\dfrac{Z_0}{2L_0\omega}\sin 2\omega\ \tau+j\left[\dfrac{Z_0}{2L_0\omega}-\dfrac{Z_0}{2L_0\omega}\cos 2\omega\ \tau+\sin 2\omega\ \tau\right]. \end{cases} \quad (8.2)$$

According to the relation between scattering matrix and transfer matrix:

$$S=\frac{1}{T_{11}+T_{12}/Z_0+T_{21}Z_0+T_{22}}\begin{bmatrix} T_{11}+T_{12}/Z_0-T_{21}Z_0-T_{22} & 2\left(T_{11}T_{22}-T_{12}T_{21}\right) \\ 2 & -T_{11}+T_{12}/Z_0-T_{21}Z_0+T_{22} \end{bmatrix} \quad (8.3)$$

the S-parameters are given by

$$\begin{cases} S_{11}=\dfrac{2j\cos\omega\ \tau\left(-2\omega L_0\sin\omega\ \tau+Z_0\cos\omega\ \tau\right)}{-jZ_0+\left(4\omega L_0-jZ_0\right)\cos 2\omega\ \tau+2\left(j\omega L_0+Z_0\right)\sin 2\omega\ \tau}, \\ S_{12}=S_{21}=\dfrac{4\omega L_0}{-jZ_0+\left(4\omega L_0-jZ_0\right)\cos 2\omega\ \tau+2\left(j\omega L_0+Z_0\right)\sin 2\omega\ \tau}, \\ S_{22}=\dfrac{6L_0\omega\sin 2\omega\ \tau+Z_0\left(2+6\sin^2\omega\ \tau\right)}{2L_0\omega\left(-2j\cos 2\omega\ \tau+\sin 2\omega\ \tau\right)-Z_0\left(1+\cos 2\omega\ \tau+2j\sin 2\omega\ \tau\right)}. \end{cases} \quad (8.4)$$

When $\tau=\dfrac{1}{4f_0}=\dfrac{\pi}{2\omega_0}$, the above equations can be simplified to

$$\begin{cases} S_{11}=\dfrac{-\left(1+\cos\dfrac{\pi\ \omega}{\omega_0}\right)+\dfrac{2\alpha\ \omega}{\omega_0}\sin\dfrac{\pi\ \omega}{\omega_0}}{1+\left(1+j\dfrac{4\alpha\ \omega}{\omega_0}\right)\cos\dfrac{\pi\ \omega}{\omega_0}+2\left(j-\dfrac{\alpha\ \omega}{\omega_0}\right)\sin\dfrac{\pi\ \omega}{\omega_0}}, \\ S_{12}=S_{21}=\dfrac{j\dfrac{4\alpha\ \omega}{\omega_0}}{1+\left(1+j\dfrac{4\alpha\ \omega}{\omega_0}\right)\cos\dfrac{\pi\ \omega}{\omega_0}+2\left(j-\dfrac{\alpha\ \omega}{\omega_0}\right)\sin\dfrac{\pi\ \omega}{\omega_0}}, \\ S_{22}=\dfrac{-\dfrac{6\alpha\ \omega}{\omega_0}\sin\dfrac{\pi\ \omega}{\omega_0}+3\cos\dfrac{\pi\ \omega}{\omega_0}-5}{1+\left(1+j\dfrac{4\alpha\ \omega}{\omega_0}\right)\cos\dfrac{\pi\ \omega}{\omega_0}+2\left(j-\dfrac{\alpha\ \omega}{\omega_0}\right)\sin\dfrac{\pi\ \omega}{\omega_0}}, \end{cases} \quad (8.5)$$

where ω_0 is the designed frequency of the circuit, $\alpha=\dfrac{\omega_0 L_0}{Z_0}$ is the ratio between the impedance of the inductor and the characteristic impedance. To have a unitary transmission, one of the reflection coefficients must be zero. When $S_{11}=0$, there are two sets of solutions:

$$\begin{cases} \dfrac{\pi}{\omega_0}\omega = (2k+1)\pi, k = 0,1,2,3\cdots \\ \dfrac{1}{2\alpha}\left(\dfrac{\omega}{\omega_0}\right)^{-1} = \tan\left(\dfrac{\pi}{2}\dfrac{\omega}{\omega_0}\right). \end{cases} \tag{8.6}$$

In the case $\dfrac{\omega}{\omega_0} = 2k+1, k = 0,1,2,3$, the scattering matrix downgrades to

$$S = \begin{bmatrix} 0 & -1 \\ -1 & -\dfrac{2j}{\alpha}\left(\dfrac{\omega}{\omega_0}\right)^{-1} \end{bmatrix}. \tag{8.7}$$

In the case $\dfrac{1}{2\alpha}\left(\dfrac{\omega}{\omega_0}\right)^{-1} = \tan\left(\dfrac{\pi}{2}\dfrac{\omega}{\omega_0}\right)$, the scattering matrix downgrades to

$$S = \begin{bmatrix} 0 & 1 \\ 1 & \dfrac{2j}{\alpha}\left(\dfrac{\omega}{\omega_0}\right)^{-1} \end{bmatrix}. \tag{8.8}$$

In summary, the solution $\dfrac{\omega}{\omega_0} = 2k+1, k = 0,1,2,3$ corresponds to a resonator operating at the odd times of resonant frequencies, while the solution $\dfrac{1}{2\alpha}\left(\dfrac{\omega}{\omega_0}\right)^{-1} = \tan\left(\dfrac{\pi}{2}\dfrac{\omega}{\omega_0}\right)$ corresponds to a resonator operating at the even times of resonant frequencies. The transmission phase of Eqs. (8.7) and (8.8) confirms this assessment. It's worth mentioning that the anisotropic transmission resonance is irrelevant to whether if the system is in exact PT phase or in broken PT phase regimes. When the loss and gain is balanced, the resonant transmission in PT-symmetric system is very similar to resonant transmission in Febry-Perot resonator.

Meanwhile, the asymmetric resonant transmission can also happen on the second port where $S_{22} = 0$. The solutions are

$$\left(\frac{\omega}{\omega_0}\right)^{-1} = \frac{6\alpha \sin \pi \dfrac{\omega}{\omega_0}}{3\cos \pi \dfrac{\omega}{\omega_0} - 5}. \tag{8.9}$$

As we see from the above equation, the solutions always exist. But the resonant frequencies are inherently different from Eq. (8.6). The smaller α is, the larger ω becomes. In this case, the $|S_{12}| = |S_{21}| = 1$ and $S_{11} \neq 0$. It indicates that this resonant transmission network can only provide unidirectional resonant transmission of signals.

Figure. B. 2 demonstrates the scattering parameters of an ideal PT-symmetric resonant transmission device. There are ten forward unidirectional resonant transmission points. They are: $\frac{\omega}{\omega_0} = 1, 3, 5, 7, 9$ and $\frac{\omega}{\omega_0} = 0.88, 2.68, 4.53, 6.42, 8.35$. There are two backward unidirectional resonant transmission point, they are: $\frac{\omega}{\omega_0} = 7.56, 7.82, 9.44, 9.88$. These resonant transmission points are consistent with Eqs. (8.6) and (8.9).

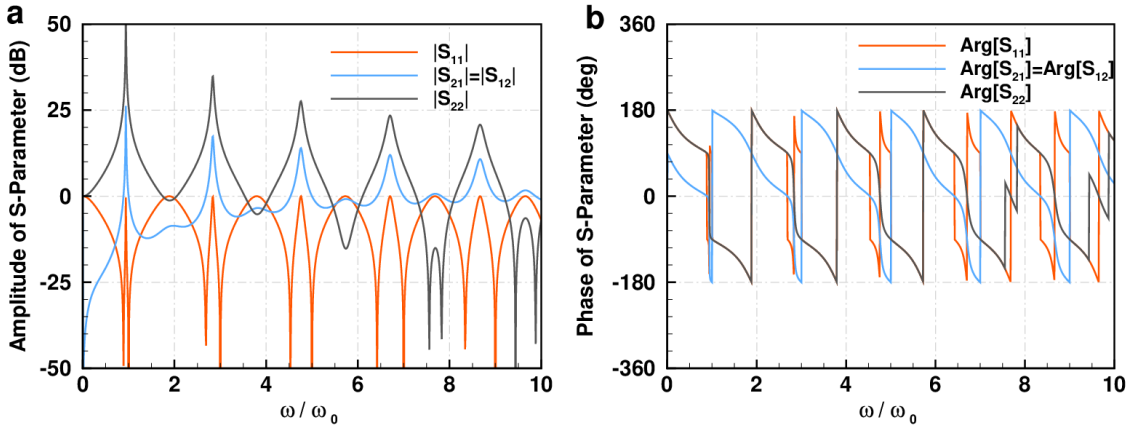

Figure B.2: PT-symmetric resonant transmission circuit model. Scattering parameters of ideal PT-symmetric resonant transmission device. We choose $\alpha = 0.1$ in the above graph. **a**. The amplitude of scattering parameters. **b**. The phase of scattering parameters.

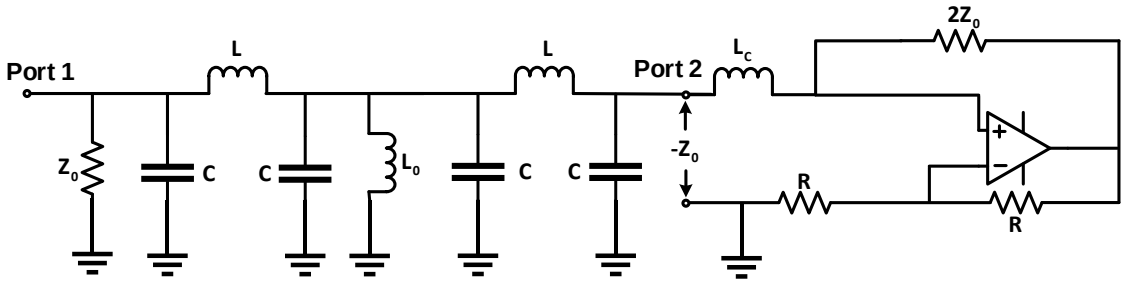

Figure B.3: PT-symmetric resonant transmission circuit model. Scattering parameters of ideal PT-symmetric resonant transmission device. We choose $\alpha = 0.1$ in the above graph. **a**. The amplitude of scattering parameters. **b**. The phase of scattering parameters. Realistic implementation of PT-symmetric resonant transmission circuit. $L_C = 3Z_0/\omega_{3dB}$ is the compensating inductor. ω_{3dB} is the 3dB bandwidth of the amplifier. The negative impedance converter exhibits $-Z_0$ impedance at operational frequency $\omega_0 = \omega_{3dB}/\sqrt{3}$. The negative impedance converter is based on one-pole amplifier model. The feedback factor is $\beta = \frac{1}{2}$ and the feedback resistance is $Z_F = 2Z_0$.

2. SCATTERING PROPERTIES OF REALISTIC PT-SYMMETRIC WAVE TUNNELING CIRCUIT

For practical implementation of the PT-symmetric resonant transmission circuit. We make two major modifications over the ideal model. First, the transmission line is replaced with a π model LC tank with finite transmission window to shrink the form factor of the board. Second, the negative impedance is implemented with an amplifier feedback circuit. Figure B.3 demonstrates our final implementation of PT-symmetric resonant transmission circuit. The effective negative impedance is

$$Z_{NIC} = 2Z_0\left[\frac{\omega^2 - 3\omega_0^2}{\omega^2 + 3\omega_0^2} + \frac{j\sqrt{3}\omega}{2\omega_0}\frac{\omega^2 - \omega_0^2}{\omega^2 + 3\omega_0^2}\right], \tag{8.10}$$

where ω_0 is the operational frequency of the negative impedance converter as well as the whole PT-symmetric circuit. Therefore, the transmission line elements are

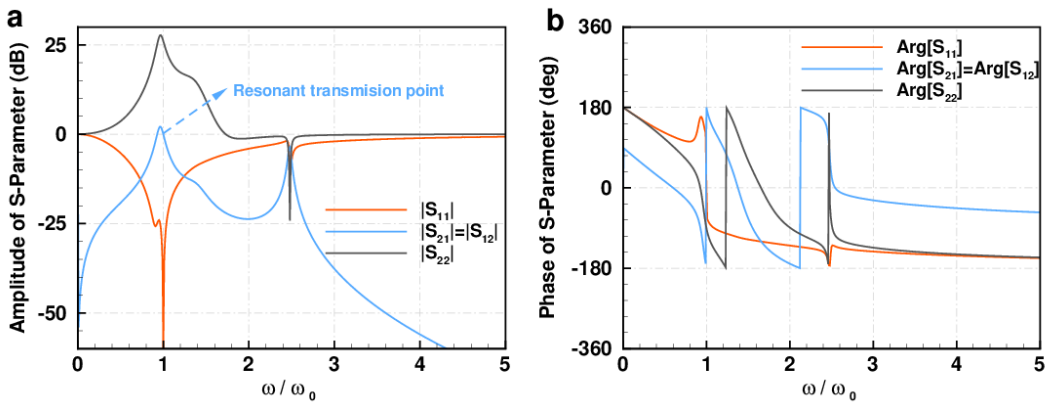

Figure B.4: Scattering parameters PT-symmetric resonant transmission device based on one-pole NIC. We choose $\alpha = 0.1$ in the above graph. **a**. The amplitude of scattering parameters. **b**. The phase of scattering parameters.

$L = \frac{Z_0}{\omega_0}, C = \frac{1}{Z_0 \omega_0}$, which offers full signal transmission and quarter period delay at frequency ω_0. We apply the transfer matrix formalism:

$$T = \begin{bmatrix} 1 & 0 \\ \frac{1}{Z_0} & 1 \end{bmatrix} \begin{bmatrix} 1 & 0 \\ j\omega C & 1 \end{bmatrix} \begin{bmatrix} 1 & j\omega L \\ 0 & 1 \end{bmatrix} \begin{bmatrix} 1 & 0 \\ j\omega C & 1 \end{bmatrix} \begin{bmatrix} 1 & 0 \\ \frac{1}{j\omega L_0} & 1 \end{bmatrix} \begin{bmatrix} 1 & 0 \\ j\omega C & 1 \end{bmatrix} \begin{bmatrix} 1 & j\omega L \\ 0 & 1 \end{bmatrix} \begin{bmatrix} 1 & 0 \\ j\omega C & 1 \end{bmatrix} \begin{bmatrix} 1 & 0 \\ \frac{1}{Z_{NIC}} & 1 \end{bmatrix}.$$

(8.11)

The corresponding scattering matrix can be obtained by substitute the above equation into Eq. (8.3). We plot the theoretical scattering properties of our PT-symmetric resonant transmission in Fig. B.4.

At operational frequency, the scattering matrix the transmission is unitary, and reflection is zero at port 1. The gain side has a 26 dB amplitude reflection coefficient with $-\frac{\pi}{2}$ phase. The scattering properties at resonant transmission point is consistent with that of an ideal PT-symmetric resonant transmission circuit model, which is shown in Fig. B.2 and Eq. (8.7). It's important to note that our PT-symmetric resonant

transmission circuit ideally has a single resonant transmission point due to the finite transmission bandwidth of the transmission line and the dispersion of the NIC. The scattering matrix obeys unitary condition at resonant transmission frequency $\left|Det\left[S\left(\omega_0\right)\right]\right|=1$, indicating that the circuit is perfectly PT-symmetric at this designed point.

3. SIMULATION OF REALISTIC PT-SYMMETRIC WAVE TUNNELING CIRCUIT

Implementation of the PCB board involves consideration of parasitic effects, wave leakage in the circuit channel and many more. In this section, we demonstrate our simulation results of our PCB board with ADS and Modelithics package.

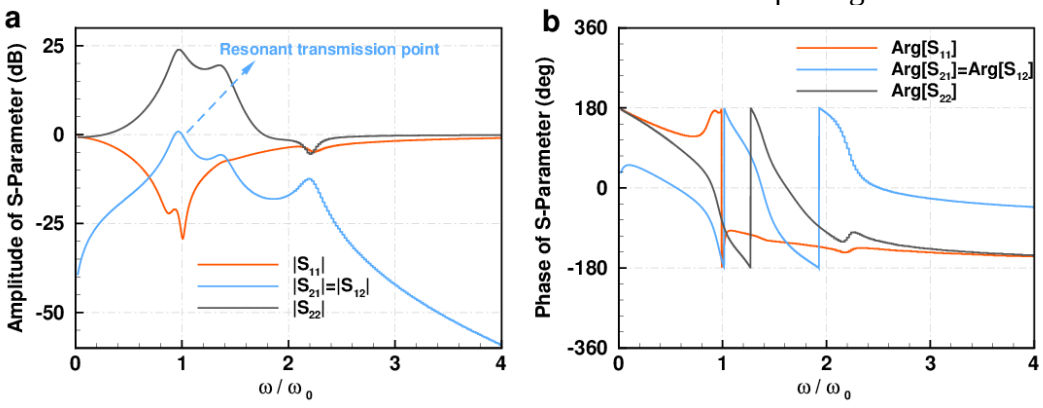

Figure B.5: Scattering parameters of PT-symmetric resonant transmission device by using ADS and Modelithics package. **a**. The amplitude of scattering parameters. **b**. The phase of scattering parameters. The following components are used: $L=150\text{nH}, C=68\text{pF}, \text{L}_0=20nH, L_C=240nH$, and the amplifier is Texas Instrument (TI) OPA355. The resistors on the converting input port of the amplifier are $R=560\Omega$, which are tunable. The theoretical operational frequency is $f_0=\frac{\omega_0}{2\pi}=\frac{1}{2\pi\sqrt{LC}}=49.8\text{MHz}$. The resonant transmission frequency inferred from the simulation results is 48.7 MHz, which is very close to theoretical value. The parameter $\alpha=\frac{\omega_0 L_0}{Z_0}$ is 0.12 in our circuit.

Figure. B.5 demonstrates our PCB board simulation results. The resonant transmission frequency is 48.7 MHz, where the transmission $|S_{12}| = |S_{21}| = 0.01\text{dB}$, and reflection $|S_{11}| = -28.8\text{dB}$, $|S_{22}| = 23.4\text{dB}$. The simulation results are in excellent agreement with our theoretical prediction in previous section.

4. PHASE TRANSITIONS OF IDEAL PT-SYMMETRIC WAVE TUNNELING CIRCUIT

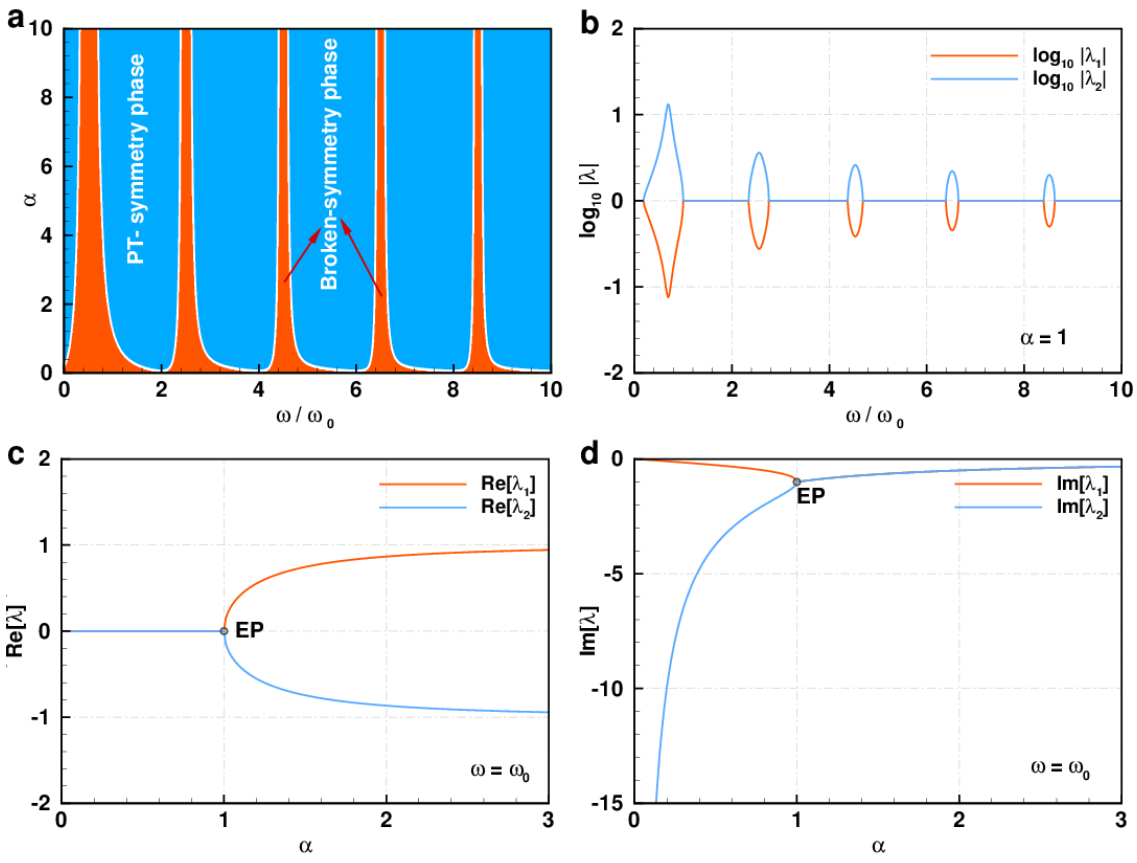

Figure B.6: Phase diagram of the PT-symmetry resonant transmission circuit. **a**. Blue region is the PT-symmetry phase while red region is the broken-symmetry phase. White line is the PT-symmetry phase transition boundary. **b**. Spectral properties of eigenvalues with $\alpha = 1$. The system exhibits multiple PT-symmetry and broken-symmetry regions. **c**. Evolution of real part of the eigenvalues versus coupling coefficient α at resonant transmission frequency ω_0. **d**. Evolution of imaginary part of the eigenvalues versus coupling coefficient α at resonant transmission frequency ω_0.

Since the system obeys PT-symmetry, it's important to study the phase diagram and phase transition. By solving the eigenvalue problem of scattering matrix in Eq. (8.5), we have the following eigenvalues

$$\begin{cases} \lambda_1 = \dfrac{3j\alpha\dfrac{\omega}{\omega_0} - j\alpha\dfrac{\omega}{\omega_0}\left(\cos\dfrac{\pi\,\omega}{\omega_0} - 2\alpha\dfrac{\omega}{\omega_0}\sin\dfrac{\pi\,\omega}{\omega_0}\right)}{-j + \left(-j + 4\dfrac{\alpha\,\omega}{\omega_0}\right)\cos\dfrac{\pi\,\omega}{\omega_0} + 2\left(1 + j\dfrac{\alpha\,\omega}{\omega_0}\right)\sin\dfrac{\pi\,\omega}{\omega_0}} \\ \quad - \dfrac{\sqrt{2}\sqrt{-3 + 4\left(\dfrac{\alpha\,\omega}{\omega_0}\right)^2 + 4\cos\dfrac{\pi\,\omega}{\omega_0} + \left[-1 + 4\left(\dfrac{\alpha\,\omega}{\omega_0}\right)^2\right]\cos\dfrac{2\pi\,\omega}{\omega_0} + 4\dfrac{\alpha\,\omega}{\omega_0}\left(-2\sin\dfrac{\pi\,\omega}{\omega_0} + \sin\dfrac{2\pi\,\omega}{\omega_0}\right)}}{-j + \left(-j + 4\dfrac{\alpha\,\omega}{\omega_0}\right)\cos\dfrac{\pi\,\omega}{\omega_0} + 2\left(1 + j\dfrac{\alpha\,\omega}{\omega_0}\right)\sin\dfrac{\pi\,\omega}{\omega_0}}, \\ \lambda_2 = \dfrac{3j\alpha\dfrac{\omega}{\omega_0} - j\alpha\dfrac{\omega}{\omega_0}\left(\cos\dfrac{\pi\,\omega}{\omega_0} - 2\alpha\dfrac{\omega}{\omega_0}\sin\dfrac{\pi\,\omega}{\omega_0}\right)}{-j + \left(-j + 4\dfrac{\alpha\,\omega}{\omega_0}\right)\cos\dfrac{\pi\,\omega}{\omega_0} + 2\left(1 + j\dfrac{\alpha\,\omega}{\omega_0}\right)\sin\dfrac{\pi\,\omega}{\omega_0}} \\ \quad + \dfrac{\sqrt{2}\sqrt{-3 + 4\left(\dfrac{\alpha\,\omega}{\omega_0}\right)^2 + 4\cos\dfrac{\pi\,\omega}{\omega_0} + \left[-1 + 4\left(\dfrac{\alpha\,\omega}{\omega_0}\right)^2\right]\cos\dfrac{2\pi\,\omega}{\omega_0} + 4\dfrac{\alpha\,\omega}{\omega_0}\left(-2\sin\dfrac{\pi\,\omega}{\omega_0} + \sin\dfrac{2\pi\,\omega}{\omega_0}\right)}}{-j + \left(-j + 4\dfrac{\alpha\,\omega}{\omega_0}\right)\cos\dfrac{\pi\,\omega}{\omega_0} + 2\left(1 + j\dfrac{\alpha\,\omega}{\omega_0}\right)\sin\dfrac{\pi\,\omega}{\omega_0}}. \end{cases}$$

(8.12)

From the above equation, we know that the eigenvalues are dependent on the input signal frequency and the coupling coefficient α. The PT-symmetry phase transition boundary can be obtained by equating $\lambda_1 = \lambda_2$:

$$\alpha_{EP}(\omega) = \frac{1-\cos\frac{\pi\,\omega}{\omega_0}}{2\left(1-\sin\frac{\pi\,\omega}{\omega_0}\right)}\left(\frac{\omega}{\omega_0}\right)^{-1}, \tag{8.13}$$

where α_{EP} is the exceptional point (EP) of this PT-symmetric scattering system, which is marked as white line in Fig.B.6(a). At resonant transmission frequency $\omega_k = (2k+1)\omega_0, k = 0,1,2,3\cdots$, the exceptional point is $\alpha_{EP}(\omega = \omega_k) = \frac{1}{2k+1}$. At resonant transmission frequency $\omega_k = \left(\frac{2}{\pi}\arctan\frac{1}{2} + 2k\right)\omega_0$, the exceptional point is $\alpha_{EP}(\omega = \omega_k) = \frac{\pi}{2\arctan\frac{1}{2} + 2k\pi}$. At frequency $\omega = \frac{1}{2}\omega_0, \frac{5}{2}\omega_0, \frac{9}{2}\omega_0\cdots$, the system is always in broken-symmetry region. At frequency $\omega = 2\omega_0, 4\omega_0, 6\omega_0\cdots$, the system is always in PT-symmetry region.

Figure B.6(b) demonstrates the spectral properties of eigenvalues with coupling coefficient $\alpha = 1$. For regions $\log_{10}|\lambda_1(\omega)| = \log_{10}|\lambda_2(\omega)| = 0$, we can infer that $|\lambda_1(\omega)| = |\lambda_2(\omega)| = 1$, indicating that the system is in the PT-symmetry phase. For regions $\log_{10}|\lambda_1(\omega)| = -\log_{10}|\lambda_2(\omega)|$, we can infer that $|\lambda_1(\omega)| = 1/|\lambda_2(\omega)| < 1$. The PT-symmetry is broken in these regions and the PT operator will not share the same eigenvalues and eigenstates with the scattering matrix. When the input signal frequency is known, the eigenvalues experience phase transition with respect to coupling coefficient α. Figures B.6(c) and (d) show the evolution of eigenvalues at resonant transmission frequency $\omega = \omega_0$. The EP point is $\alpha_{EP}(\omega_0) = 1$, which is consistent with the phase diagram Fig. B.6(a) and Eq. (8.13). When $\alpha < \alpha_{EP}$, the real part of the two eigenvalues

are zero and the imaginary part of the two eigenvalues are nonzero. They obey relation $\left|\mathrm{Im}\left[\lambda_1\right]\right| = 1/\left|\mathrm{Im}\left[\lambda_2\right]\right| < 1$, exhibiting a broken-symmetry phase. When $\alpha > \alpha_{EP}$, both real and imaginary parts are nonzero, but they obey $\left|\lambda_1\right| = \left|\lambda_2\right| = 1$, exhibiting a PT-symmetry exact phase.

5. PHASE TRANSITIONS OF REALISTIC PT-SYMMETRIC WAVE TUNNELING CIRCUIT

For realistic PT-symmetric resonant transmission circuit, the system is PT-symmetric at resonant transmission frequency. Therefore, the scattering matrix obeys the following properties of PT-symmetric scattering systems at resonant transmission frequency

$$PS^*\left(\omega_0\right)P \equiv S^{-1}\left(\omega_0\right), \tag{8.14}$$

where $P = \begin{pmatrix} 0 & 1 \\ 1 & 0 \end{pmatrix}$ is the parity operator. For input frequency other than ω_0, the above equation is not respected in general and the system is categorized as a non-Hermitian scattering system where gain is involved but imbalanced with loss.

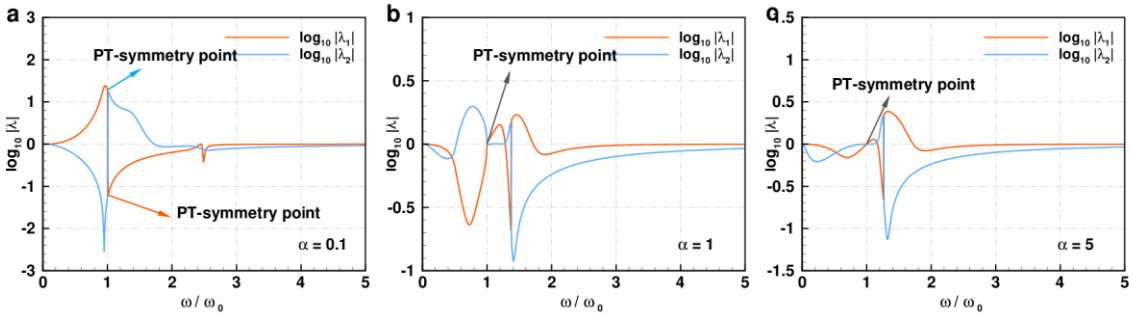

Figure B.7: Spectral properties of the eigenvalues of the realistic PT-symmetric circuit. **a**. With coupling coefficient $\alpha = 0.1$. **b**. With coupling coefficient $\alpha = 1$. **c**. With coupling coefficient $\alpha = 5$. When coupling coefficient varies, the system is always PT-symmetric at resonant transmission frequency as evidenced by the unitary condition $\left|\lambda_1\left(\omega_0\right)\lambda_2\left(\omega_0\right)\right| = 1$.

At operational frequency, the scattering matrix reduces to

$$S = \begin{bmatrix} 0 & -1 \\ -1 & -\dfrac{2j}{\alpha} \end{bmatrix}, \tag{8.15}$$

where the eigenvalues are $\lambda_{1,2} = \dfrac{-j \pm \sqrt{1-\alpha^2}}{\alpha}$. The exceptional point is $\alpha_{EP} = 1$, which demonstrates identical dynamics shown in Fig. B. 6(c) and (d).

6. STABILITY ANALYSIS OF AN IDEAL PT-SYMMETRIC WAVE TUNNELING CIRCUIT

In this section, we provide a detailed derivation of the transfer function and stability analysis of an ideal PT-symmetric resonant transmission circuit. To analyze the influence of parameter detuning, we assume two small perturbations on the circuit: relative time delay perturbation $\dfrac{\Delta\ \tau}{\tau}$ on the second segment of transmission and small perturbation $\dfrac{\Delta Z}{Z_0}$ on the ideal negative impedance.

At port 2, the effective load impedance is a negative impedance in parallel with the characteristic impedance $\left[1+\left(\dfrac{\Delta Z}{Z_0}\right)^{-1}\right]Z_0$. Therefore, the effective reflection coefficient on the load side is

$$\Gamma_{l_2} = \frac{1}{1+2\dfrac{\Delta Z}{Z_0}}. \tag{8.16}$$

The input impedance on the second transmission line is

$$Z_{in2} = Z_0 \frac{e^{\tau_2 s} + \Gamma_{l_2} e^{-\tau_2 s}}{e^{\tau_2 s} - \Gamma_{l_2} e^{-\tau_2 s}}, \tag{8.17}$$

where τ_2 is the time delay of the second transmission line. For the first transmission line, the load impedance is an inductor in parallel with input impedance on the second transmission line

$$Z_{L_1} = sL_0 \| Z_{in2}, \tag{8.18}$$

where $\|$ is an operator to calculate the shunt impedance on the left and right side of this symbol. Then, the load impedance on the first transmission line can be simplified to

$$Z_{L_1} = \frac{sZ_0L_0\left(e^{\tau_2 s} + \Gamma_{l_2}e^{-\tau_2 s}\right)}{\left(Z_0 + sL_0\right)e^{\tau_2 s} + \left(Z_0 - sL_0\right)\Gamma_{l_2}e^{-\tau_2 s}}. \tag{8.19}$$

So, for the first transmission line the reflection coefficient is

$$\Gamma_{l_1} = \frac{-Z_0e^{\tau_2 s} + \left(2sL_0 - Z_0\right)\Gamma_{l_2}e^{-\tau_2 s}}{\left(2sL_0 + Z_0\right)e^{\tau_2 s} + Z_0\Gamma_{l_2}e^{-\tau_2 s}}. \tag{8.20}$$

The transfer function on the inductor can be expressed as

$$H_{inductor}\left(s\right) = \frac{1+\Gamma_{l_1}}{3e^{\tau_1 s} + \Gamma_{l_1}e^{-\tau_1 s}}, \tag{8.21}$$

where τ_1 is the time delay on the first transmission line. As a result, the transfer function on the load of the second transmission line can be written as

$$H\left(s\right) = \frac{1+\Gamma_{l_1}}{3e^{\tau_1 s} + \Gamma_{l_1}e^{-\tau_1 s}} \times \frac{1+\Gamma_{l_2}}{e^{\tau_2 s} + \Gamma_{l_2}e^{-\tau_2 s}}, \tag{8.22}$$

where Γ_{l_1} is expressed in Eq. (8.20). We continue to simplify the transfer function to

$$H\left(s\right) = \frac{4\left(1+\frac{\Delta Z}{Z_0}\right)L_0 s}{3\left(1+2\frac{\Delta Z}{Z_0}\right)\left(2L_0 s + Z_0\right)e^{(\tau_1+\tau_2)s} + 3Z_0e^{(\tau_1-\tau_2)s} - Z_0\left(1+2\frac{\Delta Z}{Z_0}\right)e^{(\tau_2-\tau_1)s} + \left(2L_0 s - Z_0\right)e^{-(\tau_1+\tau_2)s}}. \tag{8.23}$$

Now, we assume $\tau_1 = \tau$ and $\tau_2 = \tau\left(1+\frac{\Delta\,\tau}{\tau}\right)$. The above equation will be simplified to

$$H(s)=\frac{4\left(1+\frac{\Delta Z}{Z_0}\right)L_0 s}{3\left(1+2\frac{\Delta Z}{Z_0}\right)\left(2L_0 s+Z_0\right)e^{\tau\left(2+\frac{\Delta\tau}{\tau}\right)s}+3Z_0e^{-\Delta\tau s}-Z_0\left(1+2\frac{\Delta Z}{Z_0}\right)e^{\Delta\tau s}+\left(2L_0 s-Z_0\right)e^{-\tau\left(2+\frac{\Delta\tau}{\tau}\right)s}}.$$

(8.24)

The above equation is the transfer function of an ideal PT-symmetric resonant transmission circuit with parameter detuning. We apply simple numerical calculations and figure out the poles of the transfer function.

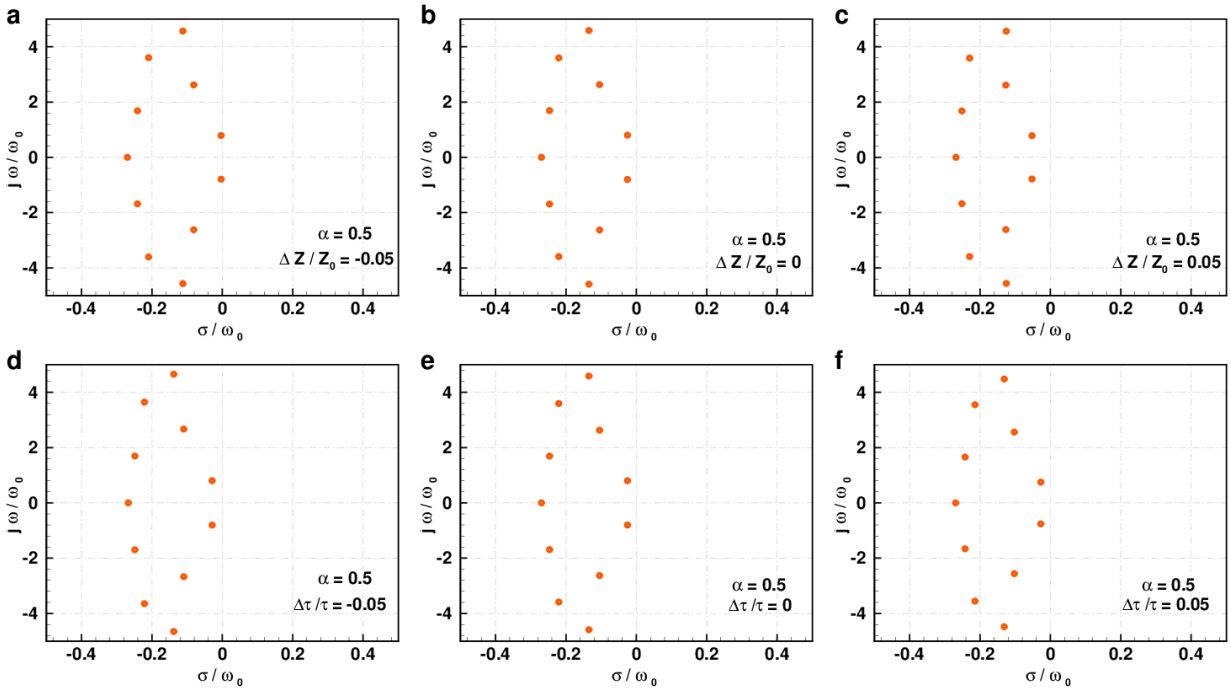

Figure B.8: Pole locations of transfer function with parameter detuning. **a**. Pole locations with $\alpha = 0.5,\ \frac{\Delta Z}{Z_0} = -0.05$. **b**. Pole locations with $\alpha = 0.5,\ \frac{\Delta Z}{Z_0} = 0$. **c**. Pole locations with $\alpha = 0.5,\ \frac{\Delta Z}{Z_0} = 0.05$. **d**. Pole locations with $\alpha = 0.5,\ \frac{\Delta \tau}{\tau} = -0.05$. **e**. Pole locations with $\alpha = 0.5,\ \frac{\Delta \tau}{\tau} = 0$. **f**. Pole locations with $\alpha = 0.5,\ \frac{\Delta \tau}{\tau} = 0.05$. Note that the number of poles is infinite, and we only show the poles that will potentially cause stability problems.

Figure B.8 demonstrates the pole locations with parameter detuning. Our study indicates that the circuit remains stable for any value $\alpha > 0$ based on the assumption that there's no parameter detuning. If imperfection exists, the coupling coefficient α should be larger than 0.1 to ensure stable operation. In summary, the ideal PT-symmetric resonant transmission is stable for any coupling coefficient. To ensure a more robust operation [5% tolerance on impedance and delay detuning], the coupling coefficient should be larger than 0.1.

Appendix C

1. HARMONIC ANALYSIS OF SINGLY-BALANCED GYRATOR

For the upper branch gyrator, we assume that the input signal at the port 1 of the singly-balanced gyrator is monochromatic with $e^{j\omega t}$. Performing the Fourier transform of Eqs. (5.1)-(5.2) in the main text we obtain the reflected and transmitted signals

$$V_2^-(t)=\sum_{n=-\infty}^{n=+\infty}\frac{(-1)^n\sin\frac{n\pi}{2}}{n\pi}e^{-j\omega\frac{T_m}{4}}e^{j(\omega+n\omega_m)t}, \tag{8.25}$$

$$V_1^-(t)=\sum_{n=-\infty}^{n=+\infty}\frac{e^{j\frac{n\pi}{2}}\sin\frac{n\pi}{2}}{n\pi}e^{j(\omega+n\omega_m)t}. \tag{8.26}$$

Similarly, Fourier-transforming Eqs. (5.3)-(5.4) in the main text we obtain the reflected and transmitted signals for excitation from port 2:

$$V_1^-(t)=\sum_{n=-\infty}^{n=+\infty}\frac{e^{-j\frac{n\pi}{2}}\sin\frac{n\pi}{2}}{n\pi}e^{-j\omega\frac{3T_m}{4}}e^{j(\omega+n\omega_m)t}, \tag{8.27}$$

$$V_2^-(t)=\sum_{n=-\infty}^{n=+\infty}\frac{\sin\frac{n\pi}{2}}{n\pi}e^{j(\omega+n\omega_m)t}. \tag{8.28}$$

We notice that all the scattering parameters of the fundamental tone are multiplied with a factor $1/2$, leading to 6 dB insertion loss for the transmitted signal in both directions. There are two mechanisms contributing to this factor. First, the switches transmit only during half of the modulation period, whichever port is excited, allowing only half of the incident power to enter the device. Second, again due to the switches, in the reflected and transmitted signals, the total power distributed to all the higher-order harmonic is

$$\sum_{\substack{n=-\infty\\ n\neq 0}}^{+\infty}\frac{\sin^2\left(\frac{n\pi}{2}\right)}{n^2\pi^2}=\sum_{n=\pm1,\pm3,\pm5\ldots}\frac{1}{n^2\pi^2}=\frac{1}{4}, \tag{8.29}$$

which is half of the power that gets into the circuit. Therefore, the power that gets out of the circuit at the fundamental tone is $1/4$ of the input power, resulting in an insertion loss of 6 dB.

We continue to perform the harmonic analysis of a slightly desynchronized single branch gyrator. To analyze the scattering properties, we transform Eqs. (5.9)-(5.12) to Fourier series:

$$V_2^-(t)=\sum_{n\neq 0}\frac{j^{n+1}\left[1-(-1)^n e^{-jn\omega_m|\Delta\tau|}\right]}{2n\pi}e^{-j\omega\frac{T_m}{4}}e^{j(\omega+n\omega_m)t}+\left(\frac{1}{2}-\frac{|\Delta\tau|}{T_m}\right)e^{-j\omega\frac{T_m}{4}}e^{j\omega t}$$
$$+\sum_{n\neq 0}\frac{j^{n+1}\left[-1+e^{-jn\omega_m|\Delta\tau|}\right]}{2n\pi}e^{-j\omega\frac{3T_m}{4}}e^{j(\omega+n\omega_m)t}+\frac{|\Delta\tau|}{T_m}e^{-j\omega\frac{3T_m}{4}}e^{j\omega t}, \tag{8.30}$$

$$V_1^-(t)=\sum_{n=-\infty}^{n=+\infty}\frac{e^{j\frac{n\pi}{2}}\sin\frac{n\pi}{2}}{n\pi}e^{j(\omega+n\omega_m)t}, \tag{8.31}$$

$$V_1^-(t)=\sum_{n\neq 0}\frac{j\left[(-1)^n-e^{-jn\omega_m|\Delta\tau|}\right]}{2n\pi}e^{-j\omega\frac{3T_m}{4}}e^{j(\omega+n\omega_m)t}+\left(\frac{1}{2}-\frac{|\Delta\tau|}{T_m}\right)e^{-j\omega\frac{3T_m}{4}}e^{j\omega t}$$
$$+\sum_{n\neq 0}\frac{j\left[-1+e^{-jn\omega_m|\Delta\tau|}\right]}{2n\pi}e^{-j\omega\frac{T_m}{4}}e^{j(\omega+n\omega_m)t}+\frac{|\Delta\tau|}{T_m}e^{-j\omega\frac{T_m}{4}}e^{j\omega t}, \tag{8.32}$$

$$V_2^-(t)=\sum_{n=-\infty}^{n=+\infty}\frac{\sin\frac{n\pi}{2}}{n\pi}e^{j(\omega+n\omega_m)t}e^{-jn\omega_m|\Delta\tau|}. \tag{8.33}$$

The above equations reduce to Eqs. (8.25)-(8.28) when timing error $\Delta\tau$ is set to zero. When the second switch is desynchronized, the transmitted signals possess both odd and even harmonics rather than odd harmonics only as in perfect synchronization case.

The harmonic analyses of a double branch gyrator with timing error are again given by:

$$V_2^-(t)=\sum_{n\neq 0}\frac{j\cos\frac{n\pi}{2}\left[1-e^{-jn\omega_m|\Delta\ \tau|}\right]}{n\pi}\left(e^{-j\omega\frac{T_m}{4}}-e^{-j\omega\frac{3T_m}{4}}\right)e^{j(\omega+n\omega_m)t}$$
$$+\left[\left(1-\frac{2|\Delta\ \tau|}{T_m}\right)e^{-j\omega\frac{T_m}{4}}+\frac{2|\Delta\ \tau|}{T_m}e^{-j\omega\frac{3T_m}{4}}\right]e^{j\omega t}, \tag{8.34}$$

$$V_1^-(t)=0, \tag{8.35}$$

$$V_1^-(t)=\sum_{n\neq 0}\frac{j\left[(-1)^n+1\right]\left[1-e^{-jn\omega_m|\Delta\ \tau|}\right]}{2n\pi}\left(e^{-j\omega\frac{3T_m}{4}}-e^{-j\omega\frac{T_m}{4}}\right)e^{j(\omega+n\omega_m)t}$$
$$+\left[\left(1-\frac{2|\Delta\ \tau|}{T_m}\right)e^{-j\omega\frac{3T_m}{4}}+\frac{2|\Delta\ \tau|}{T_m}e^{-j\omega\frac{T_m}{4}}\right]e^{j\omega t}, \tag{8.36}$$

$$V_2^-(t)=0, \tag{8.37}$$

The above equations indicate that the double branch gyrator has residual even-order harmonics in the presence of the desynchronization.

2. HARMONIC ANALYSIS OF DIFFERENTIAL GYRATOR

To study the IM products and scattering properties of the fundamental tone, we perform a Fourier transform over the temporal response and get the Fourier series of the responses:

$$V_2^-(t)=\sum_{n\neq 0}\frac{2j\cos\frac{n\pi}{2}\left[1-e^{-jn\omega_m|\Delta\ \tau|}\right]}{n\pi}e^{j(\omega+n\omega_m)t}e^{-j\omega\frac{T_m}{4}}+\left(1-\frac{4|\Delta\ \tau|}{T_m}\right)e^{-j\omega\frac{T_m}{4}}e^{j\omega t}, \tag{8.38}$$

$$V_1^-(t)=0, \tag{8.39}$$

$$V_1^-(t)=\sum_{n\neq 0}\frac{-j\left[1+(-1)^n\right]\left[1-e^{-jn\omega_m|\Delta\ \tau|}\right]}{n\pi}e^{j(\omega+n\omega_m)t}e^{-j\omega\frac{T_m}{4}}-\left(1-\frac{4|\Delta\ \tau|}{T_m}\right)e^{-j\omega\frac{T_m}{4}}e^{j\omega t}, \tag{8.40}$$

$$V_2^-(t)=0. \tag{8.41}$$

The above equation demonstrates the same IM products as Eqs. (8.34)-(8.37). Therefore, they share the identical IM products distribution as shown in Fig. 5.4.

3. TEMPORAL AND SPECTRAL ANALYSIS OF SINGLY-BALANCED ISOLATOR

For a single branch isolator, the temporal domain responses are expressed in Eqs. (5.25)-(5.28). The Fourier series can be easily obtained:

$$V_2^-(t)=\sum_{n=-\infty}^{n=+\infty}\frac{\sin\frac{n\pi}{2}}{n\pi}\left[(-1)^n+\mathrm{T}^2\right]e^{-j\omega\frac{T_m}{4}}e^{j(\omega+n\omega_m)t}, \tag{8.42}$$

$$V_1^-(t)=\sum_{n=-\infty}^{n=+\infty}\frac{\Gamma\left(e^{j\frac{n\pi}{2}}+\mathrm{T}e^{-j\frac{n\pi}{2}}e^{-j\omega\frac{T_m}{2}}\right)\sin\frac{n\pi}{2}}{n\pi}e^{j(\omega+n\omega_m)t}, \tag{8.43}$$

$$V_1^-(t)=\mathrm{T}e^{-j\omega\frac{T_m}{4}}e^{j\omega t}+\sum_{n=-\infty}^{n=+\infty}\frac{\Gamma^2e^{-j\frac{n\pi}{2}}\sin\frac{n\pi}{2}}{n\pi}e^{-j\omega\frac{3T_m}{4}}e^{j(\omega+n\omega_m)t}, \tag{8.44}$$

$$V_2^-(t)=\sum_{n=-\infty}^{n=+\infty}\Gamma\left[1+\mathrm{T}e^{-j\omega\frac{T_m}{2}}\right]\frac{\sin\frac{n\pi}{2}}{n\pi}e^{j(\omega+n\omega_m)t}, \tag{8.45}$$

For a singly-balanced isolator, the analysis is much more complicated. Assume that the network is excited with a monochromatic signal $V_1^+(t)=\exp(j\omega t)$ at port 1. The left side of the network is essentially a Wye-topology network with time-varying scattering properties $S(t)$. The output and input signals obey the following relation:

$$\begin{bmatrix}V_1^-(t)\\V_a^+(t)\\V_b^+(t)\end{bmatrix}=S(t)\begin{bmatrix}V_1^+(t)\\V_a^-(t)\\V_b^-(t)\end{bmatrix}, \tag{8.46}$$

where the time-domain scattering matrix is

$$S(t)=\begin{bmatrix}\frac{R}{3R+8} & \frac{4}{3R+8}+\frac{2R}{3R+8}P_1(t) & \frac{2R+4}{3R+8}+\frac{-2R}{3R+8}P_1(t)\\ \frac{8}{3R+8}+\frac{4R}{3R+8}P_1(t) & \frac{3R-4}{3R+8}-\frac{4R}{3R+8}P_1(t) & \frac{4}{3R+8}\\ \frac{4R+8}{3R+8}-\frac{4R}{3R+8}P_1(t) & \frac{4}{3R+8} & \frac{-R-4}{3R+8}+\frac{4R}{3R+8}P_1(t)\end{bmatrix}, \tag{8.47}$$

and $R=R_m/Z_0$ is the relative resistance. Meanwhile, the right side of the network is also a Wye-topology network with the following scattering relations

$$\begin{bmatrix} V_2^-(t) \\ V_a^-\left(t+\frac{T_m}{4}\right) \\ V_b^-\left(t+\frac{T_m}{4}\right) \end{bmatrix} = S\left(t-\frac{T_m}{4}\right)\begin{bmatrix} 0 \\ V_a^+\left(t-\frac{T_m}{4}\right) \\ V_b^+\left(t-\frac{T_m}{4}\right) \end{bmatrix}. \tag{8.48}$$

From Eqs. (8.46) and (8.48), we have the following relations

$$\begin{cases} V_a^+(t) = S_{21}V_1^+(t) + S_{22}V_a^-(t) + S_{23}V_b^-(t), \\ V_b^+(t) = S_{31}V_1^+(t) + S_{32}V_a^-(t) + S_{33}V_b^-(t), \end{cases} \tag{8.49}$$

and

$$\begin{cases} V_a^-\left(t+\frac{T_m}{2}\right) = S_{22}V_a^+(t) + S_{23}V_b^+(t), \\ V_b^-\left(t+\frac{T_m}{2}\right) = S_{32}V_a^+(t) + S_{33}V_b^+(t). \end{cases} \tag{8.50}$$

We substitute Eq. (8.49) into Eq. (8.50) and get

$$\begin{cases} V_a^-\left(t+\frac{T_m}{2}\right) = S_{22}\left[S_{21}V_1^+(t) + S_{22}V_a^-(t) + S_{23}V_b^-(t)\right] + S_{23}\left[S_{31}V_1^+(t) + S_{32}V_a^-(t) + S_{33}V_b^-(t)\right], \\ V_b^-\left(t+\frac{T_m}{2}\right) = S_{32}\left[S_{21}V_1^+(t) + S_{22}V_a^-(t) + S_{23}V_b^-(t)\right] + S_{33}\left[S_{31}V_1^+(t) + S_{32}V_a^-(t) + S_{33}V_b^-(t)\right]. \end{cases}$$

(8.51)

Shifting the reference time of the above equation by $\frac{T_m}{2}$ and employing the Bloch theorem

$$\begin{cases} V_a^-(t+T_m) = V_a^-(t)\exp(j\omega T_m), \\ V_b^-(t+T_m) = V_b^-(t)\exp(j\omega T_m), \end{cases} \tag{8.52}$$

we obtain the following linear equations for V_a^- and V_b^-

$$
\begin{cases}
V_a^-(t)\exp(j\omega T_m)=\left[S_{22}\left(t+\frac{T_m}{2}\right)S_{21}\left(t+\frac{T_m}{2}\right)+S_{23}\left(t+\frac{T_m}{2}\right)S_{31}\left(t+\frac{T_m}{2}\right)\right]V_1^+\left(t+\frac{T_m}{2}\right)\\
+\left[S_{22}\left(t+\frac{T_m}{2}\right)S_{22}\left(t+\frac{T_m}{2}\right)+S_{23}\left(t+\frac{T_m}{2}\right)S_{32}\left(t+\frac{T_m}{2}\right)\right]\\
\times\left[\left(S_{22}S_{21}+S_{23}S_{31}\right)V_1^+(t)+\left(S_{22}S_{22}+S_{23}S_{32}\right)V_a^-(t)+\left(S_{22}S_{23}+S_{23}S_{33}\right)V_b^-(t)\right]\\
+\left[S_{22}\left(t+\frac{T_m}{2}\right)S_{23}\left(t+\frac{T_m}{2}\right)+S_{23}\left(t+\frac{T_m}{2}\right)S_{33}\left(t+\frac{T_m}{2}\right)\right]\\
\times\left[\left(S_{32}S_{21}+S_{33}S_{31}\right)V_1^+(t)+\left(S_{32}S_{22}+S_{33}S_{32}\right)V_a^-(t)+\left(S_{32}S_{23}+S_{33}S_{33}\right)V_b^-(t)\right],\\
V_b^-(t)\exp(j\omega T_m)=\left[S_{32}\left(t+\frac{T_m}{2}\right)S_{21}\left(t+\frac{T_m}{2}\right)+S_{33}\left(t+\frac{T_m}{2}\right)S_{31}\left(t+\frac{T_m}{2}\right)\right]V_1^+\left(t+\frac{T_m}{2}\right)\\
+\left[S_{32}\left(t+\frac{T_m}{2}\right)S_{22}\left(t+\frac{T_m}{2}\right)+S_{33}\left(t+\frac{T_m}{2}\right)S_{32}\left(t+\frac{T_m}{2}\right)\right]\\
\times\left[\left(S_{22}S_{21}+S_{23}S_{31}\right)V_1^+(t)+\left(S_{22}S_{22}+S_{23}S_{32}\right)V_a^-(t)+\left(S_{22}S_{23}+S_{23}S_{33}\right)V_b^-(t)\right]\\
+\left[S_{32}\left(t+\frac{T_m}{2}\right)S_{23}\left(t+\frac{T_m}{2}\right)+S_{33}\left(t+\frac{T_m}{2}\right)S_{33}\left(t+\frac{T_m}{2}\right)\right]\\
\times\left[\left(S_{32}S_{21}+S_{33}S_{31}\right)V_1^+(t)+\left(S_{32}S_{22}+S_{33}S_{32}\right)V_a^-(t)+\left(S_{32}S_{23}+S_{33}S_{33}\right)V_b^-(t)\right].
\end{cases}
\tag{8.53}
$$

We solve the linear equations (8.49) and (8.53) together and get the solutions of V_a^+, V_b^+, V_a^-, V_b^-. Then, the reflected signals and transmitted signals can be expressed as a linear combination of the above known signals

$$
\begin{cases}
V_1^-(t)=S_{11}(t)+S_{12}(t)V_a^-(t)+S_{13}(t)V_b^-,\\
V_2^-(t)=\left[S_{12}(t)V_a^+(t)+S_{13}(t)V_b^+\right]e^{-j\omega\frac{T_m}{4}},
\end{cases}
\tag{8.54}
$$

The frequency-domain scattering parameters of the fundamental tone is essentially the time-average value of the envelope of the above equation, which can be easily obtained

$$\mathscr{S}_{11}(\omega)=\frac{\left(1+\mathrm{e}^{j\omega\frac{T_m}{2}}\right)R\left[8-3R+\mathrm{e}^{j\omega\frac{T_m}{2}}(8+3R)\right]}{-16\mathrm{e}^{j\omega\frac{T_m}{2}}(-4+R)-R^2+\mathrm{e}^{j\omega T_m}(8+3R)^2},$$
$$\mathscr{S}_{21}(\omega)=\frac{8\mathrm{e}^{j\omega\frac{T_m}{4}}\left[8-4R+4\mathrm{e}^{j\omega\frac{T_m}{2}}(R^2+4R+8)\right]}{-16\mathrm{e}^{j\omega\frac{T_m}{2}}(-4+R)-R^2+\mathrm{e}^{j\omega T_m}(8+3R)^2}. \quad (8.55)$$

We follow the same procedures for excitation at port 2 and figure out the scattering parameters

$$\mathscr{S}_{22}(\omega)=\frac{\left(1+\mathrm{e}^{j\omega\frac{T_m}{2}}\right)R\left[8-3R+\mathrm{e}^{j\omega\frac{T_m}{2}}(8+3R)\right]}{-16\mathrm{e}^{j\omega\frac{T_m}{2}}(-4+R)-R^2+\mathrm{e}^{j\omega T_m}(8+3R)^2},$$
$$\mathscr{S}_{12}(\omega)=\frac{8\mathrm{e}^{j\omega\frac{T_m}{4}}\left[8+(-4+R)R+4\mathrm{e}^{j\omega\frac{T_m}{2}}(2+R)\right]}{-16\mathrm{e}^{j\omega\frac{T_m}{2}}(-4+R)-R^2+\mathrm{e}^{j\omega T_m}(8+3R)^2}. \quad (8.56)$$

Equations (8.55) and (8.56) are the major results of this section. They will degenerate to Eq. (5.33) in the main text at operational frequency $\omega=(2k+1)\omega_m$, $k=0,\ 1,\ 2,\ 3...$

4. SYNCHRONIZATION ANALYSIS OF SINGLY-BALANCED ISOLATOR

In this appendix, we will perform a rigorous time and frequency analysis of a single branch isolator with timing error. Assume that port 1 is excited with a monochromatic signal $\exp(j\omega t)$. In the first half modulation period, most of the signal passes through the second switch with time delay $T_m/4$, apart from a small tail that experiences partial transmission through port 2. The mismatched tail is partially reflected at port 2 and bounces back to port 1 with another partial reflection at port 1. The partially reflected signal is transmitted through the transmission line again and fully transports through the

second switch. In the second half modulation period, a small tail experiences partial transmission through port 1 and fully transmits through port 2 due to time mismatch. However, most of the signal during this modulation period is partially transmitted through switch 1 and switch 2 with transmission coefficient T^2. The reflected signal at port 1 can be analyzed in a similar way, and we summarize the responses for excitation from port 1 below:

$$\begin{cases} V_2^-(t) = V_1^+\left(t-\dfrac{T_m}{4}\right)\left[\xi_1(t)+\mathrm{T}\,\xi_2(t)+\mathrm{T}\,\xi_2\left(t-\dfrac{T_m}{2}\right)\right] \\ +\Gamma^2 V_1^+\left(t-\dfrac{3T_m}{4}\right)\xi_2\left(t-\dfrac{T_m}{2}\right)+\mathrm{T}^2 V_1^+\left(t-\dfrac{3T_m}{4}\right)\xi_1\left(t-\dfrac{T_m}{2}\right), \\ V_1^-(t) = \Gamma\mathrm{T}V_1^+\left(t-\dfrac{T_m}{2}\right)\xi_2\left(t-\dfrac{T_m}{4}\right)+\Gamma V_1^+(t)\left[1-P_1(t)\right]+\Gamma\mathrm{T}V_1^+\left(t-\dfrac{T_m}{2}\right)\xi_1\left(t-\dfrac{3T_m}{4}\right), \end{cases}$$

(8.57)

where $\xi_1(t)$ and $\xi_2(t)$ are envelopes of the modulated signal [see Fig. 5.19], $V_2^-(t)$ is the transmitted signal, and $V_1^-(t)$ is the reflected signal at port 1. The above temporal responses at port 1 can be analyzed to a Fourier series as

$$\begin{cases} V_2^-(t) = \displaystyle\sum_{n\neq 0}\frac{j^{n+1}(1-\mathrm{T})\left[1-(-1)^n\mathrm{T}\right]\left[1-(-1)^n e^{-jn\omega|\Delta\tau|}\right]}{2n\pi}e^{-j\omega\frac{T_m}{4}}e^{j(\omega+n\omega_m)t}+\left(\frac{1+\mathrm{T}^2}{2}-\Gamma^2\frac{|\Delta\tau|}{T_m}\right)e^{-j\omega\frac{T_m}{4}}e^{j\omega t} \\ +\displaystyle\sum_{n\neq 0}\Gamma^2\frac{j^{n+1}}{2n\pi}\left(-1+e^{-jn\omega|\Delta\tau|}\right)e^{-j\omega\frac{3T_m}{4}}e^{j(\omega+n\omega_m)t}+\Gamma^2\frac{|\Delta\tau|}{T_m}e^{-j\omega\frac{3T_m}{4}}e^{j\omega t}, \\ V_1^-(t) = \displaystyle\sum_{n\neq 0}\frac{j\left[-1+(-1)^n\right]e^{-jn\omega|\Delta\tau|}}{2n\pi}\Gamma\mathrm{T}e^{-j\omega\frac{T_m}{2}}e^{j(\omega+n\omega_m)t}+\frac{\Gamma\mathrm{T}}{2}e^{-j\omega\frac{T_m}{2}}e^{j\omega t} \\ +\displaystyle\sum_{n\neq 0}\frac{j\Gamma\left[1-(-1)^n\right]}{2n\pi}e^{j(\omega+n\omega_m)t}+\frac{\Gamma}{2}e^{j\omega t}. \end{cases} \quad (8.58)$$

For monochromatic excitation $\exp(j\omega t)$ at port 2, most of the signal is fully transmitted through switch 2 and partially transmitted through switch 1. The reflected

signal bounces back and forth and transmits through switch 1 with an amplitude Γ^2. In the first half modulation period, a small desynchronized tail passes through switch 1 without loss. In the second half modulation period, most of the signal is partially transmitted through switch 2 with amplitude T, and then fully transmitted through switch 1. A small tail partially transmits through switch 2 and then partially transmits through switch 1, with an amplitude T^2. The reflected signal at port 2 can be analyzed in a similar way, and we summarize the responses for excitation from port 2 below

$$\begin{cases} V_1^-(t) = V_2^+\left(t-\dfrac{T_m}{4}\right)\left[\xi_3(t)+\mathrm{T}\,\xi_4(t)+\mathrm{T}\,\xi_4\left(t-\dfrac{T_m}{2}\right)\right] \\ +\Gamma^2 V_2^+\left(t-\dfrac{3T_m}{4}\right)\xi_4\left(t-\dfrac{T_m}{2}\right)+\mathrm{T}^2 V_2^+\left(t-\dfrac{T_m}{4}\right)\xi_3\left(t-\dfrac{T_m}{2}\right), \\ V_2^-(t) = \Gamma\mathrm{T}V_2^+\left(t-\dfrac{T_m}{2}\right)P_2(t)+\Gamma V_2^+(t)\left[1-P_2\left(t-|\Delta\ \tau|\right)\right], \end{cases} \tag{8.59}$$

where $\xi_3(t)$ and $\xi_4(t)$ are envelopes of modulated signal [see Fig. 19], $V_1^-(t)$ is transmitted signal, and $V_2^-(t)$ is the reflected signal at port 1. The above temporal responses can be expressed in frequency domain as

$$\begin{cases} V_1^-(t) = \displaystyle\sum_{n\neq 0}\frac{j(1-\mathrm{T})\left[1-(-1)^n\mathrm{T}\right]\left(-1+e^{-jn\omega|\Delta\ \tau|}\right)}{2n\pi}e^{-j\omega\frac{T_m}{4}}e^{j(\omega+n\omega_m)t}+\left(\mathrm{T}+\Gamma^2\frac{|\Delta\ \tau|}{T_m}\right)e^{-j\omega\frac{T_m}{4}}e^{j\omega t} \\ \displaystyle\sum_{n\neq 0}\frac{j\Gamma^2}{2n\pi}\left[(-1)^n-e^{-jn\omega|\Delta\ \tau|}\right]e^{-j\omega\frac{3T_m}{4}}e^{j(\omega+n\omega_m)t}+\frac{\Gamma^2}{2}\left(1-\frac{2|\Delta\ \tau|}{T_m}\right)e^{-j\omega\frac{3T_m}{4}}e^{j\omega t}, \\ V_2^-(t) = \displaystyle\sum_{n\neq 0}\frac{\Gamma\sin\frac{n\pi}{2}}{n\pi}\left(e^{-jn\omega|\Delta\ \tau|}+\mathrm{T}e^{-j\omega\frac{T_m}{2}}\right)e^{j(\omega+n\omega_m)t} \\ +\dfrac{\Gamma\mathrm{T}}{2}e^{-j\omega\frac{T_m}{2}}e^{j\omega t}+\dfrac{\Gamma}{2}e^{j\omega t}. \end{cases} \tag{8.60}$$

In summary, we have analyzed the temporal as well as frequency responses of a desynchronized single branch isolator. Equations (8.58) and (8.60) are our major results and they become Eqs. (8.42)-(8.45) when the timing error is zero.

5. SYNCHRONIZATION ANALYSIS OF ULTRA-BALANCED ISOLATOR

When there's timing error in the ultra-broadband isolator, we transform the time-domain responses into Fourier series:

$$V_2^-(t)=\sum_{n\neq 0}\frac{j\cos\frac{n\pi}{2}\left[1-e^{-jn\omega_m|\Delta\ \tau|}\right]}{n\pi}e^{j(\omega+n\omega_m)t}e^{-j\omega\frac{T_m}{4}}+\left(1-\frac{2|\Delta\ \tau|}{T_m}\right)e^{-j\omega\frac{T_m}{4}}e^{j\omega t}, \tag{8.61}$$

$$V_1^-(t)=0, \tag{8.62}$$

$$V_1^-(t)=\sum_{n\neq 0}\frac{-j\left[1+(-1)^n\right]\left[1-e^{-jn\omega_m|\Delta\ \tau|}\right]}{2n\pi}e^{j(\omega+n\omega_m)t}e^{-j\omega\frac{T_m}{4}}+\frac{2|\Delta\ \tau|}{T_m}e^{-j\omega\frac{T_m}{4}}e^{j\omega t}, \tag{8.63}$$

$$V_2^-(t)=0. \tag{8.64}$$

From the above equations, we can infer that the both forward and backward propagation signal share the same IM products distribution, which is enveloped by a sinc function: $2|\Delta\ \tau|/T_m\,\mathrm{sinc}\left(n\pi|\Delta\ \tau|/T_m\right)$. Fig. 5.14 demonstrates the IM products of this isolator with relative timing error $|\Delta\ \tau|/T_m=0.1$. The fundamental tone of the forward transmission signal is 0.8, while the fundamental of the backward transmission signal is 0.2.

6. ANALYSIS OF SINGLY-BALANCED CIRCULATOR

In this appendix, we will present a rigorous temporal and frequency domain analysis of the singly-balanced circulator. Assume that the network is excited with a monochromatic signal $V_1^+(t)=\exp(j\omega t)$ at port 1. Then, we have the following relation:

$$\begin{bmatrix}V_1^-(t)\\V_b^+(t)\\V_a^+(t)\end{bmatrix}=S(t)\begin{bmatrix}V_1^+(t)\\V_b^-(t)\\V_a^-(t-T_m/2)\end{bmatrix}, \tag{9.1}$$

where time-domain scattering parameters is

$$S(t)=\begin{bmatrix} -\frac{1}{3} & \frac{2}{3} & \frac{2}{3} \\ \frac{2}{3} & -\frac{1}{3} & \frac{2}{3} \\ \frac{2}{3} & \frac{2}{3} & -\frac{1}{3} \end{bmatrix}, \tag{9.2}$$

Meanwhile, at port 2 we have

$$\begin{bmatrix} V_2^-(t) \\ V_c^+(t) \\ V_a^-(t) \end{bmatrix} = S(t) \begin{bmatrix} 0 \\ V_c^-(t) \\ V_a^+(t-T_m) \end{bmatrix}. \tag{9.3}$$

At port 3, we have

$$\begin{bmatrix} V_3^-(t) \\ V_b^-\left(t+\frac{T_m}{4}\right) \\ V_c^-\left(t+\frac{T_m}{4}\right) \end{bmatrix} = S(t) \begin{bmatrix} 0 \\ V_b^+\left(t-\frac{T_m}{4}\right) \\ V_c^+\left(t-\frac{T_m}{4}\right) \end{bmatrix}. \tag{9.4}$$

Since the scattering parameters are time-independent, we can perform a Fourier-transform over Eqs. (9.1), (9.3) and (9.4). The matrix form of these equations is

$$\begin{bmatrix} 0 & -1 & 0 & S_{23}e^{-j\omega\frac{T_m}{2}} & S_{22} & 0 \\ -1 & 0 & 0 & S_{33}e^{-j\omega\frac{T_m}{2}} & S_{32} & 0 \\ 0 & S_{22}e^{-j\omega\frac{T_m}{2}} & S_{23}e^{-j\omega\frac{T_m}{2}} & 0 & -1 & 0 \\ 0 & S_{32}e^{-j\omega\frac{T_m}{2}} & S_{33}e^{-j\omega\frac{T_m}{2}} & 0 & 0 & -1 \\ S_{23}e^{-j\omega T_m} & 0 & -1 & 0 & 0 & S_{22} \\ S_{33}e^{-j\omega T_m} & 0 & 0 & -1 & 0 & S_{32} \end{bmatrix} \begin{bmatrix} V_a^+(\omega) \\ V_b^+(\omega) \\ V_c^+(\omega) \\ V_a^-(\omega) \\ V_b^-(\omega) \\ V_c^-(\omega) \end{bmatrix} = \begin{bmatrix} -S_{21}V_1^+(\omega) \\ -S_{31}V_1^+(\omega) \\ 0 \\ 0 \\ 0 \\ 0 \end{bmatrix}. \tag{9.5}$$

We solve the above linear equation, substitute the solution into (9.1), (9.3), and (9.4), and get the scattering parameters

$$\begin{cases} \mathscr{S}_{11}(\omega) = -\dfrac{2+5\cos\left(\dfrac{\pi\ \omega}{\omega_m}\right)+3\cos\left(\dfrac{2\pi\ \omega}{\omega_m}\right)+j6\sin\left(\dfrac{\pi\ \omega}{\omega_m}\right)+j6\sin\left(\dfrac{2\pi\ \omega}{\omega_m}\right)}{6+11\cos\left(\dfrac{\pi\ \omega}{\omega_m}\right)+13\cos\left(\dfrac{2\pi\ \omega}{\omega_m}\right)+j10\sin\left(\dfrac{\pi\ \omega}{\omega_m}\right)+j14\sin\left(\dfrac{2\pi\ \omega}{\omega_m}\right)}, \\ \mathscr{S}_{21}(\omega) = -\dfrac{2\left[5+5\cos\left(\dfrac{\pi\ \omega}{\omega_m}\right)-j\sin\left(\dfrac{\pi\ \omega}{\omega_m}\right)\right]}{6+11\cos\left(\dfrac{\pi\ \omega}{\omega_m}\right)+13\cos\left(\dfrac{2\pi\ \omega}{\omega_m}\right)+j10\sin\left(\dfrac{\pi\ \omega}{\omega_m}\right)+j14\sin\left(\dfrac{2\pi\ \omega}{\omega_m}\right)}, \\ \mathscr{S}_{31}(\omega) = \dfrac{4\left[3\cos\left(\dfrac{\pi\ \omega}{2\omega_m}\right)+2\cos\left(\dfrac{3\pi\ \omega}{2\omega_m}\right)-j\sin\left(\dfrac{\pi\ \omega}{2\omega_m}\right)+j\sin\left(\dfrac{3\pi\ \omega}{2\omega_m}\right)\right]}{6+11\cos\left(\dfrac{\pi\ \omega}{\omega_m}\right)+13\cos\left(\dfrac{2\pi\ \omega}{\omega_m}\right)+j10\sin\left(\dfrac{\pi\ \omega}{\omega_m}\right)+j14\sin\left(\dfrac{2\pi\ \omega}{\omega_m}\right)}. \end{cases}$$

(9.6)

We execute similar analyses at port 2 and port 3 and get the scattering parameters

$$\begin{cases} \mathscr{S}_{12}(\omega) = -\dfrac{2\left[3+7\cos\left(\dfrac{\pi\ \omega}{\omega_m}\right)+j3\sin\left(\dfrac{\pi\ \omega}{\omega_m}\right)\right]}{6+11\cos\left(\dfrac{\pi\ \omega}{\omega_m}\right)+13\cos\left(\dfrac{2\pi\ \omega}{\omega_m}\right)+j10\sin\left(\dfrac{\pi\ \omega}{\omega_m}\right)+j14\sin\left(\dfrac{2\pi\ \omega}{\omega_m}\right)}, \\ \mathscr{S}_{22}(\omega) = -\dfrac{2+5\cos\left(\dfrac{\pi\ \omega}{\omega_m}\right)+3\cos\left(\dfrac{2\pi\ \omega}{\omega_m}\right)+j6\sin\left(\dfrac{\pi\ \omega}{\omega_m}\right)+j6\sin\left(\dfrac{2\pi\ \omega}{\omega_m}\right)}{6+11\cos\left(\dfrac{\pi\ \omega}{\omega_m}\right)+13\cos\left(\dfrac{2\pi\ \omega}{\omega_m}\right)+j10\sin\left(\dfrac{\pi\ \omega}{\omega_m}\right)+j14\sin\left(\dfrac{2\pi\ \omega}{\omega_m}\right)}, \\ \mathscr{S}_{32}(\omega) = \dfrac{4\cos\left(\dfrac{\pi\ \omega}{2\omega_m}\right)\left[1+4\cos\left(\dfrac{\pi\ \omega}{\omega_m}\right)+j2\sin\left(\dfrac{\pi\ \omega}{\omega_m}\right)\right]}{6+11\cos\left(\dfrac{\pi\ \omega}{\omega_m}\right)+13\cos\left(\dfrac{2\pi\ \omega}{\omega_m}\right)+j10\sin\left(\dfrac{\pi\ \omega}{\omega_m}\right)+j14\sin\left(\dfrac{2\pi\ \omega}{\omega_m}\right)}. \end{cases}$$

(9.7)

and

$$\begin{cases} \mathscr{S}_{13}(\omega) = \dfrac{4\cos\left(\dfrac{\pi\,\omega}{2\omega_m}\right)\left[1+4\cos\left(\dfrac{\pi\,\omega}{\omega_m}\right)+j2\sin\left(\dfrac{\pi\,\omega}{\omega_m}\right)\right]}{6+11\cos\left(\dfrac{\pi\,\omega}{\omega_m}\right)+13\cos\left(\dfrac{2\pi\,\omega}{\omega_m}\right)+j10\sin\left(\dfrac{\pi\,\omega}{\omega_m}\right)+j14\sin\left(\dfrac{2\pi\,\omega}{\omega_m}\right)}, \\ \mathscr{S}_{23}(\omega) = \dfrac{4\left[3\cos\left(\dfrac{\pi\,\omega}{2\omega_m}\right)+2\cos\left(\dfrac{3\pi\,\omega}{2\omega_m}\right)-j\sin\left(\dfrac{\pi\,\omega}{2\omega_m}\right)+j\sin\left(\dfrac{3\pi\,\omega}{2\omega_m}\right)\right]}{6+11\cos\left(\dfrac{\pi\,\omega}{\omega_m}\right)+13\cos\left(\dfrac{2\pi\,\omega}{\omega_m}\right)+j10\sin\left(\dfrac{\pi\,\omega}{\omega_m}\right)+j14\sin\left(\dfrac{2\pi\,\omega}{\omega_m}\right)}, \\ \mathscr{S}_{33}(\omega) = -\dfrac{2+5\cos\left(\dfrac{\pi\,\omega}{\omega_m}\right)+3\cos\left(\dfrac{2\pi\,\omega}{\omega_m}\right)+j10\sin\left(\dfrac{\pi\,\omega}{\omega_m}\right)+j6\sin\left(\dfrac{2\pi\,\omega}{\omega_m}\right)}{6+11\cos\left(\dfrac{\pi\,\omega}{\omega_m}\right)+13\cos\left(\dfrac{2\pi\,\omega}{\omega_m}\right)+j10\sin\left(\dfrac{\pi\,\omega}{\omega_m}\right)+j14\sin\left(\dfrac{2\pi\,\omega}{\omega_m}\right)}. \end{cases}$$

(9.8)

Equations (9.6)-(9.8) are the major results of this section. They transform into Eq. (5.37) at operational frequency $\omega=(2k+1)\omega_m$, $k=0,\ 1,\ 2,\ 3\cdots$.

7. ANALYSIS OF DOUBLY-BALANCED CIRCULATOR

In this appendix, we will present a rigorous temporal and frequency domain analysis of the doubly-balanced circulator. Assume that the network is excited with a monochromatic signal $V_1^+(t)=\exp(j\omega t)$ at port 1. Then, we have the following relation:

$$\begin{bmatrix} V_1^-(t) \\ V_b^+(t) \\ V_a^+(t) \end{bmatrix} = S(t) \begin{bmatrix} V_1^+(t) \\ V_b^-(t) \\ V_a^-(t-T_m/2) \end{bmatrix}, \tag{9.9}$$

where time-domain scattering parameters is

$$S(t)=\begin{bmatrix} -\frac{1}{3} & \frac{2}{3} & \frac{2}{3} \\ \frac{2}{3} & -\frac{1}{3} & \frac{2}{3} \\ \frac{2}{3} & \frac{2}{3} & -\frac{1}{3} \end{bmatrix}, \tag{9.10}$$

Meanwhile, at port 2 we have

$$\begin{bmatrix} V_2^-(t) \\ V_c^+(t) \\ V_a^-(t) \end{bmatrix} = S(t) \begin{bmatrix} 0 \\ V_c^-(t) \\ -V_a^+\left(t-\frac{T_m}{2}\right) \end{bmatrix}. \tag{9.11}$$

At port 3, we have

$$\begin{bmatrix} V_3^-(t) \\ V_b^-\left(t+\frac{T_m}{4}\right) \\ V_c^-\left(t+\frac{T_m}{4}\right) \end{bmatrix} = S(t) \begin{bmatrix} 0 \\ V_b^+\left(t-\frac{T_m}{4}\right) \\ V_c^+\left(t-\frac{T_m}{4}\right) \end{bmatrix}. \tag{9.12}$$

Since the scattering parameters are time-independent, we can perform a Fourier-transform over Eqs. (9.9), (9.11) and (9.12). The matrix form of these equations is

$$\begin{bmatrix} 0 & -1 & 0 & S_{23}e^{-j\omega\frac{T_m}{2}} & S_{22} & 0 \\ -1 & 0 & 0 & S_{33}e^{-j\omega\frac{T_m}{2}} & S_{32} & 0 \\ 0 & S_{22}e^{-j\omega\frac{T_m}{2}} & S_{23}e^{-j\omega\frac{T_m}{2}} & 0 & -1 & 0 \\ 0 & S_{32}e^{-j\omega\frac{T_m}{2}} & S_{33}e^{-j\omega\frac{T_m}{2}} & 0 & 0 & -1 \\ -S_{23}e^{-j\omega\frac{T_m}{4}} & 0 & -1 & 0 & 0 & S_{22} \\ -S_{33}e^{-j\omega\frac{T_m}{4}} & 0 & 0 & -1 & 0 & S_{32} \end{bmatrix} \begin{bmatrix} V_a^+(\omega) \\ V_b^+(\omega) \\ V_c^+(\omega) \\ V_a^-(\omega) \\ V_b^-(\omega) \\ V_c^-(\omega) \end{bmatrix} = \begin{bmatrix} -S_{21}V_1^+(\omega) \\ -S_{31}V_1^+(\omega) \\ 0 \\ 0 \\ 0 \\ 0 \end{bmatrix}. \tag{9.13}$$

We solve the above linear equation, substitute the solution into (9.9), (9.11) and (9.12), and get the scattering parameters

$$\begin{cases} \mathscr{S}_{11}(\omega) = \dfrac{1-2\cos\left(\dfrac{\pi\,\omega}{\omega_m}\right)-3\cos\left(\dfrac{2\pi\,\omega}{\omega_m}\right)-j6\sin\left(\dfrac{2\pi\,\omega}{\omega_m}\right)}{1-2\cos\left(\dfrac{\pi\,\omega}{\omega_m}\right)+13\cos\left(\dfrac{2\pi\,\omega}{\omega_m}\right)-j4\sin\left(\dfrac{\pi\,\omega}{\omega_m}\right)+j14\sin\left(\dfrac{2\pi\,\omega}{\omega_m}\right)}, \\ \mathscr{S}_{21}(\omega) = \dfrac{4\left[1+\cos\left(\dfrac{\pi\,\omega}{\omega_m}\right)-2j\sin\left(\dfrac{\pi\,\omega}{\omega_m}\right)\right]}{1-2\cos\left(\dfrac{\pi\,\omega}{\omega_m}\right)+13\cos\left(\dfrac{2\pi\,\omega}{\omega_m}\right)-j4\sin\left(\dfrac{\pi\,\omega}{\omega_m}\right)+j14\sin\left(\dfrac{2\pi\,\omega}{\omega_m}\right)}, \\ \mathscr{S}_{31}(\omega) = \dfrac{4\left[2\cos\left(\dfrac{3\pi\,\omega}{2\omega_m}\right)-3j\sin\left(\dfrac{\pi\,\omega}{2\omega_m}\right)+j\sin\left(\dfrac{3\pi\,\omega}{2\omega_m}\right)\right]}{1-2\cos\left(\dfrac{\pi\,\omega}{\omega_m}\right)+13\cos\left(\dfrac{2\pi\,\omega}{\omega_m}\right)-j4\sin\left(\dfrac{\pi\,\omega}{\omega_m}\right)+j14\sin\left(\dfrac{2\pi\,\omega}{\omega_m}\right)}. \end{cases} \tag{9.14}$$

We execute similar analyses at port 2 and port 3 and get the scattering parameters

$$\begin{cases} \mathscr{S}_{12}(\omega)=\dfrac{4\left[-1+3\cos\left(\dfrac{\pi\,\omega}{\omega_m}\right)+2j\sin\left(\dfrac{\pi\,\omega}{\omega_m}\right)\right]}{1-2\cos\left(\dfrac{\pi\,\omega}{\omega_m}\right)+13\cos\left(\dfrac{2\pi\,\omega}{\omega_m}\right)-j4\sin\left(\dfrac{\pi\,\omega}{\omega_m}\right)+j14\sin\left(\dfrac{2\pi\,\omega}{\omega_m}\right)}, \\ \mathscr{S}_{22}(\omega)=\dfrac{1-2\cos\left(\dfrac{\pi\,\omega}{\omega_m}\right)-3\cos\left(\dfrac{2\pi\,\omega}{\omega_m}\right)-j6\sin\left(\dfrac{2\pi\,\omega}{\omega_m}\right)}{1-2\cos\left(\dfrac{\pi\,\omega}{\omega_m}\right)+13\cos\left(\dfrac{2\pi\,\omega}{\omega_m}\right)-j4\sin\left(\dfrac{\pi\,\omega}{\omega_m}\right)+j14\sin\left(\dfrac{2\pi\,\omega}{\omega_m}\right)}, \\ \mathscr{S}_{32}(\omega)=\dfrac{4\left[2\cos\left(\dfrac{3\pi\,\omega}{2\omega_m}\right)+j\sin\left(\dfrac{\pi\,\omega}{2\omega_m}\right)+j\sin\left(\dfrac{3\pi\,\omega}{2\omega_m}\right)\right]}{1-2\cos\left(\dfrac{\pi\,\omega}{\omega_m}\right)+13\cos\left(\dfrac{2\pi\,\omega}{\omega_m}\right)-j4\sin\left(\dfrac{\pi\,\omega}{\omega_m}\right)+j14\sin\left(\dfrac{2\pi\,\omega}{\omega_m}\right)}. \end{cases} \tag{9.15}$$

and

$$\begin{cases} \mathscr{S}_{13}(\omega)=\dfrac{4\left[2\cos\left(\dfrac{3\pi\,\omega}{2\omega_m}\right)+j\sin\left(\dfrac{\pi\,\omega}{2\omega_m}\right)+j\sin\left(\dfrac{3\pi\,\omega}{2\omega_m}\right)\right]}{1-2\cos\left(\dfrac{\pi\,\omega}{\omega_m}\right)+13\cos\left(\dfrac{2\pi\,\omega}{\omega_m}\right)-j4\sin\left(\dfrac{\pi\,\omega}{\omega_m}\right)+j14\sin\left(\dfrac{2\pi\,\omega}{\omega_m}\right)}, \\ \mathscr{S}_{23}(\omega)=\dfrac{4\left[2\cos\left(\dfrac{3\pi\,\omega}{2\omega_m}\right)-3j\sin\left(\dfrac{\pi\,\omega}{2\omega_m}\right)+j\sin\left(\dfrac{3\pi\,\omega}{2\omega_m}\right)\right]}{1-2\cos\left(\dfrac{\pi\,\omega}{\omega_m}\right)+13\cos\left(\dfrac{2\pi\,\omega}{\omega_m}\right)-j4\sin\left(\dfrac{\pi\,\omega}{\omega_m}\right)+j14\sin\left(\dfrac{2\pi\,\omega}{\omega_m}\right)}, \\ \mathscr{S}_{33}(\omega)=\dfrac{1-2\cos\left(\dfrac{\pi\,\omega}{\omega_m}\right)-3\cos\left(\dfrac{2\pi\,\omega}{\omega_m}\right)-j4\sin\left(\dfrac{\pi\,\omega}{\omega_m}\right)-j6\sin\left(\dfrac{2\pi\,\omega}{\omega_m}\right)}{1-2\cos\left(\dfrac{\pi\,\omega}{\omega_m}\right)+13\cos\left(\dfrac{2\pi\,\omega}{\omega_m}\right)-j4\sin\left(\dfrac{\pi\,\omega}{\omega_m}\right)+j14\sin\left(\dfrac{2\pi\,\omega}{\omega_m}\right)}. \end{cases} \tag{9.16}$$

Equations (9.14)-(9.16) are the major results of this section. They transform into Eq. (5.37) at operational frequency $\omega=(2k+1)\omega_m$, $k=0,\ 1,\ 2,\ 3\cdots$.

8. ANALYSIS OF SYNCHRONIZATION OF DOUBLY-BALANCED CIRCULATOR

With timing error, the Fourier series at three ports can be expressed as

$$V_1^-(t) = 0, \tag{9.17}$$

$$V_2^-(t) = \sum_{n\neq 0} \frac{j\cos\frac{n\pi}{2}\left[1-\exp\left(-jn\omega_m\left|\Delta\ \tau\right|\right)\right]}{n\pi} e^{j(\omega+n\omega_m)t} e^{-j\omega\frac{T_m}{4}} + \left(1-\frac{2\left|\Delta\ \tau\right|}{T_m}\right) e^{-j\omega\frac{T_m}{4}} e^{j\omega t}, \tag{9.18}$$

$$V_3^-(t) = \sum_{n\neq 0} \frac{-j\left[1+(-1)^n\right]\left[1-\exp\left(-jn\omega_m\left|\Delta\ \tau\right|\right)\right]}{2n\pi} e^{j(\omega+n\omega_m)t} e^{-j\omega\frac{T_m}{2}} + \frac{2\left|\Delta\ \tau\right|}{T_m} e^{-j\omega\frac{T_m}{2}} e^{j\omega t}. \tag{9.19}$$

The above equation indicates that the ultra-broadband circulator has the same IM products compared with ultra-broadband isolator.

Bibliography

[1] N. Engheta and R. W. Ziolkowski, *Metamateirals: physics and engineering explorations* (John & Sons, 2006).

[2] W. Cai and V. Shalaev, Optical metamaterials: fundamentals and applications (Springer, 2010).

[3] A. Alù, M. G. Silveirinha, A. Salandrino, and N. Engheta, Epsilon-near-zero metamaterials and electromagnetic sources: Tailoring the radiation phase pattern, Phys. Rev. B **75**, 155410 (2007).

[4] O. Reshef, I. De Leon, M. Z. Alam, and R. W. Boyd, Nonlinear optical effects in epsilon-near-zero media, Nat. Rev. Materials **4**, 535 (2019).

[5] X. Niu, X. Hu, S. Chu, and Q. Gong, Epsilon-near-zero photonics: a new platform for integrated devices, Adv. Opt. Materials **6**, 1701292 (2018).

[6] H.-T. Chen, A. J. Taylor, and N. Yu, A review of metasurfaces: physics and applications, Reports on Progress in Physics **79**, 076401 (2016).

[7] N. Yu and F. Capasso, Flat optics with designer metasurfaces, Nature Materials **13**, 139 (2014).

[8] S. B. Glybovski, S. A. Tretyakov, P. A. Belov, Y. S. Kivshar, and C. R. Simovski, Metasurfaces: From microwaves to visible, Physics Reports 634, 1 (2016).

[9] C. M. Bender and S. Boettcher, Real spectra in non-Hermitian hamiltonians having PT symmetry, PT-symmetric quantum mechanics, Physical Review Letters **80**, 5243 (1998).

[10] C. M. Bender, S. Boettcher, and P. N. Meisinger, PT-symmetric quantum mechanics, Journal of Mathematical Physics **40**, 2201 (1999).

[11] C. M. Bender, D. C. Brody, and H. F. Jones, Complex extension of quantum mechanics, Physical Review Letters **89**, 270401 (2002).

[12] L. Feng, R. El-Ganainy, and L. Ge, Non-Hermitian photonics based on parity–time symmetry, Nature Photonics **11**, 752 (2017).

[13] R. El-Ganainy, K. G. Makris, M. Khajavikhan, Z. H. Musslimani, S. Rotter, and D. N. Christodoulides, Non-Hermitian physics and PT symmetry, Nature Physics **14**, 11 (2018).

[14] Ş. K. Özdemir, S. Rotter, F. Nori, and L. Yang, Parity–time symmetry and exceptional points in photonics, Nature Materials **18**, 783 (2019).

[15] C. Caloz and Z. Deck-Léger, Spacetime metamaterials—Part I: General concepts, IEEE Transactions on Antennas and Propagation **68**, 1569 (2020).

[16] C. Caloz and Z. Deck-Léger, Spacetime metamaterials—Part II: Theory and applications, IEEE Transactions on Antennas and Propagation **68**, 1583 (2020).

[17] S. Taravati and A. A. Kishk, Space-Time Modulation: Principles and Applications IEEE Microwave Magazine **21**, 30 (2020).

[18] A. Nagulu, N. Reiskarimian, and H. Krishnaswamy, Non-reciprocal electronics based on temporal modulation Nature Electronics **3**, 241 (2020).

[19] I. A. D. Williamson, M. Minkov, A. Dutt, J. Wang, A. Y. Song, and S. Fan, Integrated nonreciprocal photonic devices with dynamic modulation, Proceedings of the IEEE **108**, 1759 (2020).

[20] V. S. Asadchy, M. S. Mirmoosa, A. Díaz-Rubio, S. Fan, and S. A. Tretyakov, Tutorial on electromagnetic nonreciprocity and its origins, Proceedings of the IEEE **108**, 1684 (2020).

[21] A. Kord, D. L. Sounas, and A. Alù, Microwave nonreciprocity, Proceedings of the IEEE **108**, 1728 (2020).

[22] X. Ni, K. Chen, M. Weiner, D. J. Apigo, C. Prodan, A. Alù, E. Prodan, and A. B. Khanikaev, Observation of Hofstadter butterfly and topological edge states in reconfigurable quasi-periodic acoustic crystals, Communications Physics **2**, 55 (2019).

[23] J. Herzog-Arbeitman, Z.-D. Song, N. Regnault, and B. A. Bernevig, Hofstadter Topology: Noncrystalline Topological Materials at High Flux, Physical Review Letters **125**, 236804 (2020).

[24] A. Silva, F. Monticone, G. Castaldi, V. Galdi, A. Alù, and N. Engheta, Performing Mathematical Operations with Metamaterials, Science **343**, 160 (2014).

[25] H. Kwon, D. Sounas, A. Cordaro, A. Polman, and A. Alù, Nonlocal Metasurfaces for Optical Signal Processing, Physical Review Letters **121**, 173004 (2018).

[26] T. J. Davis, F. Eftekhari, D. E. Gómez, and A. Roberts, Metasurfaces with Asymmetric optical oransfer functions for optical signal processing, Physical Review Letters **123**, 013901 (2019).

[27] Y. Zhou, H. Zheng, I. I. Kravchenko, and J. Valentine, Flat optics for image differentiation, Nature Photonics **14**, 316 (2020).

[28] F. Zangeneh-Nejad, D. L. Sounas, A. Alù, and R. Fleury, Analogue computing with metamaterials, Nature Reviews Materials **6**, 207 (2021).

[29] Z. Lin, H. Ramezani, T. Eichelkraut, T. Kottos, H. Cao, and D. N. Christodoulides, Unidirectional invisibility induced by PT-symmetric periodic structures, Physical Review Letters **106**, 213901 (2011).

[30] R. Fleury, D. L. Sounas, and A. Alù, Negative refraction and planar focusing based on Parity-Time symmetric metasurfaces, Physical Review Letters **113**, 023903 (2014).

[31] F. Monticone, C. A. Valagiannopoulos, and A. Alù, Parity-Time symmetric nonlocal metasurfaces: All-angle negative refraction and volumetric imaging, Physical Review X 6, 041018 (2016).

[32] S. Assawaworrarit, X. Yu, and S. Fan, Robust wireless power transfer using a nonlinear parity–time-symmetric circuit, Nature **546**, 387 (2017).

[33] S. Assawaworrarit and S. Fan, Robust and efficient wireless power transfer using a switch-mode implementation of a nonlinear parity–time symmetric circuit, Nature Electronics **3**, 273 (2020).

[34] Y. D. Chong, L. Ge, and A. D. Stone, PT-symmetry breaking and laser-absorber modes in optical scattering systems, Physical Review Letters **106**, 093902 (2011).

[35] B. Midya and V. V. Konotop, Coherent-perfect-absorber and laser for bound states in a continuum, Optics Letters **43**, 607 (2018).

[36] D. A. Zezyulin, H. Ott, and V. V. Konotop, Coherent perfect absorber and laser for nonlinear waves in optical waveguide arrays, Optics Letters **43**, 5901 (2018).

[37] Z. Xiao, Y. Radi, S. Tretyakov, and A. Alu, Microwave tunneling and robust information transfer based on parity-time-symmetric absorber-emitter Pairs, Research **2019**, 10 (2019).

[38] J. Wiersig, Enhancing the sensitivity of frequency and energy splitting detection by using Exceptional Points: application to microcavity sensors for single-particle detection, Physical Review Letters **112**, 203901 (2014).

[39] J. Wiersig, Review of exceptional point-based sensors, Photon. Res. **8**, 1457 (2020).

[40] M. Parto, Y. G. N. Liu, B. Bahari, M. Khajavikhan, and D. N. Christodoulides, Nanophotonics **10**, 403 (2021).

[41] R. Shankar, *Principles of quantum mechanics* (Springer, 2012).

[42] C. M. Bender, D. C. Brody, and H. F. Jones, Extension of PT-symmetric quantum mechanics to quantum field theory with cubic interaction, Physical Review D **70**, 025001 (2004).

[43] C. M. Bender and S. P. Klevansky, Families of particles with different masses in PT-symmetric quantum field theory, Physical Review Letters **105**, 031601 (2010).

[44] C. E. Ruter, K. G. Makris, R. El-Ganainy, D. N. Christodoulides, M. Segev, and D. Kip, Observation of parity-time symmetry in optics, Nat Phys **6**, 192 (2010).

[45] L. Ge, Y. D. Chong, and A. D. Stone, Conservation relations and anisotropic transmission resonances in one-dimensional PT-symmetric photonic heterostructures, Physical Review A **85**, 023802 (2012).

[46] M. Minkov, Y. Shi, and S. Fan, Exact solution to the steady-state dynamics of a periodically modulated resonator, APL Photonics **2**, 076101 (2017).

[47] M. Minkov and S. Fan, Localization and time-reversal of light through dynamic modulation, Physical Review B **97**, 060301 (2018).

[48] G. B. Arfken, H. J. Weber, and F. E. Harris, *Mathematical methods for physicists: a comprehensive guide* (Academic Press, 2013).

[49] Z. Xiao, H. Li, T. Kottos and A. Alù, Enhanced sensing and nondegraded thermal noise performance based on PT-symmetric electronic circuits with a sixth-order exceptional point. Phys. Rev. Lett. **123**, 213901 (2019).

[50] L. Fortuna, S. Graziani, A. Rizzo, and M. G. Xibilia, *Soft sensors for monitoring and control of industrial processes* (Springer, London, 2007).

[51] K. Chughtai and R. M. A. Heeren, Mass spectrometric imaging for biomedical tissue analysis, Chem. Rev. **110**, 3237 (1010).

[52] F. Juefei-Xu, C. Bhagavatula, A. Jaech, U. Prasad, and M. Savvides, *in 2012 IEEE Fifth International Conference on Biometrics: Theory, Applications and Systems (BTAS)*, 2012.

[53] L. Mainetti, L. Patrono, and A. Vilei, Evolution of wireless sensor networks towards the Internet of Things: A survey, *in 19th International Conference on Software, Telecommunications and Computer Networks*, 2011.

[54] N. Khalil, M. R. Abid, D. Benhaddou, and M. Gerndt, Wireless sensors networks for Internet of Things, in *IEEE Ninth International Conference on Intelligent Sensors, Sensor Networks and Information Processing (ISSNIP), 2014.*

[55] R. Nopper, R. Has, and L. Reindl, A wireless sensor readout system-circuit concept, simulation, and accuracy, IEEE Trans. Instrum. Meas. **60**, 2976 (2011).

[56] J. Zhu, S. K. Ozdemir, Y. F. Xiao *et al.* On-chip single nanoparticle detection and sizing by mode splitting in an ultrahigh-Q microresonator, Nat. Photon. **4**, 46 (2010).

[57] R. Nopper, R. Has, and L. Reindl, A wireless sensor readout system-circuit concept, simulation, and accuracy, IEEE. Trans. Instrum. Meas. 60, 2976 (2011).

[58] M. V. Berry and M. Wilkinson, Diabolical points in the spectra of triangles, Proc. R. Soc. London, Ser. A **392**, 15 (1984).

[59] D. Dubbers and H.-J. Stockmann, *Diabolic points, geometric phases, and quantum chaos (*Springer, Berlin, 2013).

[60] C. M. Bender, Making sense of non-Hermitian Hamiltonians, Rep. Prog. Phys. 70, 947 (2007).

[61] R. El-Ganainy, K. G. Makris, D. N. Christodoulides, and Z. H. Musslimani, Theory of coupled optical PT-symmetric structures, Opt. Lett. **32**, 2632 (2007).

[62] J. Schindler, A. Li, M. C. Zheng, F. M. Ellis, and T. Kottos, Experimental study of active LRC circuits with PT symmetries, Phys. Rev. A **84**, 040101 (2011).

[63] J. Schindler, Z. Lin, J. M. Lee, H. Ramezani, F. M. Ellis, and T. Kottos, PT-symmetric electronics, J. Phys. A: Math. Theor. **45**, 444029 (2012).

[64] R. Fleury, D. Sounas, and A. Alu, An invisible acoustic sensor based on parity-time symmetry, Nat. Commun. **6**, 5905 (2015).

[65] D. L. Sounas, R. Fleury, and A. Alu, Unidirectional cloaking based on metasurfaces with balanced loss and gain, Phys. Rev. Appl. **4**, 014005 (2015).

[66] M.-A. Miri and A. Alu, Exceptional points in optics and photonics, Science **63**, 7709 (2019).

[67] J. Wiersig, Sensors operating at exceptional points: General theory, Phys. Rev. A **93**, 033809 (2016).

[68] W. Chen, S. K. Ozdemir, G. Zhao, J. Wiersig, and L. Yang, Exceptional points enhance sensing in an optical microcavity, Nature **548**, 192 (2017).

[69] H. Hodaei, A. U. Hassan, S. Wittek, H. Garcia-Gracia, R. El-Ganainy, D. N. Christodoulides, and M. Khajavikhan, Enhanced sensitivity at higher order exceptional points, Nature **548**, 187 (2017).

[70] P.-Y. Chen, M. Sakhdari, M. Hajizadegan, Q. Cui, M. M.-C. Cheng, R. El-Ganainy, and A. Alu, Generalized parity-time symmetry condition for enhanced sensor telemetry, Nat. Electron. **1**, 297 (2018).

[71] Z. Dong, Z. Li, F. Yang, C.-W. Qiu, and J. S. Ho, Sensitive readout of implantable microsensors using a wireless system locked to an exceptional point, Nat. Electron. **2** 335 (2019).

[72] K. Kato, *Perturbation theory for linear operators* (Springer, Berlin, 1995).

[73] W. Langbein, No exceptional precision of exceptional-point sensors, Phys. Rev. A **98**, 023805 (2018).

[74] H.-K. Lau and A. A. Clerk, Fundamental limits and non-reciprocal approaches in non-Hermitian quantum sensing, Nat. Commun. **9**, 4320 (2018).

[75] M. Zhang, W. Sweeney, C. W. Hsu, L. Yang, A. D. Stone, and L. Jiang, Quantum noise theory of exceptional point sensors, Phys. Rev. Lett. **123**, 180501 (2019).

[76] C. Chen, L. Jin, and R.-B. Liu, Sensitivity of parameter estimation near the exceptional point of a non-Hermitian system, New J. Phys. **21**, 083002 (2019).

[77] N. A. Mortensen, P. A. D. Gonçalves, M. Khajavikhan, D. N. Christodoulides, C. Tserkezis, and C. Wolff, Fluctuations and noise-limited sensing near the exceptional point of parity-time-symmetric resonator systems Optica **5**, 1342 (2018).

[78] H. Wang, Y.-H. Lai, Z. Yuan, M.-G. Suh, and K. Vahala, Petermann-factor sensitivity limit near an exceptional point in a Brillouin ring laser gyroscope, Nat. Commun. **11**, 1610 (2020).

[79] M. Born and E. Wolf, *Pinciples of optics* (Cambridge University Press, Cambridge, 1997).

[80] J. W. Goodman, *Introduction to Fourier optics* 3rd ed (Roberts and Company Publsihers, Englewood, Colorado, 2004).

[81] D. M. Pozar, *Microwave Engineering* (Wiley, New York, 2011).

[82] H. Nyquist, Thermal agitation of electric charge in conductors, Phys. Rev. **32**, 110 (1928).

[83] R. Kubo, The fluctuation-dissipation theorem, Rep. Prog. Phys. **29**, 255 (1966)

[84] L. Reggiani and E. Alfinito, Fluctuation dissipation theorem and electrical noise revisited, Fluct. Noise Lett. **18**, 1930001 (2019).

[85] P. R. Gray, P. J. Hurst, S. H. Lewis, and R. G. Meyer, *Analysis and design of analog integrated circuits* 5th ed (Wiley, New York, 2009).

[86] Z. Xiao, S. A. Mann, R. Duggan, S. Kim, T. Kottos, and A. Alù, Exceptional point sensing: a gem or a gimmick?, under review.

[87] S. H. Strogatz, Nonlinear Dynamics and Chaos (CRC Press, Taylor & Francis Group, 2014).

[88] J. K. Hale and Hüseyin Koçak, Dynamics and Bifurcations (Springer, New York, 1991).

[89] O. Svelto and D. C. Hanna, Principles of Lasers (Springer, New York, 2010).

[90] H. Haaken, Synergetics (Springer, Berlin, 1983).

[91] A. Yu. Perevaryukha, A model of development of spontaneous outbreak of an insect with aperiodic dynamics, Entomological Rev. 95, 397 (2015).

[92] I. R. Epstein and J. a. Pojman, *An Introduction to Nonlinear Chemical Dynamics: Oscillations, Waves, Patterns, and Chaos* (Oxford University Press, New York, 1998).

[93] X. Zhu, H. Ramezani, C. Shi, J. Zhu, and X. Zhang, PT-symmetric acoustics, Phys. Rev. X 4, 031042 (2014).

[94] R. Fleury, D. Sounas, and A. Alù, An invisible acoustic sensor based on parity-time symmetry, Nat. Commun. 6, 5905 (2015).

[95] C. Shi, M. Dubois, Y. Chen, L. Chen. H. Ramezani, Y. Wang, and X. Zhang, Accessing the exceptional points of parity-time symmetric acoustics, Nat. Comm. 7, 11110 (2016).

[96] T. Stehmann, W. D. Heiss, and F. G. Scholtz, Observation of exceptional points in electronic circuits, J. Phys. A: Math. Gen. 37, 7813 (2004).

[97] K. Kato, *Perturbation Theory for Linear Operators* (Springer, Berlin, 1995).

[98] J. Doppler, A. A. Mailybaev, J. Bohm, U. Kuhl, A. Girschik, F. Libisch, T. J. Milburn, P. Rabl, N. Moiseyev, and Stefan Rotter, Dynamically encircling an exceptional point for asymmetric mode switching, Nature 537, 76 (2016).

[99] H. Xu, D. Mason, L. Jiang and J. G. E. Harris, Topological energy transfer in an optomechanical system with exceptional points, Nature 537, 80 (2016).

[100] A. U. Hassan, B. Zhen, M. Soljacic, M. Khajavikhan and D. N. Christodoulides, Dynamically encircling exceptional points: exact evolution and polarization state conversion, Phys. Rev. Lett. 118, 093002 (2017).

[101] M. P. Hokmabadi, A. Schumer, D. N. Christodoulides and M. Khajavikhan, Non-Hermitian ring laser gyroscopes with enhanced Sagnac sensitivity, Nature 576, 70 (2019).

[102] Y-H. Lai, Y-K. Lu, M-G. Suh, Z. Yuan and K. Vahala, Observation of the exceptional-point-enhanced Sagnac effect, Nature 576, 65 (2019).

[103] J-H. Park, A. Nado, W. Cai, L. Cai, A. Kodigala, T. Lepetit, Y-H Lo, B. Kante, Symmetry-breaking-induced plasmonic exceptional points and nanoscale sensing, Nat. Phys. 16, 462 (2020).

[104] A. Bergman, R. Duggan, K. Sharma, M. Tur, A. Zadok and A. Alù, Observation of anti-parity-time-symmetry, phase transitions, and exceptional points in an optical fibre, Nat. Comm., 12, 486 (2021).

[105] J. Wiersig, Prospects and fundamental limits in exceptional point-based sensing, Nat. Commn., 11, 2454 (2020).

[106] J. Wiersig, Robustness of exceptional-point-based sensors against parametric noise: the role of Hamiltonian and Liouvillian degeneracies, Phys. Rev. A 101, 053846 (2020).

[107] Z. Lin, A. Pick, M. Loncar, A. W. Rodriguez, Enhanced spontaneous emission at third-order Dirac exceptional points in inverse-designed photonic crystals, Phys. Rev. Lett. 117, 107402 (2016).

[108] A. Pick, B. Zhen, O. D. Miller, C. W. Hsu, F. Hernandez, A. W. Rodriguez, M. Soljacic, S. G. Johnson, General theory of spontaneous emission near exceptional points, Opt. Express, 25, 012325 (2017).

[109] D. Pellegrino, D. Balestri, N. Granchi, M. Ciardi, F. Intonti, F. Pagliano, A. Yu, F. W. Otten, T. Wu, K. Vynck, P. Lalanne, A. Fiore, M. Gurioli, Non-Lorentzian local density of states in coupled photonic crystal cavities probed by near-and far-field emission, Phys. Rev. Lett. 124, 123902 (2020).

[110] S. Yu, Y. Meng, J-S. Tang, X-Y. Xu, Y-T. Yang, P. Yin, Z-J. Ke, W. Liu, Z-P. Liu, G. Chen, Y-J. Han, C. F. Li, G-C. Guo, Experimental investigation of quantum PT-enhanced sensor, Phys. Rev. Lett. 125, 240506 (2020).

[111] S. Fan, W. Suh, and J. D. Joannopoulos, Temporal coupled-mode theory for the Fano resonance in optical resonators, J. Opt. Soc. of Am. A 20, 569 (2003).

[112] S. Wonjoo, W. Zheng, and F. Shanhui, Temporal coupled-mode theory and the presence of non-orthogonal modes in lossless multimode cavities, IEEE J. Quantum Electron. 40, 1511 (2004).

[113] Gibson, G. et al. Free-space information transfer using light beams carrying orbital angular momentum. Opt. Express 12, 5448 (2004).

[114] Northup, T. T., & Blatt, R., Quantum information transfer using photons. Nat Photon. 8, 356 (2014).

[115] Clerckx, B. et al. Fundamentals of wireless information and power transfer: from RF energy harvester models to signal and systems designs. IEEE J. Sel. Areas Commun. 37, 4 (2019).

[116] Ng, D. W. K., Lo, E. S., & Schober, R., Robust beamforming for secure communication in systems with wireless information and power transfer. IEEE Trans. Wirel. Commun. 13, 4599 (2014).

[117] Chang, L. L., Esaki, L., & Tsu, R. Resonant tunneling in semiconductor double barriers. Appl. Phys. Lett. 24, 593 (1974).

[118] Hayashi, S., Kurokawa, H., & Oga, H. Observation of resonant photon tunneling in photonic double barrier structures. Opt. Rev. 6, 204 (1999).

[119] Liu, R. et al. Experimental demonstration of electromagnetic tunneling through an epsilon-near-zero metamaterial at microwave frequencies. Phys. Rev. Lett. 100, 023903 (2008).

[120] Edwards, B., Alù, A., Young, M. E., Silveirinha, M. and Engheta, N. Experimental verification of epsilon-near-zero metamaterial coupling and energy squeezing using a microwave waveguide. Phys. Rev. Lett. 100, 033903 (2008).

[121] Kim, S., Ho, J. S., Chen, L. Y. & Poon, A. S. Y. Wireless power transfer to a cardiac implant. Appl. Phys. Lett. 101, 073701 (2012).

[122] Kim, S. et al. Health monitoring of civil infrastructures using wireless sensor networks. Proceedings. 6th International Conference on Information Processing in Sensor Networks. 254 (2007).

[123] Ra'di, Y., Sounnas, D. L., Alù, A. & Tretyakov, S. A. Parity-time-symmetric teleportation. Phys. Rev. B 93, 235127 (2016).

[124] Wimmer, M. et al. Observation of optical solitons in PT-symmetric lattices. Nat. Commun. 6, 7782 (2015).

[125] Jahromi, A.K., Hassan, A.U., Christodoulides, D.N. & Abouraddy, A.F. Statistical parity-time-symmetric lasing in an optical fiber network. Nat. Commun. 8, 1359 (2017).

[126] Regensburger, A. et al. Parity-time synthetic photonic lattices. Nature 488, 167-171 (2012).

[127] Peng, B. et al. Parity-time-symmetric whispering-gallery microcavities. Nat. Phys. 10, 394-398 (2014).

[128] Peng, B. et al. Loss-induced suppression and revival of lasing. Science 346, 328-332 (2014).

[129] Zhang, J. et al. A phonon laser operating at an exceptional point. Nat. Photon. 12, 479-484 (2018).

[130] Chitsazi, M., Li, H., Ellis, F.M. & Kottos, T. Experimental realization of floquet PT-symmetric systems. Phys. Rev. Lett. 119, 093901 (2017).

[131] Ramezani, H., Schindler, J., Ellis, F.M., Günther, U. & Kottos, T. Bypassing the bandwidth theorem with PT symmetry. Phys. Rev. A 85, 062122 (2012).

[132] Kremer, M. et al. Demonstration of a two-dimensional PT-symmetric crystal. Nat. Commun. 10, 435 (2019).

[133] Lv, B. et al. Unidirectional invisibility induced by parity-time symmetric circuit. Sci. Rep. 7, 40575 (2017).

[134] Fante, R. L., & Mccormack M. T., Reflection properties of the Salisbury screen. IEEE Trans. Antennas and Propag. 36, 1443 (1998).

[135] Loncar, J., Hrabar, S. & Muha, D. Stability of simple lumped-distributed networks with negative capacitors. IEEE Trans. Antennas and Propag. 65, 390 (2017).

[136] Ugarte-Munoz, E., Hrabar, S., Segovia-Vargas, D. & Kiricenko, A. Stability of non-Foster reactive elements for use in active metamaterials and antennas. IEEE Trans. Antennas Propag. 60, 3490-3494 (2012).

[137] Alexander, C. K. & Sadiku, M. N. O. *Fundamentals of electric circuits* (McGraw-Hill, New York, 2013).

[138] Z. Xiao, D. L. Sounas, A. Nagulu, M. Tymchenko, T. Dinc, H. Krishnaswamy, and A. Alù, Role of Synchronization in magnetless nonreciprocal devices based on commutated transmission lines, Physical Review Applied **13**, 064033 (2020).

[139] L. Onsager, Reciprocal relations in irreversible processes. I., Phys. Rev. **7**, 405 (1931).

[140] L. Onsager, Reciprocal relations in irreversible processes. II., Phys. Rev. **38**, 2265 (1931).

[141] H. B. G. Casimir, Reciprocity theorems and irreversible processes, Proc. IEEE **51**, 1570 (1963).

[142] C. Caloz, A. Alù, S. Tretyakov, D. Sounas, K. Achouri, and Z-L. D. Leger, Electromagnetic nonreciprocity, Phys. Rev. Appl. **10**, 047001 (2018).

[143] Z. Yu and S. Fan, Complete optical isolation created by indirect interband photonic transitions, Nat. Photon. **3**, 91 (2009).

[144] H. Lira, Z. Yu, S. Fan, and M. Lipson, Electrically driven nonreciprocity induced by interband photonic transition on a silicon chip, Phys. Rev. Lett. **109**, 033901 (2012).

[145] K. Fang, Z. Yu, and S. Fan, Photonic Aharonov-Bohm effect based on dynamic modulation, Phys. Rev. Lett. **108**, 153901 (2012).

[146] D. L. Sounas, C. Caloz, and A. Alù, Giant non-reciprocity at the subwavelength scale using angular momentum-biased metamaterials, Nat. Commun. **4**, 2407 (2013).

[147] S. Qin, Q. Xu, and Y. E. Wang, Nonreciprocal components with distributedly modulated capacitors, IEEE Trans. Microw. Theory Techn. **62**, 2260 (2014).

[148] N. A. Estep, D. L. Sounas, J. Soric, and A. Alù, Magnetic-free non-reciprocity and isolation based on parametrically modulated coupled-resonator loops, Nat. Phys. **10**, 923 (2014).

[149] R. Fleury, D. L. Sounas, C. F. Sieck, M. R. Haberman, and A. Alù, Sound isolation and giant linear nonreciprocity in a compact acoustic circulator, Science **343**, 516 (2014).

[150] N. Reiskarimian and H. Krishnaswamy, Magnetic-free non-reciprocity based on staggered commutation, Nat. Commun. **7**, 11217 (2016).

[151] D. L. Sounas and A. Alù, Non-reciprocal photonics based on time modulation, Nat. Photon. **11**, 774 (2017).

[152] T. Dinc, M. Tymchenko, A. Nagulu, D. Sounas, A. Alù, and H. Krishnaswamy, Synchronized conductivity modulation to realize broadband lossless magnetic-free non-reciprocity, Nat. Commun. **8**, 795 (2017).

[153] L. Bi, J. Hu, P. Jiang, D. H. Kim, G. F. Dionne, L. C. Kimerling, and C. A. Ross, On-chip optical isolation in monolithically integrated non-reciprocal optical resonators, Nat. Photon. **5**, 758 (2011).

[154] L. Fan, J. Wang, L. T. Varghese, H. Shen, B. Niu, Y. Xuan, A. M. Weiner, and M. Qi, An all-silicon passive optical diode, Science **335**, 447 (2012).

[155] B. J. Chapman, et al., Widely tunable on-chip microwave circulator for superconducting quantum circuits, Phys. Rev. X **7**, 041043 (2017).

[156] A. Kord, D. L. Sounas, and A. Alù, Magnet-less circulators based on spatiotemporal modulation of bandstop filters in a delta topology, IEEE Trans. Microw. Theory Techn. **66**, 911 (2018).

[157] T. Dinc, A. Nagulu, and H. Krishnaswamy, A millimeter-wave non-magnetic passive SOI CMOS circulator based on spatio-temporal conductivity modulation, IEEE J. Solid-State Circuits **52**, 3276 (2017).

[158] N. Reiskarimian, A. Nagulu, T. Dinc, and H. Krishnaswamy, Nonreciprocal electronic devices: a hypothesis turned into reality, IEEE Microw. Mag. **20**, 94 (2019).

[159] M. Duarte, C. Dick, and A. Sabharwal, Experiment-driven characterization of full-duplex wireless systems, IEEE Trans. Wireless Commun. **11**, 4296 (2012).

[160] A. Kord, D. L. Sounas, Z. Xiao, A. Alù, Broadband cyclic-symmetric magnetless circulators and theoretical bounds on their bandwidth, IEEE Trans. Microw. Theory Techn. **66**, 5472 (2018).

[161] J. Zhou et al., Integrated full duplex radios, IEEE Commun. Mag. **55**, 142 (2017).

[162] Y. Yu, G. Michetti, A. Kord, M. Pirro, D. Sounas, Z. Xiao, C. Cassella, A. Alù, M. Rinaldi, Highly-linear magnetfreee microelectromechanical circulators, IEEE J. Microelectromechanical Systems **28**, 933 (2019).

[163] Y. Yu, G. Michetti, M. Pirro, A. Kord, D. Sounas, Z. Xiao, C. Cassella, A. Alù, M. Rinaldi, Radio frequency magnetfree circulators based on spatialtemporal modulation of surface acoustic wave filters, IEEE Trans. Microw. Theory Techn. **67**, 4773 (2019).

[164] D. L. Sounas, J. Soric, and A. Alù, Broadband passive isolators based on coupled nonlinear resonances, Nat. Electron. **1**, 113 (2018).

[165] Y. Shi, Z. Yu, and S. Fan, Limitations of nonlinear optical isolators due to dynamic reciprocity, Nat. Photon. **9**, 388 (2015).

[166] D. L. Sounas and A. Alù, Fundamental bounds on the operation of Fano nonlinear isolators, Phys. Rev. B **97**, 115431 (2018).

[167] B. D. H. Tellegen, The gyrator, a new electric network element, Philips Res. Rept. **3**, 81 (1948).

[168] K. M. Adams, E. F. A. Deprettere, and J. O. Voorman, The gyrator in electronic systems, Advances in Electronics and Electron Physics. **37**, 79 (1975).

[169] M. Tymchenko, D. Sounas, and A. Alù, Composite Floquet scattering matrix for the analysis of time-modulated systems, IEEE international symposium on antennas and propagation and USNC/URSI National radio science meeting, 2017.

[170] E. I. Rosenthal, B. J. Chapman, A. P. Higginbotham, J. Kerckhoff, and K. W. Lehnert, Breaking Lorentz reciprocity with frequency conversion and delay, Phys. Rev. Lett. **119**, 147703 (2017).

[171] A. Kord, D. Sounas, A. Alù, Pseudo-linear time-invariant magnetless circulators based on differential spatiotemporal modulation of resonant junctions, IEEE Trans. Microw. Theory Techn. **66**, 2731 (2018).

[172] D. Sounas, N. A. Estep, A. Kord, A. Alù, Angular-momentum biased circulators and their power consumption, IEEE Antennas Wirel. Propag. Lett. **17**, 1963 (2018).

[173] D. J. Thouless, M. Kohmoto, M. P. Nightingale, and M. den Nijs, Quantized Hall Conductance in a two-dimensional periodic potential, Phys. Rev. Lett., 49, 405, (1982).

[174] Z. Wang, Y. D. Chong, J. D. Joannopoulos, and M. Soljacic, Nature, 461, 772, (2009).

[175] A. B. Khanikaev and G. Shvets, Two-dimensional topological photonics, Nat. Photonics, 11, 763, 2017.

[176] D. R. Hofstadter, Energy levels and wave functions of Bloch electrons in rational and irrational magnetic fields, Phys. Rev. B, 14, 2239, (1976).

[177] M. Hafezi, E. A. Demler, M. D. Lukin, and J. M. Taylor, Robust optical delay lines with topological protection, Nat. Phys. 7, 907, (2011).

[178] C. R. Dean, et al, Hofstadter's butterfly and the fractal quantum Hall effect in moire superlattices, Nature, 497, 598, (2013).

[179] B. Hunt, et al, Massive Dirac fermonins and Hofstadter butterfly in a van der Waals herterostructure,", Science, 10, 1237240, (2013).

[180] X. Ni, et al, Experimental observation of Hofstadter butterfly and fractal topological edge states in reconfigurable acoustic quasicrystals", Comm. Phys. 2, 55 (2019).

VITA

Zhicheng Xiao graduated from Hunan University with a B.S. in applied physics and M. Eng. in electrical engineering. He obtained his M.S. in electro-optics at the University of Dayton. He is now a Ph.D. candidate in the electrical and computer engineering department, at the University of Texas at Austin. His research interests include parity-time symmetry, exceptional points, nonreciprocity, topological physics.

Permanent address (or email): zhichengxiao@utexas.edu/xzc1987@gmail.com

This dissertation was typed Zhicheng Xiao.